

Cobalt-Catalyzed Olefin Hydrogenation

Dissertation

for the award of the degree
"Doctor rerum naturalium" (Dr.rer.nat.)
of the Georg-August-Universität Göttingen

within the doctoral program of the
Georg-August University School of Science (GAUSS)

submitted by:

Sier Sang

from Nei Mongol (China)

Göttingen, 2023

Thesis Committee

Prof. Dr. Sven Schneider

Institut für Anorganische Chemie, Georg-August-Universität Göttingen

Prof. Dr. Inke Siewert

Institut für Anorganische Chemie, Georg-August-Universität Göttingen

Prof. Dr. Dirk Schwarzer

Max-Planck-Institut für Multidisziplinäre Naturwissenschaften

Members of the Examination Board

Reviewer **Prof. Dr. Sven Schneider**

Institut für Anorganische Chemie, Georg-August-Universität Göttingen

Second Reviewer **Prof. Dr. Inke Siewert**

Institut für Anorganische Chemie, Georg-August-Universität Göttingen

Further members of the Examination Board

Prof. Dr. Dirk Schwarzer

Max-Planck-Institut für Multidisziplinäre Naturwissenschaften

Prof. Dr. Manuel Alcarazo

Institut für Organische und Biomolekulare Chemie, Georg-August-Universität Göttingen

Dr. Daniel Janßen-Müller

Institut für Organische und Biomolekulare Chemie, Georg-August-Universität Göttingen

Dr. Michael John

Institut für Organische und Biomolekulare Chemie, Georg-August-Universität Göttingen

Date of the oral examination: 15.05.2023

Acknowledgements

I would like to thank my thesis supervisor Prof. Dr. Sven Schneider, who provided me an opportunity to work on this interesting project and offered me his guidance and encouragement throughout the course of my research and dissertation.

I also want to thank Prof. Dr. Inke Siewert und Prof. Dr. Dirk Schwarzer to be my second and third supervisors and Prof. Dr. Manuel Alcarazo, Dr. Daniel Janßen-Müller and Dr. Michael John to be the member in the examination commission.

Till Schmidt-Räntsch, Niyaz Alizadeh and Zejie Lv, thank you for your contribution to make my dissertation better.

Furthermore, my thanks go to the people who assisted me in my research:

-Dr. Christian Würtele, Dr. Matthias Otte and Dr. Zejie Lv for the crystal measurement by X-ray diffraction.

-Dr. Finger Markus for density functional theory studies and your constant support during my stay.

-Dr. A. Claudia Stückl and Dr. Serhiy Demeshko for EPR and SQUID measurements and interpretation, respectively.

-The members of the analytical lab, the mass department and NMR department for measuring my samples.

-Kai-Sebastian Kopp for helping me when I messed with the lab.

-Dalila Griffin and Dr. A. Claudia Stückl for administrative support.

I want to express my gratitude to all the members in the working group for giving me advice and suggestions and encouraging me to blend in this friendly working group. Besides, I appreciate the pleasant and funny working environment provided by my office colleagues Niyaz Alizadeh, Till Schmidt-Räntsch, Anne Goetz and Katharina Wenderoth.

My very sincere thanks to Felix Schneck for giving me access to organometallic chemistry, thanks for your systematic guidance starting from my practical course to dissertation and always by my side to answer questions about the research.

Finally, I must send my gratitude to my family and my partner Marian Knolle for providing me with support and encouragement throughout my years of study.

Table of Contents

1	Introduction	1
1.1	Homogeneous olefin hydrogenation	2
1.2	Methods of mechanistic investigation	5
1.2.1	Spectroscopic methods	5
1.2.2	Kinetics	6
1.3	Homogeneous olefin hydrogenation with earth-abundant metals.....	8
1.4	Cobalt-catalyzed homogeneous olefin hydrogenation	12
1.4.1	Non-radical reactivity.....	12
1.4.2	Radical pathway via Hydrogen Atom Transfer (HAT)	20
1.5	Scope of this work.....	26
2	Results and Discussion	27
2.1	Synthesis and characterization of cobalt complexes.....	28
2.1.1	Synthesis and characterization of cobalt alkyl complexes	28
2.1.2	Synthesis and characterization of cobalt(II) hydride and cobalt(I) complexes	32
2.1.3	Reactivity of cobalt complexes with H ₂	48
2.2	Olefin hydrogenation with cobalt complexes.....	60
2.3	Photochemical reactivity of [CoH(L ³)] (9).....	62
2.3.1	Photochemical H/D exchange with deuterated solvents	62
2.3.2	Photochemical reactivity studied by transient spectroscopy	65
2.3.3	Photo-initiated cobalt catalyzed olefin hydrogenation	68
2.3.4	Mechanistic examinations	70
3	Conclusion	82
4	Experimental Section	87
4.1	General working techniques	88
4.2	Chemicals and purification methods.....	88
4.3	Analytical methods	89
4.3.1	NMR Spectroscopy	89
4.3.2	Mass Spectrometry	89
4.3.3	Elemental analysis (EA)	89
4.3.4	UV/Vis Spectroscopy.....	89
4.3.5	Infrared Spectroscopy (IR)	89
4.3.6	EPR Spectroscopy	90
4.3.7	Quantum yield determination.....	90

4.3.8	Magnetic measurements	91
4.3.9	Transient Spectroscopy.....	92
4.3.10	Computational Details.	93
4.4	Synthesis and characterization.....	93
4.5	Photo-induced cobalt-catalyzed olefin hydrogenation.....	101
4.5.1	Procedure for catalytic hydrogenation in different conditions	101
4.5.2	Spectroscopic data of substrate screening	102
4.5.3	Parahydrogen induced polarization	110
4.5.4	Radical clock experiments.....	113
4.5.5	Hammett Plot	117
4.5.6	Control reactions	121
4.6	Crystallographic Data	124
4.6.1	[CoCH ₂ SiMe ₃ (L ¹)] (1).....	124
4.6.2	[CoCH ₂ SiMe ₃ (L ²)] (2).....	126
4.6.3	[CoCH ₂ SiMe ₃ (L ¹ H)] (3 ^{BARF}).....	127
4.6.4	[CoH(L ¹)] (6).....	130
4.6.5	[CoH(L ³)] (9).....	131
4.6.6	[CoN ₂ (L ¹)] (10).....	133
4.6.7	[CoN ₂ (L ³)] (11).....	134
4.6.8	[CoH(L ¹ H)]BARF ₄ (7 ^{BARF})	136
4.6.9	[CoH(L ¹ H)]BF ₄ (7 ^{BF4})	137
4.6.10	[Co(L ¹ H)]BARF ₄ (5 ^{BARF}).....	139
4.6.11	[CoH(L ² H)]BARF ₄ (13 ^{BARF})	140
4.6.12	[CoF(L ³)] (18)	142
5	Reference.....	145
6	Appendix	153
6.1	List of compounds	154
6.2	List of abbreviations	155
6.3	Curriculum Vitae.....	157

1 Introduction

1.1 Homogeneous olefin hydrogenation

Hydrogenation is one of the most important catalytic methodologies in academia and industries.^[1–4] A commonly-used hydrogen source is hydrogen gas (H₂) itself, which is produced massively using fossils, in which 48% H₂ production comes from steam reforming of natural gas.^[5] Hydrogen gas is in most cases inert to organic compounds, arising from insufficient frontier orbital interactions between H₂ and unsaturated organic substrates.^[6] Therefore, catalysts, particularly metal catalysts, are needed to bridge H₂ and unsaturated compounds to accomplish chemical transformations. Catalysts for homogeneous hydrogenation are widely used in synthesis of fine chemicals and pharmaceuticals, while hydrogenation catalysis in petrochemical transformation is mainly operated with heterogeneous systems, which can be readily separated and recycled.^[1] Using defined transition metal catalysts, in contrast to their heterogeneous counterparts, provides the opportunity to fine-tuning chemo- and enantioselectivity through either metal substitution or ligand modification.^[1] In this introduction, only the well-defined catalysts for homogeneous olefin hydrogenation are reviewed.

Complexes bearing scarcest metal elements, such as Wilkinson's catalyst (Ph₃P)₃RhCl^[7,8], Noyori's catalyst Ru-BINAP complexes,^[9] Schrock-Osborn-type catalyst [(P–P)Rh(COD)]^{+ [10]}, and Crabtree's catalysts [Ir-(COD)(py)(PCy₃)]^{+ (COD = 1,5-cyclooctadiene, py = pyridine, Cy = cyclohexyl)^[11], have been introduced since early years in industrial applications, in which asymmetric hydrogenation in pharmaceutical productions is considered as the most valuable application.^[12]}

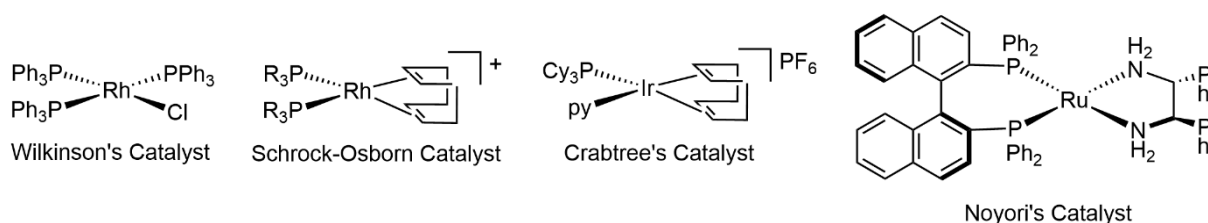
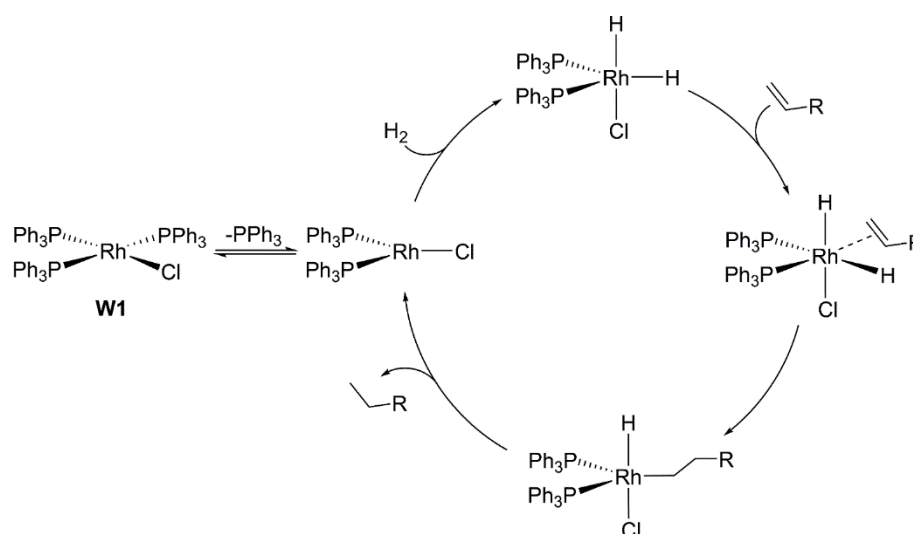


Figure 1: Commonly used precious metal catalysts for hydrogenation.

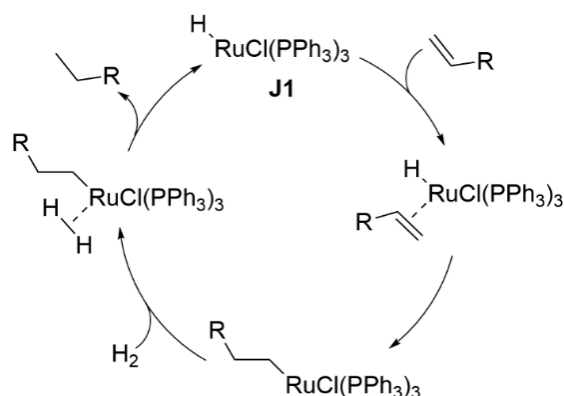
The Wilkinson's catalyst is one of the most classic and well-known catalysts for olefin hydrogenation using molecular hydrogen as reductant.^[7,13] Synthesis of the precatalyst (Ph₃P)₃RhCl was achieved by treating RhCl₃(H₂O)₃ with excess amount of PPh₃ in refluxing ethanol. PPh₃ acts as a reductant, while excess of PPh₃ avoids dimerization of the precatalyst.^[13,14] Steric bulk around Rh-center disfavors hydrogenation of sterically hindered substrates.^[13] However, hydrogenation of ethylene was not successful, which ended up with formation of Rh ethylene adduct. The mechanism of this reaction has been thoroughly investigated since its discovery in the 1960s.^[13–17] As shown in Scheme 1, the reaction is

initiated upon dissociation of one PPh₃, which is followed by oxidative addition of H₂ molecule. After coordination of alkene, migratory insertion of the alkene and subsequent reductive elimination of the alkane product complete one turnover.



Scheme 1: Proposed mechanism of **W1** catalyzed olefin hydrogenation.

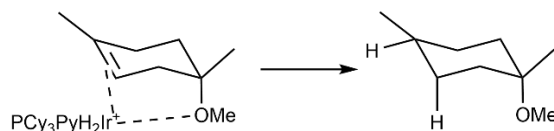
James and coworkers developed a ruthenium catalyst [HRuCl(PPh₃)₃] (**J1**), which can be prepared by reaction of RuCl₂(PPh₃)₃ with H₂ in the presence of NEt₃.^[18,19] In contrast to Wilkinson's catalyst, **J1** was proposed to activate H₂ after olefin coordination and insertion (Scheme 2). In the absence of H₂, alkene can be hydrogenated stoichiometrically by **J1**, accompanied by formation of a dimeric *ortho*-metallated complex via C–H activation of a phenyl group.^[19] This *ortho*-metallated complex reacts with H₂ to **J1**, suggesting a distinct catalytic pathway via H₂ activation by the dimeric intermediate, which is, however, kinetically less favored than the mechanism in Scheme 2.



Scheme 2: Proposed mechanism of olefin hydrogenation catalyzed by **J1**.^[19]

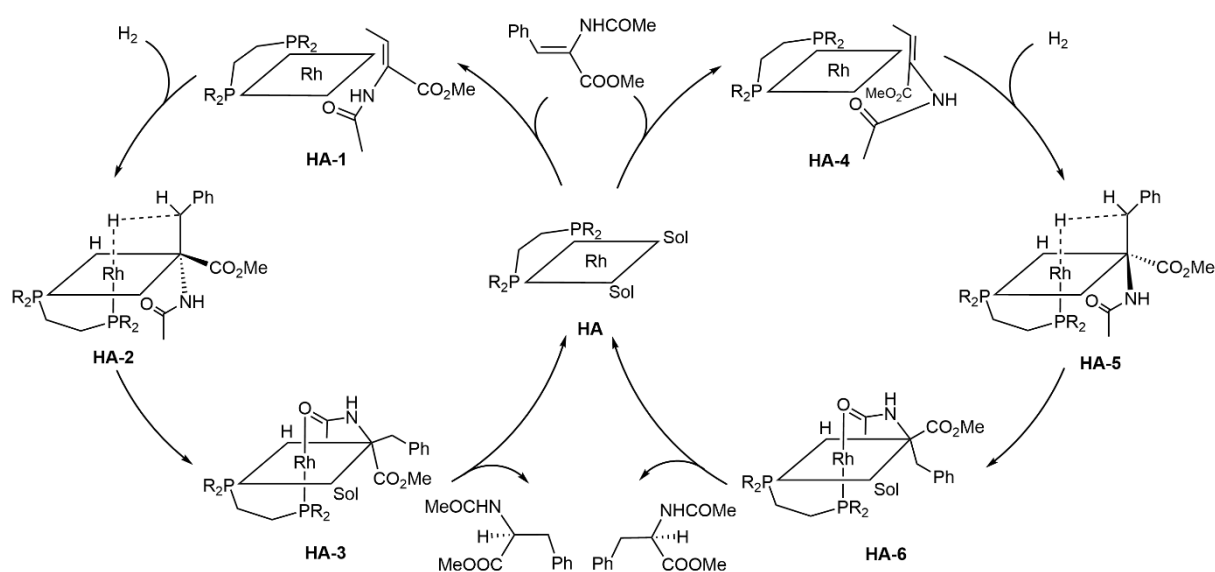
Crabtree and coworkers observed a directing effect in stereoselective hydrogenation of cyclohexene with Crabtree's catalyst [Ir(COD)(PCy₃)(Py)]PF₄.^[20] They observed a direct addition of H₂ to a C–C double bond from the face of the substrate containing the directing

group (Scheme 3), such as hydroxyl, carboxyl, carbonyl or methoxy groups. Dissociation of COD ligand leads to the formation of intermediate $[\text{Ir}(\text{PCy}_3)(\text{Py})]^+$ with 12-electron configuration, which enables H_2 activation and coordination directing group and C–C double bond to the metal center.



Scheme 3: Directing effect in hydrogenation of cyclohexene with the use of Crabtree catalyst.^[20]

Asymmetric hydrogenation is important in industrial applications, where often only one isomer is needed from racemic mixtures. A cationic rhodium catalyst ligated with a chiral chelating diphosphine ligand can catalyze hydrogenation of methyl-(*Z*)- α -acetamidocinamate with high enantiomeric excess (>99% at 25 °C).^[21] Halpern and coworkers proposed a mechanism involving substrate coordination as the first step, followed by H_2 activation and alkene hydrogenation (Scheme 4).^[21–23] Alkene coordination prior to H_2 activation can be contributed to the strong chelating ability of the substrate, which can be coordinated by the catalyst through either of the two faces, forming two diastereomers **HA-1** and **HA-4**. Slightly different thermodynamic stabilities lead to different concentrations of these two diastereomers, in which **HA-4** has the higher concentration. Oxidative addition of H_2 is the rate-determining step, as derived by kinetic studies. H_2 addition to the minor diastereomer **HA-1** is 500-times faster than the major intermediate **HA-4**, therefore, the time taken to complete one turnover differs from the left- and right catalytic cycle and then different amount of *S*- and *R*-isomers are formed. In this case, the predominant product enantiomer is the (*S*)-*N*-acetylphenylalanine methyl ester.



Scheme 4: Proposed mechanism of hydrogenation of methyl-(*Z*)- α -acetamidocinamate with a cationic Rh-catalyst. (Sol denotes a solvent molecule)^[21–23]

1.2 Methods of mechanistic investigation

Catalytic transformation is a sequence of elementary steps in a cycle, in which the active catalyst is generally regenerated at the end of the process.^[24] Mechanistic investigation provides us the knowledge of the sequence of each elementary step and the identity of the species participated in the catalytic cycle. Elucidating catalytic mechanisms is important and essential for assisting ligand design, selection of metals and reaction conditions, which have contributions to improve the overall rates of the catalysis, enhance the selectivity and reduction of by-product formation. In this section, some available approaches towards elucidation of the catalytic mechanisms in homogeneous catalysis will be briefly introduced.

1.2.1 Spectroscopic methods

Spectroscopic methods, such as nuclear magnetic resonance (NMR) and infrared (IR) spectroscopies, have been commonly used in the study of homogeneous catalysis.^[25] These methods have made important contributions in the elucidation of catalytic cycles by characterization of new species, including *in situ* spectroscopic studies of the resting states and other low-energy intermediates under catalytic or stoichiometric conditions, and monitoring the catalytic processes for kinetic study, or the spectroscopic measurements under various temperatures for thermodynamic investigation.

In situ monitoring techniques have been developed to study the nature of the resting states and low-energy intermediates in the catalytic cycle.^[25] Due to the limitations of measuring conditions, the *in situ* spectroscopic study is not always successful under actual catalytic conditions, for instance the catalytic temperature is outside of the range tolerated by the measuring devices or the concentration of active catalyst is too low to be detected with an acceptable signal-to-noise ratio. In those cases, small changes such as higher concentration of precatalyst or lower temperature enable the spectroscopic detection of the species involved in a catalytic run.

A special technique in *in situ* spectroscopic study is to use *para*-hydrogen (*p*-H₂, a spin isomer of hydrogen with antiparallel spins, Figure 2) in catalysis where H₂ is consumed. *p*-H₂ is a form of H₂, where two nuclear spins are aligned antiparallel. This technique, referred to as *para*-hydrogen induced polarization (PHIP), is a method to enable signal enhancement in NMR spectra or MIR images by transferring strongly antiphase nuclear spin of enriched *p*-H₂ into a substrate.^[26] PHIP NMR spectroscopy enables detection of reaction intermediates, which

cannot be characterized by conventional methods, providing further insight into reaction mechanism.^[26] Signal enhancement in hydrogenative PHIP arises from addition of *p*-H₂ to magnetically distinct positions of a substrate, while both hydrogen atoms should remain jointly coupled.^[27] *Para*-H₂ addition should occur faster than relaxation of nuclear spin populations in the reaction intermediates.^[27] Signal enhancement of other nuclei with lower sensitivity can also be detected via polarization transfer from *p*-H₂.^[27]

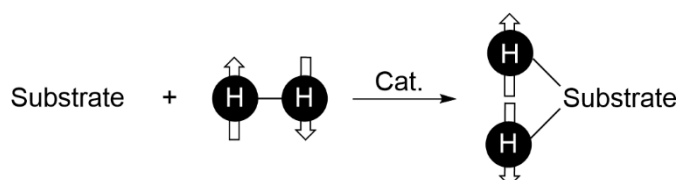


Figure 2: Addition of *para*-H₂ to a substrate.

1.2.2 Kinetics

Kinetics is a physical chemical method to understand the rates of the reactions, which provides information on the activation energy between the resting state and the transition state of the rate-determining step (RDS).^[24] A kinetic study can be carried out by monitoring of any reactants and/or products by suitable techniques. Catalytic intermediates are often not the target to be monitored, since the concentrations of which remains approximately constant during the catalysis.

Linear free-energy relationships (LFER) describe how the rates or the equilibrium changes for a given reaction by changing the reactants, which is an attempt to establish a quantitative relationship between the structure and activity.^[28] The experiment to probe the free-energy relationship should be conducted under nearly identical conditions, where only the reactants are varied slightly. The linear relationship can be correlated by Hammett equation: $\log(k/k_0) = \sigma\rho$, where k is the reaction rate with substituent R, k_0 is the reference reaction rate with an unsubstituted reactant, σ is substitution constant and ρ is reaction constant which depends on the reaction type. In non-radical reactions, different types of substitution constants, involving inductive and resonance effects, have been developed and used in various situations, such as σ , σ^+ , σ^- and σ_{mb} .^[28,29] In contrast to non-radical pathways, the free-energy relationship of radical reactions is additionally complicated by the spin delocalization effect of the substituents, involving the unpaired electrons.^[29] Different types of substitution constants have been developed to scale the spin delocalization effect, such as $\sigma_{\alpha^{\cdot}}$ and σ_{jj} .^[29,30] Some radical reactions need dual parameters to achieve better correlations, namely $\log(k/k_0) = \sigma^X\rho^X + \sigma^{\cdot}\rho^{\cdot} + C$.^[29]

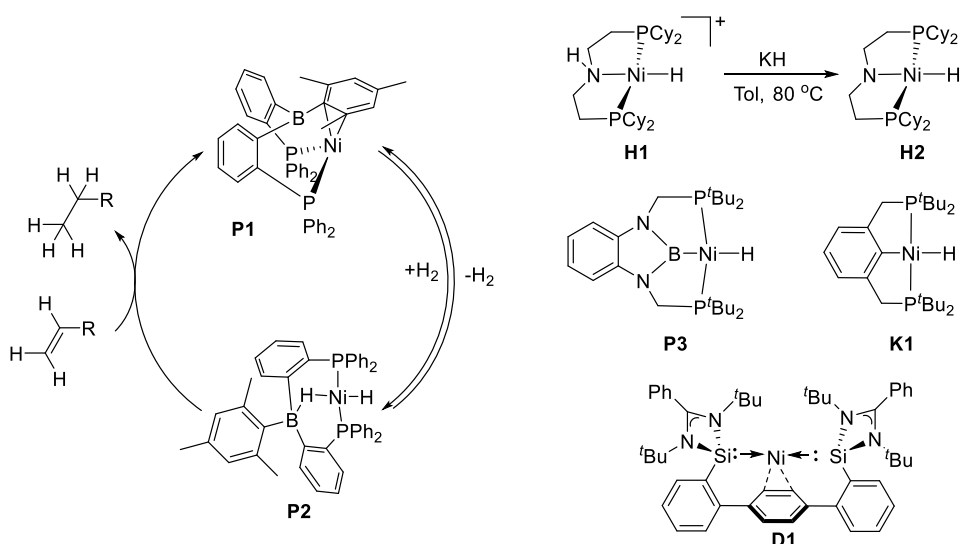
Kinetic isotope effect (KIE) is another physical chemistry tool to probe the rate-determining steps involving X–H/D bond cleavage or formation.^[31] A normal kinetic isotope effect ($k_X/k_H > 1$) can be observed in a situation, where substitution of H with D results in a greater stabilization of the resting state and a weaker stabilization of the transition state. In this case, the activation energy increases and the reaction rate decreases due to deuterium substitution. On the contrary, when the reactive center is far from the X–H/D bond or the only hybridation occurs in this bond in the slow steps, a small normal isotope effect or an inverse kinetic isotope effect ($k_X/k_H < 1$) can be expected.^[31] Beside the kinetic isotope effect, the catalytic mechanism can also be distinguished among several proposed mechanisms through isotope incorporation into a specific regio- or stereo-position of the products. Furthermore, isotope incorporation into incompletely converted reactants suggests a reversible reaction pathway.

1.3 Homogeneous olefin hydrogenation with earth-abundant metals

Second- and third-row late-transition metal complexes have been substantially used in current catalysis due to their high activity, selectivity and tolerance towards poisons.^[32] Even then, high costs and great environmental and health hazards of noble metals are driving people to search for more desirable replacements, such as abundant, less toxic and inexpensive first-row transition metals. In nature, enzymatic catalysts feature exclusively earth-abundant metals, accompanied by ligands with different steric and electronic properties around the metal centers, enabling substantial catalytic transformations.^[32] However, introduction of enzymes in industrial applications remains challenging, since many industrial processes are operated under different conditions, relative to conditions in the organisms, such as harsh temperatures, pH values, pressures and use of organic substrates and solvents.

Compared to 4d and 5d orbitals, 3d orbitals have poorer orbital overlap with bonding partners, resulting in more ionic character in M–X bonds and weaker ligand field splitting.^[32] High-spin electronic configurations, arising from weak ligand field splitting, result in one-electron bond activation reactivity of 3d transition metal complexes, such as homolytic cleavage of M–X bonds.^[33] Due to weaker metal-ligand bonds in 3d metal complexes relative to 4d and 5d counterparts, polydentate ligands are used to realize high thermal stability of 3d metal complexes.^[4] Utilization of sophisticated ligands with different steric and electronic natures tunes electronic configurations and reaction environments of the metal centers, enabling distinct redox processes and reaction mechanisms of catalytic transformations of organic substrates. With proper combinations and arrangements of transition metals and ligand systems, significant progress has recently been made in catalytic olefin hydrogenation using well-defined first-row transition-metal complexes under mild conditions.^[3,4,32,34–38]

Homogeneous hydrogenation catalyzed by nickel complexes is rarely reported despite their application in a range of catalytic transformations.^[39–47] The Peters group reported a diphosphane-borane nickel(0) complex **P1** for styrene hydrogenation at room temperature.^[40] H₂ activation was proposed to be mediated via metal-ligand cooperativity, in which H₂ is heterolytically added to metal and boron atoms, in the form of proton and hydride, respectively (Scheme 5, left).

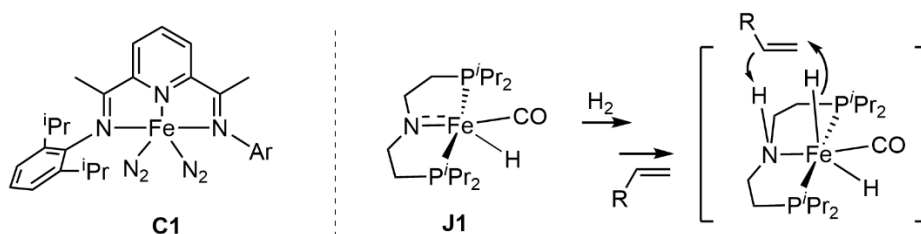


Scheme 5: Nickel-catalysts for olefin hydrogenation.^[41,43,44]

A cationic hydrido nickel(II) complex **H1** bearing a PNP pincer ligand with cyclohexyl substituents was developed by Hanson group, which was employed in hydrogenation of polar and nonpolar unsaturated bonds.^[43] **H1** was found to be a good catalyst for hydrogenation of certain alkenes at slightly harsh conditions (80 °C, 4 atm H₂), whereas, low conversions were observed in the transformation of sterically hindered alkenes and carbonyl substrates. Backbone-*N*-methylated analog was equally efficient towards hydrogenation, supporting of a metal-centered mechanism. Furthermore, neutral complex **H2** was tested in hydrogenation catalysis, which turned out to be less efficient than **H1**. Nickel(II) hydrido complex **P3** ligated with bis(phosphino)-boryl ligand catalyzes hydrogenation of styrene, 1-octene and *tert*-butyl ethylene at room temperature with 1 atm H₂.^[41] Kinetic studies indicate reversible olefin insertion, followed by hydrogenolysis of nickel alkyl intermediate. Compared to amino- (**H1**) and phenyl-based (**K1**) analogous, **P3** performs better in olefin hydrogenation, arising from activation of Ni–H bond by using strong-field boryl ligand in **P3**.^[41,44] Recently, Driess and coworkers reported a Ni(0)/Si(II) complex **D1**, which activates H₂ via metal-ligand cooperativity, enabling hydrogenation of olefins assisted by main group element.^[47]

Iron as the third most abundant metals in earth's upper crust has low cost and exhibits low toxicity, which are highly attractive in catalytic transformations mediated by iron complexes.^[4,6,38,48–50] C=C bond reduction catalyzed by iron-based catalysts has been gaining more and more interests.^[51–57] An iron carbonyl complex Fe(CO)₅ was first synthesized by Berthelot in 1891, which was introduced and explored thoroughly in olefin hydrogenation.^[58] Carbonyl ligand dissociation from Fe(CO)₅ was achieved by photolysis with near ultraviolet light, followed by H₂ activation and olefin reduction at the remaining coordination site.^[58] Recently, a highly efficient iron(0) bis(dinitrogen) complex **C1** bearing pyridine(diimine) (PDI) ligand was constructed and probed by Chirik and coworkers in alkene hydrogenation.^[52] With

0.3 mol% catalyst loading and 4 atm H₂, terminal alkenes can be reduced to completion within minutes at r.t., reaching up to a TOF of 1814 mol/h in 1-hexene hydrogenation, while more hindered internal and *gem*-disubstituted olefins required longer time to be hydrogenated under the same conditions. However, no reduction occurred with tri- or tetrasubstituted olefins, such as 1-methylcyclohexene and tetramethylethylene. Notably, olefin hydrogenation by **C1** was also performed in neat alkenes, proceeding to completion of 1-hexene and cyclohexene in 19 and 26 h, respectively, with 0.04 mol% catalyst loading and 4 atm H₂. Substrates with different functional groups were further probed by **C1**, in which olefins with primary amine and ketone moieties are less favored, due to coordination of functional groups to the iron center.^[59] Furthermore, isomerization of external olefins and *cis-trans* isomerization of pure internal olefins can also be achieved by **C1**.^[52] Mechanistic investigations suggest olefin coordination prior to oxidative addition of H₂, supported by isolation of an iron(0) alkyne complex and extreme N₂-affinity of an iron dihydrogen complex, which is stable only under H₂ atmosphere.^[52]

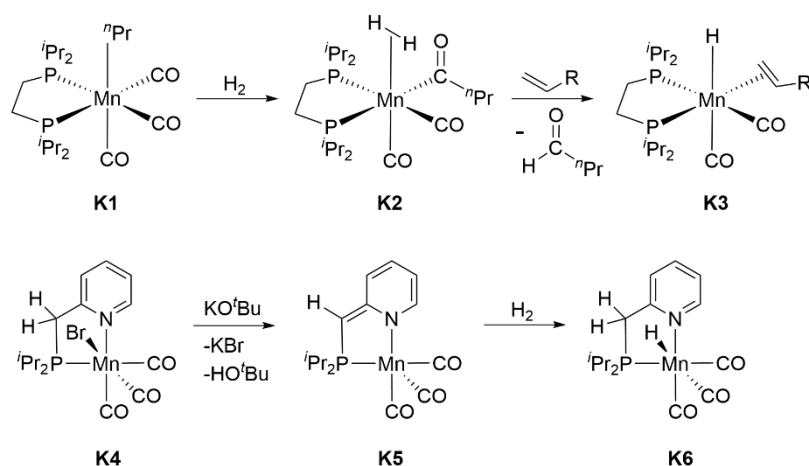


Scheme 6: Iron-based catalysts for olefin hydrogenation.^[51,52]

Polarized C=X (X = C or O) bond hydrogenation using an iron-based catalyst [(PNP^{iPr})Fe(H)(CO)] (**J1**) was reported by Jones and coworkers, which activates H₂ and reduces C=X bonds via metal-ligand cooperation.^[51] Hydrogenation of *para*-substituted styrene derivatives with electron-withdrawing groups are faster than that with electron-donating groups, while reduction of C=O bond is more favorable than reduction of C=C bond. Combined with computational studies, a consecutive metal-ligand cooperative pathway was proposed, which undergoes heterolytic addition of H₂ to Fe–N moiety, followed by hydride transfer from the Fe–H bond and proton transfer from amine in ligand backbone to accomplish reduction of unsaturated substrates (Scheme 6, right).

Catalytic hydrogenation of C–O and C–N bonds by manganese catalysts have achieved significant progress in recent years.^{[4,6,34,37,60][61]} The reported manganese catalysts often possess typical coordinatively saturated 18e⁻ configuration with two or three CO ligands, resulting in outer-sphere substrate binding, which favors hydrogenation of polar multiple bonds instead of C–C multiple bond reduction.^[34,62] Kirchner and coworkers enabled metal-centered H₂ activation and olefin insertion by using a well-defined Mn(I) alkyl carbonyl complex **K1**.^[63] Hydrogenation of mono- or disubstituted internal and external alkenes requires high pressure of H₂ (50 bar) and mild temperature (25 – 60 °C) with a catalyst loading of 2 mol%,

accomplishing good to excellent yields. **K1** shows functional group tolerance towards halides, hydroxyl group, ethers and esters. Mechanistic investigation was carried out computationally, suggesting precatalyst initiation via migratory insertion of CO ligand into Mn–C bond to form an active $16e^-$ Mn(I) catalyst **K2**, followed by H_2 coordination on the metal center. Hydrogenolysis of acyl ligand was proposed to be initiated by alkene coordination, forming Mn(I) hydride intermediate **K3** (Scheme 7, top). After one year, a new Mn-based catalyst **K4** was reported by Khusnutdinova and coworkers for olefin hydrogenation, bearing a non-pincer, picolylphosphine ligand.^[61] Harsh conditions, such as high pressure of H_2 (30 bar) and high temperature (100 °C), were required in catalytic hydrogenation of up to di-substituted olefins to achieve decent yields within 48 h. Control reactions and computations supported **K6** as an active intermediate in catalytic turnover, which is formed by deprotonation of the methylene arm on ligand backbone, followed by heterolytic H_2 cleavage (Scheme 7, bottom). Olefins were then reduced by **K6** via consecutive hydride transfer and proton transfer.



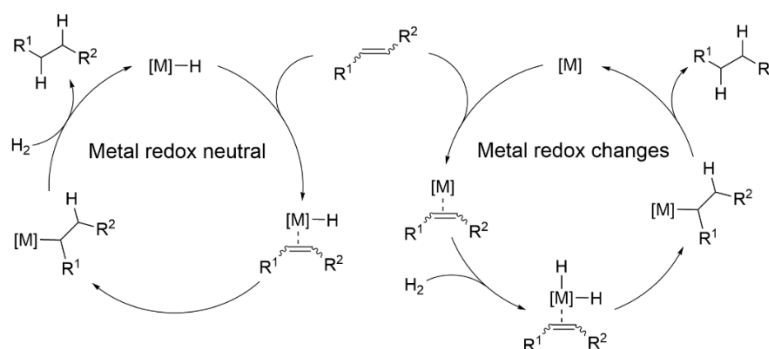
Scheme 7: Initiation step of olefin hydrogenation catalyzed by Mn(I) complex **K1** and **K4**.^[62,63]

1.4 Cobalt-catalyzed homogeneous olefin hydrogenation

Cobalt, as one of the first-row transition metals, is much cheaper and more abundant than its 4d- and 5d-counterparts. Introduction of cobalt in organic transformation is beneficial due to its low cost, biological compatibility and unique performances in homogeneous catalysis, which has been developed recently.^[3,4,38] Cobalt complexes can catalyze a range of organic transformations, including (de)hydrogenation, hydrosilylation, polymerization, etc.^[3,4,38] Alkene hydrogenation catalyzed by cobalt complexes can be traced back to the 1940s, in which hydrogenation of conjugated dienes was reported by Iguchi, using hydrido pentacyanocobaltate $[\text{CoH}(\text{CN})_5]^{3-}$.^[3] However, early examples were restricted in substrate scope and limitations in ligand modification. In recent years, development of cobalt complexes for olefin hydrogenation has achieved great progress, which benefits from rational design of supporting ligands, enabling expansion of substrate scope and enhancement of selectivity.^[3] The following review covers recent progress in homogeneous olefin hydrogenation catalysis using well-defined cobalt complexes, including their scope and proposed catalytic mechanisms.

1.4.1 Non-radical reactivity

Metal catalysts in olefin hydrogenation have generally two functions: H_2 activation and transfer activated hydrogen to unsaturated bond. Olefin hydrogenation catalyzed by noble metal complexes can be distinguished by two general mechanisms: the left cycle in Scheme 8 involves migratory insertion of substrate into $\text{M}-\text{H}$ bond, followed by H_2 cleavage and product formation. No metal-centered redox event occurs in whole process. In the right cycle in Scheme 8, H_2 oxidative addition to the metal center occurs before migratory insertion of the substrate, which features two-electron redox event on the metal center.^[6]



Scheme 8: Simplified metal-centered reactivity of C–C double bond hydrogenation catalyzed by metal complexes.^[6]

The Cationic cobalt(II) pincer precatalyst **H4** that was constructed by Hanson has been used to hydrogenate a broad range of substrates, including aliphatic and aromatic olefins, ketones, aldehydes and imines.^[64] **H4** can be generated *in situ* by protonation of the neutral cobalt(II) alkyl complex **H3** with Brookhart's acid (Figure 3, left). The protonated product **H4** is stable and isolable. **H4** was reported as a cationic amine-based complex.^[64] However, crystal structure of **H4** shows a short C–N bond in the ligand backbone (Figure 3, right), which suggests that **H4** might be an imine-based complex. Hydrogenation of terminal or 1,2-disubstituted olefins proceeded under mild conditions (2 mol% catalyst loading, 1 atm H₂ and at room temperature), giving decent yields within 24 h. The Zhang and Jones groups have extended the reactivity of **H4** in other catalytic transformations, such as ester hydrogenation, α -alkylation of ketones with primary alcohols, acceptorless dehydrogenation and olefin transfer hydrogenation using *iso*-propanol as hydrogen source.^[65–69]

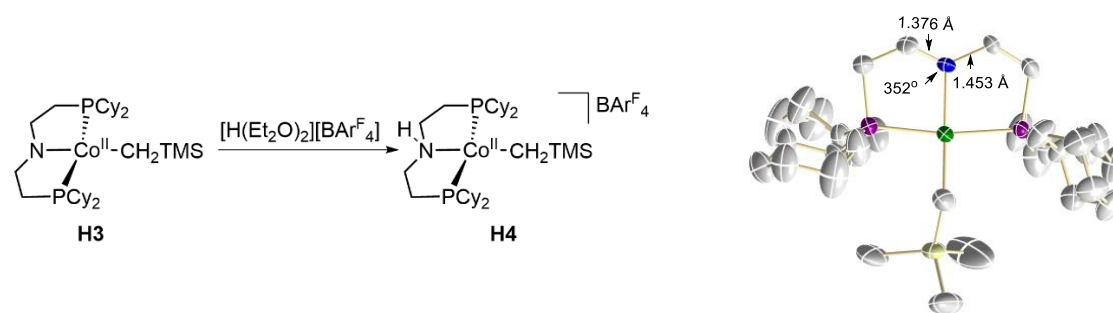
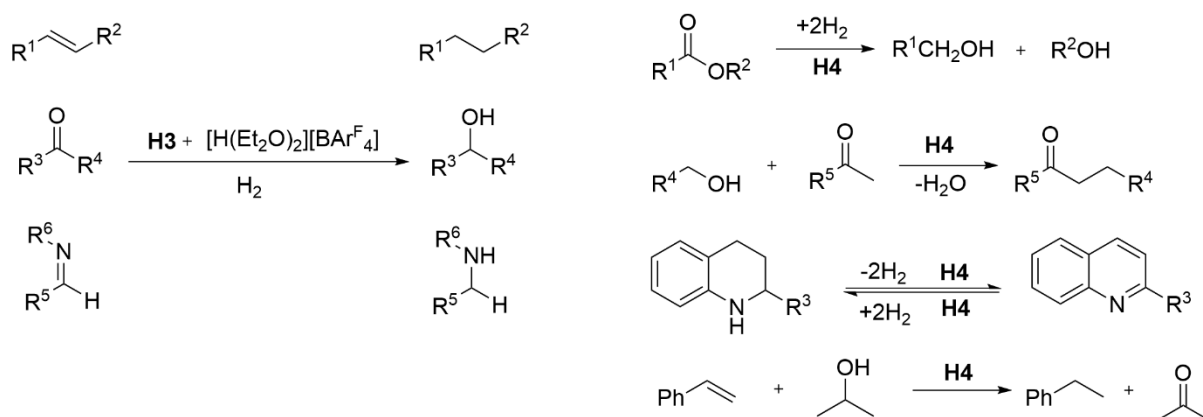


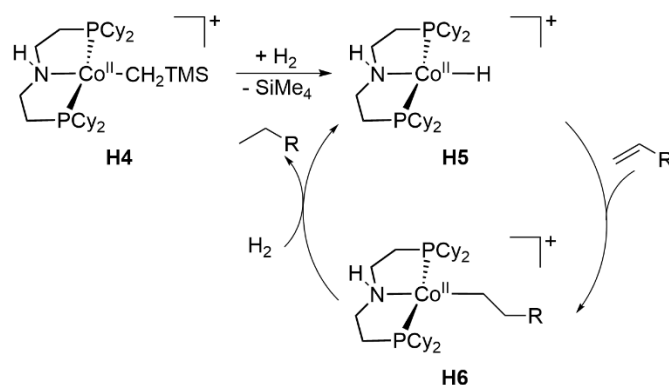
Figure 3: (Left) Protonation of **H3** with [H(Et₂O)₂][BARF₄]. (Right) Single crystal X-Ray structure of **H4**.^[64]



Scheme 9: Catalytic hydrogenation catalyzed by *in situ* generated and isolated pre-catalyst **H2**.^[64–69]

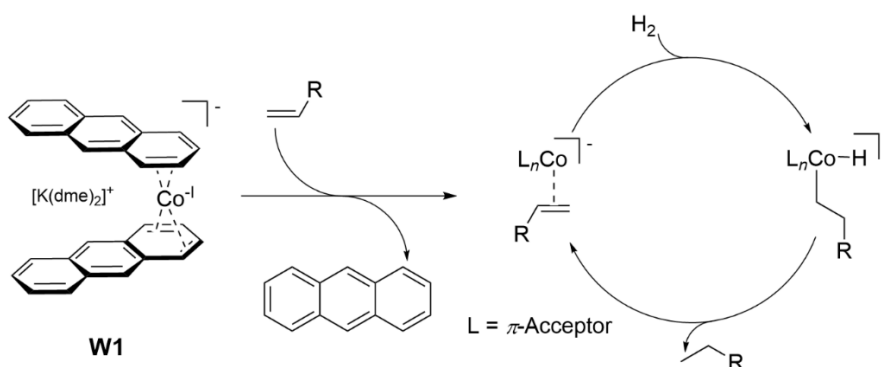
Control experiments were carried out to further study the reaction mechanism.^[64] **H4** was exposed to H₂ atmosphere, resulting in the formation of Me₄Si, as judged *in situ* by ¹H NMR spectroscopy. However, no signal related to a cobalt complex was observed. Chloroform was then added into the resulting solution, in which the cobalt chloride complex was formed. These observations suggest the formation of a cobalt monohydride intermediate **H5** upon H₂ addition, which was proposed as an initiation step of precatalyst **H4** (Scheme 10). However, isolation of

the hydride complex **H5** was not successful. Formation of **H5** was further supported by olefin isomerization and H/D scrambling crossover experiments. Backbone *N*-methylated complex **H4-Me** can hydrogenate olefins, ruling out the involvement of N–H moiety in olefin hydrogenation, suggesting metal-centered reactivity.^[70] DFT calculations agree with the formation of monohydride complex **H5** and proposed that olefin hydrogenation undergoes an insertion pathway.



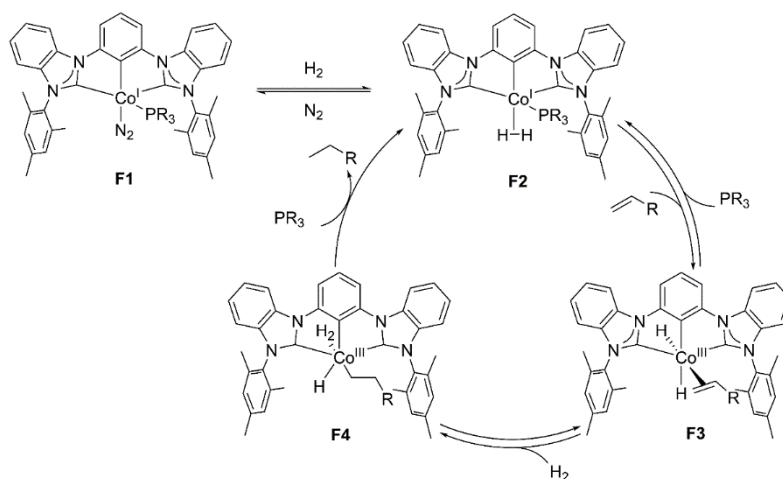
Scheme 10: Proposed mechanism of olefin hydrogenation catalyzed by **H4**.^[64,70]

Von Wangelin and co-workers developed a bis(anthracene)cobaltate complex **W1**, in which cobalt(-I) center is stabilized by π -coordination with non-heteroatom-based hydrocarbons.^[71] Hydrogenation by **W1** was first probed with styrene under mild conditions (1 mol% catalyst loading, 1 bar H₂ at 20 °C), giving a yield of 89% within 3 h. Hydrogenation of 2-Cl- and 2-Br-styrene was unsuccessful, instead, **W1** was deactivated via oxidation and the substrates were hydrodehalogenated, as observed in cross-coupling reaction catalyzed by **W1**.^[72] Hydrogenation of sterically more hindered substrates required a higher temperature (up to 80 °C) and higher pressure of H₂ (up to 10 bar) to achieve decent yields (60 – 100%). Functional group tolerance was shown in ethers and esters. Mechanistic studies indicate that catalytic turnover is initiated by ligand substitution with π -acidic substrates, which is followed by H₂ activation and olefin insertion.^[71,73] Introduction of strong coordination ligands reduced the activities of the catalyst, due to slow ligand substitution with the substrate.



Scheme 11: Generation of the active catalyst via ligand substitution by substrates.^[71]

Fout and coworkers introduced the cobalt(I) dinitrogen complex **F1** ligated with CCC-pincer ligand (CCC = bis(mesitylbenimidazol-2-ylidene)phenyl), which was shown to be an efficient catalyst for alkene hydrogenation^[74] and alkyne semi-hydrogenation^[75,76]. Terminal olefins can be reduced under ambient conditions (2 mol% of catalyst loading and 4 atm H₂ at RT), whereas hydrogenation of internal C=C bonds such as cyclohexene should be heated to 60 °C for 22 h to complete conversion. Functional groups such as hydroxyl groups, aldehydes, ketones and anhydrides are inert to this catalyst. *Para*-hydrogen (*p*-H₂) induced polarization transfer NMR spectroscopy was introduced to study the mechanism. Addition of *p*-H₂ to magnetically distinct positions of a substrate results in signal enhancement in NMR spectra over the normal Boltzmann distribution.^[26] Reaction of **F1** with *p*-H₂ displayed no signal enhancement in the ¹H NMR spectrum, suggesting the formation of cobalt(I) dihydrogen complex **F2** without H₂ cleavage. In contrast, addition of *p*-H₂ to a solution of **F1** and styrene resulted in polarization transfer to both styrene and ethylbenzene, suggesting that the styrene coordination onto the cobalt center is reversible. **F2** is proposed to be a resting state of the catalyst, which undergoes oxidative addition of H₂ to the cobalt center upon olefin coordination (Scheme 12). Deuterium incorporation to styrene further supports reversible olefin insertion to the Co–H bond. Notably, distinct preference between external and internal alkenes enables semi-hydrogenation of alkynes, resulting in the formation of corresponding *trans*-alkene products without further hydrogenation.



Scheme 12: Proposed mechanism of olefin hydrogenation catalyzed by **F1**.^[74]

As mentioned above, 3d transition metals prefer undergoing the single-electron redox event. However, catalytic hydrogenation mostly proceeds via multi-electron pathways, for which expensive and scarce noble metals are more suitable. In this regard, redox-active ligands provide an attractive solution. Redox-active ligands possess low-lying electron donor or acceptor orbitals, which are beneficial for ligand-centered redox events owing to their extended π -system, enabling 3d-metal complexes to participate in bond-breaking and -making processes in various organic transformations.^{[3,4,35,77,78][49]}

Cobalt has a preference of +2 and +3 oxidation states, hence, a strong π -accepting ligand is necessary to stabilize low spin Co(I).^[79] Bis(imino)pyridine ligands display a non-innocent character and are able to accept one electron from the metal centers.^[79,80] This type of ligand has two low-lying π^* orbitals composed of two imine π^* orbitals, with anticipation of an aromatic system of pyridine moiety.^[81] In contrast to CO, which has strong interaction with metal center, $d - \pi^*$ orbital overlap between the metal center and the bis(imino)pyridine ligand is relatively weak, hence electrons from the metal center can be temporarily transferred and stored on the ligand, enabling stabilization of unusual oxidation states of the metal center.^{[81][34]}

Gal and Budzelaar reported two bis(imino)pyridine Co(I) alkyl complexes for olefin hydrogenation catalysis.^[77] Both complexes can be distinguished by different substituents on imine nitrogen atoms. They exhibit unusual bonding features and chemical shifts in ^1H NMR spectra, relative to their closed-shell Rh(I) and Ir(I) analogues.^[80] DFT calculations by Budzelaar demonstrated a low spin Co(II) center antiferromagnetically coupled with a bis(imino)pyridine radical anion. Furthermore, the transition ($3d_{z^2} \rightarrow \pi^*$) between ground state and triplet state is thermally accessible, resulting in the unusual NMR shifts from these cobalt complexes. Catalytic conversion of substrates is linearly related to H_2 pressure, whereas, non-linear relationship is observed with catalyst loading, which is presumably attributed to a bimolecular catalyst deactivation event. Addition of H_2 to **B1** with 2,6-diisopropylphenyl substituents resulted in the formation of an unknown species with diamagnetic resonances, which was proposed to be a hydride complex, as judged by ^1H NMR spectroscopy.^[80]

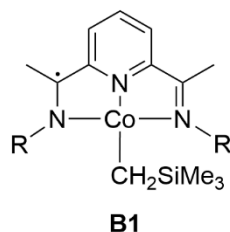
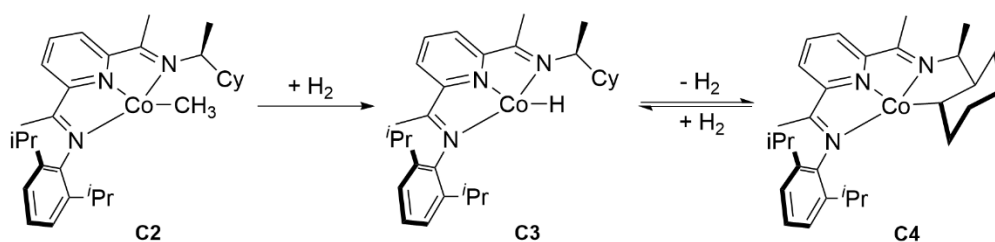


Figure 4: Bis(imino)pyridine ligated Co(I) complex (R = 2,6-diisopropylphenyl or hexyl).^[79]

In 2012, a series of C_1 -symmetric cobalt complexes were constructed by Chirik and coworkers for asymmetric alkene hydrogenation, using the same platform as **B1** with either cyclohexyl or *tert*-butyl substituents on chiral carbon atoms.^[82] One of donor sites of the pincer ligand connects with a large 2,6-diisopropylphenyl ring, which prevents dimerization of the monomeric cobalt complexes to catalytically inactive species. Cobalt methyl complex **C2** can be obtained by methylation of its chloride precursor with methyl lithium (MeLi). Methyl ligand in **C2** is slightly lifted off the plane, arising from steric hindrance from a large cyclohexyl group on the chiral carbon atom. **C2** possesses a low-spin Co(II) center, which is antiferromagnetically coupled to its bis(imino)pyridine radical ligand, supported by metrical parameters of bis(imino)pyridine chelate. Complex **C2** converted to a hydride complex **C3** upon addition of H_2 , which was

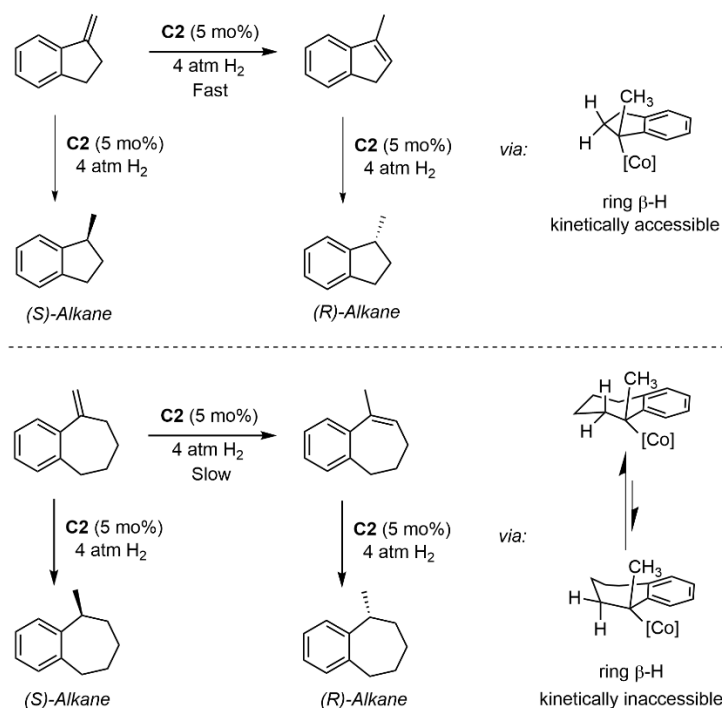
characterized by NMR spectroscopy and X-ray diffraction. **C3** is stable under N₂ atmosphere for hours at room temperature but converts directly to a cyclometalated product **C4** under vacuum.



Scheme 13: The reactivities of **C2** under H₂ atmosphere.^[82,83]

C2 was proved to be an outstanding precatalyst for asymmetric hydrogenation of alkenes. Hydrogenation of α -substituted styrene derivatives was conducted under mild conditions (5 mol% catalyst loading, 4 atm H₂) for 24 h, achieving excellent yields (over 90%) and enantiomeric excesses (over 90% ee in substrates with electron-donating group on *para*-position), in which substrates with electron-donating groups on the *para*-position provide higher enantioselectivity than those with electron-withdrawing groups.

The Substrate scope was further expanded to benzo-fused five-, six- or seven-membered exo- and endocyclic alkenes.^[83] Different stereoselectivity was observed in five- and seven-membered exocyclic alkenes, arising from competing reactions between alkene hydrogenation and alkene isomerization (Scheme 14). Under standard catalytic conditions, rapid isomerization occurs in alkenes with five-membered ring, resulting in the formation of endocyclic alkenes, which is further selectively hydrogenated to (*R*)-1-methylene (Scheme 14, top). In contrast, exocyclic substrates with a seven-membered ring undergo relatively slow isomerization to their endocyclic isomer. Both isomers are hydrogenated to a mixture of (*S*)- and (*R*)-1-methylbenzosuberan (Scheme 14, bottom). Therefore, stereoselectivities of **C2**-mediated hydrogenation originate not only from the orientation of alkene substrates against unfavorable steric interactions with larger substituent on pincer ligand, but also from the potential isomerization of prochiral substrates.



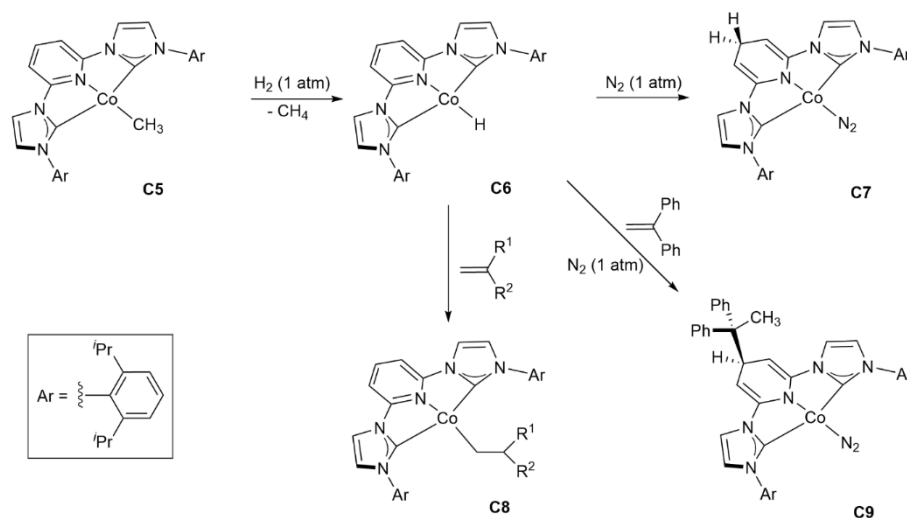
Scheme 14: Selectivity between hydrogenation and isomerization in five- and seven-membered rings.^[83]

Asymmetric hydrogenation of alkenes was further expanded by Chirik and coworkers to trisubstituted 1,1-diboryl alkenes, catalyzed by a variant of **C4** with *tert*-butyl substituents in place of the cyclohexyl substituents.^[84] Introduction of the boronate substituents in substrates overcomes the steric effect of hydrogenating hindered alkenes. The Yield and enantioselectivity can be controlled by the steric and electronic properties of the boronate substituents.

A highly active precatalyst **C5** for alkene hydrogenation was constructed by Chirik and coworkers, using a redox-active pyridine-based ligand.^[85] Sterically hindered trisubstituted alkenes can be hydrogenated in a yield greater than 95% under mild conditions (5 mol% catalyst loading of **C5**, r.t. and 4 atm H₂ within 10 h), including one of the most challenging substrates tetramethylethylene, which gave a decent yield at higher temperature (15% at r.t. or 69% at 50 °C for 24 h). The Electronic structure of **C5** was studied spectroscopically and computationally, revealing a low-spin Co(II) metal center antiferromagnetically coupled to the ligand-centered radical. Reaction of **C5** and H₂ resulted in rapid formation of methane and cobalt hydride complex **C6**, which decomposed slowly, as monitored by ¹H and ¹³C NMR spectroscopy. Reactivity of in situ formed **C6** was further probed with N₂ and alkenes with different sizes. Upon addition of N₂ (1 atm) into the solution of **C6**, a dinitrogen complex **C7** was formed via migratory hydride transfer to 4-position of the backbone ring (Scheme 15).

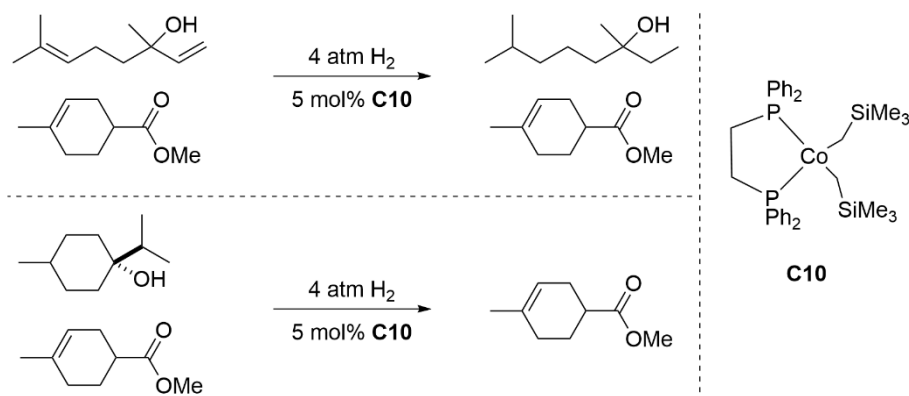
C7 was labile and slowly decomposed to unknown species. Moreover, treatment of 1,1-diphenylethylene to **C6** resulted in the migration of the alkyl group to the backbone, whereas

with less-hindered alkenes, such as 1-butene and 1,1-dimethylethylene, only insertion products were identified in the reaction mixture. The computational studies suggest a pyridine-localized radical, which likely contributes to the migration of the hydride and alkyl groups.



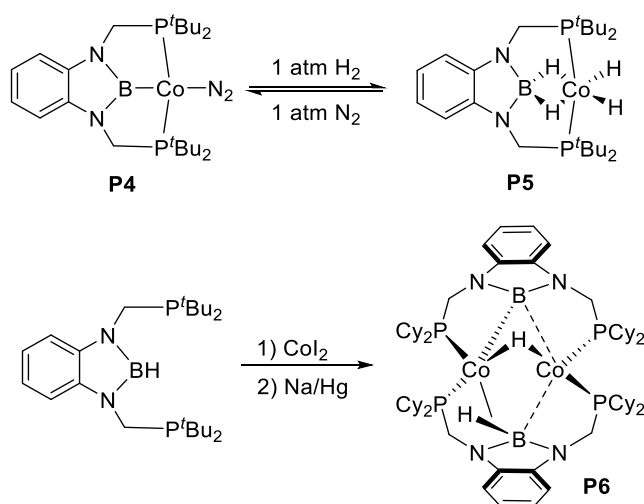
Scheme 15: Reactivity of **C5** and **C6** ($R^1 = \text{CH}_2\text{CH}_3$, $R^2 = \text{H}$ or $R^1 = R^2 = \text{CH}_3$).^[86]

A series of low-spin Co(II) dialkyl complexes with four achiral bidentate phosphine ligands was synthesized by Chirik and coworkers.^[87] Hydrogenation of di- or tri-substituted substrates by these cobalt precatalysts gave decent yields under mild conditions (1 - 5 mol% catalyst loading, 4 atm H_2 and at r.t.). Precatalysts with less hindered and more electron-donating phosphine substituents showed better catalytic activity. Notably, introduction of the hydroxy group in substrates can significantly enhance the catalytic activity, enabling hydrogenating of hindered alkenes, such as tetramethylethylene (< 5%) and 2,3-dimethylbut-2-en-1-ol (86%). Control experiments with **C10** (Scheme 16) precluded the possibility of the precatalyst activation by the hydroxyl group, suggesting an intramolecular hydroxyl functionality in hydrogenation of hindered alkenes.



Scheme 16: Control experiments to elucidate the functionality of hydroxyl group in alkene hydrogenation.^[87]

H₂ activation and the following hydride transfer to unsaturated substrates can be mediated by boron-centered ligands (*tert*-butyl- or cyclohexyl-substituted bis-phosphino boryl), as reported by Peters and coworkers.^[41,88] Exposure of *tert*-butyl substituted cobalt complex **P4** to 1 atm H₂ yielded a monomeric dihydridoborato cobalt dihydride complex **P5**, supported by NMR, IR spectroscopy and X-ray diffraction.^[88] Hydrogenation of terminal olefins, such as 1-octene and styrene, with 2 mol% catalyst loading of **P4**, achieved a turnover frequency of 1000/h under 1 atm H₂ at ambient temperature. However, internal alkenes cannot be reduced by **P4**. Bimetallic cyclohexyl analogue **P6** also serves as a catalyst for alkene hydrogenation, which catalyzed hydrogenation of styrene and 1-octene two orders of magnitude slower than **P4**.^[41] In contrast to **P4**, catalytic hydrogenation of internal olefins, such as cyclooctene and nonbornene, was achieved by **P6** under 1 atm H₂ at r.t..

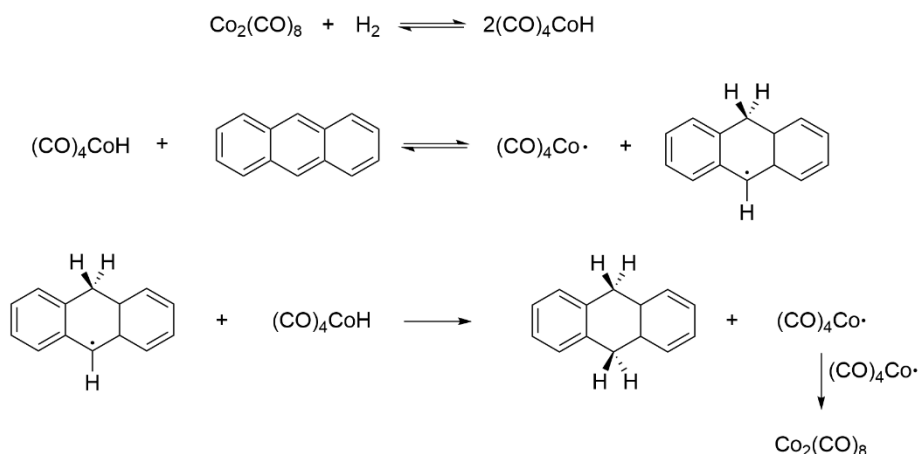


Scheme 17: H₂ activation by **P4** and synthesis of **P6**.^[41,88]

1.4.2 Radical pathway via Hydrogen Atom Transfer (HAT)

HAT from metal hydrides via homolytic M–H bond cleavage has provided an attractive alternative to catalytic olefin hydrogenation.^[38,89] First-row transition metal hydride complexes often have weak M–H bonds making them the best candidates in hydrogenation involving HAT.^[58]

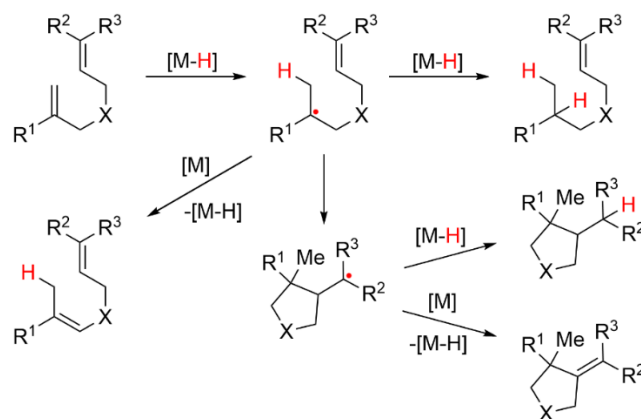
In the 1950s, Orchin and coworkers reported synthesis of a dinuclear cobalt carbonyl complex Co₂(CO)₈ and its reactivity in the hydrogenation of polycyclic aromatic compounds at ca. 190 °C under syngas.^[90–93] Halpern proposed a mechanism involving HAT (Scheme 18), supported by H/D exchange between DCo(CO)₄ and anthracene. Further evidence for a HAT pathway was given by a good correlation between reaction rates and radical localization energies of substrates.^[94]



Scheme 18: Hydrogenation of anthracene by $\text{Co}_2(\text{CO})_8$ with syngas.^[94]

Further evidence for a radical mechanism was provided by the chemically induced dynamic nuclear polarization effect (CIDNP), which was observed in the reaction of $\text{HCo}(\text{CO})_4$ and 1,1-diphenylethylene by ^1H NMR spectroscopy.^[95] Collision of a metal hydride complex and substrate results in one hydrogen atom transfer (HAT), generating a carbon-centered radical and a metalloradical species, which are packed in a “cage” of solvent molecules.^[96] The CIDNP effect arises from the reversible formation of a radical pair in a solvent cage, which results in non-Boltzmann spin state distributions, enabling observation of enhanced absorption or emission resonances by NMR spectroscopy.^[97] A reversible radical-pair mechanism can also be evidenced by the inverse isotope effect, which was observed in the hydrogenation of α -methylstyrene with a carbonyl manganese hydride complex ($k_{\text{H}}/k_{\text{D}} = 0.4$, at 65 °C).^[98]

Once the organic radical intermediate escapes from the solvent cage, it undergoes hydrogenation, reductive cyclization or isomerization with either the metalloradical intermediate or another hydride complex to form different products (Scheme 19).^[99] This methodology has been introduced by Shenvi, Norton and Herzon in the synthesis of complex molecules and natural products using first-row transition metals.^[38,100] Shenvi and coworker used $\text{Co}(\text{dpm})_2$ and $\text{Mn}(\text{dpm})_3$ (dpm = dipivaloyl methane) as catalysts for olefin hydrogenation via HAT, using PhSiH_3 or $\text{Ph}(\text{iPrO})\text{SiH}_2$ as hydrogen source and stoichiometric *tert*-butyl hydroperoxide (TBHP) as oxidant in isopropanol (iPrOH).^{[101][102]} TBHP can re-oxidate the catalysts and suppress side-reactions, such as hydrosilylation.^[38] High chemoselectivity and functional group tolerance were achieved with these catalytic systems, including tolerance of C–X (X = F, Cl, Br, I) bonds. Herzon observed that the hydrogenation of α -halogen-substituted olefins is more favorable, arising from the stabilization effect of the adjacent halogen atoms in the carbon-centered radicals, which avoids formation of the alkyl-metal intermediates that are further converted to the dehalogenated products.^[103]



Scheme 19: Hydrogenation, isomerization and cyclization reactions via metal hydride hydrogen atom transfer.^[96]

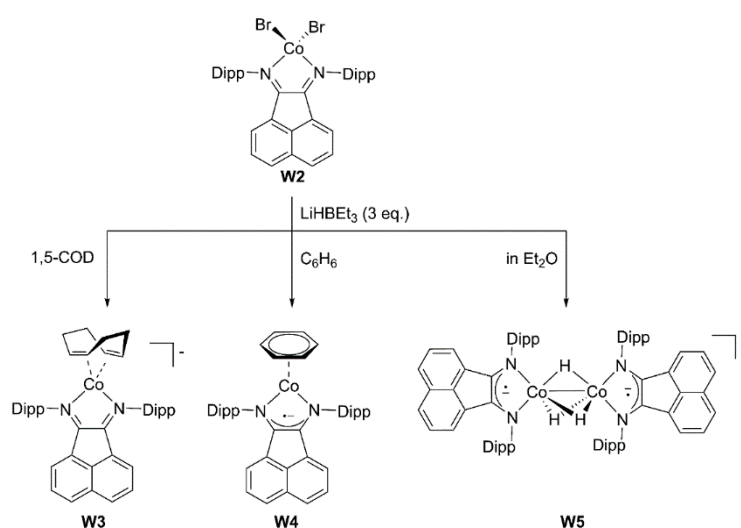
The Reaction rate of hydrogenation via HAT depends on the steric and electronic nature of the metal catalysts and substrates.^[101,103–106] In regard to metal hydrides, the reaction rate of HAT depends on the bond dissociation energy (BDE) of M–H bonds and the steric natures of chelating ligands.^[58] The Radical localization ability and steric natures of the substrates also play roles in the reaction rate of HAT.^[58] For example, HAT from $\text{dppe}(\text{CO})_4\text{VH}$ (BDE = 57.5 kcal/mol) (dppe = 1,2-bis(diphenylphosphino)ethane) to styrene is about ten times faster than HAT from $\text{Cp}(\text{CO})_3\text{CrH}$ (BDE = 62.2 kcal/mol) (Cp = cyclopentadienyl) to the substrate.^[107] Concerning the radical stabilization ability, Herzon reported that hydrogenation of 2,2-disubstituted and trisubstituted alkenes by $\text{Co}(\text{acac})_2$ catalyst were favored over monosubstituted alkene.^[103] Besides, hydrogenation of conjugated diene was conducted by $\text{HMn}(\text{CO})_5$ and $\text{HCo}(\text{CO})_4$, which produced monoalkene via the formation of stabilized allylic radical intermediate, whereas, further hydrogenation of the resulting monoalkene was unsuccessful, indicating the importance of radical stabilization in HAT reactions.^[108]

Olefin hydrogenation catalyzed by $\text{CpCr}(\text{CO})_3\text{H}$ used H_2 as reductant.^[109,110] $\text{CpCr}(\text{CO})_3\text{H}$ is a typical low-spin hydride complex with a strong field ligand, which possesses a M–H bond with BDE of 62.2 kcal/mol^[107]. H_2 activation by metal complexes ($2\text{M} + \text{H}_2 \rightarrow 2\text{M-H}$) is thermodynamically accessible, if the BDE of the M–H bond is greater than 56 kcal/mol, which includes the entropic factor of 8 kcal/mol at room temperature.^[111] However, high M–H bond strength thermodynamically disfavors the first HAT to unactivated alkenes due to relatively low BDE of C–H bond in a carbon-centered radical intermediate. In contrast, metal hydrides with weak M–H bond strengths favor hydrogenation of unactivated olefins via HAT, whereas H_2 activation by these catalytic systems is thermodynamically unfavorable.^[96] In this case, alternative reductants, such as organosilanes, and oxidants are introduced to regenerate the active metal hydride species for further HAT.^[38]

Bis(imino)acenaphthenes, (BIANs) as redox-active ligands, are capable of accommodating up to four electrons, enabling their application in catalysis with first-row transition metals.^[112] Von

Wangelin and coworkers introduced a cobalt-based catalyst ligated with bidentate BIANs ligand, which benefits hydrogenation of some challenging substrates, such as tetrasubstituted alkene.^[113] Olefin hydrogenation was probed with (^{Dipp}BIAN)CoBr₂ (Dipp = 2,6-diisopropylphenyl) (**W2**) (3mol% catalyst loading), which was initiated by addition of LiHBEt₃ (9 mol%). Up to 80 °C heating and 10 bar H₂ are required to reach high efficacy in hydrogenation of tri- and tetrasubstituted substrates within 24 h, such as α -pinene (92% yield, 10 bar H₂, 20°C in 24 h), myrcene (76% yield, 10 bar H₂, 20°C in 24 h) and α,β,β -trimethylstyrene (> 99% yield, 10 bar H₂, 80°C in 24 h). Functional group tolerance of halogenides, ethers and esters is only possible, when LiHBEt₃ is added prior to substrate addition.

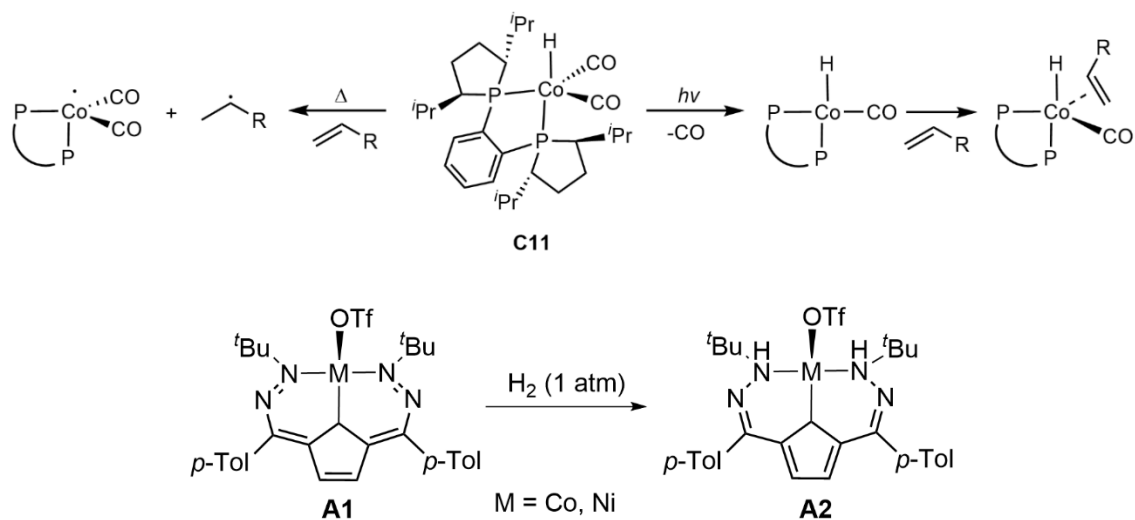
Mechanistic investigation indicates a radical pathway via HAT, supported by the hydrogenation of a radical clock test substrate α -cyclopropylstyrene to a ring-opened product under standard conditions.^[113] Furthermore, a zero-order rate law was derived towards substrate, indicating that olefin coordination is unlikely to be the rate-determining step. Kinetic poisoning experiments were conducted with mercury, P(OMe)₃ and dibenzo[a,e]cyclooctatetraene to rule out the possibility of heterogeneous catalysis. Catalytically relevant complexes **W3-W5** were isolated and probed in 1,5-cyclooctadiene with or without additives. Without any additives, **W3** and **W5** displayed significantly lower efficacy than *in situ* formed catalyst. In contrast, addition of BEt₃ (3 eq.) in the reaction mixture resulted in an enhancement of the catalytic performance, indicating Lewis acid-assisted catalysis. The best performance of **W5** was achieved by addition of LiHBEt₃ (0.5 eq. with respect to **W5**), indicating a function of **W5** as a reservoir for monohydride complexes, which is consistent with a mechanism involving mononuclear metal complexes, supported by the first order rate law towards [Co].



Scheme 20: Synthesis and isolation of catalytically relevant cobalt complexes derived from **W2**.^[113]

Light has been becoming a new energy source in organic synthesis catalyzed by transition-metal complexes, either direct or indirect (for example, a photocatalyst transfers energy to a secondary catalyst) energy transfer from excited-state of transition metal complexes to the substrates.^[114–120] The use of light in catalysis coupled with transition metal complexes provides the opportunity to either switch the on/off states of the catalysis, or change the catalytic mechanisms and selectivity differing from those under thermal conditions.^[115,117,118]

In 2021, Chirik discovered a cobalt(I) hydride complex **C11**, which performs catalytic olefin hydrogenation either thermally or photochemically.^[115,121] Thermal hydrogenation is achieved via HAT to substrates (Scheme 21, top), supported by a relatively weak Co–H bond (BDFE = 54 kcal/mol), derived by DFT calculations. HAT from **C11** to TEMPO and the ring-opening hydrogenation of the radical clock test substrate further support the radical pathway under thermal conditions. Furthermore, the reaction of styrene and deuterated analogue **C11-D** under 1 atm CO resulted in deuterium incorporation in styrene and ethylbenzene, indicating a reversible HAT and that dissociation of CO was unnecessary in thermal hydrogenation. In contrast, irradiation with blue light induces dissociation of one carbonyl ligand from **C11**, enabling a consecutive coordination and insertion of a substrate to the cobalt center (Scheme 21, top). Hydrogenation of α -methylstyrene by **C11** (5 mol%) under photochemical conditions gave isopropylbenzene in almost 100% yield over 18 h, whereas hydrogenation at 100 °C without irradiation achieved 37% yield over the same period. Less than 0.5% yield was observed without heating and light. In substrate scope screening, the photocatalytic method shows enhanced reactivity to sterically hindered substrates, including hydrogenation of tri-substituted substrates in good yields. After one year, Anderson and coworkers reported cobalt- and nickel-based catalysts (Scheme 21, bottom) for hydrogenation, ligated with dihydrazonopyrrole scaffold.^[99,122] Both complexes can activate H₂ without redox changes of metal centers, enabling ligand-centered storage of protons and electrons, which is an unusual case of metal-ligand cooperation.^[122] The cobalt-based catalyst **A1-Co** was employed in olefin hydrogenation. A radical mechanism via HAT was suggested by hydrogenation of the radical clock test substrate to exclusively ring-opened products.^[99]



Scheme 21: (Top) Thermal and photochemical hydrogenation of alkenes by **C11**. (Bottom) H₂ activation by **A1**.^{[115][99]}

1.5 Scope of this work

The increasing application of cobalt complexes in homogeneous catalysis provides us the major incentive for thermochemical and kinetic studies of olefin hydrogenation catalyzed by cobalt complexes. Computational and experimental studies proposed mechanisms involving migratory insertion of unsaturated substrate into M–H bond, forming a metal hydrocarbyl key intermediate.^[70,123] However, the structural or spectroscopic characterization of these proposed hydride or alkyl key intermediates is challenging. Well-defined cobalt hydride complexes have been rarely reported for olefin hydrogenation.^[85,124–126] For this concern, synthesis and isolation of cobalt(II) hydride complexes will be performed with different derivatives of *tert*-butyl substituted PNP-pincer ligands (Figure 5), starting from cobalt chloride counterparts as precursors reported by our group.^[127] The hydride complexes were then fully characterized and probed in olefin hydrogenation using H₂ as hydrogen source.

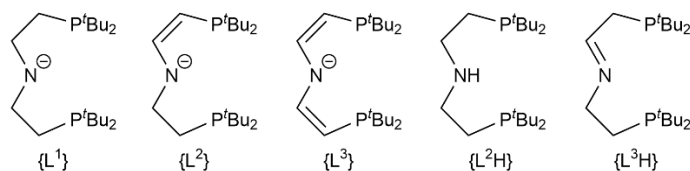


Figure 5: Derivatives of PNP pincer ligands.

Hanson's catalyst used a cyclohexyl-substituted pincer ligand, however, the proposed active hydride species in the hydrogenation reaction cannot be isolated and characterized. Our attempt to synthesize this hydride species in another pathway was unsuccessful. We will synthesize and isolate the cobalt hydride complexes, using our ligand system with *tert*-butyl substituents. The neutral and cationic cobalt hydrides will be further probed in olefin hydrogenation to examine the influence of ligand bulkiness in the reaction rate.

Starting from the Co(II) hydride complex [CoH(L¹)], photochemical reactivity in olefin hydrogenation is to be investigated. Substrate screening will be carried out with mono-, di- and tri-substituted olefins ligated with aromatic or aliphatic substituents. Mechanistic investigation will be performed by spectroscopic and kinetic studies. Photophysical processes will be examined by transient spectroscopy to figure out the influence of photoexcitation and the corresponding photoproduct. The role of the photoproduct in hydrogenation will be evaluated. Control reactions, hydrogenation of radical clock substrates and *para*-hydrogen molecules will be introduced to gather more information about the reaction pathways.

2 Results and Discussion

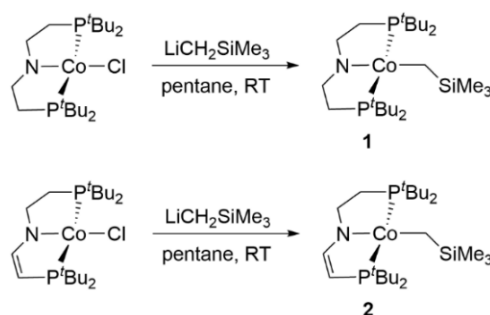
2.1 Synthesis and characterization of cobalt complexes

Part of the results of this chapter has been published (S. Sang, T. Unruh, S. Demeshko, L. Domenianni, N. P. van Leest, P. Marquetand, F. Schneck, C. Würtele, F. J. de Zwart, B. de Bruin, L. González, P. Vöhringer, S. Schneider, *Chem. Eur. J.* **2021**, *27*, 16978-16989.) and citation of the original work is permitted by the publishers.

Hanson's catalyst **H4**, a cationic cobalt(II) alkyl complex ligated with a cyclohexyl-substituted PNP-pincer ligand, is efficient in C–X multiple bond (X = C, O, N) hydrogenation.^[64] The crystal structure of this **H4** shows a short C–N bond in the ligand backbone, which suggests that **H4** might be an imine-based complex. Besides, mechanistic investigation suggested that the active catalyst is a cationic cobalt hydride complex, which cannot be isolated and spectroscopically characterized. To get further insight into the catalytic mechanism in olefin hydrogenation catalyzed by cobalt pincer complexes, we synthesized model complexes ligated with *tert*-butyl-substituted analogue of the pincer ligand used by Hanson and probed all cobalt complexes in olefin hydrogenation.

2.1.1 Synthesis and characterization of cobalt alkyl complexes

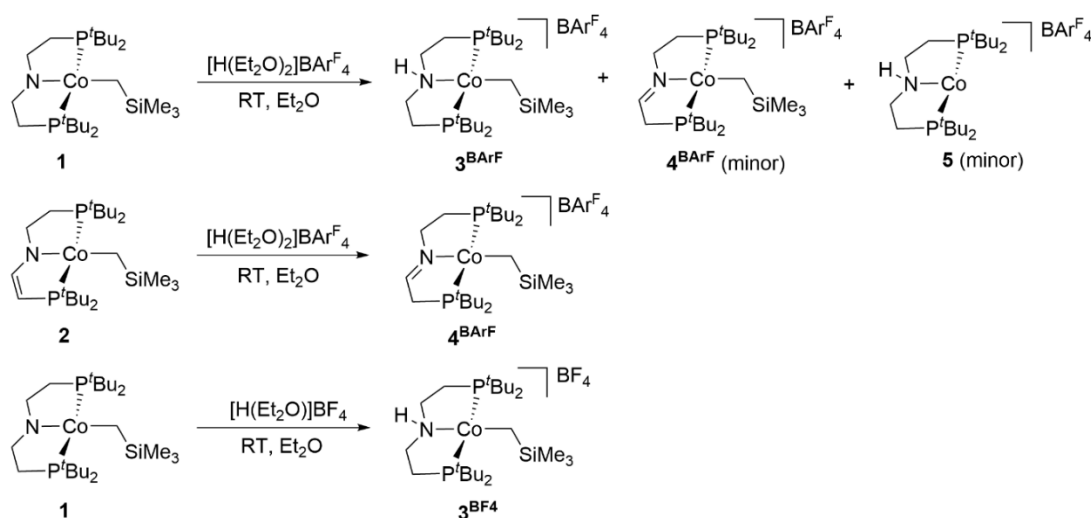
Alkylation of cobalt(II) chloride complexes [CoCl(L¹)] and [CoCl(L²)] with LiCH₂SiMe₃ (1.1 eq.) in pentane gave cobalt(II) alkyl complexes [CoCH₂SiMe₃(L¹)] (**1**) and [CoCH₂SiMe₃(L²)] (**2**). The ¹H NMR spectrum of complex **1** shows three broadened signals, assigned to *tert*-butyl substituents, the trimethylsilyl group ($\delta_{\text{H}} = -4.94$ ppm) and the methylene groups on the pincer backbone, which are consistent with C_{2v} symmetry of **1**. Complex **2**, instead, displays C_s symmetry with four signals assigned to methylene and methyne groups in ligand backbone, accompanied with one resonance of the trimethylsilyl group at $\delta_{\text{H}} = -12.44$ ppm.



Scheme 22: Syntheses of hydride complexes **1** and **2**.

Protonation of **1** and **2** was conducted at room temperature with Brønsted acids [H(Et₂O)₂]BAr^F₄ (1 eq.) or [H(Et₂O)]BF₄ (1 eq.) in Et₂O. Protonation of **1** with [H(Et₂O)₂]BAr^F₄

resulted in the formation of a *N*-protonated cationic cobalt alkyl complex $[\text{CoCH}_2\text{SiMe}_3(\text{L}^1\text{H})]\text{BAR}^{\text{F}_4}$ ($\mathbf{3}^{\text{BAR}^{\text{F}_4}}$) as main product, accompanied by the formation of a cationic imine-based cobalt(II) complex $[\text{CoCH}_2\text{SiMe}_3(\text{L}^2\text{H})]\text{BAR}^{\text{F}_4}$ ($\mathbf{4}^{\text{BAR}^{\text{F}_4}}$) (< 1%) and three-coordinated cobalt(I) complex $\mathbf{5}^{\text{BAR}^{\text{F}_4}}$ (< 1%), as judged by ^1H NMR spectroscopy (Scheme 23). $\mathbf{4}^{\text{BAR}^{\text{F}_4}}$ can be selectively synthesized by protonation of $\mathbf{2}$ with $[\text{H}(\text{Et}_2\text{O})_2]\text{BAR}^{\text{F}_4}$ (1 eq.) at room temperature. The ^1H NMR spectrum of $\mathbf{3}^{\text{BAR}^{\text{F}_4}}$ demonstrates only one broadened resonance of *tert*-butyl substituents, accompanied by four signals belonging to four methylene groups and one signal to trimethylsilyl group. Synthesis and isolation of complex $\mathbf{5}^{\text{BAR}^{\text{F}_4}}$ will be discussed in chapter 2.1.2.



Scheme 23: Protonation of **1** and **2** with Brønsted acids.

In contrast, no formation of cationic three-coordinate Co(I) or imine Co(II) alkyl complexes was observed in the protonation of **1** with $[\text{H}(\text{Et}_2\text{O})]\text{BF}_4$ at room temperature. The ^1H NMR spectrum of $\mathbf{3}^{\text{BF}_4}$ supports C_s symmetry, with a doublet resonance belonging to *tert*-butyl substituents and three resonances to methylene and methyne groups on the backbone. The N–H stretching vibration of $\mathbf{3}^{\text{BF}_4}$ at $\nu = 3211\text{ cm}^{-1}$ was observed by IR spectroscopy. Addition of $\text{NaBAR}^{\text{F}_4}$ in solution of $\mathbf{3}^{\text{BF}_4}$ resulted in counterion exchange, as observed by ^1H NMR spectroscopy (Figure 6), in which the two resonances of *tert*-butyl groups in $\mathbf{3}^{\text{BF}_4}$ exchanged to one resonance of *tert*-butyl groups of $\mathbf{3}^{\text{BAR}^{\text{F}_4}}$, indicating a different effect of anion interaction with $\mathbf{3}^+$, likely due to hydrogen bonding.

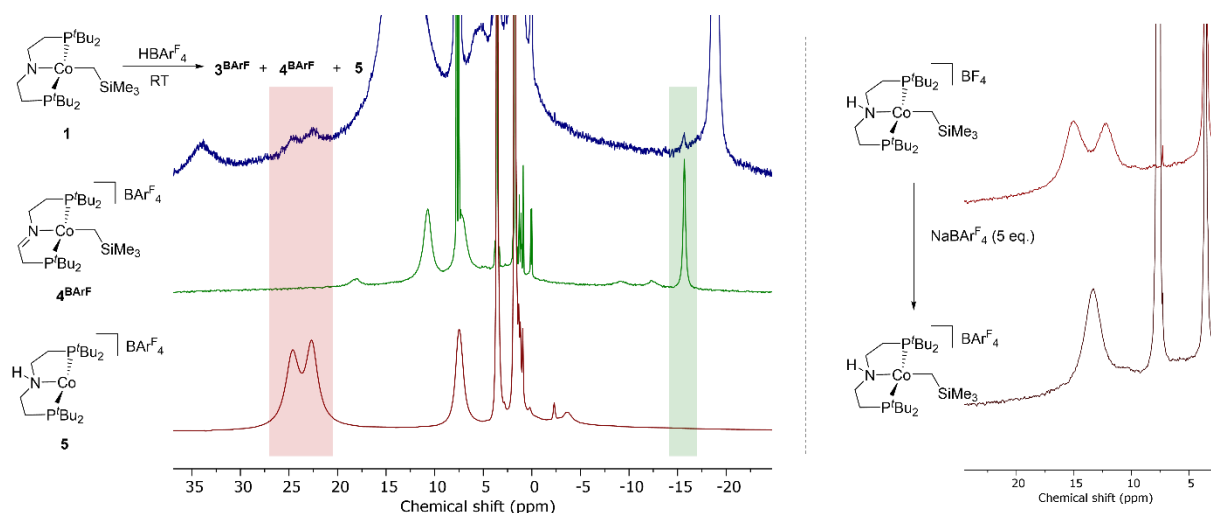


Figure 6: (Left) ^1H NMR of the reaction mixture after protonation of **1** with $[\text{H}(\text{Et}_2\text{O})_2]\text{BARF}_4$ at room temperature in comparison with spectra of isolated BARF_4 -complexes **4** BARF and **5** BARF . All spectra were recorded in $\text{THF-}d_8$. (Right) ^1H NMR spectra of counterion exchange of **3** BARF to **3** BF_4 with NaBF_4 (5 eq.) in $\text{THF-}d_8$.

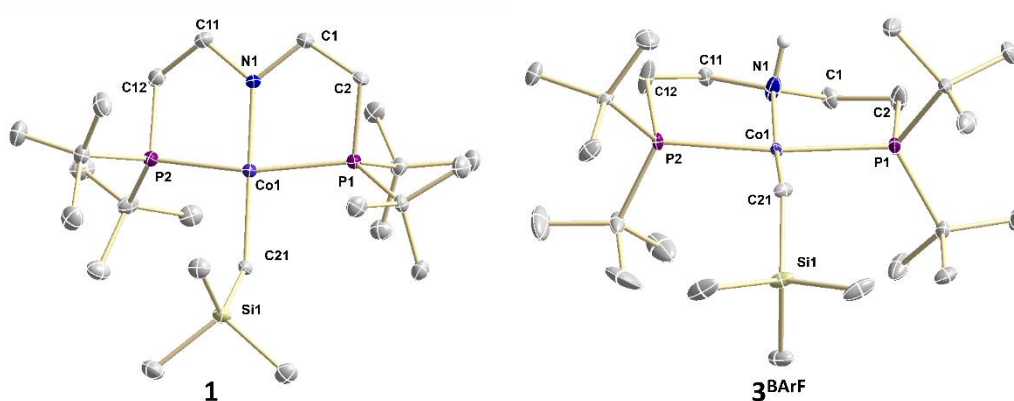


Figure 7: Single crystal x-ray structures of **1** (left) and cation of **3** BARF (right) with the anisotropic displacement parameters drawn at the 50% probability level. Except N–H and Co–H, all other hydrogen atoms and BARF_4 anions are omitted for clarity. Selected bond distances (\AA) and angles ($^\circ$) for **1**: Co1–C21 = 2.041(3); Co1–N1 = 1.871(2); Co1–P1 = 2.2298(8); Co1–P2 = 2.22447(8); C1–N1 = 1.460(4); C11–N1 = 1.458(4); N1–Co1–C21 = 178.25(12); N1–Co1–P1 = 83.12(8); N1–Co1–P2 = 84.51(8); P1–Co1–P2 = 162.58(3). **3** BARF : Co1–C21 = 2.026(5); Co1–N1 = 2.053(4); Co1–P1 = 2.2862(13); Co1–P2 = 2.2728(14); C1–N1 = 1.459(7); C11–N1 = 1.474(6); N1–Co1–P1 = 83.85(3); N1–Co1–P2 = 84.31(13); P1–Co1–P2 = 168.13(6).

As reported by Hanson, as the active precatalyst **H4** was exposed to H_2 atmosphere, no signal attributed to a cobalt-containing product was observed by the NMR spectroscopy. In contrast to this result, exposure of **1** and **3** BARF to H_2 (1 bar) atmosphere leads to the formation of corresponding cobalt hydride complexes **6** and **7** BARF , which are stable at room temperature,

as observed in ^1H NMR spectra (Figure 8). These observations prompted us to synthesize and isolate the hydride complexes and investigate their role in olefin hydrogenation.

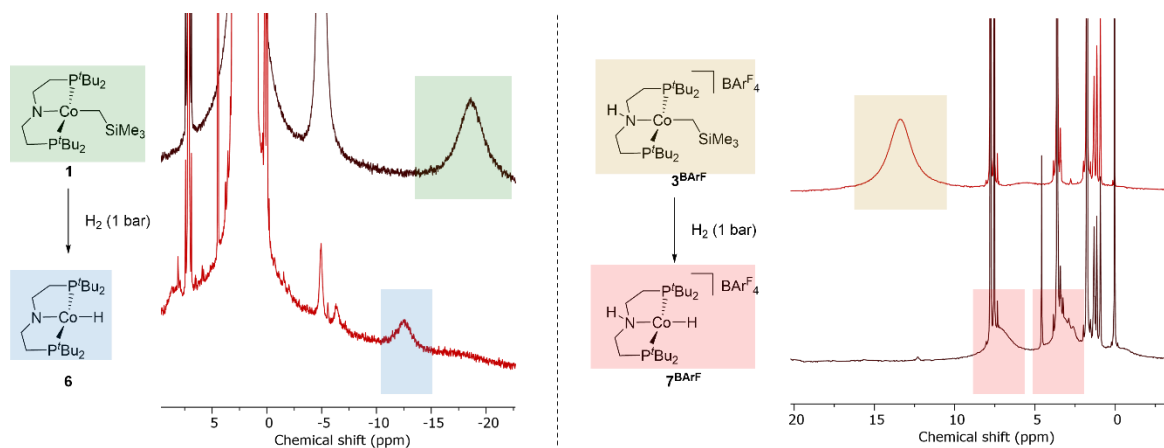
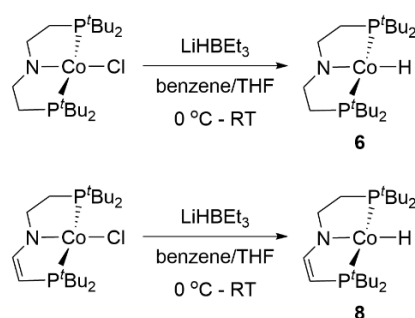


Figure 8: ^1H NMR spectra of reactivity of **1** and **3^{BARF}** with H₂ (1 bar) in C₆D₆.

2.1.2 Synthesis and characterization of cobalt(II) hydride and cobalt(I) complexes

2.1.2.1 Synthesis and characterization of neutral cobalt(II) hydride and cobalt(I) complexes



Scheme 24: Synthesis of cobalt(II) hydride complexes **6** and **8**.

Cobalt hydride complex $[\text{CoH}(\text{L}^1)]$ (**6**)¹ ligated with saturated PNP pincer ligand ($\text{L}^1 = \text{N}(\text{CH}_2\text{CH}_2\text{P}^t\text{Bu}_2)_2$) can be obtained by salt metathesis of previously reported chloride precursor $[\text{CoCl}(\text{L}^1)]$ ^[127] with LiHBEt_3 (1.1 equiv.), which gave **6** in a yield of 85% (Scheme 24). The ^1H NMR spectrum (Figure 9) of **6** exhibits two broadened resonances at $\delta = 2.49$ and -12.55 ppm, which can be assigned to *tert*-butyl (*t*Bu) substituents and four methylene groups in the ligand backbone based on integration, whereas, no hydride signal was found. No phosphorus signal was detected by $^{31}\text{P}\{^1\text{H}\}$ NMR spectroscopy, which is consistent with the paramagnetic nature of d^7 cobalt(II) complexes. The Magnetic susceptibility of **6** was determined by Evans' method in C_6D_6 at room temperature. The Magnetic moment ($\mu_{\text{eff}} = 1.75 \mu_{\text{B}}$) reveals a low-spin electronic configuration with one unpaired electron, which was further supported by X-Band EPR spectroscopy² (Figure 9). The EPR spectrum was recorded at 16 K and fitted with a rhombic g -tensor ($g = 2.77, 2.04, 1.96$) and partially resolved ^{59}Co hyperfine coupling ($A_3 = 105$ MHz, $I = 7/2$, 100% natural abundance), indicating a cobalt-centered radical character.

The structural characterization of **6** by X-ray diffraction (Figure 9) shows a square-planar coordination geometry around the cobalt center with little distortion. Bond lengths and angles around the metal center resemble its chloride precursor, with a small elongation of the Co–N bond ($\Delta d = 0.02$ Å), arising from the *trans*-effect of the hydride ligand.^[127] The hydride ligand can be detected by IR spectroscopy, which has an absorption at $\nu_{\text{Co-H}} = 1727$ cm^{-1} . Compared

¹ Complex **6** was synthesized and characterized by Dr. Suresh Raju.

² EPR spectrum was recorded and fitted by Dr. Eva Zolnhofer and Prof. Dr. Karsten Meyer.

to a modified pyridine-based cobalt(II) hydride complex reported by Chirik and co-workers, the Co–N bond of **6** is shorter ($\Delta d = 0.1 \text{ \AA}$) and the Co–H bonding is weaker ($\Delta \nu = 92 \text{ cm}^{-1}$), indicating stronger *trans*-influence of the dialkylamide ligand due to increased σ -donation ability.^[85]

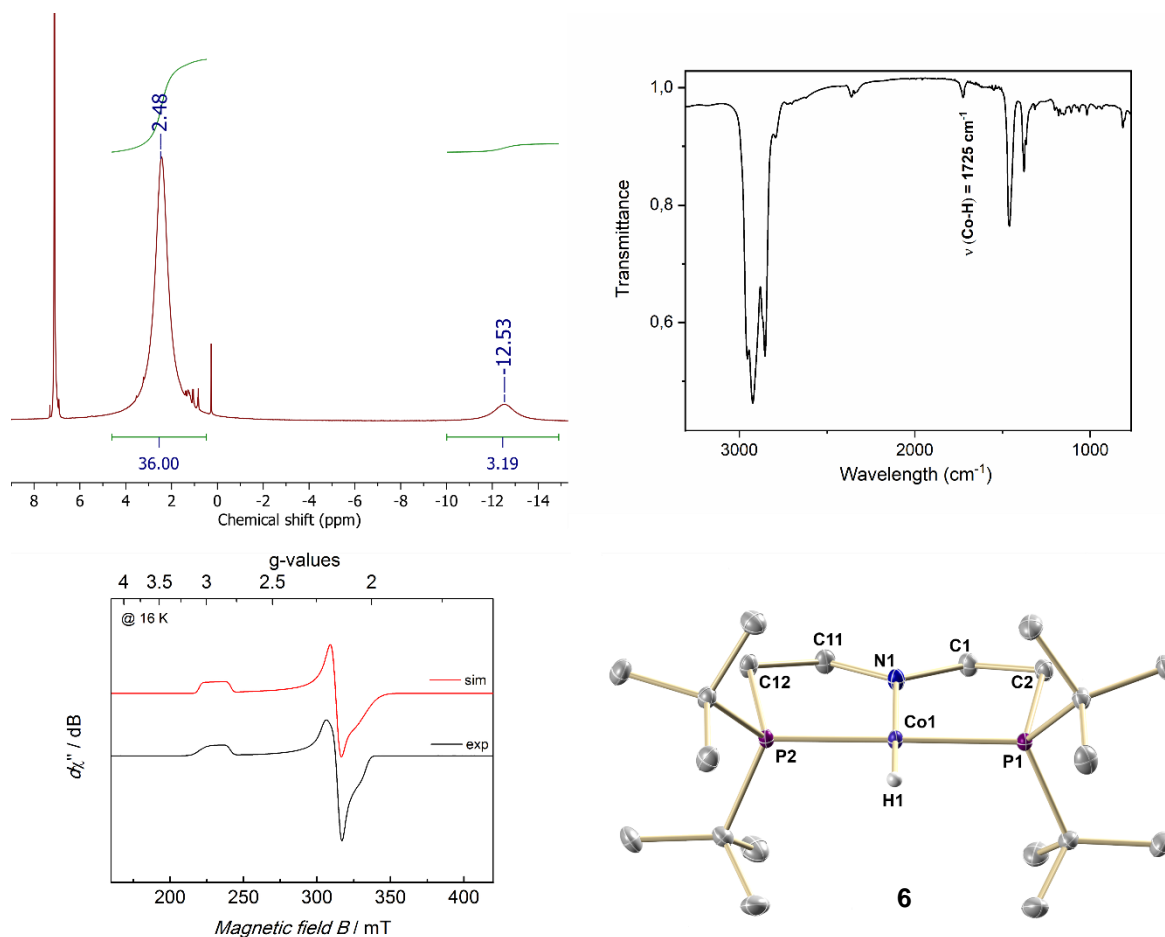


Figure 9: (top, left) ^1H NMR spectrum of **6** in benzene- d_6 ; (top, right) IR spectrum of **6** measured by FT-IR spectroscopy in nujol; (bottom, left) CW X-band EPR spectrum of **6** recorded in frozen toluene at 16 K (black trace), and simulation results (red trace); simulation parameters: $g = 2.77, 2.04, 1.96$; $A_x = 105 \text{ MHz}$ (microwave frequency ν : 8.959 GHz, modulation amplitude 300 mT, microwave power 2 mW, modulation frequency 100 kHz, time constant 0.1 s); (bottom, right) Molecular structure of **6** with anisotropic displacement parameters drawn at the 50% probability level; all hydrogen atoms except Co–H omitted for clarity. The hydrogen atom in Co–H bond was found from the residual density map and isotopically refined; selected bond distances (\AA) and angles ($^\circ$): Co1–H1 = 1.57(2); Co1–N1 = 1.8520(18); Co1–P1 = 2.1543(6); Co1–P2 = 2.1520(6); C1–N1 = 1.4611(14); C11–N1 = 1.4618(14); N1–Co1–H1 = 173.4(8); N1–Co1–P1 = 87.53(6); N1–Co1–P2 = 87.29(6); P1–Co1–P2 = 174.59(3).

Synthesis of cobalt(II) hydride complex $[\text{CoH}(\text{L}^2)]$ (**8**) ligated with a semi-unsaturated PNP pincer ligand ($\text{L}^2 = \text{N}(\text{CH}_2\text{CH}_2\text{P}^t\text{Bu}_2)(\text{CHCHP}^t\text{Bu}_2)$) was achieved in a yield of 75% upon salt metathesis of the reported chloride precursor^[127] with LiHBEt_3 (1.1 equiv.) (Scheme 24). The

^1H NMR spectrum (Figure 10, left) of **8** measured in C_6D_6 is indicative of C_s symmetry, which displays two resonances ($\delta = 8.63$ and 8.25 ppm) for *tert*-butyl substituents on the phosphorus atoms and four resonances for the remaining pincer backbone protons from methylene and methine groups. As usual, no hydride signal was found in the ^1H NMR spectrum. The deuteride isotopologue **8-D** can be obtained via rapid H/D exchange of **8** with D_2 . Two pronounced isotope shifts of up to 1.2 ppm are observed for backbone protons. IR spectrum (Figure 10, right, red) of **8** exhibits absorptions at 1738 cm^{-1} attributable to Co–H stretching vibration and at 1526 cm^{-1} , which is the C=C double bond stretching vibration. IR spectrum (Figure 10, right, blue) of **8-D** exhibits an absorption at 1238 cm^{-1} , which is consistent with calculated value ($\nu_{\text{Co-D}} = 1238\text{ cm}^{-1}$) based on the assumption of similar force constants.

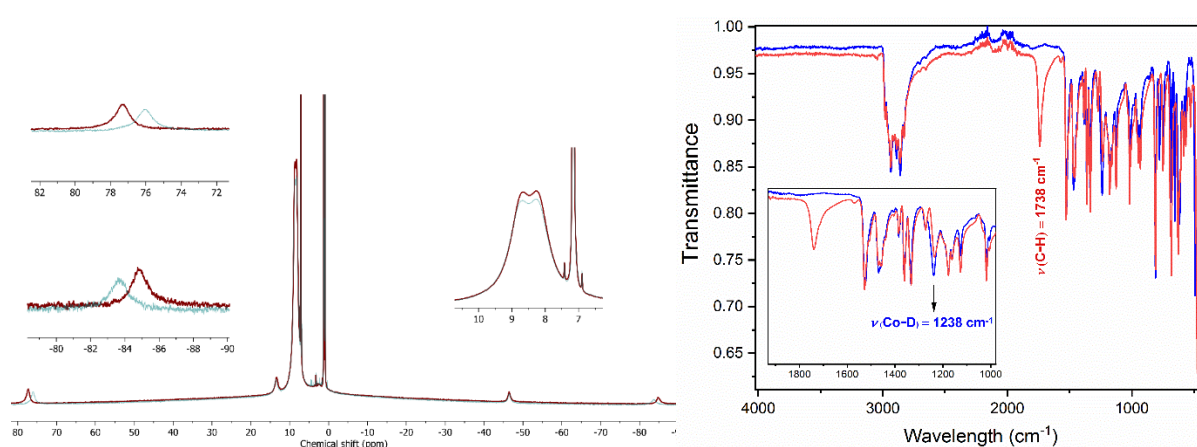
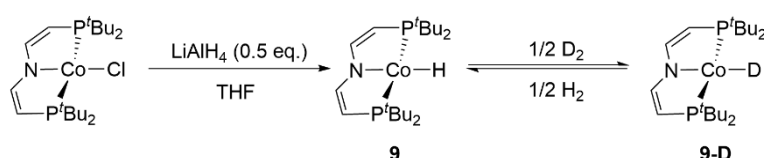


Figure 10: (left) ^1H NMR spectra of **8** (red) and **8-D** (green) in C_6D_6 and (right) ATR-IR spectra of **8** (red) and **8-D** (blue) in the solid state.



Scheme 25: Synthesis of cobalt hydride complex **9** and **9-D**.

The cobalt chloride precursor $[\text{CoCl}(\text{L}^3)]$ with an unsaturated backbone was synthesized following the procedure reported by Lagaditis *et al.*^[127] The hydride counterpart $[\text{CoH}(\text{L}^3)]$ (**9**) is prepared by treatment of $[\text{CoCl}(\text{L}^3)]$ with 0.5 equivalent of lithium aluminium hydride (LiAlH_4). Dropwise addition of LiAlH_4 suspension into the solution of $[\text{CoCl}(\text{L}^3)]$ in tetrahydrofuran (THF) resulted in gradual color change from violet to orange, which gave **9** in over 70% isolated yield. The deuteride analogue $[\text{CoD}(\text{L}^3)]$ (**9-D**) can be synthesized with LiAlD_4 or, alternatively, by fast H/D exchange of **9** under D_2 atmosphere (Scheme 25). Three broadened and highly shifted signals are observed in ^1H NMR spectra of **9** and **9-D** (Figure 11, left), which can be assigned to *tert*-butyl groups and two different methine moieties on the ligand backbone, supporting C_{2v} symmetry of **9**. No hydride resonance visible in the ^1H NMR spectrum due to

particularly fast relaxation of the hydride proton that is bonded to the paramagnetic cobalt center.^[128]

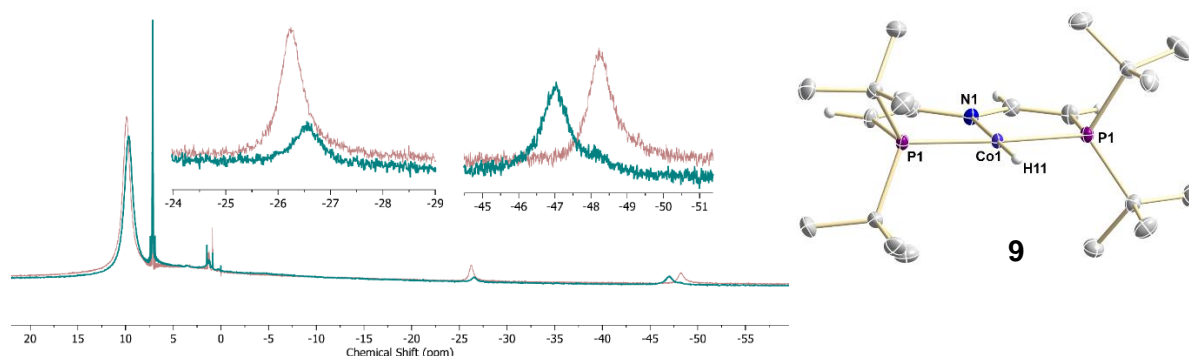


Figure 11: (Left) ^1H NMR spectra of **9** (red) and **9-D** (green) in C_6D_6 . (Right) Molecular structure of **9** in the crystal from X-ray diffraction with the anisotropic displacement parameters drawn at the 50% probability level. ^tBu hydrogen atoms are omitted for clarity. Selected bond distances (\AA) and angles ($^\circ$): $\text{Co1-H11} = 1.45(2)$; $\text{Co1-N1} = 1.9369(12)$; $\text{Co1-P1} = 2.2062(3)$; $\text{Co1-P2} = 2.2062(3)$; $\text{N1-Co1-H} = 180.000(10)$; $\text{N1-Co1-P1} = 85.264(8)$; $\text{N1-Co1-P2} = 85.264(8)$; $\text{P1-Co1-P2} = 170.528(16)$.

The crystal for X-ray structure determination of **9** (Figure 11, right) is obtained from a saturated solution in pentanes at $-35\text{ }^\circ\text{C}$. Similar to the parent chloride complex, **9** possesses a slightly distorted square-planar geometry, arising from the pincer bite angle ($170.528(16)\text{ }^\circ$). The Co-N_{PNP} bond length is elongated ($1.9369(12)\text{ \AA}$) compared to the parent chloride complex ($1.893(2)\text{ \AA}$), indicating a stronger *trans*-effect of the hydride ligand with respect to chloride. IR spectra (Figure 12) of **9** show a strong Co-H stretching vibration band at $\nu = 1756\text{ cm}^{-1}$ (solid state) and $\nu = 1778\text{ cm}^{-1}$ (in hexanes), which is at lower energy than other reported neutral Co(II) hydride complexes^[85,124–126], indicating a strong *trans*-effect of the divinylamide ligand. **9-D** displays a Co-D stretching band at $\nu_{\text{D}} = 1269\text{ cm}^{-1}$ (solid state) and $\nu_{\text{D}} = 1285\text{ cm}^{-1}$ (in hexanes), which are consistent with the prediction of ν_{D} based on the assumption of similar force constants.

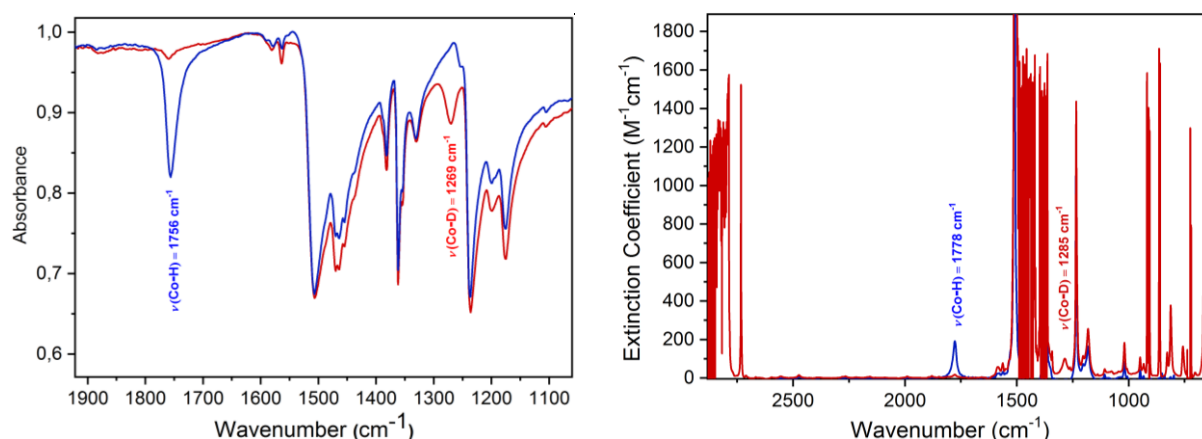


Figure 12: Infrared spectra of **9** (blue) and **9-D** (red) measured by ATR-IR (left) and in hexanes (right).

The UV-Vis spectrum of **9** (Figure 13, blue line) shows two intense bands at 337 nm and 285 nm, accompanied by one shoulder at around 400 nm and one broad band at 522 nm ($\epsilon = 124 \text{ M}^{-1}\cdot\text{cm}^{-1}$) with low intensity. To study the nature of the electronic excitations observed in the UV-Vis spectrum, multiconfiguration calculations³ (SCNEVPT2/CASSCF(11,14)/def2-TZVP) were performed to reproduce the absorptions (Figure 13, red line and Table 1), in which the low-lying $4p_z$ orbital in the active space is included. The absorption at 337 nm is assigned to a ligand field transition, which consists of two $3d$ to $4p_z$ transitions with contributions of 62% and 12%, respectively, and a smaller contribution (8%) of an excitation to the Co–H σ^* antibonding orbital. The absorption at 294 nm is assigned to doublet configurations: two involves $3d$ to $4p_z$ transitions with contributions of 36% and 32%, respectively, and a smaller contribution (8%) of an excitation to the Co–H σ^* antibonding orbital.

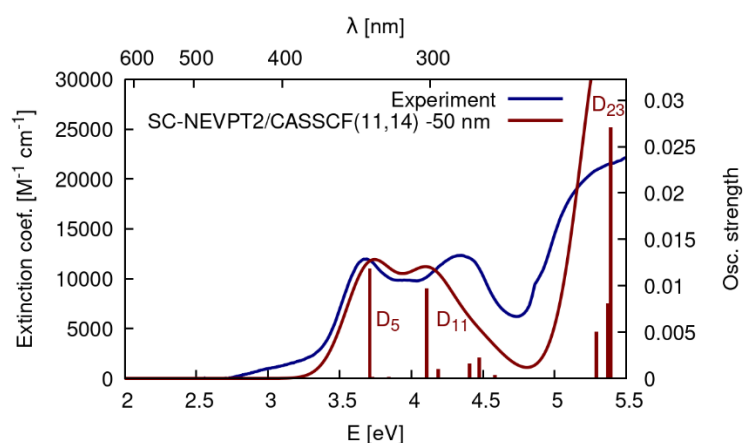


Figure 13: Comparison of the experimental electronic absorption spectrum of **9** in THF (blue, -95°C) with the computations (red, NEVPT2/CASSCF(11,14)/def2-TZVP) for the PMe_2 truncated model, shifted by -50 nm .

Table 1: Contributions (c^2 configuration interaction coefficients) of electronic configurations to selected doublet and quartet states (oscillator strengths f in parenthesis) of **9**. The calculated excitation wavelength λ is shifted by -50 nm to best match the experimental electronic absorption spectrum (λ_{exp}) in nm.

	σ	π	$3d_{xy}$	$3d_{yz}$	$3d_{xz}$	$3d_{z^2}$	$4p_z$	σ^*	c^2	λ [nm]	λ_{exp} [nm]
D_0	2	2	2	2	2	1	0	0	0.88		
D_5 (0.0118)	2	2	2	2	1	1	1	0	0.62	334	337
	2	2	1	1	2	2	1	0	0.12		
	2	2	2	2	0	2	0	1	0.08		
D_{11} (0.0097)	2	2	2	1	2	1	1	0	0.36	302	294
	2	2	1	2	1	2	1	0	0.32		
	2	2	2	1	1	2	0	1	0.11		
D_{23} (0.0271)	2	2	2	2	2	0	1	0	0.53	230	<222
	2	2	2	2	0	1	1	0	0.32		
Q_3	2	2	1	2	2	1	0	1	0.85	564	522

³ Calculation was performed by Prof. Dr. Leticia González and Dr. Philipp Marquetand.

The susceptibility measurement of **9** by Evans method ($\mu_{\text{eff}} = 1.97 \pm 0.27 \mu\text{B}$) indicates an electronic low-spin configuration with one unpaired electron ($S = 1/2$). This observation agrees with the temperature dependent susceptibility measurement⁴ of a powdered sample with an isotropic g -tensor of 2.84 (Figure 14). The electronic spectra of **9** and **9-D** were further examined with X-band EPR spectroscopy. Measurements were conducted in toluene glasses at 20 K. EPR spectra⁵ (Figure 14, b and c) of **9** and **9-D** gave rhombic signals with one large g value at 4.35 and 4.29, respectively, which are split into eight lines due to hyperfine interaction with ^{59}Co ($S = 7/2$, 100% natural abundance). Highly anisotropic resonances and a large ^{59}Co hyperfine coupling suggest metal-centered radical character of **9**, which resembles the pyridine-based PNP pincer cobalt (II) hydride complex reported by Chirik and co-workers.^[85] Low spin and square-planar cobalt(II) complexes are known to exhibit large hyperfine coupling and g -anisotropy due to their strong spin-orbit coupling arising from mixing of the ground state with low-lying excited state.^[85] A truncated model of **9**, where *tert*-butyl groups are replaced by methyl groups, was calculated with multifunctional SC-NEVPT2/CASSCF(11, 14)⁶ and gave satisfactorily a large g -anisotropy ($g = 4.80, 1.50, 1.25$) when including spin-orbit couplings in the calculation, which is consistent with the experimental data.

Although the hydride signal of **9** cannot be found in the ^1H NMR spectra, **9** and **9-D** can be differentiated by the secondary isotope shifts of the ^1H NMR signals of the pincer ligand, as observed in the isotopic effect of the chemical shift between **8** and **8-D**. Resonances of *tert*-butyl substituents and one set of methine in the pincer ligand exhibit isotope shifts of $\Delta\delta_{\text{D-H}} = -0.21$ and -0.31 ppm, respectively, while resonance of the other set of methine displays a greater isotope shift (Figure 11, left) of $\Delta\delta_{\text{D-H}} = 1.22$ ppm upon replacement of hydride with deuteride. Paramagnetic complexes with significant NMR isotope effects on distant protons have been reported previously, which was termed by Theopold and coworkers as paramagnetic isotope effect on chemical shift (PIECS).^[128–137] Holland and coworkers reported hydride-bridged multinuclear complexes, which display PIECS in the ^1H NMR spectra upon isotopic substitution.^[134] They proposed that the isotopic substitution might slightly change metal–H(D) bond length in a dihydride-bridged binuclear complex, leading to structural changes of the metal–metal bond distance, which then changes the antiferromagnetic interaction between two open-shell iron centers and causes a shift in magnetic susceptibility.^[134] In our case with a mononuclear hydride complex, isotope substitution may cause ligand field perturbation, supported by slight differences in g -anisotropy and ^{59}Co

⁴ SQUID measurement was conducted and the data was simulated by Dr. Serhiy Demeshko.

⁵ EPR spectra were recorded by Nicolaas P. van Leest, Felix J. de Zwart and simulated by Prof. Dr. Bas de Bruin.

⁶ Calculation was performed by Prof. Dr. Leticia González and Dr. Philipp Marquetand.

hyperfine coupling in the low field component between **9** and **9-D** in the EPR spectra (Figure 14, d and e).

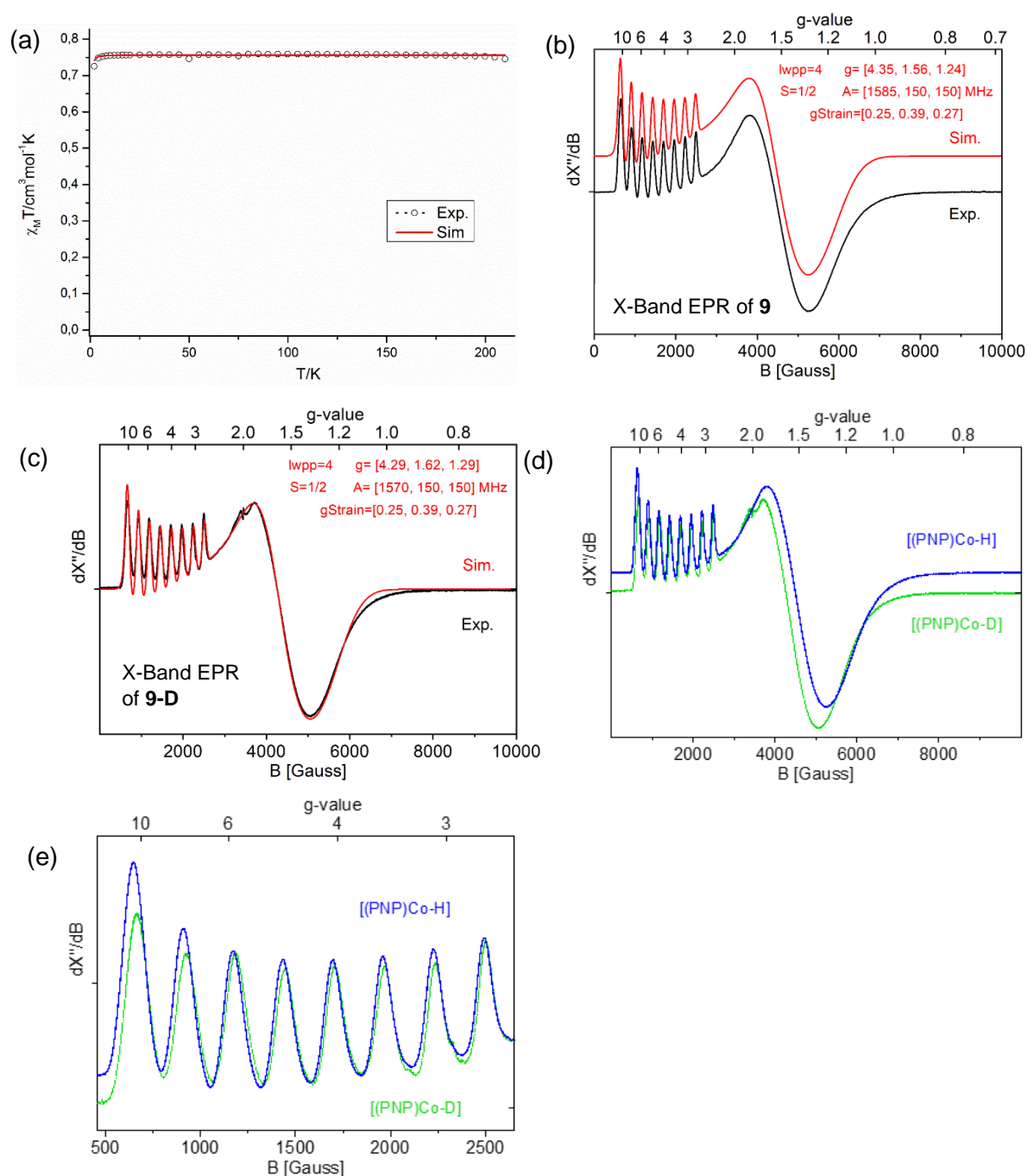


Figure 14: (a) $\chi_M T$ vs. T plot for **9**; the open circles are the observed values and the red solid line corresponds to the best fit with the parameters $g = 2.84$ and $TIP = 740 \cdot 10^{-6} \text{ cm}^3 \text{ mol}^{-1}$ (TIP: temperature independent paramagnetism). (b) Experimental and simulated EPR spectra of **9** measured in toluene glass at 20 K (MW freq. = 9.6427 GHz, MW power = 0.6325 mW, Mod. amp. = 4 G). (c) Experimental and simulated EPR spectra of **9-D** measured in toluene glass at 20 K (MW freq. = 9.6427 GHz, MW power = 0.6325 mW, Mod. amp. = 4 G). (d and e) Overlays of the experimental EPR spectra of **9** and **9-D** (g -value scaled, normalized).

Paramagnetic shifts in ^1H NMR spectra are results of Fermi interaction and dipolar interaction.^[138] Both are hyperfine interactions between nuclear spins and magnetic moments of unpaired electrons. Fermi interaction is transmitted over covalent metal-ligand interactions, while dipolar interaction occurs through space without covalent bonds.^[139] Isotope substitution of **9** causes high-field shift of two resonances and low-field shift of one resonance observed in ^1H NMR spectra (Figure 11), indicating a predominant contribution from dipolar shift.

Comparison of IR absorptions (Figure 15) of Co–H stretching vibration in three neutral hydride complexes reveals a blue shift upon dehydrogenation of the ligand backbone (**6** (1725 cm^{-1}) > **8** (1738 cm^{-1}) > **9** (1756 cm^{-1})). Introduction of C–C double bonds delocalizes the π -electron density from the *N*-donor to the ligand backbone, which weakens the π -donor character of nitrogen atoms and resulting *trans*-effect to hydride ligands.

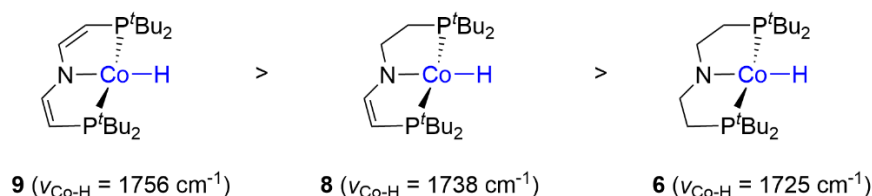


Figure 15: IR absorptions of Co–H stretching vibration in three neutral hydride complexes.

In the synthesis of **6**, trace amounts of a reduced cobalt(I) dinitrogen complex [$\text{CoN}_2(\text{L}^1)$] (**10**) (< 5%) was formed as side-product, as judged by ^1H NMR spectroscopy. A selective synthesis of **10** can be achieved by treatment of the cobalt chloride precursor [$\text{CoCl}(\text{L}^1)$] with potassium graphite (KC_8) in dry THF under N_2 atmosphere, which afforded **10** in a yield of 90%. The $^{31}\text{P}\{^1\text{H}\}$ spectrum features one broadened resonance at $\delta = 104.9\text{ ppm}$, measured in C_6D_6 . Line broadening in the $^{31}\text{P}\{^1\text{H}\}$ spectrum arises from hyperfine interaction of phosphorus atoms with ^{59}Co ($I = 7/2$). The ^1H NMR spectrum displays one multiplet signal for *tert*-butyl substituents and two signals for methylene moieties in the backbone, which indicates a C_{2v} symmetry of **10**. The IR spectrum of **10** in the solid state (ATR-IR) shows a strong dinitrogen stretching band at 1980 cm^{-1} , which is at least $\Delta\nu = 20\text{ cm}^{-1}$ red-shifted than those reported for cobalt(I) dinitrogen complexes ligated with pincer ligands,^[85,88,140–143] supporting the strong *trans*-effect of divinylamide ligand. The molecular structure of **10** was confirmed by X-ray diffraction. Distorted square-planar geometry around cobalt center arises from P–Co–P bite angle ($171.16(2)^\circ$).

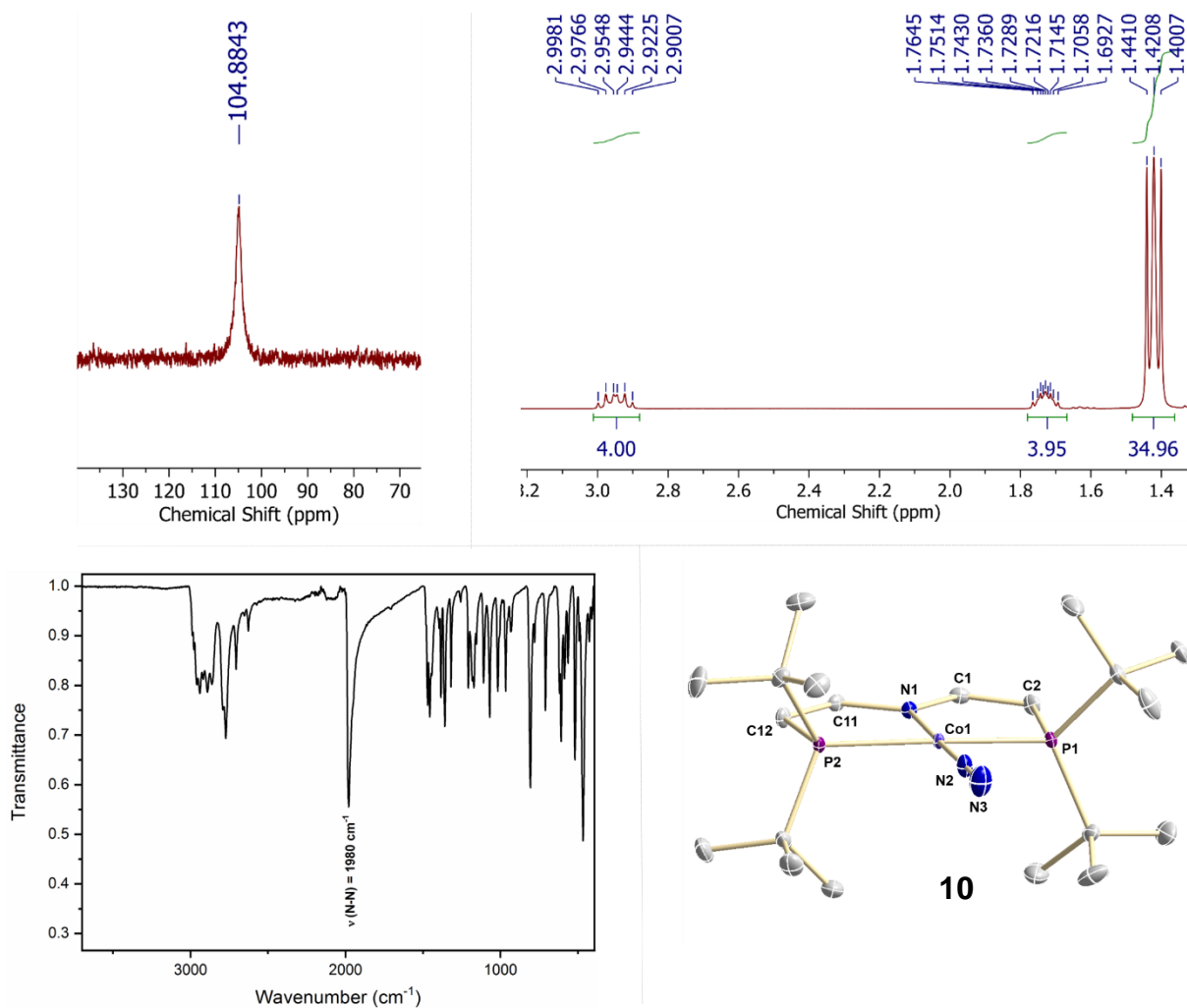
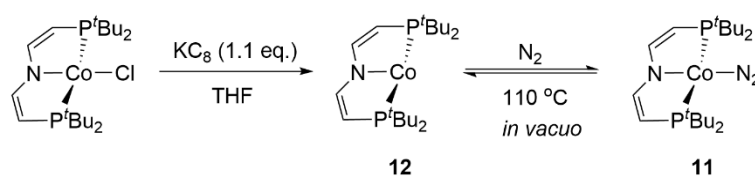


Figure 16: (top, left) $^{31}\text{P}\{^1\text{H}\}$ NMR spectrum of **10** in benzene- d_6 ; (top, right) ^1H NMR spectrum of **10** in benzene- d_6 ; (bottom, left) IR spectrum of **10** measured by ATR-IR spectroscopy in solid state; (bottom, right) Molecular structure of **10** with anisotropic displacement parameters drawn at the 50% probability level; all hydrogen atoms except Co–H omitted for clarity; selected bond distances (\AA) and angles ($^\circ$): Co1–N1 = 1.8544(15); Co1–N2 = 1.771(2); Co1–P1 = 2.1885(5); Co1–P2 = 2.1919(5); N2–N3 = 1.033(3); C1–N1 = 1.457(2); C11–N1 = 1.459(2); N1–Co1–N2 = 174.14(8); N1–Co1–P1 = 85.71(5); N1–Co1–P2 = 85.95(5); P1–Co1–P2 = 171.16(2).



Scheme 26: Synthesis cobalt complexes **11** and **12**.

The cobalt(I) dinitrogen complex $[\text{CoN}_2(\text{L}^3)]$ (**11**) is also a side-product in the synthesis of **9** and was prepared in high yield by reduction of the chloride precursor with KC_8 under N_2 atmosphere (Scheme 26). The molecular structure of **11** (Figure 17, left) that was confirmed by X-ray

diffraction, exhibits a slightly distorted square-planar geometry arising from a P(1)–Co(1)–P(2) bite angle (167.88(2) °). In agreement with a closed-shell electronic configuration, **11** displays three diamagnetic signals in an ^1H NMR spectrum and a broad resonance in the $^{31}\text{P}\{^1\text{H}\}$ NMR spectrum (Figure 17, middle and right), which is consistent with a C_{2v} symmetric complex. The strong N_2 stretching vibration and the C–C double bonds stretching vibration exhibit two absorptions at $\nu = 2012$ and 1524 cm^{-1} in the solid state IR spectrum, respectively.

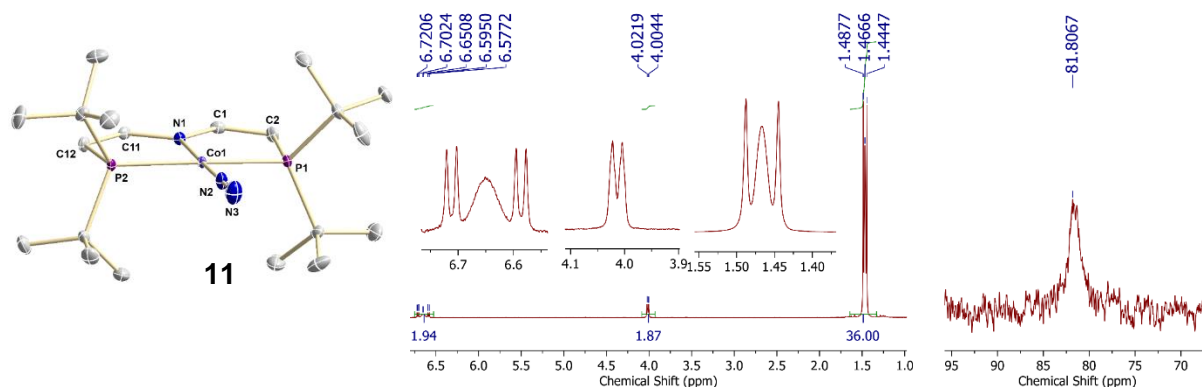


Figure 17: (left) Molecular structure of **11** in the crystal from X-ray diffraction with the anisotropic displacement parameters drawn at the 50% probability level. t Bu and methylenes hydrogen atoms are omitted for clarity. Selected bond distances (\AA) and angles ($^\circ$): Co1–N1 = 1.9138(14); Co1–N2 = 1.7329(16); N2–N3 = 1.128(2); Co1–P1 = 2.2290(5); Co1–P2 = 2.2238(5); N1–Co1–N2 = 177.72(7); N1–Co1–P1 = 84.60(5); N1–Co1–P2 = 84.24(5); P1–Co1–P2 = 167.88(2). (middle) ^1H NMR spectrum of **11** in C_6D_6 . (right) $^{31}\text{P}\{^1\text{H}\}$ NMR spectrum of **11** in C_6D_6 .

Synthesis of the three-coordinate cobalt(I) complex **12** was attempted by reduction of the chloride precursor with KC_8 under argon (Ar) atmosphere. Upon addition of the solvent (THF) into the solid mixture, the color changed immediately from purple to greenish yellow. However, isolation of **12** from the reaction mixture was problematic due to the extremely high dinitrogen affinity of **12**, even in the presence of traces N_2 . N_2 -binding of **12** also occurs via a solid-gas reaction. Exposure of solid complex **12** to N_2 atmosphere (1 bar) resulted in a slow color change from yellowish green to purple, while exposure of the solution of **12** to N_2 atmosphere (1 bar) led to an immediate color change. As shown in Scheme 26, **12** can be obtained alternatively by sublimation of **11** at $110\text{ }^\circ\text{C}$. In contrast to **11**, **12** exhibits no signal in the $^{31}\text{P}\{^1\text{H}\}$ NMR spectrum, while three strongly paramagnetically shifted and broadened resonances can be observed in the ^1H NMR spectrum (Figure 18), which is in agreement with a d^8 open-shell electronic configuration. DFT calculation predicts that the triplet state of **12** is 20 kcal/mol lower than its singlet state in energy, which is consistent with the experimental observation.⁷

⁷ Calculation was performed by Prof. Dr. Leticia González and Dr. Philipp Marquetand.

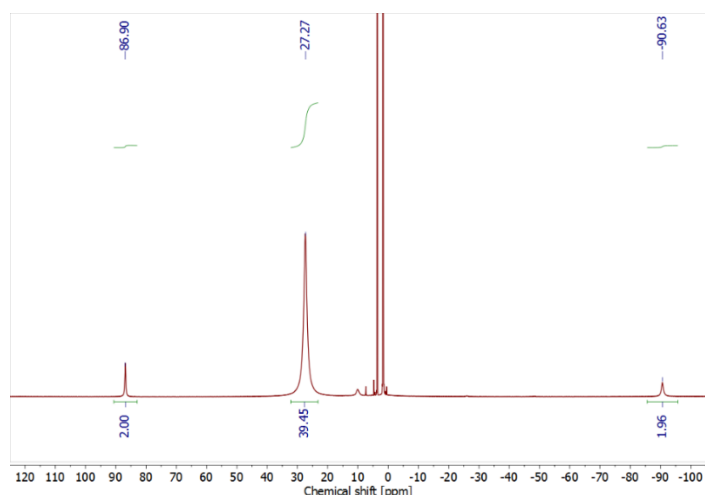


Figure 18: ^1H NMR spectrum of **12** in $\text{THF-}d_8$ (minor impurity of **9** at 9.9 ppm).

Due to its significant N_2 affinity, complex **12** for spectroscopic characterization was generated by sublimation of **11** under a dynamic vacuum. Dinitrogen complex **11** was first measured by UV/Vis spectroscopy in benzene, which gave an absorption spectrum with two absorptions at 505 and 622 nm (Figure 19, left, black line). The solvent of the measured solution was then removed *in vacuo* and the solid residual was sublimized until the color changed from purple to yellowish green, which was followed by trap-to-trap transfer of benzene to the cuvette under static vacuum. The resulting solution was then measured by UV/Vis spectroscopy, which gave a spectrum with an absorption at 435 nm (Figure 19, left, red line). Upon addition of N_2 , the species with the absorption at 435 nm was converted back to **11** (Figure 19, left, blue line), which suggests that this unknown species should be **12**. The IR spectrum (Figure 19, right) was recorded by an ATR-IR spectrometer, in which the C–C double bond stretching vibration of **12** at 1504 cm^{-1} is lower in energy than that of **11** at 1524 cm^{-1} , indicating higher electron density on the ligand backbone of **12** due to stronger π -backbonding.

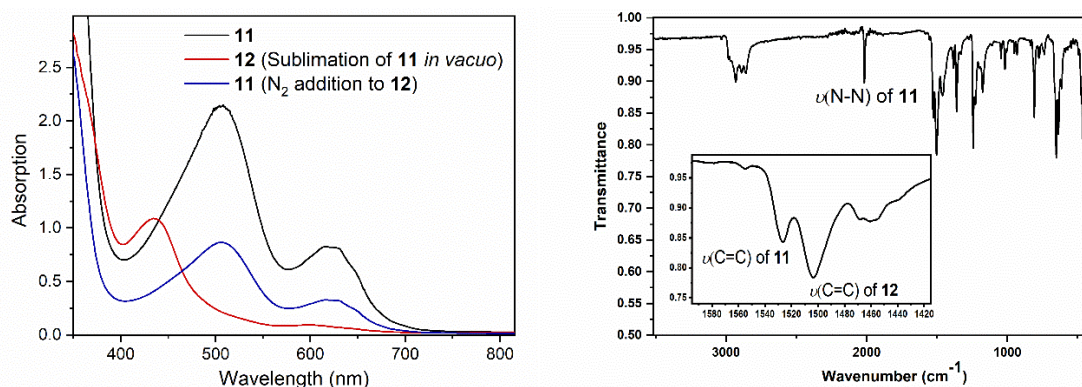
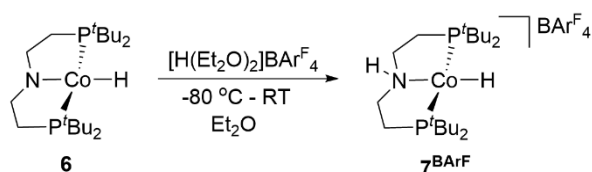


Figure 19: (Left) UV-Vis spectra (in benzene) of **11** (red), **12** after sublimation of **11** (blue), and **11** after addition of N_2 to the solution of freshly sublimed **12** (black). (Right) Infrared spectrum of **12** in the solid state (ATR-IR, small impurity of **11**).

2.1.2.2 Synthesis and characterization of cationic cobalt(II) hydride and cobalt(I) complexes

The active pre-catalyst **H4** for olefin hydrogenation, reported by Hanson and coworkers, was obtained upon protonation of its neutral cobalt(II) alkyl precursor **H3** by Brønsted acid $[\text{H}(\text{Et}_2\text{O})_2]\text{BAr}^{\text{F}}_4$ (Figure 3, left).^[64] In Hanson's catalytic system, cationic hydride intermediate was proposed experimentally and computationally as the active species, which was, however, not detected or isolated.^[70,123] Since we have neutral hydride complexes in hand, corresponding cationic hydride complexes were synthesized and characterized, followed by investigation of their reactivity in catalytic hydrogenation of alkenes.



Scheme 27: Protonation of **6** by $[\text{H}(\text{Et}_2\text{O})_2]\text{BAr}^{\text{F}}_4$.

Protonation of **6** by $[\text{H}(\text{Et}_2\text{O})_2]\text{BAr}^{\text{F}}_4$ (1 eq.) at $-80\text{ }^\circ\text{C}$ resulted in selective *N*-protonation on the ligand backbone, which gave a cationic cobalt(II) hydride complex $[\text{CoH}(\text{L}^2\text{H})]\text{BAr}^{\text{F}}_4$ (**7^{BArF}**) in a yield of 79%. In the ^1H NMR spectrum of **7^{BArF}** (Figure 20), two broadened signals were found for *tert*-butyl groups ($\delta = 7.08$ and 3.16 ppm) due to the change of symmetry compared to **6**. Three smaller signals were found for methylene groups on the backbone. No phosphorus signal was found in $^{31}\text{P}\{^1\text{H}\}$ NMR spectra. The hydride ligand and the N–H bond can be evidenced by IR spectroscopy, which gave relatively weak absorptions at $\nu = 1869$ and 3230 cm^{-1} , respectively, compared to stronger absorptions of counterion. The X-Band EPR spectrum of **7^{BArF}** features a rhombic, anisotropic *g*-tensor ($g = 3.65, 2.12, 1.78$) with ^{59}Co hyperfine coupling (100%, $I=7/2$, $A_{xx} = 1180$ MHz), indicating a metal-centered radical with a low spin electronic configuration.

Protonation of **6** at room temperature by $[\text{H}(\text{Et}_2\text{O})_2]\text{BAr}^{\text{F}}_4$ resulted in the formation of **7^{BArF}** as main product, while the cationic three-coordinate cobalt(I) complex $[\text{Co}(\text{L}^2\text{H})]\text{BAr}^{\text{F}}_4$ (**5^{BArF}**) was obtained in a yield less than 10%, as judged by ^1H NMR spectroscopy. **5^{BArF}** can be selectively synthesized upon protonation of **10** by $[\text{H}(\text{Et}_2\text{O})_2]\text{BAr}^{\text{F}}_4$ at room temperature with dissociation of N_2 (Scheme 28). The ^1H NMR spectrum (Figure 21) of **5^{BArF}** displays two broadened resonances ($\delta = 24.6$ and 22.7 ppm) for *tert*-butyl substituents and four backbone methylene resonances, indicating C_s symmetry. The line broadening and chemical shifts over a wide range suggest a high-spin electronic configuration.

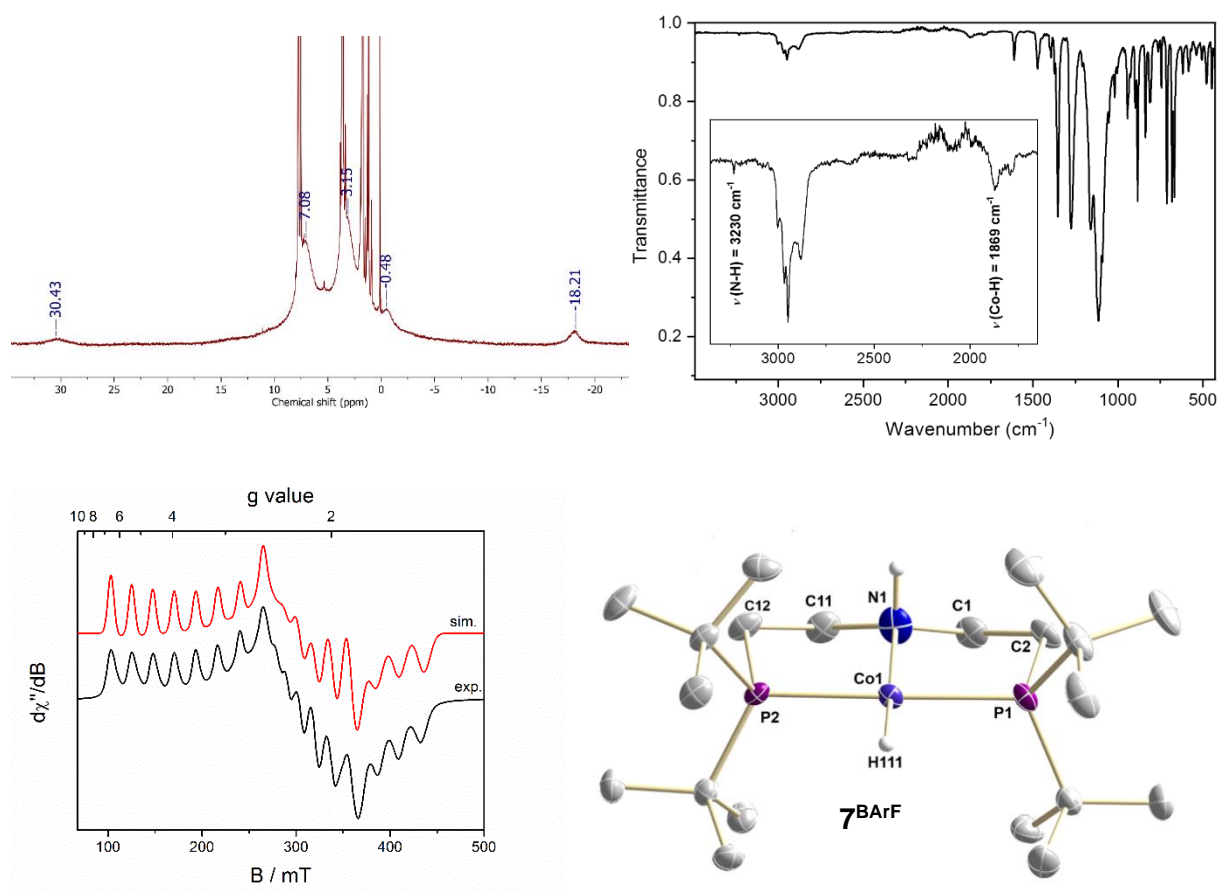
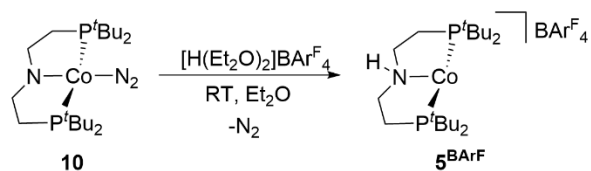


Figure 20: (top, left) ^1H NMR spectrum of 7^{BARF} in $\text{THF-}d_8$; (top, right) IR spectrum of 7^{BARF} measured by ATR-IR spectroscopy in solid state; (bottom, left) CW X-band EPR spectrum of 7^{BARF} in frozen THF at 145 K (black trace) and simulation (red trace); simulation parameters: $g = 3.65, 2.12, 1.78$; $A[\text{MHz}] = 1180, 374, 434$; (microwave frequency: 9.441 GHz, modulation amplitude: 400 mT, microwave power: 10.02 mW, modulation frequency: 100 kHz, time constant: 81.92 ms); (bottom, right) Molecular structure of 7^{BARF} in the crystal from x-ray diffraction with anisotropic displacement parameters drawn at the 50% probability level; hydrogen atoms except Co–H and counter anion omitted for clarity. The hydrogen atom in Co–H bond was found from the residual density map and isotopically refined; selected bond distances (\AA) and angles ($^\circ$): Co1–H111 = 1.43(3); Co1–N1 = 2.0163(18); Co1–P1 = 2.1948(6); Co1–P2 = 2.1923(6); C1–N1 = 1.461(3); C11–N1 = 1.454(3); N1–Co1–H111 = 177.7(12); N1–Co1–P1 = 88.41(6); N1–Co1–P2 = 87.64(6); P1–Co1–P2 = 175.58(2).



Scheme 28: Synthesis of 5^{BARF} .

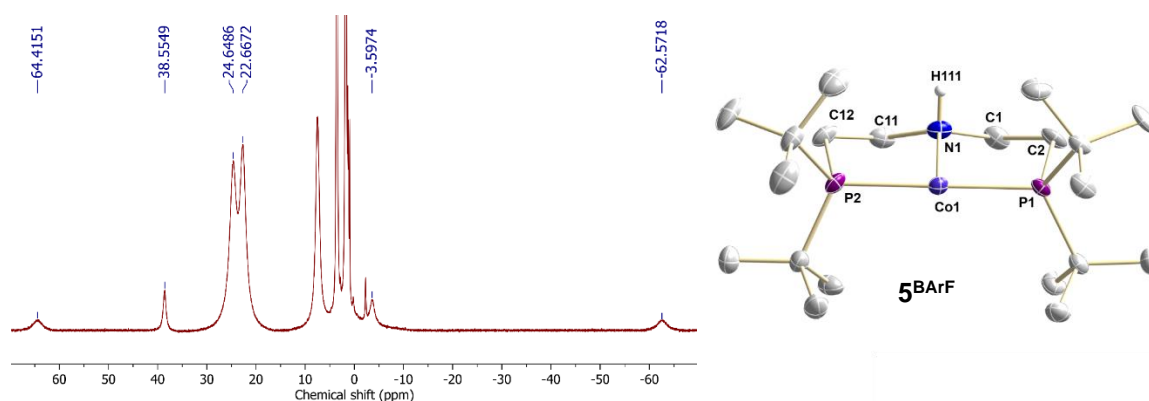


Figure 21: (left) ^1H NMR spectrum of 5^{BARF} in THF-d_8 . (right) Single crystal x-ray structures of 5^{BARF} with the anisotropic displacement parameters drawn at the 50% probability level. Except N–H and Co–H, all other hydrogen atoms and BARF_4 anions are omitted for clarity. The hydrogen atom in Co–H bond was found from the residual density map and isotopically refined. Selected bond distances (\AA) and angles ($^\circ$) for 5^{BARF} : Co1–N1 = 2.064(3); Co1–P1 = 2.2134(9); Co1–P2 = 2.2176(9); C1–N1 = 1.483(4); C11–N1 = 1.487(4); N1–Co1–P1 = 87.68(8); N1–Co1–P2 = 88.27(8); P1–Co1–P2 = 175.17(3).

Furthermore, protonation of **6** with $[\text{H}(\text{Et}_2\text{O})]\text{BF}_4$ at room temperature selectively gave cationic cobalt(II) hydride complex 7^{BF_4} in a yield of 57%. NMR and EPR data of 7^{BF_4} can be comparable to 7^{BARF} . The IR spectrum shows strong vibrations at 1816 and 3214 cm^{-1} corresponding to Co–H and N–H stretching vibrations, respectively, supporting *N*-protonation and an intact Co–H bond against protonation. A short N–H \cdots F hydrogen bridge with BF_4^- anion was found (2.09 \AA) in 7^{BF_4} by X-Ray diffraction. Presence of hydrogen bonding (N–H \cdots F = 1.98–2.07 \AA) in 7^{BF_4} reasons for relative low energy N–H vibrations ($\Delta d = 16\text{ cm}^{-1}$) and low Co–H vibrations ($\Delta d = 53\text{ cm}^{-1}$), due to stronger *trans*-effect of the nitrogen atom compared to 7^{BARF} .

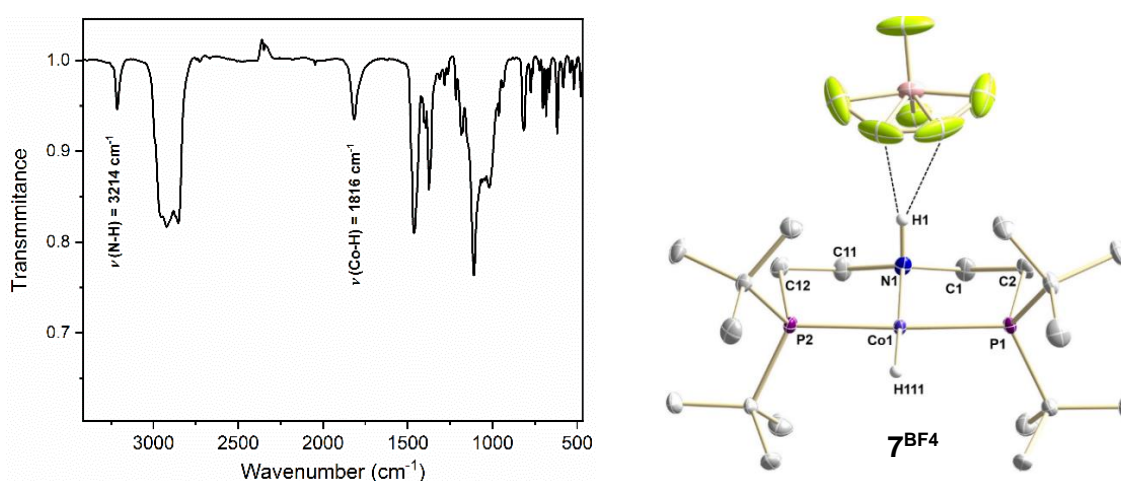


Figure 22: (left) IR spectrum of 7^{BF_4} in nujol. (right) Single crystal x-ray structures of 7^{BF_4} with the anisotropic displacement parameters drawn at the 50% probability level. Except N–H and Co–H. The Co–H hydrogen atom was found from the residual density map and isotopically refined. Selected bond distances (\AA) and angles ($^\circ$) for 7^{BF_4} : Co1–H111 = 1.77(3); Co1–N1 = 2.0147(19); Co1–P1 = 2.2039(7);

Co1–P2 = 2.2014(7); C1–N1 = 1.487(4); C11–N1 = 1.490(4); N1–Co1–H111 = 172.4(10); N1–Co1–P1 = 87.10(7); N1–Co1–P2 = 87.58(7); P1–Co1–P2 = 174.46(2).

Neutral hydride complex **6** has two potential basic centers, namely the amide moiety in the ligand backbone and the hydride ligand. *N*-atom protonation of **6** by Brønsted acids gives **7⁺**, whereas, hydride protonation results in the formation of a proposed dihydrogen species or a cationic three-coordinate cobalt(II) species upon H₂ dissociation. Formation of cationic three-coordinate Co(I) complex **5⁺** is proposed to undergo protonation of hydride ligand in **6** by Brønsted acid, forming the cationic three-coordinate cobalt(II) intermediate, which comproportionates subsequently with **7⁺** to form the final product **5⁺** (Figure 23, right). This proposed mechanism was further evidenced by protonation of **6** with varied concentrations (Figure 23, left), which was monitored by ¹H NMR spectroscopy. As shown in the NMR spectra, formation of **5⁺** (resonance in green box) arised with increasing concentration of **6**, which is consistent with the proposed mechanism that **7⁺** gets involved in the formation of **5** (Figure 23, right).

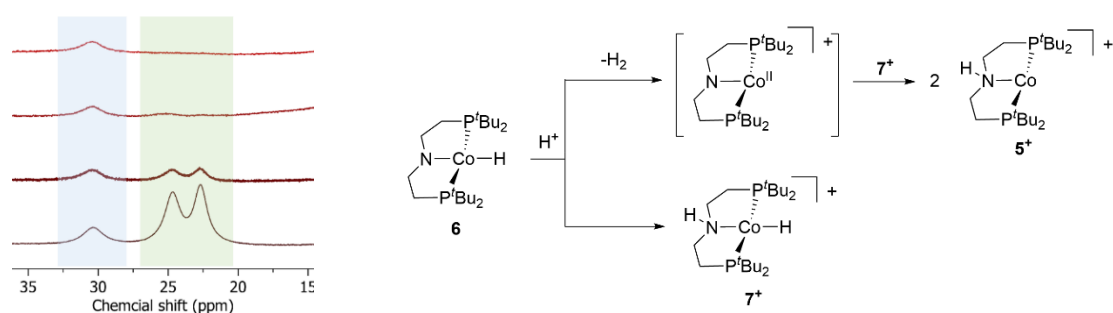


Figure 23: (Left) ¹H NMR spectra of protonation of **6** with [H(Et₂O)₂]BARF₄ in THF (1 mL) at room temperature. (Concentrations of **6** from top to bottom: 1.19 mM, 2.38 mM, 4.76 mM and 9.52 mM; blue denotes the signal belonging to the methylene group in the backbone of **7^{BARF}**, green denotes the signal belonging to the *tert*-butyl groups of **5^{BARF}**). (Right) Proposed mechanism of protonation of **6** with Brønsted acid at room temperature.

In contrast to **6**, the reaction of **8** with HX (X = BARF₄⁻ or BF₄⁻) at room temperature resulted in the protonation of the carbon atom on the ligand backbone, forming a cationic imine cobalt(II) hydride complex [Co(L³H)]X (**13^X**). The ¹H MNR spectra of **13^X** in THF-*d*₈ (Figure 24) shows two broadened *tert*-butyl and three backbone signals. Chemical shifts of *tert*-butyl groups slightly differ between **13^{BARF}** (+5.37, +3.40 ppm) and **13^{BF4}** (+5.71, +3.66 ppm), while the chemical shift difference is even more pronounced in backbone protons with Δδ of up to 6 ppm. **13^{BF4}** can be converted to **13^{BARF}** upon addition of NaBARF₄ (1 equiv.). The ion exchange was found to be driven by poor solubility of NaBF₄ compared to NaBARF₄ in THF, supported by the observation of white powder precipitation upon addition of NaBARF₄ into the solution of **13^{BF4}**.

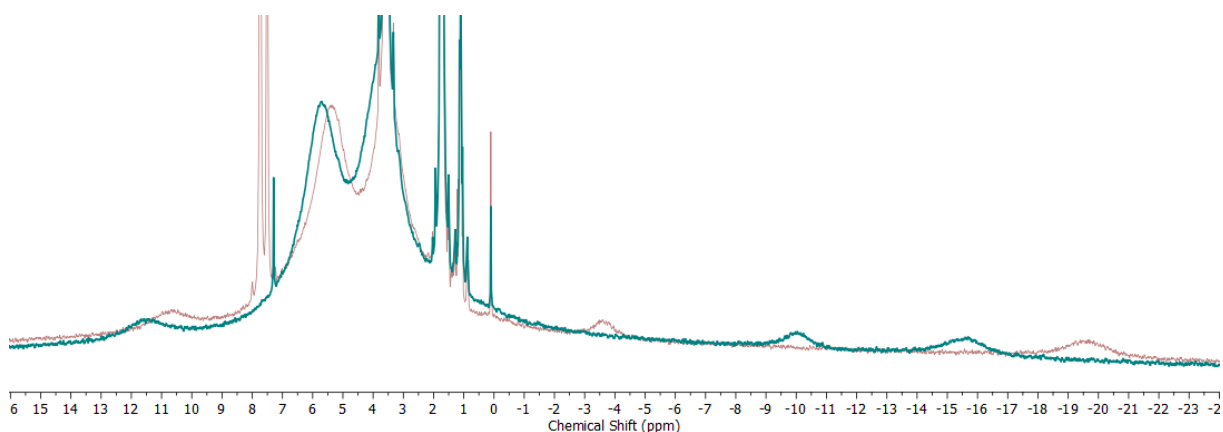


Figure 24: ^1H NMR spectra of $\mathbf{13}^{\text{BArF}}$ (red) $\mathbf{13}^{\text{BF}_4}$ (green) in $\text{THF-}d_6$.

The EPR spectrum of $\mathbf{13}^{\text{BArF}}$ was recorded by X-Band EPR spectroscopy, which was fitted with a rhombic, anisotropic g -tensor ($g = 3.28, 2.19, 1.87$) and a large ^{59}Co hyperfine coupling for the low field component ($A_{xx} = 952$ MHz), supporting metal-centered radical character. Structural characterization of $\mathbf{13}^{\text{BArF}}$ confirms the imine formation in the ligand backbone, with C–N bond length of 1.365(3) Å. The IR spectrum of $\mathbf{13}^{\text{BF}_4}$ exhibits bands that can be assigned to Co–H ($\nu = 1804$ cm^{-1} ; $\Delta\nu_{\text{Co-H/D}} = 509$ cm^{-1}) and C=N ($\nu = 1623$ cm^{-1}) stretching vibrations.

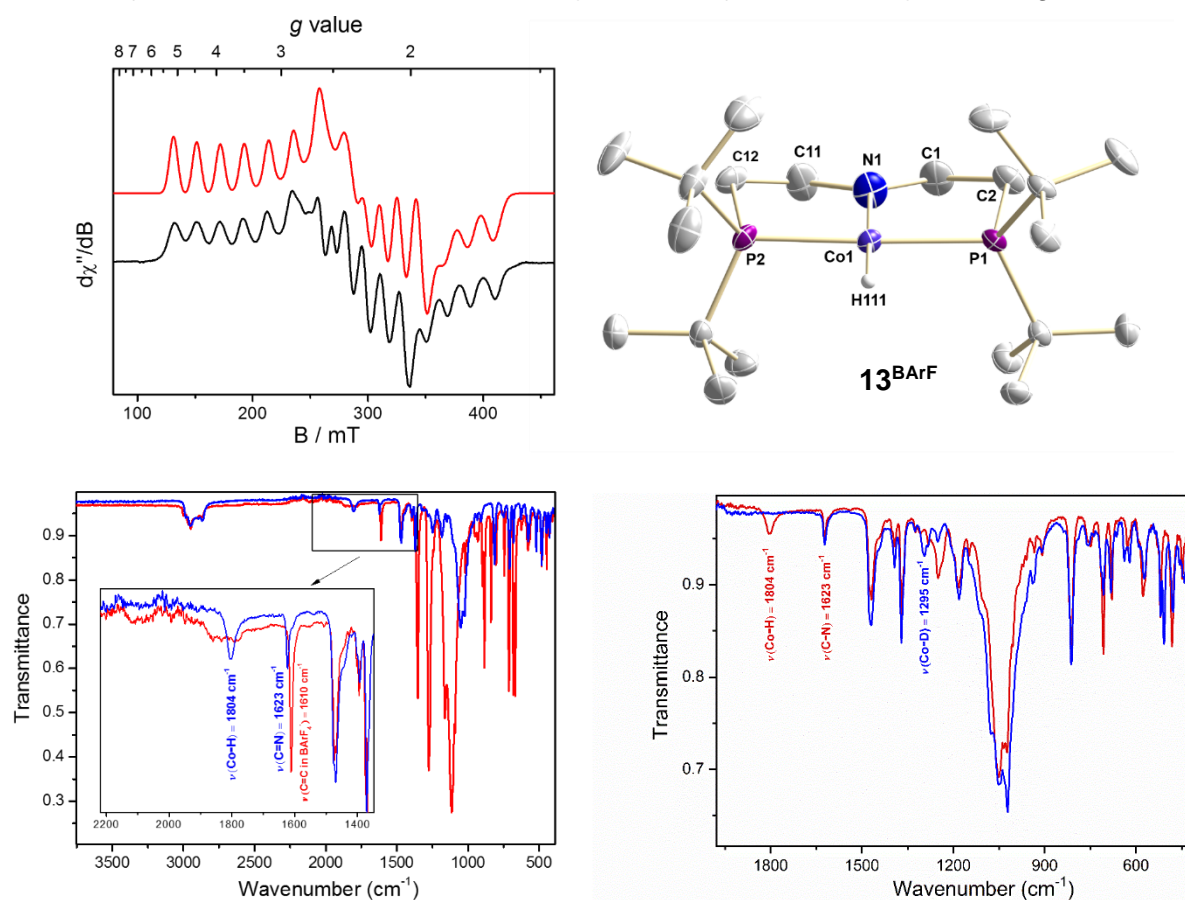


Figure 25: (Top, left) CW X-band EPR spectrum of $\mathbf{13}^{\text{BArF}}$ in frozen THF at 146 K (black trace) and simulation (red trace); simulation parameters: $g = 3.28, 2.19, 1.87$; $A[\text{MHz}] = 952, 371, 412$; (microwave frequency: 9.426 GHz, modulation amplitude: 400 mT, microwave power: 9.863 mW, modulation frequency: 100 kHz, time constant: 40.96 ms). (Top, right) Molecular structure of $\mathbf{13}^{\text{BArF}}$ in the crystal

from x-ray diffraction with anisotropic displacement parameters drawn at the 50% probability level; hydrogen atoms except Co–H and counter anion omitted for clarity; selected bond distances (Å) and angles (°): Co1–H111 = 1.49(3); Co1–N1 = 1.9622(19); Co1–P1 = 2.1942(6); Co1–P2 = 2.1933(6); C1–N1 = 1.365(3); C11–N1 = 1.405(3); N1–Co1–H111 = 178.9(12); N1–Co1–P1 = 87.19(7); N1–Co1–P2 = 88.08(7); P1–Co–P2 = 175.27(2). (Bottom, left) ATR-IR spectra of **13**^{BArF} (red) and **13**^{BF4} (blue) and in solid state. (Bottom, right) ATR-IR spectra of **13**^{BF4} (red) and **13**^{BF4}-D (blue) in solid state.

Molecular structures of **7**^{BArF}, **7**^{BF4} and **5**^{BArF}, **13**^{BArF} (Figure 26), obtained using X-ray diffraction analysis, have a square planar geometry. Hydride ligands were located on the electron density map. The Co–H bond distance of **7**^{BF4} (1.77(3) Å) was found longer than complexes **7**^{BArF} (1.43(3) Å) and **13**^{BArF} (1.49(3) Å) with non-interacting BArF₄[−] as counter ion. The Co–N bond distances are nearly the same for amine complexes **7**^{BF4}, **7**^{BArF} and **5**^{BArF}, imine complex **13**^{BArF} shows a shorter distance of 1.9622(19) Å. In comparison to neutral amido complex **6** (Co–N = 1.8520(18) Å), the N→Co π-donation follows the trend of amido (**6**) > imine (**13**^{BArF}) > amine (**7**^{BF4} and **7**^{BArF}). It resembles the observation made in amido > vinyl > divinyl Co^{II}Cl complexes.^[127]

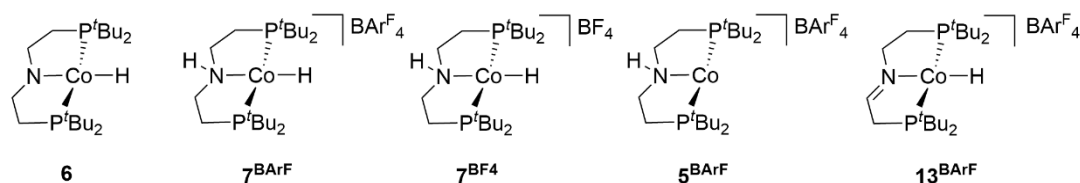


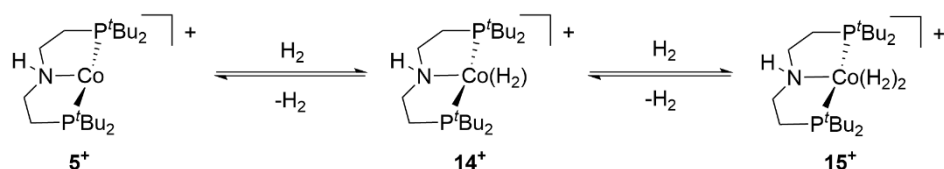
Figure 26: Complexes in comparison of molecular structures.

2.1.3 Reactivity of cobalt complexes with H₂

H₂ binding to a metal center is suggested to be an elementary step in hydrogenative catalysis.^[6] Several reported L_nCo(H₂) complexes are thermally labile and were spectroscopically characterized at low temperature under H₂ atmosphere.^[74,86,88,125,144–146] With N₂-complexes and three-coordinate cobalt(I) complexes in hand, we further investigated H₂ activation by these complexes.

2.1.3.1 Preparation of a cobalt dihydrogen complex from **5**^{BArF} and **10**

H₂-binding to cobalt complexes has been reported at three-coordinate cobalt(I) or cobalt(II) dinitrogen complexes, forming either non-classical dihydrogen cobalt(I) complexes or classical dihydrido cobalt(III) complexes.^[74,86,125,144,145,147] To probe this reactivity in our platform, reactions of **5**^{BArF} and **10** with H₂ was first investigated.



Scheme 29: Reaction of $\mathbf{5}^{\text{BARF}}$ with H_2 .

$\mathbf{5}^{\text{BARF}}$ in $\text{THF-}d_8$ was exposed to H_2 atmosphere (1 bar) at room temperature, resulting in an immediate color change from green to light brown. This reaction was first monitored by ^1H NMR spectroscopy at room temperature (Figure 27). Upon addition of H_2 (1 bar), the signals of $\mathbf{5}^{\text{BARF}}$ ($\delta_{\text{H-TBU}} = 23.7$ ppm) disappeared, while new broadened signals ($\delta_{\text{H-TBU}} = 19$ ppm) appeared. The new species in the reaction mixture are stable for at least 3 days at room temperature under H_2 atmosphere, which converted back to $\mathbf{5}^{\text{BARF}}$ upon removal of H_2 . Furthermore, cobalt(II) monohydrido complex $\mathbf{7}^{\text{BARF}}$ was slowly formed in the reaction of $\mathbf{5}^{\text{BARF}}$ and H_2 (1 bar), with a yield of 10% in 3 days. A cobalt(I) complex reported by Lee group shows the same reactivity, which are proposed to form cobalt(II) monohydride complexes via comproportionation between three-coordinate cobalt(I) complexes and their H_2 -binding intermediates.^[145]

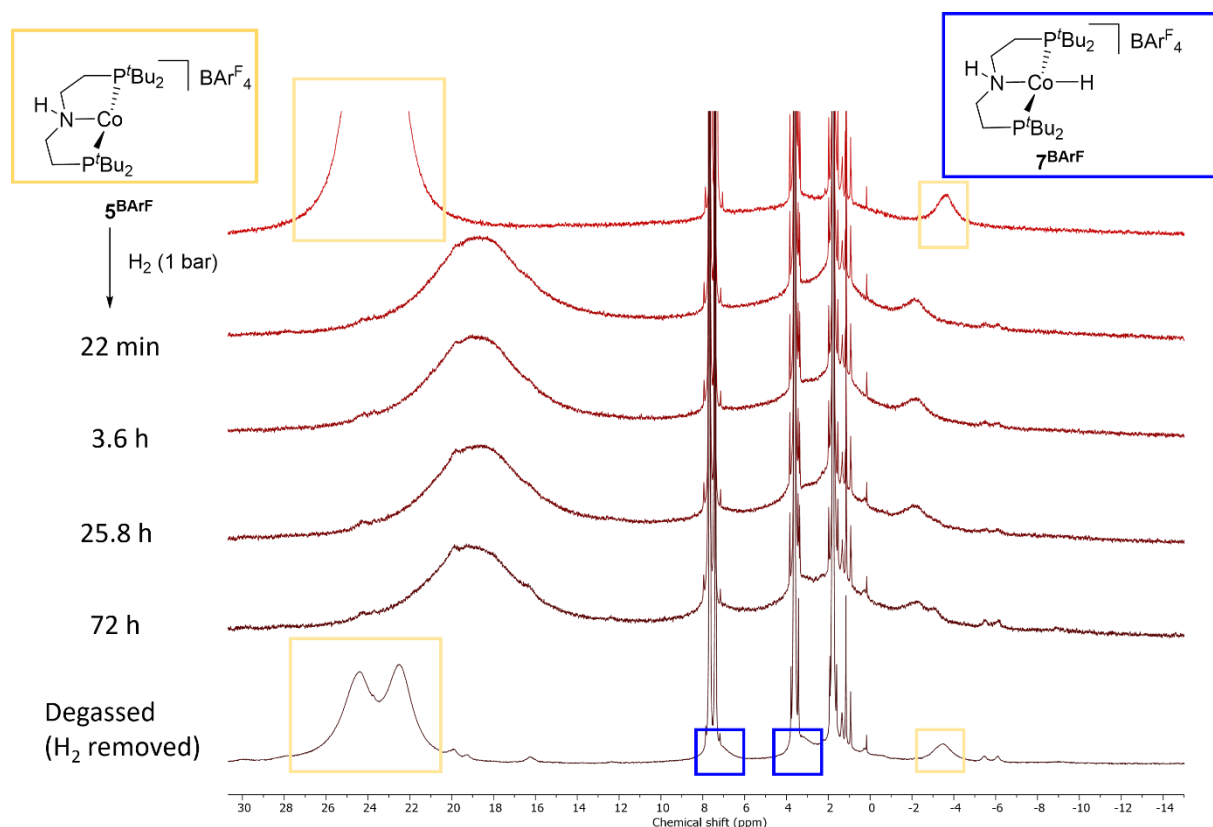


Figure 27: ^1H NMR spectra of the reaction of $\mathbf{5}^{\text{BARF}}$ with H_2 (1 bar) in $\text{THF-}d_8$.

These reactions were then measured at -50 °C by ^1H and $^{31}\text{P}\{^1\text{H}\}$ NMR spectroscopy, to avoid line broadening in the ^1H NMR spectrum due to rapid H_2 association/dissociation to the metal

center. Addition of 1 bar H₂ resulted in two slightly broadened resonances in the ³¹P{¹H} spectrum (Figure 28a, red spectrum), which are assigned based on their ¹H NMR spectra to two cobalt complexes with H₂ binding, namely [Co(H₂)(L²H)]BAR^F₄ (**14**^{BARF}, δ = 97.8 ppm) and [Co(H₂)₂(L²H)] BAR^F₄ (**15**^{BARF}, δ = 110.7 ppm) (Scheme 29). Exposure of **5**^{BARF} to a higher pressure of H₂ atmosphere (5 bar) resulted in the disappearance of the signal belonging to **14**^{BARF} in the ³¹P{¹H} spectrum (Figure 28a, black spectrum), enabling the selective formation of **15**^{BARF}, which displays in high field region two resonances at δ = -6.22 and -18.19 ppm in the ¹H NMR spectrum (Figure 28c, green box). Each resonance has an integration of two protons with respect to other ligand signals, which suggests that complex **15**^{BARF} binds with two dihydrogen molecules. Complex **14**^{BARF} gives only one signal in the high-field region in the ¹H NMR spectrum at δ = -33.15 ppm (Figure 28c, blue box), which can be integrated as two protons versus other ligand signals. However, **14**^{BARF} and **15**^{BARF} are only stable under H₂ atmosphere. Removal of H₂ atmosphere resulted in an immediate conversion back to **5**^{BARF}.

The equilibrium constant of the reaction of **5**^{BARF} and H₂ (1 bar) at room temperature can be derived based on the assumption that **5**^{BARF} reacts with H₂ to form exclusively **14**^{BARF}. The concentrations of both **5**^{BARF} and **14**^{BARF} can be determined by each of their chemical shifts of the *tert*-butyl substituents at low temperature and the chemical shift of the coalescence of both signals at room temperature (Figure 27). The concentration of H₂ in C₆D₆ was calculated based on the literature^[148]. The equilibrium constant was calculated as 0.089 mM⁻¹.

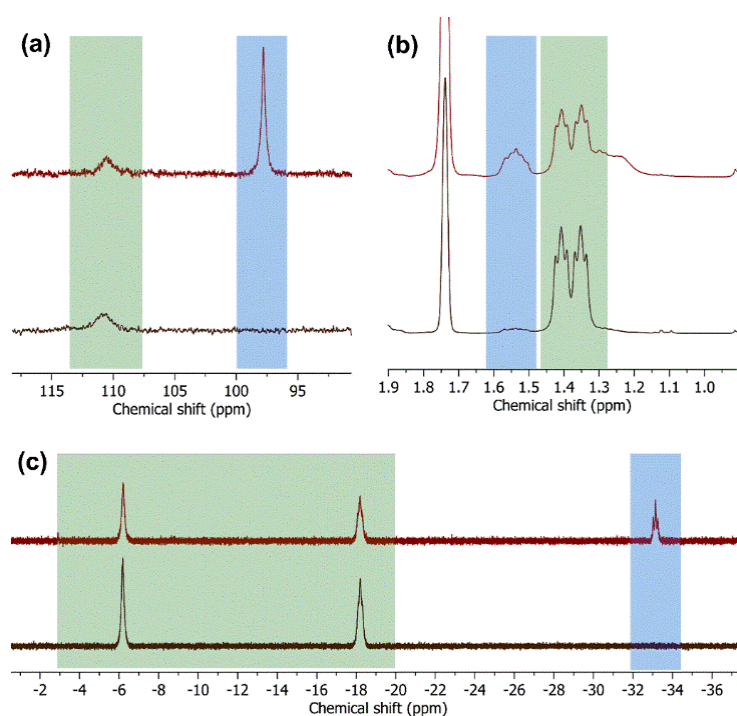


Figure 28: (a) ³¹P{¹H} NMR spectra of **5**^{BARF} in THF-*d*₈ under 1 bar (red) and 5 bar (black) H₂ atmosphere. (b and c) ¹H NMR spectra of **5**^{BARF} under 1 bar (red) and 5 bar (black) H₂ atmosphere. All spectra were recorded at -50 °C. (green signals belong to **14**^{BARF}, blue signals belong to **15**^{BARF}).

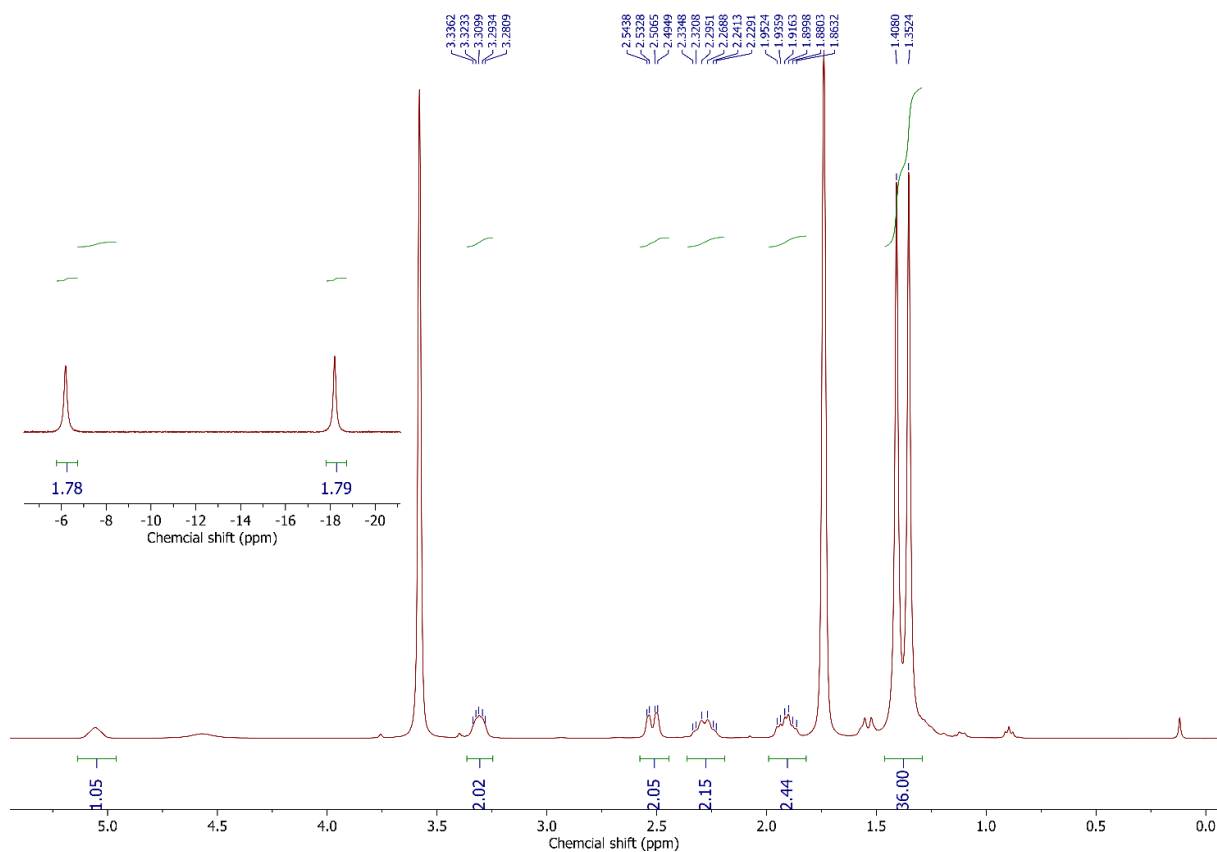


Figure 29: $^1\text{H}\{^{31}\text{P}\}$ NMR spectrum at $-50\text{ }^\circ\text{C}$ of $[\text{Co}(\text{L}^2\text{H})]\text{BARF}_4$ (5^{BARF}) under H_2 atmosphere (5 bar) in $\text{THF-}d_8$.

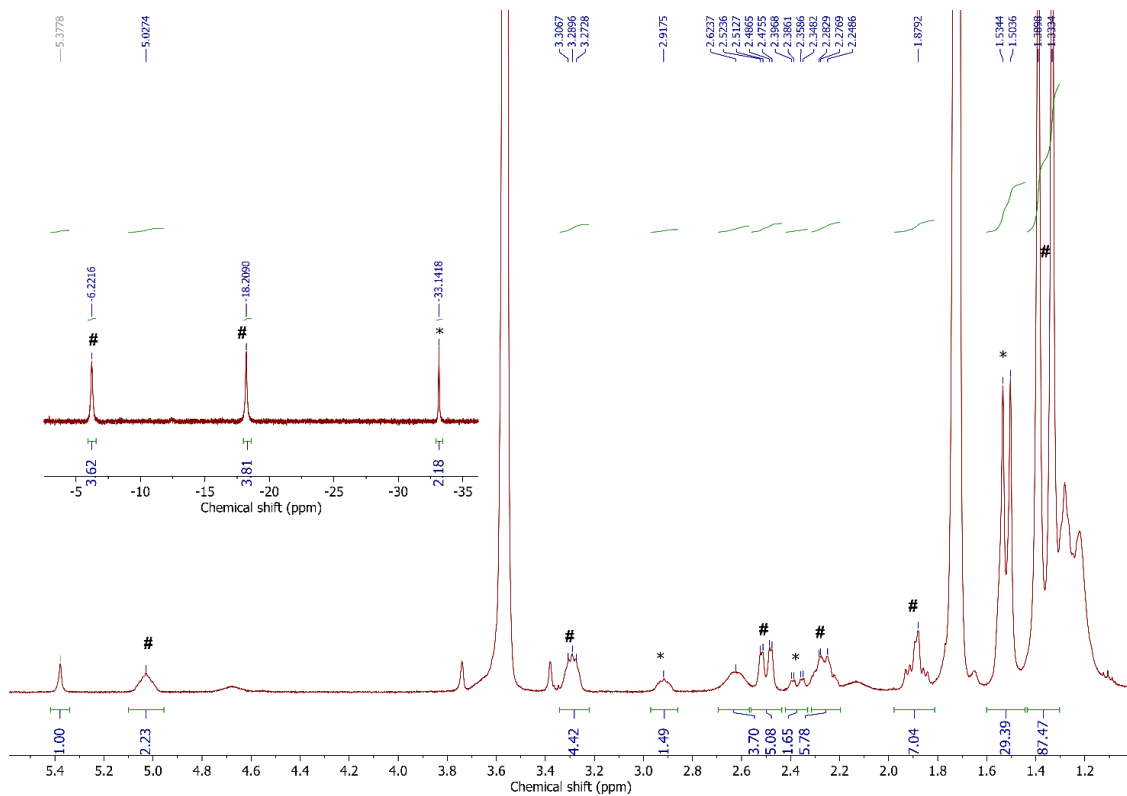
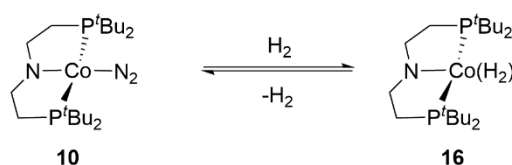


Figure 30: $^1\text{H}\{^{31}\text{P}\}$ NMR spectrum at $-50\text{ }^\circ\text{C}$ of $[\text{Co}(\text{L}^2\text{H})]\text{BARF}_4$ (5^{BARF}) under H_2 atmosphere (1 bar) in $\text{THF-}d_8$. (# denotes 15^{BARF} and * denotes 14^{BARF})

Dinitrogen complex **10** reacts with H₂ to form a new diamagnetic product **16** (Scheme 30). The ¹H NMR spectrum, which was recorded under 5 bar H₂ atmosphere, exhibits one signal at δ = -26.22 ppm in the high-field region, integrated as two protons with respect to the *tert*-butyl resonance, indicating a cobalt(I) dihydrogen or cobalt(III) dihydride complex. One *tert*-butyl and two backbone resonances in the ¹H NMR spectrum suggest C_{2v} symmetry of **16**. In contrast to the cobalt H₂-adducts **14**^{BArF} and **15**^{BArF}, **16** is stable after removal of the H₂ atmosphere, without dissociation of H₂ molecules. **16** converted immediately to dinitrogen complex **10** once N₂ was added. These observations suggest that H₂-binding to **10** is reversible (Scheme 30) and the binding strength is greater than **14**^{BArF} and **15**^{BArF}.



Scheme 30: Reaction of **10** with H₂.

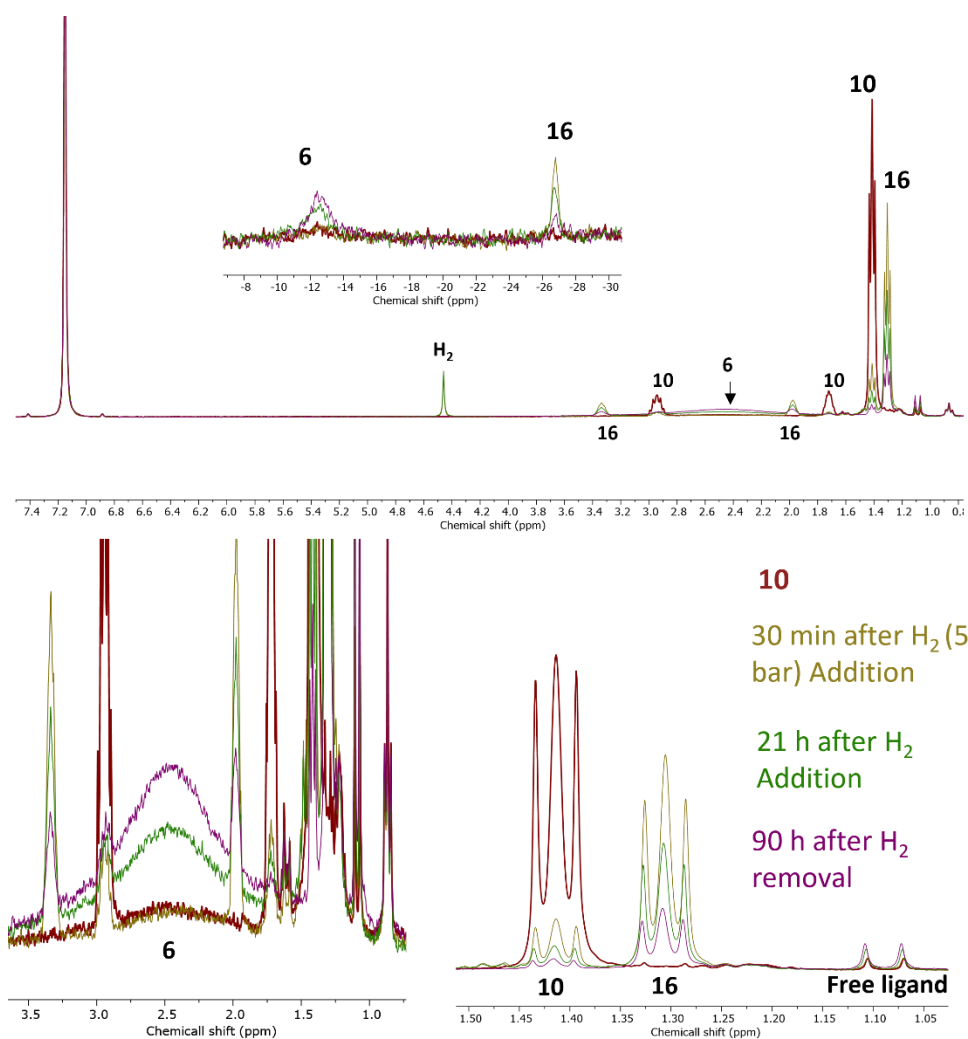


Figure 31: ¹H NMR spectrum of the reaction of **10** under H₂ (5 bar) atmosphere at room temperature.

Addition of H₂ to the solution of **10** resulted in the slow formation of monohydride complex **6** (Figure 31). In the presence of H₂ (5 bar), 41% of **16** converted to **6** in 21 h at room temperature. **16** converted further to **6** after removal of H₂ atmosphere, but with a lower reaction rate (ca. 26% conversion of **16** in 90 h).

Given the reversible nature of **14**^{BARF}, **15**^{BARF} and **16** formations, we tried to investigate the H₂ coordination and activation mode on these complexes. Our Attempt to identify the types of H₂-binding based on the *T*₁ criterion is impracticable due to the formation of cobalt(II) monohydride complexes, which are paramagnetic and influence the NMR relaxation time analysis. Exposure of **10** to HD gas (1 bar) at -90 °C resulted in a statistical mixture of H₂/HD (1:2) (Figure 33), indicating rapid H/D scrambling at low temperature. However, broad linewidth (> 30 Hz) of signals in the high-field region of ¹H{³¹P} NMR spectra precludes the structural assignment of **14**^{BARF}, **15**^{BARF} and **16** (Figure 32 and Figure 33). **16** is stable in the solid state, which enabled IR measurement of H₂- or D₂-binding complexes. **10** was exposed to H₂ and D₂ atmospheres (1 bar), followed by removal of the gas atmosphere and solvent *in vacuo*. The resulting residuals were measured by IR spectroscopy (Figure 34). The IR spectrum of the reaction residual of **10** and H₂ displays a resonance at 1861 cm⁻¹, the region in which Co–H stretching vibration is anticipated. The resonance at 1861 cm⁻¹ disappeared when **10** was exposed to D₂ atmosphere, while a new absorption emerged at 1341 cm⁻¹. The isotope shift $\Delta\nu_{\text{H/D}} = 520 \text{ cm}^{-1}$ is in line with the approximated value of $\Delta\nu_{\text{H/D}} = 534 \text{ cm}^{-1}$ by the harmonic oscillator model for the Co–H stretching vibration.

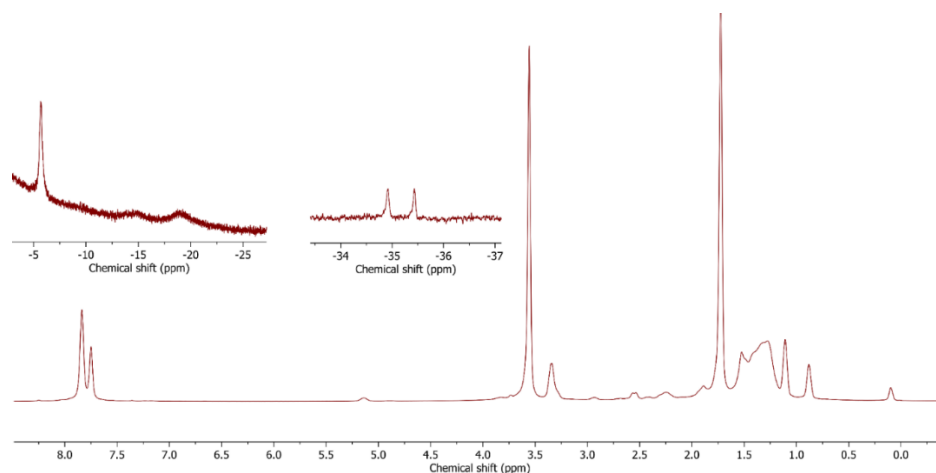


Figure 32: ¹H{³¹P} NMR spectrum of the reaction of **5**^{BARF} in THF-*d*₈ under HD (1 bar) atmosphere at -90°C.

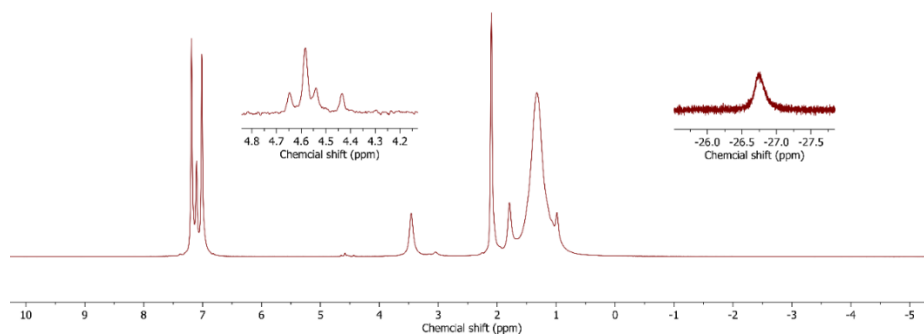


Figure 33: $^1\text{H}\{^{31}\text{P}\}$ NMR spectrum of the reaction of **10** in toluene- d_8 under HD (1 bar) atmosphere at -90°C .

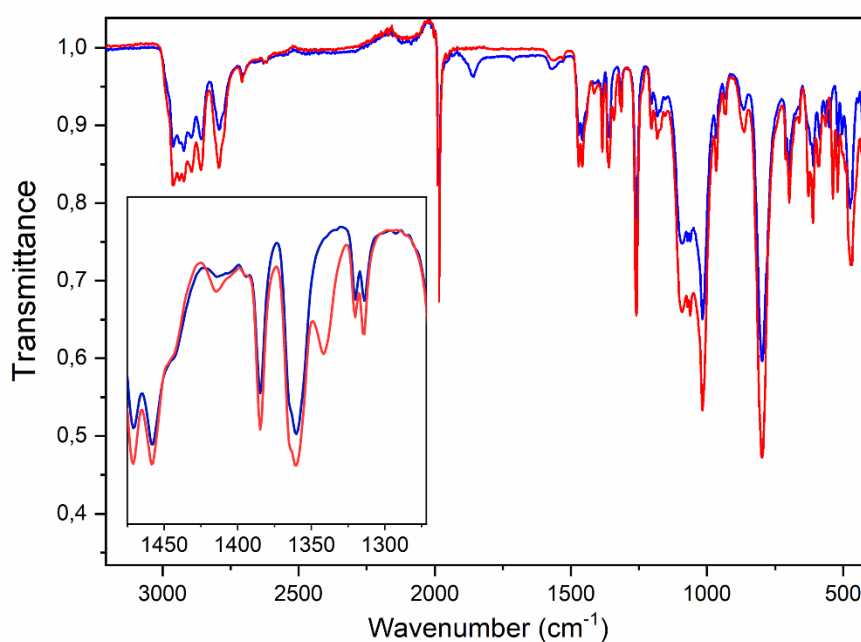


Figure 34: Solid state ATR-IR spectra of the reaction of (blue) **10** and H_2 (1 bar) in C_6D_6 and (red) **10** and D_2 in C_6D_6 [Punkt]

2.1.3.2 Preparation of a cobalt dihydrogen complex from **12**

11 is thermally stable under H_2 atmosphere (1 bar). Photolysis (390 nm LED) of **11** in the presence of H_2 (1 bar) led to a selective formation of cobalt monohydride complex **9**, taking two hours to full conversion. In contrast to **11**, exposure of a solution of **12** to the H_2 atmosphere (1 bar) resulted in an immediate color change from yellowish green to purple and the formation of a new species $[\text{Co}(\text{H}_2)(\text{L}^1)]$ (**17**), which can be observed by ^1H and ^{31}P NMR spectroscopy. H_2 removal regenerated the starting species **12**, suggesting that H_2 binding to **12** is reversible. Several hours stirring of **12** in the presence of H_2 (1 bar) led to the color change from purple to light brown, selectively forming **9**, as detected by ^1H NMR spectroscopy.

17 displays a slightly broadened resonance at 96.4 ppm in the $^{31}\text{P}\{^1\text{H}\}$ NMR spectrum at low temperature (< -30 °C), while an ^1H NMR spectrum (Figure 35) exhibits four diamagnetic signals corresponding to a C_{2v} symmetric complex. Due to fast interconversion between **17** and **12**/ H_2 , resonances of **17** in the ^1H NMR spectrum are broadened at room temperature. The sample can be cooled down to a temperature at which the interaction of H_2 with cobalt becomes slow enough to observe the coupling of protons with phosphorous atoms (Figure 35). Integration of the signal at $\delta = -28.5$ ppm over two protons indicates the initial formation of **17** as a $\text{Co}^{\text{I}}(\text{H}_2)$ or $\text{Co}^{\text{III}}(\text{H})_2$ complex.

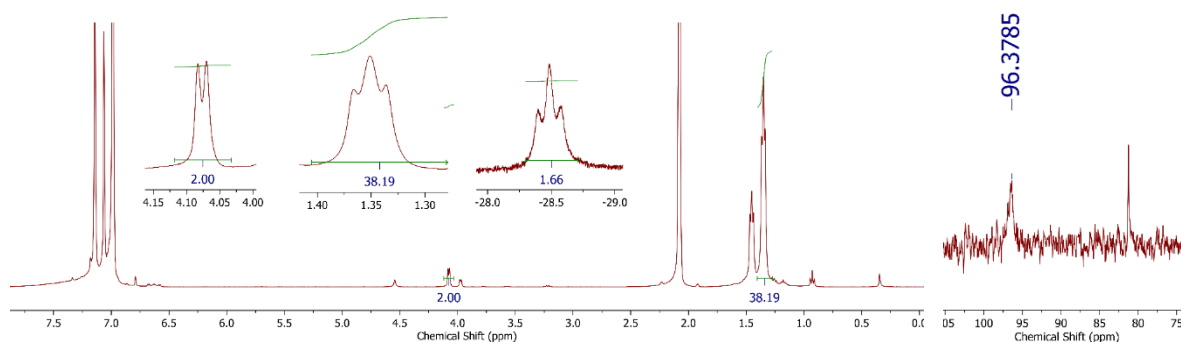


Figure 35: ^1H (left) and $^{31}\text{P}\{^1\text{H}\}$ (right) spectra of **17** at -50 °C in C_6D_6 (with minor amount of **11**).

To differentiate if complex **17** is a dihydrogen or dihydride complex, deuterium hydride (HD) gas (1 bar at room temperature) was added in an NMR tube to a frozen solution of **12**. The frozen solution was then thawed and measured by ^1H NMR spectroscopy at -100 °C. Three isotopologues of complex **17** were formed upon addition of HD gas, as speculated by the ^1H NMR spectrum (Figure 36, left), namely **17**- H_2 , **17**-HD and **17**- D_2 . H_2 was formed in the reaction, indicating extremely rapid isotope scrambling even at very low temperatures. However, differentiation of **17** between a dihydrogen or dihydride complex by NMR spectroscopy was unsuccessful, since the linewidth of the hydride signal (39 Hz) disabled an unambiguous differentiation. Further formation of paramagnetic complex **9** does not allow for defining complex **17** by T_1 relaxation time measurement, due to the strong effect of paramagnetic species on NMR relaxation times. DFT calculations⁸ of complex **17** suggests a nonclassical dihydrogen isomer, in which the bond length of $\text{H}-\text{H}$ is 0.94 Å (Figure 36, right).

⁸ Calculation was performed by Prof. Dr. Leticia González and Dr. Philipp Marquetand.

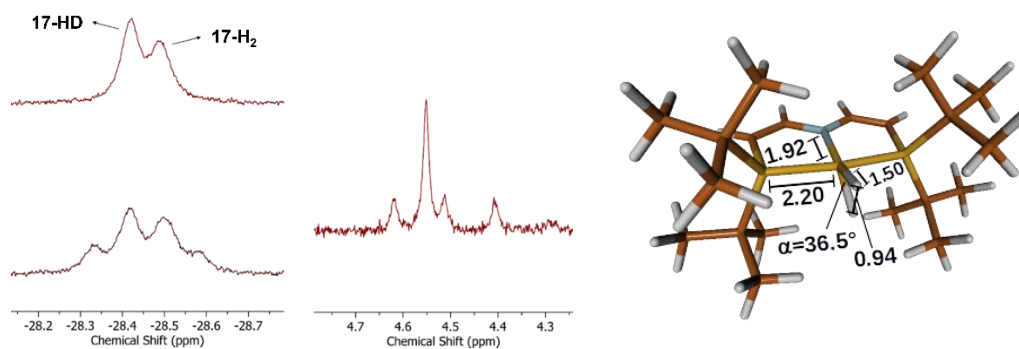
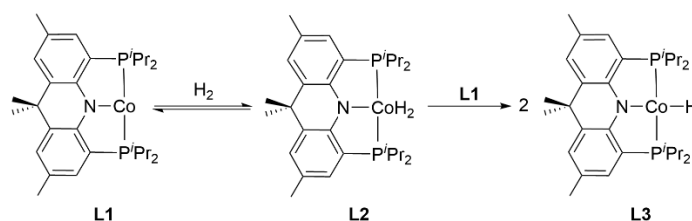


Figure 36: (Left) ^1H NMR spectra (bottom left and middle) and $^1\text{H}\{^{31}\text{P}\}$ NMR spectrum (top left) of a reaction mixture of **12** and HD (1 bar) at $-100\text{ }^\circ\text{C}$. (Right) DFT-optimized structure of complex **17** ($S = 0$). Selected bond lengths are given.



Scheme 31: H_2 activation by **L1**.^[145]

A three-coordinate cobalt(I) complex **L1** with low-spin electronic configuration, reported by Lee and coworkers, transformed to a $\text{Co}(\text{H}_2)$ complex **L2** under H_2 atmosphere, which was subsequently converted to cobalt(II) monohydride complex **L3** within 30 min at room temperature.^[145] They proposed that **L1** comproportionates with its H_2 -adduct **L2** to form **L3** via HAT (Scheme 31).^[145] The observation of the reactivity of $\text{Co}(\text{H}_2)$ complex **L2** resembles that of **17**, which provides us a starting point to further study H_2 activation by using our platform.

Formation of **9** was studied by monitoring the decay of **17** under different H_2 pressure. Starting compound **12** was produced as usual by sublimation of **11** in a high-pressure NMR tube, which was followed by addition of C_6D_6 . Various pressure of H_2 (2 – 4 bar) were applied to the resulting solution. Concentration of **17** was monitored by ^1H NMR spectroscopy (Figure 37) and determined by integration of *tert*-butyl signal of **17** in ^1H NMR spectra against internal standard (hexamethylbenzene). The reaction rate derived from the obtained experimental data follows a second order dependence on **17** and an inverse dependence on H_2 pressure (Figure 38, bottom).

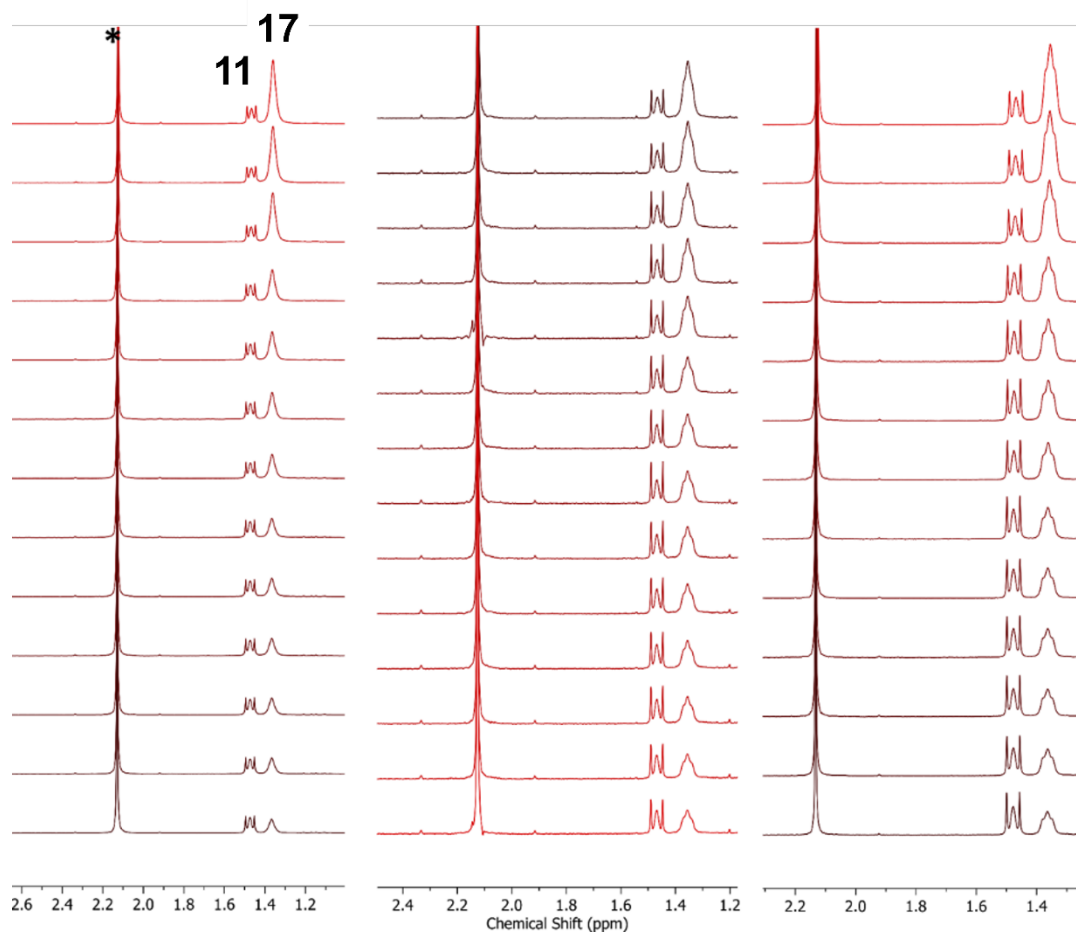


Figure 37: ^1H NMR spectra of **17** under 2 bar (left), 3 bar (middle) and 4 bar (right) H_2 showing the reaction progress between (top) $t = 20$ min and (bottom) $t \approx 3$ d (*denotes hexamethylbenzene).

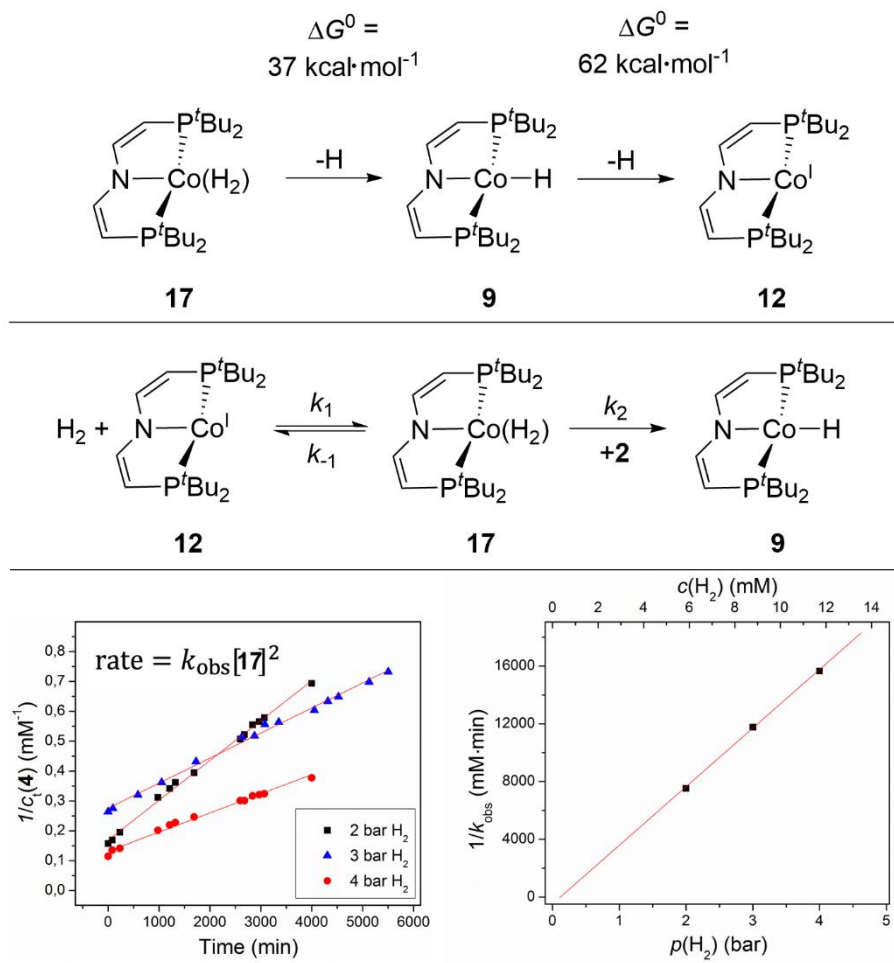


Figure 38: Top: Computed $\text{BDFE}_{\text{CoH}_2}$ of **17** and BDFE_{CoH} of **9**. Middle: Mechanistic model for the conversion of **12** to **9** with H_2 . Bottom: H_2 -pressure dependent kinetic data for the decay of **17**.

The rate law of this reaction is derived as follows (Figure 38, middle):

The rate law for decay of **17** is given by eq. 1:

$$-\frac{d[17]}{dt} = -k_1[12][\text{H}_2] + k_{-1}[17] + k_2[12][17] \quad (\text{eq. 1})$$

Assuming steady-state approximation for **12**

$$\frac{d[12]}{dt} = -k_1[12][\text{H}_2] + k_{-1}[17] - k_2[12][17] = 0 \quad (\text{eq. 2})$$

$$[12] = \frac{k_{-1}[17]}{k_1[\text{H}_2] + k_2[17]} \quad (\text{eq. 3})$$

gives for the decay of **17** the rate law:

$$-\frac{d[17]}{dt} = -\frac{k_1 k_{-1}[17][\text{H}_2]}{k_1[\text{H}_2] + k_2[17]} + k_{-1}[17] + \frac{k_2 k_{-1}[17]^2}{k_1[\text{H}_2] + k_2[17]} \quad (\text{eq. 4})$$

Assuming rapid pre-equilibrium K_1 ($k_1[\text{H}_2] \gg k_2[17]$) gives:

$$-\frac{d[17]}{dt} = \frac{k_2 k_{-1}[17]^2}{k_1[\text{H}_2]} = k_{\text{obs}}[17]^2 \quad (\text{eq. 5})$$

The derived rate law agrees with our experimental results from the kinetic measurement. Reaction of **12** and H_2 are in rapid pre-equilibrium, while the resulting H_2 -adduct **17**

comproportionates with **12** to form **9** via HAT. DFT calculation⁹ (Figure 38, top) predicts that the free energy required to remove one hydrogen atom from **17** is 37 kcal/mol, which is much lower than the Co–H bond strength of **9** (*BDFE* = 62 kcal/mol).

⁹ Calculation was performed by Prof. Dr. Leticia González and Dr. Philipp Marquetand.

2.2 Olefin hydrogenation with cobalt complexes

Part of the results of this chapter has been published (S. Sang, T. Unruh, S. Demeshko, L. Domenianni, N. P. van Leest, P. Marquetand, F. Schneck, C. Würtele, F. J. de Zwart, B. de Bruin, L. González, P. Vöhringer, S. Schneider, *Chem. Eur. J.* **2021**, *27*, 16978-16989.) and citation of the original work is permitted by the publishers.

Having stable prototypical neutral and cationic cobalt(II) hydride and cobalt(I) complexes in hand, it is worth to investigate their reactivity in catalysis. Catalytic styrene hydrogenation under 1 bar H₂ was carried out in a J-Young-NMR tube using **6** (8 mol%) either in C₆D₆ or THF-*d*₈. Only 4% conversion to ethylbenzene was observed after 17 h, and prolonged reaction time resulted only 17% of ethylbenzene in 72 h. Similar experiments with 5 mol% of the mixture of **7**^{BARF} and **13**^{BARF} in THF-*d*₈ gave no styrene or 1-hexene hydrogenation at all after 17 h. In addition, hydrogenation of styrene catalyzed by **5**^{BARF} (5 mol%) with H₂ (1 bar) resulted in 9% yield of ethylbenzene in 72 h. **6** does not undergo H atom transfer to styrene at room temperature in THF-*d*₈ or C₆D₆. In contrast to using the cyclohexyl group as substituent on phosphorus atoms in Hanson's system, steric bulk of substituents such as *tert*-butyl group might kinetically limit the insertion of olefins into the Co–H bond.^[64]

Table 2: Olefin hydrogenation catalyzed by neutral and cationic cobalt complexes.

Substrate	Cat.(mol%)	H ₂ Pressure (bar)	t [h]	Yield [%]	TON	TOF/h ⁻¹
Styrene	6 (8)	1	17	4	0.5	0.03
	7 (2)	1	20	0	0	0
	7+13 (2)	1	32	6	3	0.09
	5 (3)	1	72	9	3	0.04
	9 (10)	1	15	0	0	0
	11 (10)	1	15	0	0	0
	12 (3.8)	1	24	30	8	0.33
	H2 (2) ^[64]	1	24	100	5110	2
1-hexene	5 (5)	1	90	42	8.4	0.09
	5 (5)	5	15	23	4.6	0.3
1-octene	H2 (2) ^[64]	1	24	99	50	2

The neutral cobalt complexes **9** and **11** are inactive in thermal olefin hydrogenation. In contrast, the best catalytic activity among all cobalt complexes was obtained by using **12** as precatalyst (Figure 39). **12** was generated as usual by sublimation of **11** (2 mol%), which was followed by addition of styrene and solvent (C_6D_6). There was no reaction between **12** and styrene, as judged by 1H NMR spectroscopy, suggesting that styrene does not bind to the free coordination site of **12**. Upon addition of H_2 (1 bar), styrene converted catalytically to ethylbenzene, which confirms **12** as an active catalyst in thermal olefin hydrogenation. As shown in Figure 40 (red circles), the reaction rate of styrene hydrogenation by **12** gradually slowed down on a time scale that resembles decay of **17** to **9**. This observation indicates that **12** and **17** are key intermediates in olefin hydrogenation, while deactivation of these two species to thermally inactive catalyst **9** plays an important role in the hydrogenation rate. The deactivation rate is second order in **17**, as shown in the previous kinetic study (Figure 38). To overcome this deactivation process, the reaction mixture was photolyzed by 390 nm LED, which can activate **9** and enables the conversion of **9** to the active species **12**. This new method prompted us to thoroughly investigate the photochemical nature of **9** and its reactivity in olefin hydrogenation under photochemical conditions.

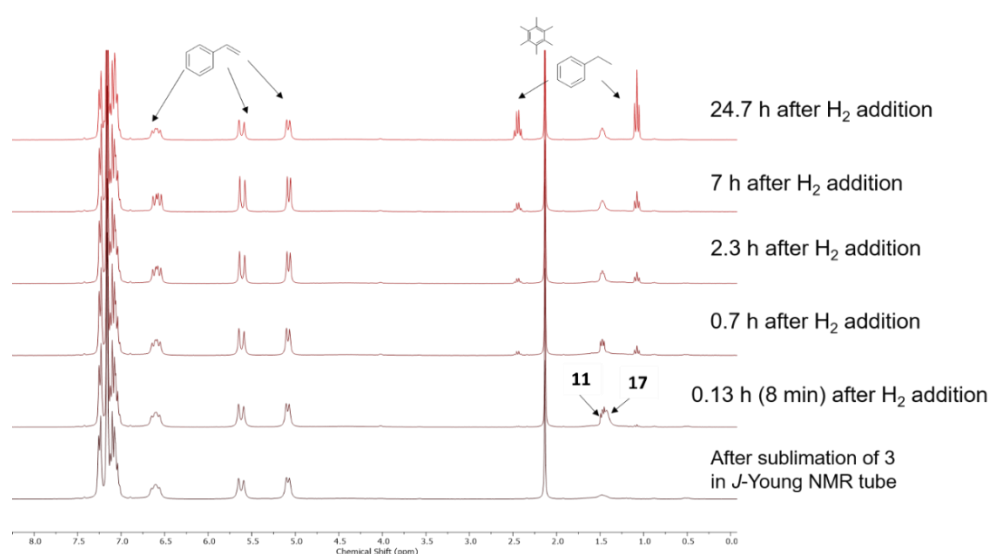


Figure 39: 1H NMR spectra of styrene hydrogenation with **12** as catalyst.

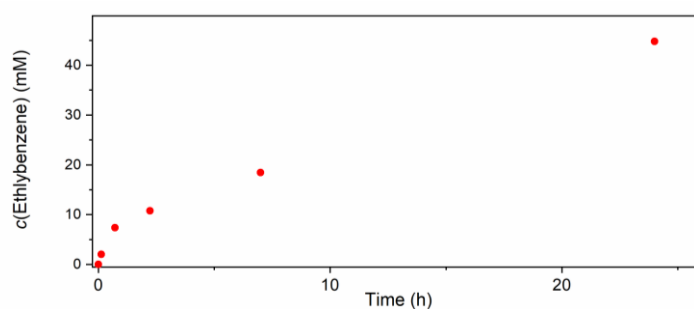
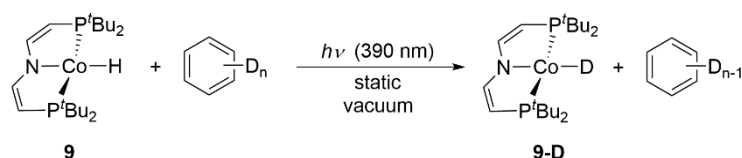


Figure 40: Time dependent ethylbenzene formation by catalytic hydrogenation of styrene (48 mmol, 1 bar H_2) using isolated **12** (3.8 mol%, red circles) as thermal catalysts.

2.3 Photochemical reactivity of [CoH(L³)] (**9**)

Part of the results of this chapter has been published (S. Sang, T. Unruh, S. Demeshko, L. Domenianni, N. P. van Leest, P. Marquetand, F. Schneck, C. Würtele, F. J. de Zwart, B. de Bruin, L. González, P. Vöhringer, S. Schneider, *Chem. Eur. J.* **2021**, *27*, 16978-16989.) and citation of the original work is permitted by the publishers.

2.3.1 Photochemical H/D exchange with deuterated solvents



Activation of **9** requires additional energy due to its strong Co–H bond. Complex **9** is thermally stable at temperature up to 60 °C in both solid and solution states. Photochemical reactivity of metal hydride complexes have been widely reported^[116], including C–H activation as one of the most important application, which motivates us to exam the photoreactivity of complex **9**.

Photolysis (LED, $\lambda = 390 \pm 20$ nm) of **9** was carried out in C₆D₆ at room temperature (Scheme 32), which resulted in a slow formation of **9-D**, as confirmed by ¹H NMR spectroscopy (Figure 41), IR spectroscopy (Figure 42, left) and mass spectrometry. In the ¹H NMR spectra, **9** and **9-D** can be differentiated by PIECS-induced chemical shifts, namely using backbone resonances at $\delta = 47.03$ and 48.23 ppm of **9-D** and **9**, respectively. Additionally, trace amount of **11** (~ 5%) was formed without further accumulation during photolysis, while formation of low quantities of *iso*-butene can also be observed due to slight photo-induced ligand decomposition. The IR spectra (Figure 42) of the reaction mixture show both $\nu_{\text{Co-H}}$ and $\nu_{\text{Co-D}}$ stretches, in agreement with the evolution of **9-D** through the H/D exchange with C₆D₆. Photolysis of **9** under dinitrogen atmosphere (1 bar) for 12 h resulted in a selective formation of N₂-complex **11**. To avoid the formation of **11**, photolysis of **9** in C₆D₆ was then carried out under a static vacuum. Under these conditions, trace quantities of three-coordinate cobalt(I) complex **12** was observed as a side product (27.26 ppm) by ¹H NMR spectroscopy, without accumulation during photolysis. A low quantum yield of $\Phi_{390} = 0.097\%$ was derived for the photolytic H/D exchange reaction of **9** with benzene-*d*₆.

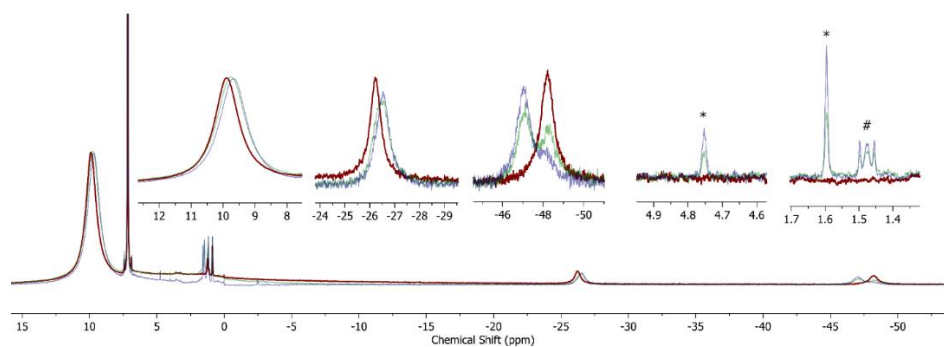


Figure 41: ^1H NMR spectra of **9** in C_6D_6 before (red) and after photolysis for 20 h (green, 53% yield in **9-D**) and 36 h (blue, 81% yield in **9-D**) (* denotes isobutene and # denotes cobalt dinitrogen complex **11**).

To further explore the photochemical reactivity of **9**, the reaction progress of the H/D exchange between **9** and C_6D_6 was monitored by ^1H NMR spectroscopy. Progress of the reaction could be stopped upon interrupting photolysis. No thermal reaction was observed between two successive irradiations. Concentrations of **9** and **9-D** were determined by integration of backbone signals at 47.20 ppm (**9-D**) and 48.22 ppm (**9**) in ^1H NMR spectra. The amount of transferred hydrogen atoms from **9** to the deuterated molecules can be determined by integration of the residual benzene signal against the internal standard $(\text{TMS})_2\text{O}$. The reaction progress (Figure 42, right) was monitored by ^1H NMR spectroscopy over three days. **9-D** formation is nearly in agreement with the increase of the residual signals of deuterated solvents (C_6D_6), thus confirming the H/D exchange between the metal center and the solvent molecules occurs quantitatively upon photolysis (Scheme 32). The same reactivity was also observed in various deuterated solvents ($\text{THF-}d_8$, $\text{Tol-}d_8$ and $\text{Cyclohexane-}d_{12}$) with comparable reaction time.

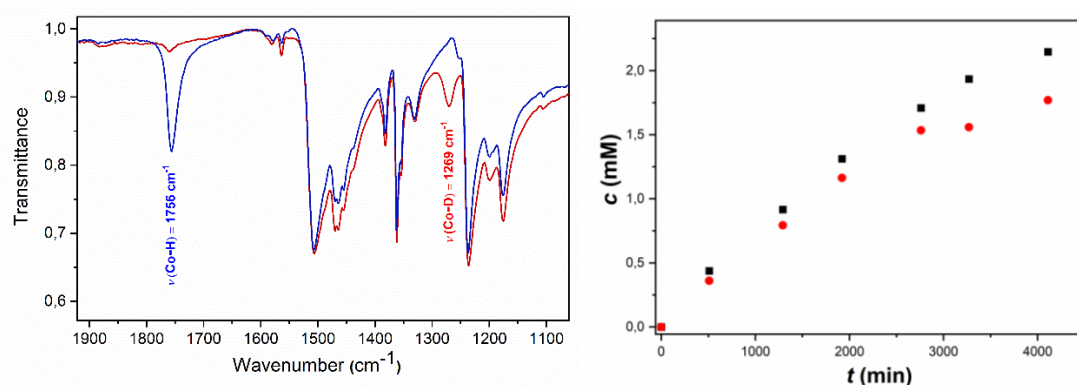


Figure 42: (left) ATR-IR spectra of **9** (solid state, red), **9-D** (solid state, blue) and **9** after photolysis in C_6D_6 for 36 h (solid residual after solvent removal, black). (right) Time-dependent formation of **9-D** (black, $[\mathbf{9}]_0 = 4.8 \text{ mM}$) and $\text{C}_6\text{D}_5\text{H}$ (red) upon photolysis of **9** in C_6D_6 .

As mentioned above, the Co–H bond of **9** undergoes H/D exchange with deuterated hydrocarbons under photochemical conditions, while immediate H/D exchange occurs

between **9** and D₂ or vice versa. Motivated by these results and considerable reported H/D exchange catalysis in hydrocarbons,^[149] the photocatalytic deuterium incorporation into benzene and toluene by **9** was studied, using D₂ as deuterium source. Photolysis (390 nm LED) of **9** in benzene or toluene under D₂ atmosphere (1 bar) was carried out. Yields of deuterium-incorporated products were determined by ²H NMR spectroscopy using cyclohexane-*d*₁₂ as internal standard (Figure 43). However, only up to three turnovers for the aromatic C–H deuteration were achieved over 40 h of photolysis due to the slow H/D exchange between **9-D** and hydrocarbons as rate determining step. No obvious deuterium incorporation was observed at the methyl position of toluene.

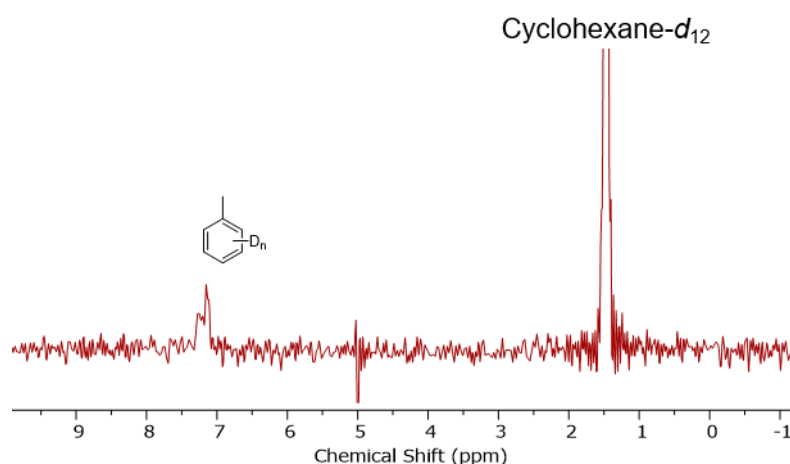
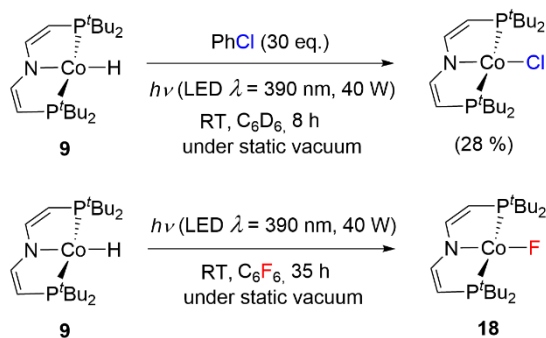


Figure 43: ¹H NMR spectrum of photocatalytic H/D exchange of toluene by **9** under 1 bar D₂ for 35 h (cyclohexane-*d*₁₂ as internal standard).

Apart from the H/D exchange, metal hydride complexes also appear to be ideal candidates for hydrodehalogenation involving hydride transfer to organic substrates.^[116,150] Photochemical hydrodehalogenation of dichloromethane (CH₂Cl₂) by iridium hydride complexes was reported by Miller and coworkers.^[151] Mechanistic investigation indicates a self-quenching electron transfer between the excited state and the ground state hydride species, followed by hydrodehalogenation of CH₂Cl₂.^[151] No dehalogenation of chlorobenzene (C₆H₅Cl) was observed.^[151] In this context, we examined CH₂Cl₂, C₆H₅Cl and hexafluorobenzene (C₆F₆) as halogenated substrates that would undergo hydrodehalogenative transformation. Unlike the iridium hydride complexes, CH₂Cl₂ reacts thermally with **9** to form the cobalt chloride complex. No thermal reaction was observed with C₆H₅Cl and C₆F₆. Irradiation of **9** and C₆H₅Cl (30 eq.) in C₆D₆ for 8 h produced the cobalt chloride complex with a yield of 28 % (Scheme 33). In contrast, no H/D exchange with C₆D₆ was observed. Chemo-selectivity is in agreement with the bond dissociation energy of the aromatic C–Cl bond (97.1 kcal mol⁻¹) and the aromatic C–H bond (112.9 kcal mol⁻¹).^[152] Due to the greater bond strength of the aromatic C–F bond (127.2 kcal mol⁻¹), C₆F₆ is rather resistant to be reduced^[152]. Irradiation of **9** in neat C₆F₆ for 35 h produced cobalt(II) fluoride complex **18** quantitatively (Scheme 33).



Scheme 33: Photochemical hydrodehydrogenation of C₆H₅Cl and C₆F₆.

2.3.2 Photochemical reactivity studied by transient spectroscopy

9 and **9-D** were further studied by UV-pump-UV-vis-probe and UV-pump-IR-probe spectroscopy to monitor the subsequent excited state evolution upon irradiation.¹⁰ To get structural information on the transient species, the transient IR absorptions of **9** and **9-D** were recorded. Excitation ($\lambda_{\text{exc.}} = 400 \text{ nm}$) of **9-D** in *n*-hexane led to immediate bleaches of ground state absorptions (negative signals) at $\nu = 1235, 1285$ and 1511 cm^{-1} (Figure 44, left). Two strong ground-state bleaches (GSB) at $\nu = 1235$ and 1511 cm^{-1} can be assigned to C–H in-plane bending vibration and C–C double bond stretching vibration of the pincer ligand, which are accompanied by slightly downshifted excited-state absorption bands (positive signals). The excited-state absorption bands are much broader than their corresponding GSB-absorption bands and gradually shift to higher wavenumbers with increasing time delay, which are likely attributed to vibrational cooling of the vibrational hot ground state. The relatively weak GSB band at $\nu = 1285 \text{ cm}^{-1}$ belongs to the Co–D stretching mode, accompanied by a weak transient absorption band at $\nu = 1246 \text{ cm}^{-1}$. Existence of a transient absorption band in the Co–D stretching mode suggests that the transient species in its vibrational hot ground state has an intact Co–D bond. **9** was measured in *n*-hexane with the same excitation wavelength, in which the C–C double bond and the Co–H stretching vibration were monitored (Figure 44, right). However, the gas phase water bending mode ($\nu = 1750 \text{ cm}^{-1}$) interferes with data collection in the region of Co–H stretching, leading to a slight perturbation at the transient absorption of the Co–H stretching mode at $\nu = 1742 \text{ cm}^{-1}$.

¹⁰ Pump probe measurement was performed by Tobias Unruh, Luis I. Domenianni and Prof. Dr. Peter Vöhringer.

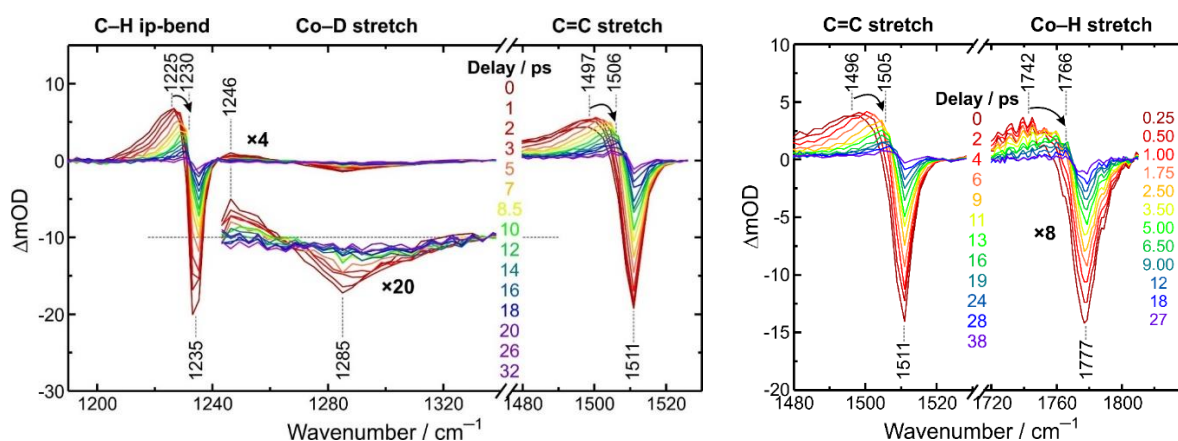


Figure 44: (Left) Time resolved UV-pump mid-IR-probe spectrum of **9-D** in n-hexane upon 400 nm pump excitation and probing the spectral regions of C–H in-plane bending, C–C double bond stretching vibration and Co–D stretching vibration. (Right) Time resolved UV-pump mid-IR-probe spectrum of **9** in n-hexane upon 400 nm pump excitation and probing the spectral regions of C–C double bond stretching vibration and Co–H stretching vibration.

As shown in the kinetic traces of **9** and **9-D** for selected wavenumbers (Figure 45), recovery to the electronic ground state takes place within a few tens of picoseconds. Due to the superposition of vibrational cooling and ground state recovery, kinetic traces demonstrate a complicated temporal evolution and are fitted using multi-exponential kinetics. No significant isotope effect is observed.

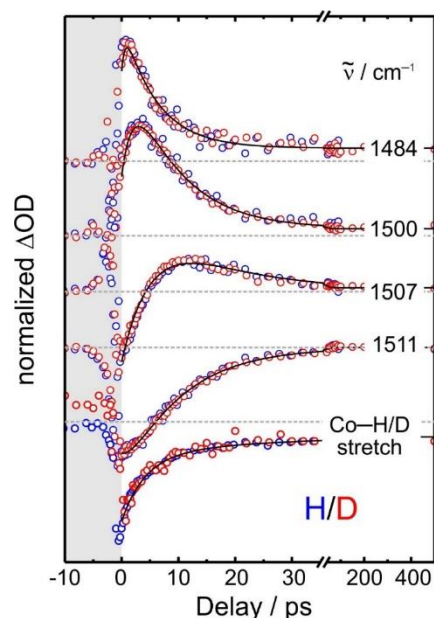


Figure 45: Comparison of kinetic traces of **9** and **9-D**.

To further rationalize the photochemical reactivity, **9-D** was measured in benzene by UV-pump-UV/vis-probe spectroscopy. Optical excitation of **9-D** at $\lambda_{\text{exc.}} = 400$ nm resulted in two strong transient absorption bands at $\lambda = 460$ and 540 nm, accompanied by a weaker transient

absorption band at 650 nm (Figure 46, a). Two major bands are both slightly blue shifted with increasing delay, whereas they have different relaxation dynamics. Immediately after excitation by pump pulse, the band at $\lambda = 540$ nm is the dominant component, which relaxes faster than the band at $\lambda = 460$ nm at early delays. After a delay time of 0.5 ps, relative amplitudes of both bands are reversed. This observation suggests that two transient absorption bands belong to different transient species. In contrast to IR-probe spectra, a photoproduct with a very weak absorption at $\lambda = 444$ nm was observed even after a delay time of 70 ps. Spectra with the delay time between 70 to 150 ps were collected and averaged to one single spectrum to achieve a better signal-to-noise ratio, which gives the absorption band of the photoproduct in Figure 46 (b). Three-coordinate cobalt(I) complex **12** has an electronic absorption band centered at $\lambda = 435$ nm, which is 9 nm close to the band of the photoproduct in the transient spectrum. The 9 nm shift as well as the negative absorption band at 420 nm can be attributed to the GSB of **9**. A good fit to the photo-product spectrum (Figure 46, b) can be given by a difference spectrum (Figure 46, c, blue) between the electronic absorption spectra of **9** (Figure 46, c, black) and **12** (Figure 46, c, red), which supports that **12** is the photo-product of **9**. However, the amplitude of the photo-product absorption band in transient spectrum is 100 times smaller than the maximal absorption band recorded at zero time delay, which suggests a much smaller quantum yield ($< 1\%$) in formation of **12**.

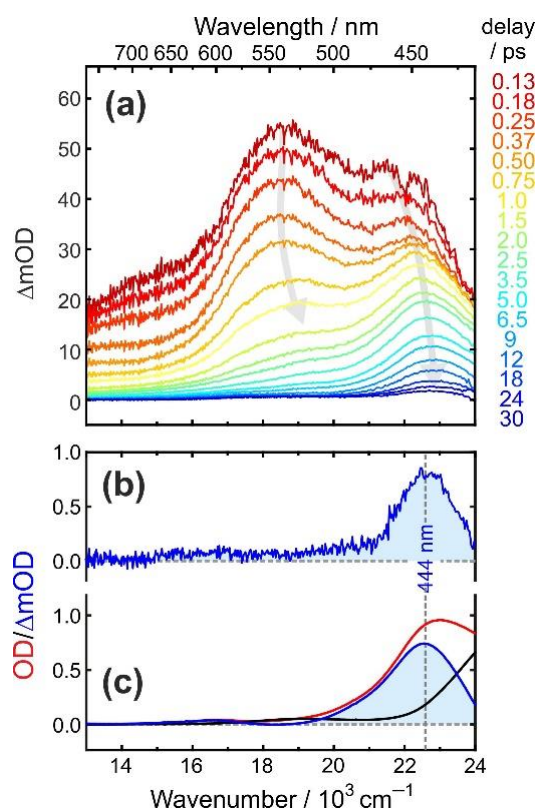
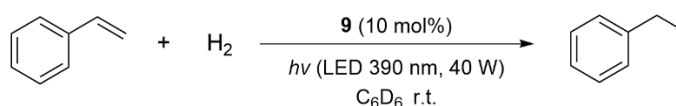


Figure 46: (a) Time resolved UV-pump Vis/near-UV probe spectra of **9-D** in benzene solution at room temperature. (b) Experimental photo-product spectrum. (c) Stationary UV/Vis spectrum of **9** (black) and **12** (red) and their difference spectrum (blue).

2.3.3 Photo-initiated cobalt catalyzed olefin hydrogenation

Cobalt hydrides have been proposed as active species in catalytic hydrogenation via either migratory insertion pathway or HAT pathway.^[4,36,38,58] However, isolation of active hydride intermediates remains challenging due to their labile nature. Since isolation of cobalt hydride complexes is accessible by using our pincer ligand platform, we intended to probe the catalytic ability of **9** in olefin hydrogenation, in which styrene was initially examined as a benchmark substrate (Table 3). Complete conversion of styrene to ethylbenzene was achieved over 15 h of photolysis (390 nm LED, 40 W) under standard conditions (10 mol% catalyst loading of **9**, 1 bar H₂ at r.t. in C₆D₆). In contrast, no conversion was observed without irradiation. Addition of excess Hg metal did not affect the reactivity (Table 3, Entry 2), suggesting a homogeneous molecular catalysis by **9**. Furthermore, the catalytic rate is positively correlated to H₂ pressure, enabling quantitative hydrogenation of styrene with 1 mol% **9** under 8 bar H₂ (Table 3, Entry 8). Styrene hydrogenation catalyzed by 5 mol% **9** gives a quantum yield of $\Phi_{390} = 2.29\%$, which is one order of magnitude more than that of H/D exchange.

Table 3: Photo-induced hydrogenation of styrene by **9**.



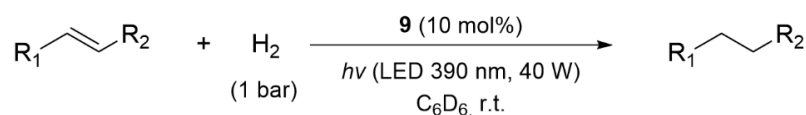
Entry	Cat.(mol%)	H ₂ Pressure (bar)	t [h]	Yield [%] ^[a]
1	10	1	15	100
2 ^[b]	10	1	15	100
3 ^[c]	10	1	15	0
4	5	1	15	68
5	5	4	15	100
6	5	8	15	100
7	1	4	15	62
8	1	8	15	100

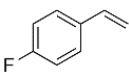
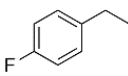
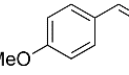
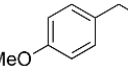
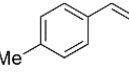
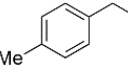
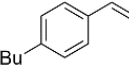
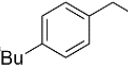
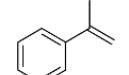
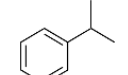
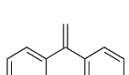
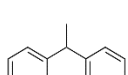
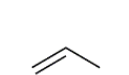

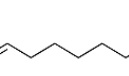
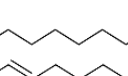
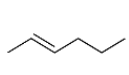
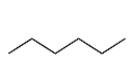
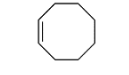

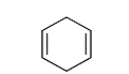
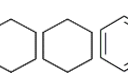
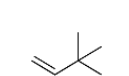
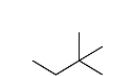
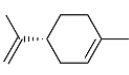
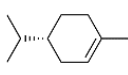
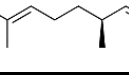
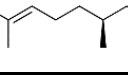
[a] Determined by ¹H NMR spectroscopy. [b] In the presence of Hg. [c] Without irradiation.

Hydrogenation of different substrates was further probed under standard catalytic conditions (10 mol% **9**, irradiated with 390 nm LED in C₆D₆ at room temperature), including terminal and internal alkenes (Table 4). Hydrogenation of *para*-substituted styrene proceeded quantitatively within 15 h (Entry 1-4), while branched α -methyl styrene or 1,1-diphenylethylene (Entry 5, 6) were reduced more slowly, which is likely attributed to the steric hindrance. The steric factor also applies to aliphatic alkenes. Propene was hydrogenated in nearly quantitative yield with

5 mol% catalyst loading and 2 bar H₂ (Entry 7). Hydrogenation of long chain alkenes was more favorable at terminal positions than at internal positions, meanwhile, significant isomerization was also observed (Entry 8, 9). Furthermore, olefin hydrogenation catalyzed by **9** is inert to tri-substituted substrates (Entry 12, 13).

Table 4: Photo-induced Hydrogenation of Styrenes and aliphatic Olefins by **1**.

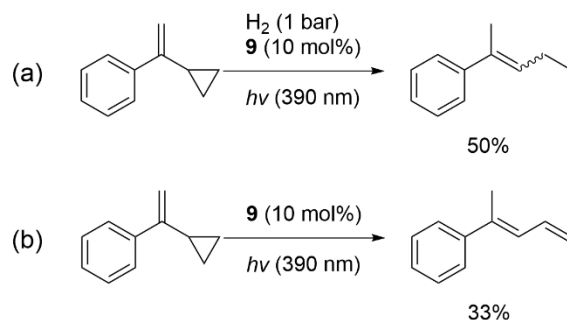


Entry	Substrate	Product	<i>t</i> [h]	Yield (conversion) [%]
1			15	100
2			15	100
3			15	100
4			15	100
5			15	39 (41)
6			40	51 (53)
7			15	92 (93)
8			15	75 (octane) 25 (2-octene)
9			40	32 (33)
10			15	37 (37)
11			40	62 (C ₆ H ₁₀), 15 (C ₆ H ₁₂) 12 (C ₆ H ₆) (90)
12			15	66 (67)
13			15	20 (22)
14			26	100

2.3.4 Mechanistic examinations

2.3.4.1 Mechanistic examinations with radical clock test substrates

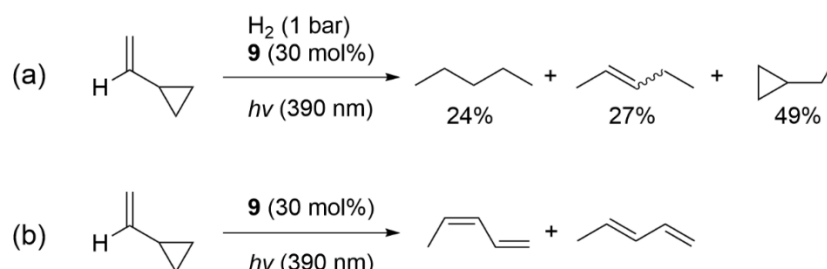
The performance of **9** in photo-catalytic olefin hydrogenation prompts us to investigate the mechanism of this reaction. To study the potential radical reactivity of **9**, experiments with α -cyclopropylstyrene, a radical clock test substrate, were carried out (Scheme 34). In the absence of light, no reaction was observed between **9** and α -cyclopropylstyrene at r.t., even under H₂ (1 bar) atmosphere. In contrast, under photochemical conditions (390 nm LED), α -cyclopropylstyrene converted exclusively to a ring-opened product 2-phenyl-2-pentene (Scheme 34, a) at a slower rate relative to hydrogenation of styrene. No ring-retention hydrogenated product was formed. The ring-opened product 2-phenyl-2-pentene was not further hydrogenated, as judged by the ¹H NMR spectrum. This observation indicates a radical mechanism, namely via formation of a tertiary alkyl radical upon initial HAT, followed by ring-opening of the resulting radical species with a rate constant of $k = 3.6 \cdot 10^5 \text{ s}^{-1}$ at 22 °C.^[153] The secondary HAT is, based on this observation, slower than intramolecular ring-opening. Furthermore, isomerization of radical clock substrate can be catalyzed by **9** to a ring-opened product 4-phenyl-1,3-pentadiene (Scheme 34, b), supporting a reversible HAT event.



Scheme 34: Radical Probe for the olefin hydrogenation by **9** with α -cyclopropylstyrene.

The proposed HAT mechanism was further probed with a monosubstituted radical clock substrate vinyl cyclopropane. As usual, no conversion was observed in the absence of light. The hydrogenation of vinyl cyclopropane (ring-opening rate constant of $7 \cdot 10^6 \text{ s}^{-1}$ in hexane at 22 °C)^[153] by **9** was conducted under the photo-catalytic conditions (390 nm LED) (Scheme 35a), which provided full conversion to a mixture including pentane, 2-pentene, ethylcyclopropane, as judged by ¹H NMR spectroscopy. The formation of ring-opened products supports a radical mechanism via HAT, whereas ca. 50% conversion of vinyl cyclopropane to ring-retention product ethylcyclopropane suggests a non-radical pathway without the formation of the carbon-centered radical intermediates. These results suggest that both radical and non-radical pathways may exist in the hydrogenation of vinyl cyclopropane, whereas the hydrogenation of bulkier α -cyclopropylstyrene gave only ring-opened product via HAT pathway. Steric factor plays a role in the hydrogenation by **9**, which is likely given the bulky *tert*-butyl

substituents on the pincer ligand. In the absence of H₂, photo-catalytic isomerization of vinyl cyclopropane to a mixture of Z/E isomers of 1,3-propadiene was observed (Scheme 35b), as with isomerization of α -cyclopropylstyrene to a ring-opened diene.

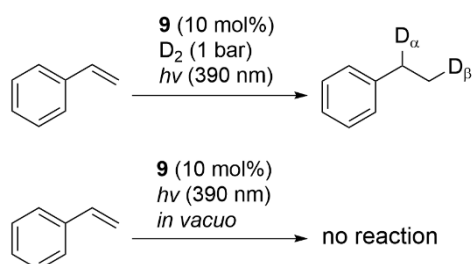


Scheme 35: Radical Probe for the olefin hydrogenation by **9** with vinyl cyclopropane.

2.3.4.2 Control experiments with D₂ and cobalt alkyl complex

The catalytic reduction of styrene with D₂ was performed under the standard reaction conditions (Scheme 36, top). The unequal incorporation of deuterium atoms in α - and β -positions of the product ethylbenzene was observed, with a ratio of 1 to 1.5, as determined by ¹H and ²H NMR spectroscopy (Figure 47). This result suggests that the first elementary step is reversible, namely a reversible hydrogen atom transfer to the substrate or a reversible migratory insertion of the substrate into the M–H bond. The β -deuteration arises more likely via HAT pathway, in which a stabilized α -carbon radical is formed, instead of a 2,1-insertion mechanism.

Furthermore, no reaction was observed between **9** and styrene in the absence of H₂, either thermally or photochemically (Scheme 36, bottom), suggesting that H₂ is an integral part of the olefin hydrogenation. The short lifetime of the excited state of **9**, measured by transient spectroscopy, also precludes direct bimolecular excited state reaction with styrene.



Scheme 36: (Top) Deuteration of styrene with D₂ (1 bar) catalyzed by **9** (α : β = 1:1.5). (Bottom) Reaction of **9** with styrene

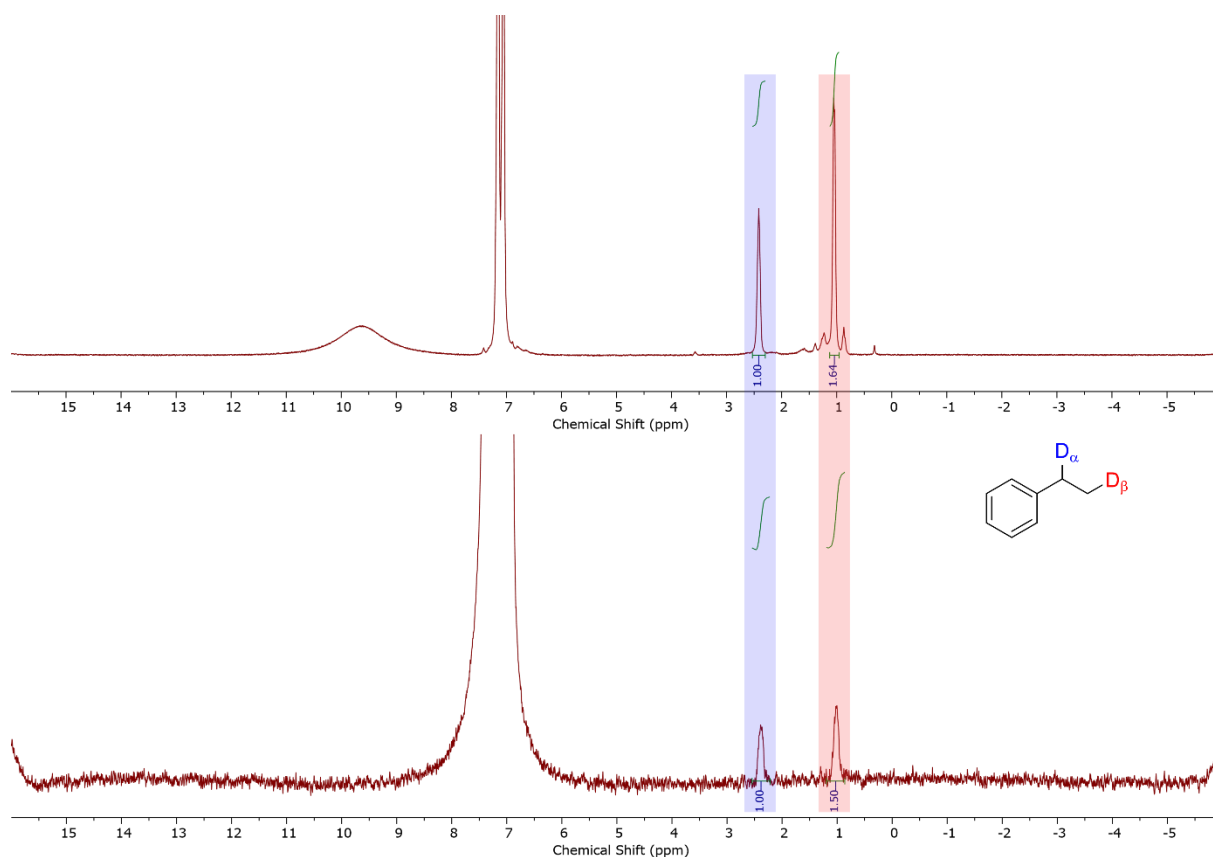


Figure 47: ^1H NMR (top) and ^2H NMR (bottom) spectra after the photo-initiated hydrogenation of styrene with D_2 (1 bar) in C_6D_6 .

Metal hydrocarbyl intermediates are commonly proposed as the key species in homogeneous olefin hydrogenation, being formed via migratory insertion of alkene into a metal hydride bond.^[4] To probe the possible insertion pathway mediated by the metal hydrides, a cobalt(II) alkyl complex was synthesized. $[\text{CoCH}_2\text{CH}_2\text{Ph}(\text{L}^1)]$ (**19**) can be prepared by salt metathesis from the cobalt chloride complex with phenethylmagnesium chloride. **19** is thermally stable and can be identified with a broadened resonance of the *tert*-butyl substituents at $\delta = 13.98$ ppm in C_6D_6 by ^1H NMR spectroscopy. **19** does not react with H_2 under thermal conditions. Instead, photolysis (390 nm LED) of solution of **19** under H_2 atmosphere (1 bar) resulted in formation of ethylbenzene and **9** in a yield of 82% in 20 min (Figure 48). The photolysis of **19** in the absence of H_2 for 20 min resulted in disproportionation of **19** to **9** and styrene (Figure 49).

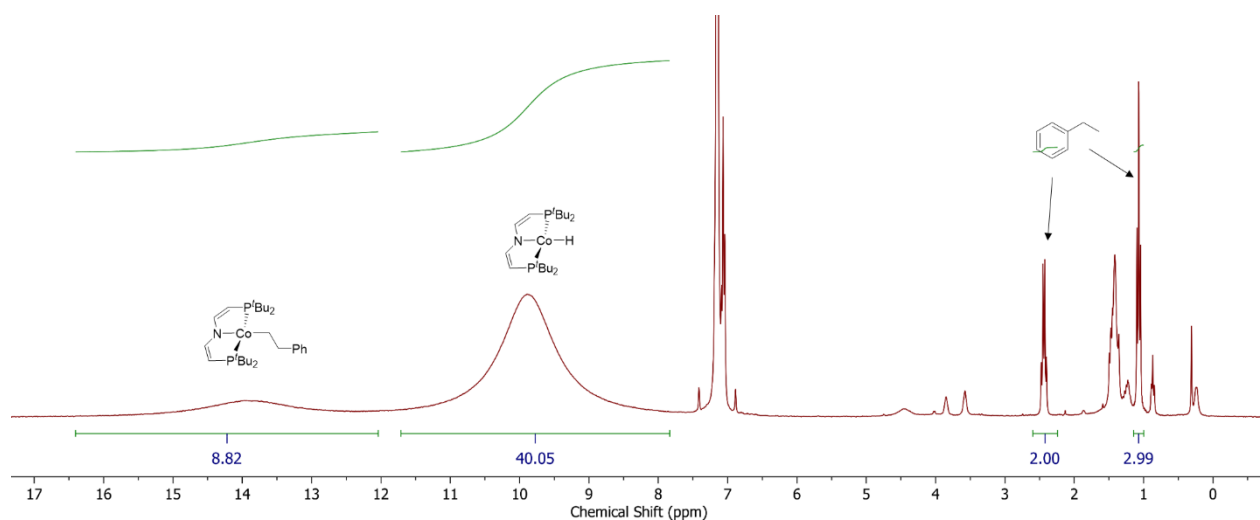


Figure 48: ^1H NMR spectrum after photolysis (390 nm LED) of **19** under H_2 (1 bar) for 20 min in C_6D_6 (resonances at 13.95 and 9.98 ppm belong to *tert*-butyl substituents).

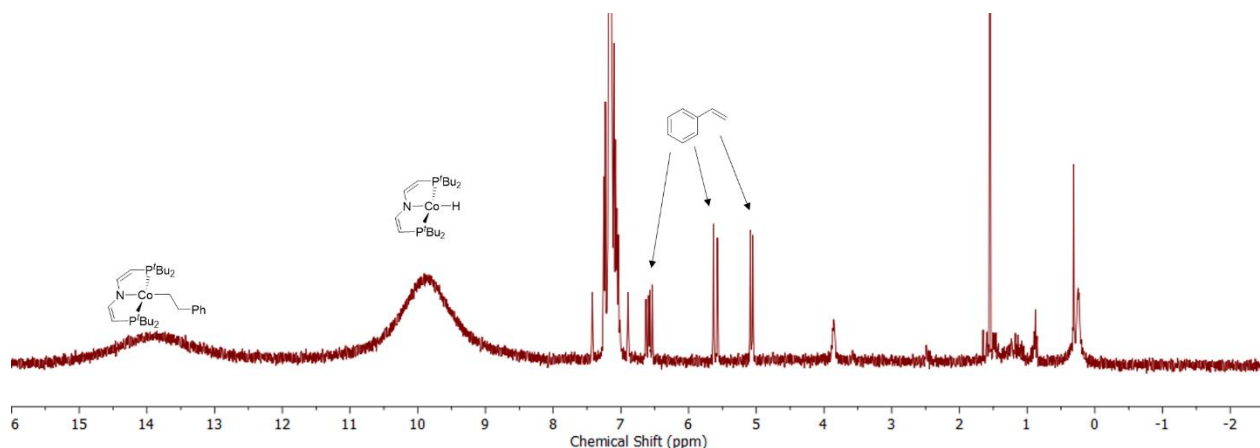
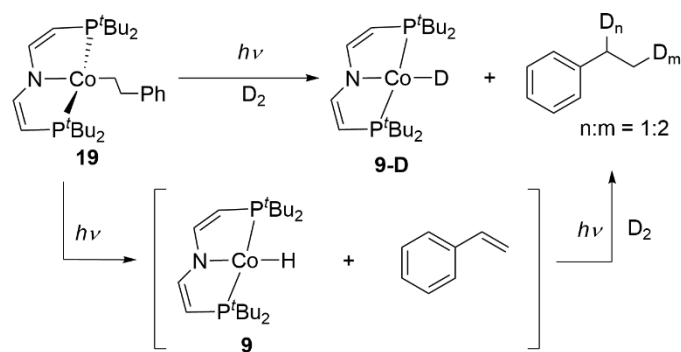


Figure 49: ^1H NMR spectrum after photolysis of **19** in C_6D_6 *in vacuo* for 20 min (resonances at 13.95 and 9.98 ppm belong to *tert*-butyl substituents).

In addition, **19** was probed with D_2 gas under the photochemical conditions, giving **9-D** and ethylbenzene with the deuterium incorporation in both α - and β -positions (Figure 50). Notably, isotopic distribution in ethylbenzene ($\alpha:\beta = 1:1.8$) resembles that of the catalytic styrene deuteration by **9** (Scheme 36), suggesting an initial photochemical disproportionation of **19** to styrene and **9** (Scheme 37). Styrene can be further reduced by **9** under H_2 atmosphere. This observation disfavors the hydrogenolysis of a cobalt alkyl intermediate as a relevant step for catalysis.



Scheme 37: Styrene deuteration with complex **19**.

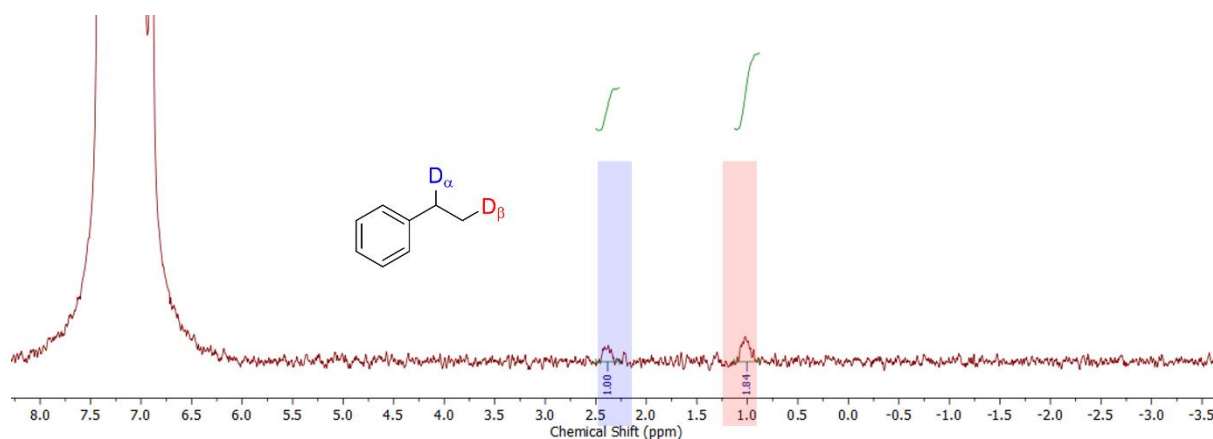


Figure 50: ^2H NMR spectrum after photolysis of **19** under D_2 (1 bar) in C_6D_6 for 90 min.

2.3.4.3 Mechanistic study in olefin hydrogenation by **12**

Based on the control experiments, HAT from **9** to an alkene or migratory insertion of an alkene into Co–H bond of **9** as the first elementary step is ruled out. Furthermore, higher quantum yield in styrene hydrogenation than quantum yield in H/D exchange is indicative of a thermal olefin hydrogenation, catalyzed by an *in situ* formed photoproduct. As mentioned above, the three-coordinate cobalt(I) complex **12** is an active catalyst in the olefin hydrogenation, while **12** is also the photo-product of **9**. The observations indicate a photo-induced olefin hydrogenation, in which **9** and **12** are both involved in the same catalytic cycle. This speculation prompts us to investigate the follow-up behavior after a short-term irradiation of the reaction mixture. Initially, a reaction mixture with **9** (10 mol%), styrene and H_2 (1 bar) in C_6D_6 was photolyzed for 1 h. Subsequently, the sample was monitored by ^1H NMR spectroscopy, which shows that styrene was further hydrogenated without irradiation, namely a thermal hydrogenation occurred without photolysis. Compared to photochemical styrene hydrogenation, the photo-initiated thermal hydrogenation proceeded at a lower reaction rate (Figure 51, black plots).

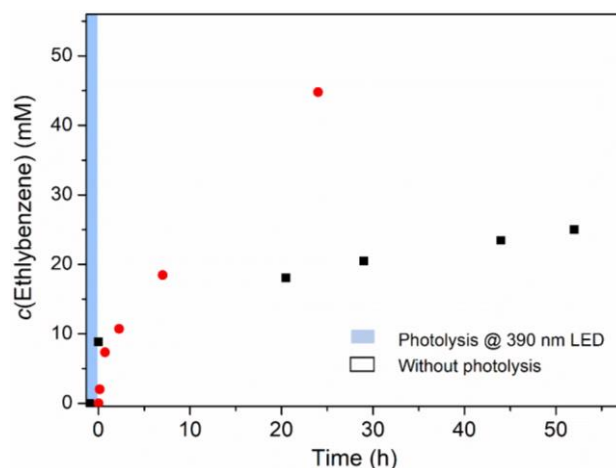
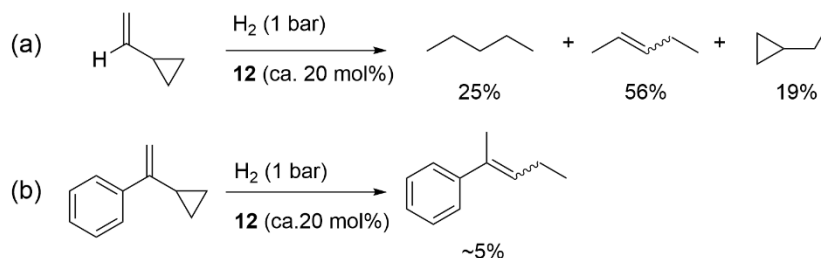


Figure 51: Time dependent ethylbenzene formation by catalytic hydrogenation of styrene (0.048 mmol, 1 bar H₂) using either **9** (black) with 1 h photolysis (blue shaded area) and subsequent reaction without irradiation, or isolated **12** (3.8 mol%, red circles) as thermal catalysts.

To get more insight into the competition between the thermal hydrogenation and the active catalyst deactivation pathway, the initial turn-over frequencies (TOF) at different catalyst loadings (under the standard reaction conditions: 1 bar H₂, 390 nm LED at room temperature with 5 or 1 mol% of **9**) were examined. Turn-over with 5 mol% of catalyst loading for 3 h irradiation (TOF = 0.7 h⁻¹) is significantly lower than that with 1 mol% of catalyst loading (TOF = 3.4 h⁻¹), which is indicative of a higher reaction order of cobalt species in the active catalyst deactivation process than the competing thermal olefin hydrogenation.

12 was further examined in the hydrogenation of the radical clock test substrates under H₂ atmosphere (1 bar). The hydrogenation of vinyl cyclopropane by **12** at room temperature gave a full conversion to the same products (Scheme 38) as being catalyzed by **9** under the photolytic conditions. However, the hydrogenation of α -cyclopropylstyrene by **12** obtained only the ring-opened product in a yield of 5% after stirring for 5 days, which suggests that the reaction rate is dependent on the steric nature of the substrate in the olefin hydrogenation by **12**.



Scheme 38: Radical Probe for the olefin hydrogenation by **12** with vinyl cyclopropane.

2.3.4.4 Mechanistic investigation with *para*-H₂

To get more mechanistic insights into the cobalt-catalyzed olefin hydrogenation, experiments with *p*-H₂ were performed.¹¹ The three-coordinate complex **12** was employed in all PHIP experiments as precatalyst, since the irradiation of the complex **9**-catalyzed reaction is inaccessible within NMR spectrometer. **12** was first probed with *p*-H₂ in the absence of substrate. ¹H NMR spectra were recorded after bubbling *p*-H₂ at 7 bar directly into the solution of **12** in C₆D₆. The ¹H NMR spectra are identical to the spectra upon addition of the conventional H₂, forming the cobalt dihydrogen/dihydride complex **17**. No hyperpolarized signal was observed. **17** is computationally proposed as a non-classical dihydrogen complex, which should give no hyperpolarized signal upon addition of *p*-H₂. A similar result was also observed in the exposure of a low-spin cobalt(I) complex ligated with CCC-pincer ligand (CCC = bis(mesitylbenzimidazol-2-ylidene)phenyl), reported by Fout and co-workers, which showed no hyperpolarization of any signals in the ¹H NMR spectrum.^[74] Fout suggested the formation of a non-classical Co(I) dihydrogen complex without cleavage of H–H bond.^[74] However, the presence of the paramagnetic compounds, such as **9** and **12** in the reaction mixture, might accelerate the relaxation time of *p*-H₂, disabling the observation of the signal hyperpolarization within the NMR timescale.

Styrene hydrogenation by **12** was then investigated with *p*-H₂ (1 bar), using C₆D₆ as the solvent. The ¹H NMR spectrum (Figure 52), recorded ca. five second after addition of *p*-H₂, displays two signals with an enhanced intensity only in the aliphatic region, which belong to the hydrogenated product of styrene (ethylbenzene). The resonance at 1.08 ppm is antiphase, whereas the resonance at 2.48 ppm is in-phase. Both hyperpolarized signals of ethylbenzene decayed within 10 s, relaxing back to its normal, thermally populated magnetic state. Observation of hyperpolarized signals suggests that the hydrogenation of styrene by **12** is more likely to undergo a non-radical pathway, since a radical intermediate can destroy PHIP effect.^[26]

¹¹ The addition of *para*-H₂ and the NMR measurements were performed by Dr. Philip Saul, assisted by Dr. Stefan Glögler.

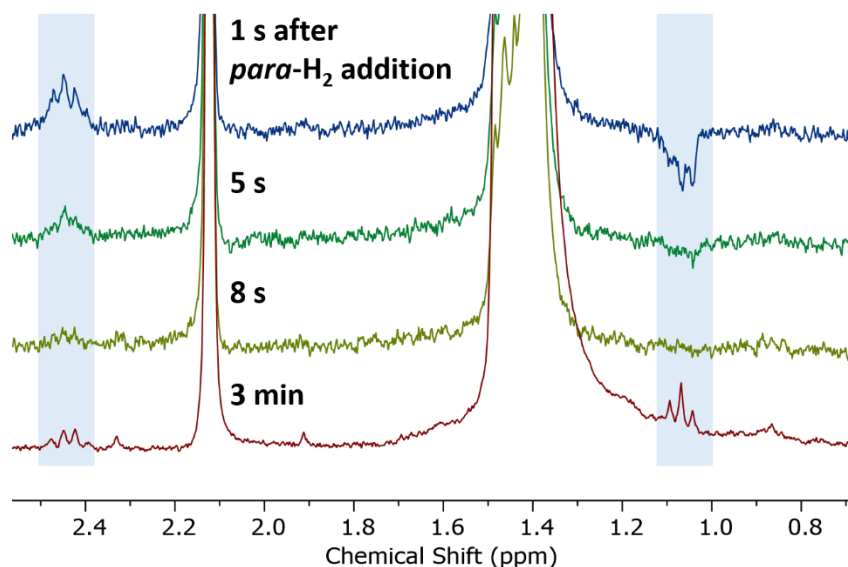


Figure 52: ^1H NMR spectra of styrene hydrogenation by **12** using $p\text{-H}_2$.

Notably, no hyperpolarization of styrene was observed in the presence of $p\text{-H}_2$. In contrast, the styrene hydrogenation with $p\text{-H}_2$ catalyzed by Fout's Co(I) complex resulted in the nuclear spin hyperpolarization transferred from $p\text{-H}_2$ to styrene without chemical transformation of the substrate, which displayed the signal enhancements in the ^1H , $^{13}\text{C}\{^1\text{H}\}$ spectra at the region of the C=C bond and the aromatic ring.^[27,74] This observation suggests a reversible exchange process in the hydrogenation reaction.^[74]

In contrast to the styrene hydrogenation, the hydrogenation of the radical clock test substrate α -cyclopropylstyrene under $p\text{-H}_2$ (7 bar) showed, however, no hyperpolarization effect. These observations are indicative of a change in mechanism between hydrogenation of styrene and a bulkier substrate, like α -cyclopropylstyrene, which might undergo an insertion pathway and a HAT pathway, respectively.

2.3.4.5 Free-energy relationship

The free-energy relationship analysis was conducted by competition experiments with a range of $para$ -substituted styrene under standard catalytic conditions (Figure 53, top left). Hammett plot shows a correlation of $\log(k_X/k_H)$ with substituent parameter σ_p ($R^2 = 0.92$), in which an increase in the relative rates is observed with an increase in the electron-withdrawing nature of the $para$ -substituents, giving $\rho = 0.85$. This ρ -value indicates a moderate degree of charge transfer in the rate-determining step, suggesting an insertion pathway or a radical pathway via HAT. In comparison, Jones reported an iron pincer catalyst for olefin hydrogenation.^[51] DFT calculation in Hammett analysis shows a good correlation in hydrogenation of styrene with different $para$ -substituents, which gives a ρ -value of 3.13 (calculated in benzene), indicating a buildup of negative charge on the alkyl unit in the transition state. This calculation is consistent with a consecutive hydride transfer and proton transfer mechanism.^[51]

The free-energy relationship was further probed with *BDFEs* of the C–H bond of the radicals¹². However, reaction rates do not correlate well with the bond strength of the C–H bond of the radicals (Figure 53, top left), which would arise from the first HAT. We also applied Jiang’s approach for linear free energy relationships of radical reactions that fits the data to two parameters (σ_{jj} and σ_p)^[29], which account for spin delocalization and polarity effects, respectively. The ratio of the reaction parameters (ρ_p/ρ_{jj}) provides a measure for the relative contributions. In the current case, $\rho_p/\rho_{jj} = 4.14$ suggests a dominant rate dependence on philicity but negligible contributions from radical stabilization.

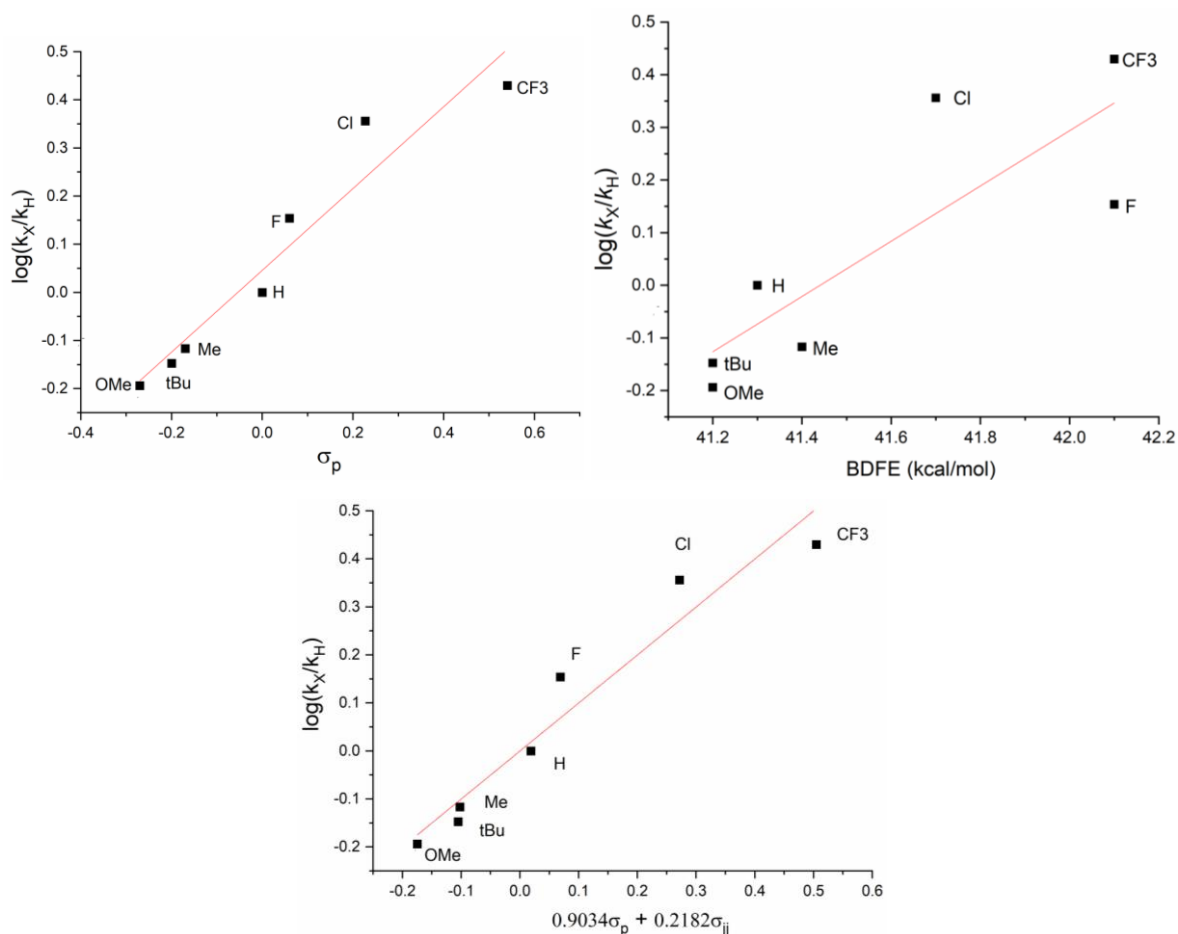
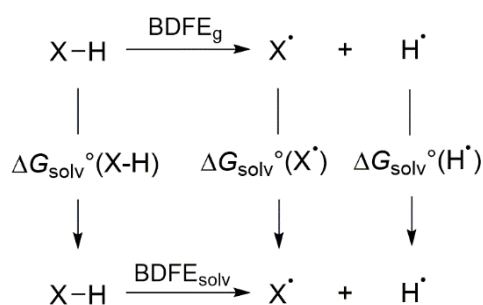


Figure 53: Hammett plot from catalytic hydrogenation of *para*-substituted styrene derivatives by **9** (10 mol%) under 1 bar H₂ atmosphere using different substitution constants.

¹² *BDFEs* of C–H bond in *para*-substituted ethylbenzene radicals were calculated by Dr. Markus Finger.

2.3.4.6 Proposed mechanism for olefin hydrogenation via HAT



Scheme 39: Relationship between gas-phase and solution bond dissociation free energies.^[154]

To compare bond strength between C–H and Co–H bonds and understand the driving force of HAT event in olefin hydrogenation, BDFEs of C–H bond in α -methylbenzyl radical and ethylbenzene are calculated. BDFE of hydrocarbon C–H bonds in solution (BDFE_s) can be calculated via a thermochemical cycle (Scheme 39) from gas-phase value (BDFE_g) and free energies of solvation (ΔG_s°) of hydrocarbon (XH), hydrocarbyl radical (X^\cdot) and hydrogen atom (H^\cdot):

$$\text{BDFE}_s(\text{XH}) = \text{BDFE}_g(\text{XH}) + \Delta G_s^\circ(\text{H}^\cdot) + \Delta G_s^\circ(\text{X}^\cdot) - \Delta G_s^\circ(\text{XH})$$

BDFE_g is related to the bond dissociation energy in the gas phase (BDE_g) by:

$$\text{BDFE}_g(\text{XH}) = \text{BDE}_g(\text{XH}) - T S^\circ(\text{H}^\cdot) - T \{ S^\circ(\text{X}^\cdot) - S^\circ(\text{XH}) \}$$

For small, organic molecules the entropy of the hydrocarbon (XH) and hydrocarbyl radical (X^\cdot) are approximately equal ($S^\circ(\text{X}^\cdot) \approx S^\circ(\text{XH})$), giving ($S^\circ_g(\text{H}^\cdot) = 27.42 \text{ cal}\cdot\text{K}^{-1}\cdot\text{mol}^{-1}$) at $T = 298.15 \text{ K}$:^[154]

$$\text{BDFE}_g(\text{XH}) = \text{BDE}_g(\text{XH}) - 8.17 \text{ kcal}\cdot\text{mol}^{-1}$$

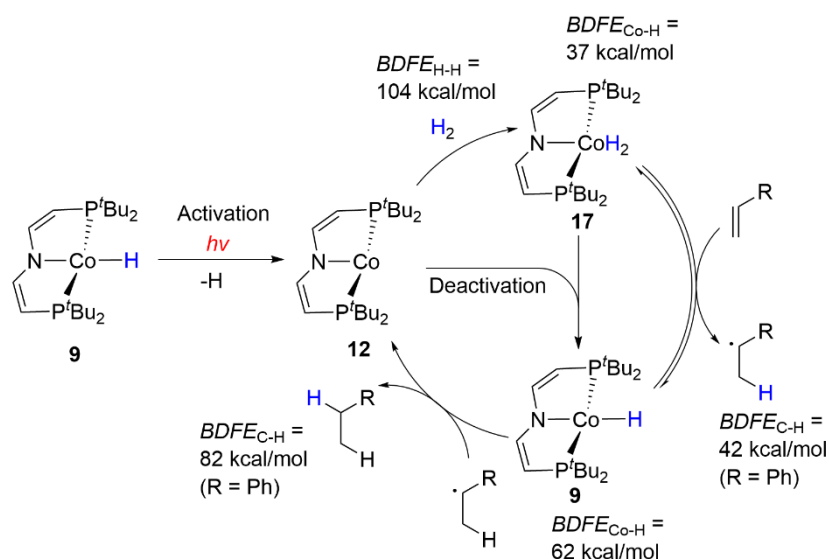
Furthermore, free energies of solvation of the hydrocarbon (XH) and hydrocarbyl radical (X^\cdot) are approximately equal ($\Delta G_s^\circ(\text{X}^\cdot) \approx \Delta G_s^\circ(\text{XH})$) and the free energy of solvation of H^\cdot can be approximated with that of H_2 ($\Delta G_s^\circ(\text{H}^\cdot) \approx \Delta G_s^\circ(\text{H}_2) = \Delta H_s^\circ(\text{H}_2) - T \Delta S_s^\circ(\text{H}_2) = 4.78 \text{ kcal}\cdot\text{mol}^{-1}$)^[155], giving the approximate relation of solution BDFE_s and gas phase BDE_g for hydrocarbon C–H bonds:

$$\text{BDFE}_s(\text{XH}) = \text{BDE}_g(\text{XH}) - 8.17 \text{ kcal}\cdot\text{mol}^{-1} + 4.78 \text{ kcal}\cdot\text{mol}^{-1} = \text{BDE}_g(\text{XH}) - 3.4 \text{ kcal}\cdot\text{mol}^{-1}$$

Gas phase BDE_g for C–H bond in α -methylbenzyl radical ($\text{BDE}_g = 44.9 \text{ kcal/mol}$)^[156] and ethylbenzene ($\text{BDE}_g = 85.4 \text{ kcal/mol}$)^[157] can be obtained from literature. The calculated $\text{BDFE}_{\text{C-H}}$ of both hydrocarbon species are 42 kcal/mol and 82 kcal/mol in toluene, respectively.

A mechanistic picture of the photo-induced olefin hydrogenation by **9** via a HAT pathway can be proposed based on all quantitative and qualitative results (Scheme 40). **9** as a pre-catalyst can be activated upon photolysis, which results in the formation of **12** via Co–H bond homolysis. H₂ binds reversibly to **12** to form the dihydrogen complex **17**, which is an active catalyst for the thermal HAT olefin hydrogenation. The bond strength of **17** ($BDFE_{\text{CoH}_2} = 37$ kcal/mol) is slightly lower than the bond strength of the C–H bond of α -methylbenzyl radical, which favors a reversible initial HAT from **17** to styrene, but also to aliphatic, unactivated olefins. HAT from **17** to styrene gives **9** and α -methylbenzyl radical. **9** cannot directly transfer one hydrogen atom to styrene, since the Co–H bond strength of **9** ($BDFE_{\text{CoH}} = 62$ kcal/mol) is greater than that of α -methylbenzyl radical. In contrast, HAT from **9** to the α -methylbenzyl radical is sufficient to produce a stronger C–H bond (ethylbenzene: $BDFE_{\text{C-H}} = 82$ kcal/mol). Formation of **12** after stepwise HAT from **17** to styrene closes the proposed catalytic cycle.

Apart from HAT of **17** to olefins, comproportionation of **17** and **12** results in the deactivation of catalytic cycle. The lower Co–H bond strength of **17** ($BDFE_{\text{CoH}_2} = 37$ kcal/mol) enables a thermal HAT event with **12** to form the inactive monohydride complex **9** ($BDFE_{\text{CoH}} = 62$ kcal/mol). Therefore, continuous photolysis maintains a steady state concentration of **17** that enables the thermal catalysis. The deactivation pathway is inversely dependent on the H₂ pressure (Figure 38), leading to a higher steady state concentration of active species **17** at increased H₂ pressure, thus resulting in higher catalytic rates.

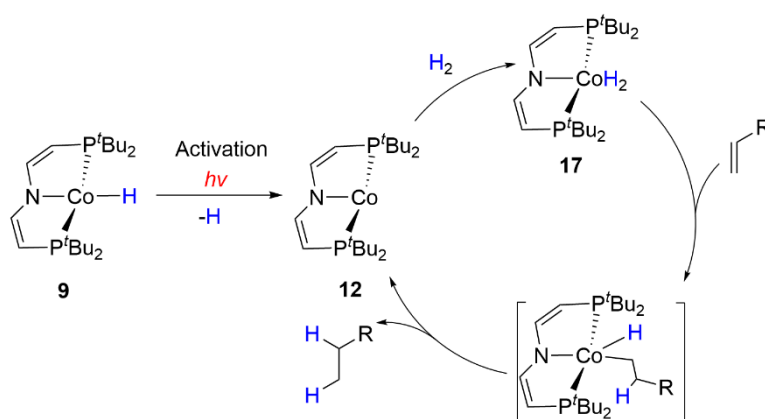


Scheme 40: Proposed mechanism for photo-initiated HAT olefin hydrogenation of **9**.

2.3.4.7 Proposed mechanism for olefin hydrogenation via insertion pathway

Olefin hydrogenation is proposed to undergo alternatively a non-radical insertion pathway, which is favored in the hydrogenation of less-hindered substrates. The reaction mechanism is supported by the hyperpolarization in styrene hydrogenation with p -H₂ and by the ring-retention

products from the hydrogenation of vinylcyclopropane. The mechanism exchange can be further evidenced by hydrogenation of different substituted alkenes (Table 4). With 10 mol% catalyst loading of **9**, monosubstituted alkenes were reduced in a yield above 90%, whereas disubstituted alkenes, including 1,2- or 1,1-substituted alkenes, were reduced in a yield below 50%. Alkene insertion into M–H bond of monohydride complex **9** is ruled out based on the control experiments with **19**. These observations are indicative of a migratory insertion of an alkene into the M–H bond of complex **17** to form a cobalt(III) alkyl hydride intermediate, followed by the reductive elimination to release hydrogenated product and regenerate the active catalyst **12**. **12** activates H₂ to initiate next catalytic turn-over (Scheme 41).



Scheme 41: Proposed mechanism for photo-initiated olefin hydrogenation via insertion pathway.

3 Conclusion

Hanson's cationic cobalt(II) alkyl complex **H4** is an active precatalyst for hydrogenation of multiple bonds.^[64] Mechanistic investigation suggests an insertion pathway involving a proposed Co(II) hydride intermediate, which was not observed via spectroscopic approaches.^[64] The main goal of this thesis was to synthesize the analogues of Hanson's precatalyst with *tert*-butyl substituted pincer ligands, and to investigate their reactivity in olefin hydrogenation.

The neutral cobalt(II) alkyl complex $[\text{CoCH}_2\text{SiMe}_3(\text{L}^1)]$ **1** and its protonated product $[\text{CoCH}_2\text{SiMe}_3(\text{L}^1\text{H})]\text{BAR}^{\text{F}_4}$ **3** were synthesized and probed with H_2 , resulting in the immediate formation of corresponding cobalt(II) hydride complexes $[\text{CoH}(\text{L}^1)]$ **6** and $[\text{CoH}(\text{L}^1\text{H})]\text{BAR}^{\text{F}_4}$ **7**. This observation resembles the proposed mechanism of activation of precatalyst **H4**, which reacts with H_2 to form the active hydride intermediate.^[64] In contrast to Hanson's system, the obtained hydride complexes with *tert*-butyl substituents are stable at room temperature, which might arise from the steric bulk of *tert*-butyl substituents. Arnold and coworkers reported dimerization of a cobalt(II) chloride complex upon reduction by KC_8 , which carries a P^iPr_2 substituted analogue of our pincer ligand.^[142] Bulky substituents around the metal center might stabilize the monomeric hydride complexes and prevent dimerization. These observations prompted us to further investigate the cobalt hydride complexes and their potentials in olefin hydrogenation.

Neutral cobalt(II) hydrides **6** and $[\text{CoH}(\text{L}^2)]$ **8** were obtained by salt metathesis with LiHBEt_3 . Electronic structure analysis of **6** confirms a singlet low-spin electronic configuration. Protonation of **8** with $[\text{H}(\text{Et}_2\text{O})_2][\text{BAR}^{\text{F}_4}]$ at room temperature results in the selective formation of a backbone C-protonated hydride complex $[\text{CoH}(\text{L}^2\text{H})][\text{BAR}^{\text{F}_4}]$ **13**^{BARF}. Structural characterization is indicative of a cationic imine hydride.

Protonation of **6** with $[\text{H}(\text{Et}_2\text{O})_2][\text{BAR}^{\text{F}_4}]$ at room temperature results in the formation of a backbone N-protonated amine hydride $[\text{CoH}(\text{L}^1\text{H})][\text{BAR}^{\text{F}_4}]$ **7**^{BARF}, accompanied by the formation of a cationic three-coordinate cobalt(I) complex $[\text{Co}(\text{L}^1\text{H})][\text{BAR}^{\text{F}_4}]$ **5**^{BARF} (< 5%). Spectroscopic analysis of **7**^{BARF} reveals a singlet low-spin electronic configuration, while the ¹N NMR spectrum with paramagnetic-shifted resonances of **5**^{BARF} indicates a high-spin electronic configuration. The formation of **5**^{BARF} can be resulted from hydride ligand protonation of **6**, which is followed by H_2 dissociation to form a cationic three-coordinate Co(II) intermediate. Comproportionation of the three-coordinate Co(II) intermediate with **7**^{BARF} gives **5**^{BARF}. In contrast, protonation of **6** with $[\text{H}(\text{Et}_2\text{O})_2][\text{BAR}^{\text{F}_4}]$ at -80 °C results in the selective formation of **7**^{BARF} without formation of **5**^{BARF}, likely arising from unfavored hydride protonation at low temperature. Furthermore, protonation of **6** with $[\text{H}(\text{Et}_2\text{O})][\text{BF}_4]$ at room temperature results in the selective formation of **7**^{BF4}, which shows a N–H...F hydrogen bonding (1.98-2.07 Å) between cationic cobalt species and its counterion BF_4^- .

[CoH(L³)] **9** can be prepared by salt metathesis of the parent Co(II) chloride with LiAlH₄ (0.5 eq.). **9** possesses a distorted square-planar geometry and C_{2v} symmetry, supported by the crystallographic and ¹H NMR spectroscopic analysis. The Co–H stretching vibration of **9** ($\nu = 1756 \text{ cm}^{-1}$) is red-shifted compared with other neutral cobalt(II) pincer hydrides, reflecting a large *trans*-effect of divinylamide ligand. Electronic structure analysis of **9** suggests a metal-centered radical character. Notably, the ¹H NMR spectrum of the deuteride isotopologue **9-D** shows isotope shifts of up to 1 ppm for protons in the pincer backbone. This observation can be explained by ligand-field perturbation upon the Co–H/D exchange, supported by a slightly shifted *g*-anisotropy in the EPR characterization. The computational analysis revealed a Co–H bond strength ($BDFE_{\text{CoH}}$) of 62 kcal/mol. Stationary photolysis of **9** in deuterated solutions results in H/D exchange to **9-D**, accompanied by the formation (< 5%) of three-coordinate Co(I) complex [Co(L³)] **12** as a direct photoproduct, which is further evidenced by the transient absorption analysis. ¹H NMR and DFT computations suggest a triplet ground state of **12**. **12** binds N₂ to form a diamagnetic cobalt(I) dinitrogen complex [CoN₂(L³)] **11**. **12** can be obtained alternatively via N₂ dissociation by sublimation of **11** at 110 °C in dynamic vacuum. Photolysis of **11** under H₂ atmosphere gives **9**, whereas **11** does not react with H₂ under the thermal conditions.

5^{BArF} converts to a mixture of [Co(H₂)(L¹H)][BAr^F₄] **14** and [Co(H₂)₂(L¹H)][BAr^F₄] **15** upon exposure to H₂ atmosphere (1 bar). An equilibrium constant of 0.089 mM⁻¹ can be calculated for the reaction of **5^{BArF}** with H₂ (1 bar) at room temperature. Under higher H₂ pressure (5 bar), only **15** is formed. **14** and **15** were characterized by ¹H NMR spectroscopy at low temperature (up to 100 °C) to avoid line broadening due to rapid interaction with H₂ molecules. Both dihydrogen complexes are only stable under H₂ atmosphere. Removal of H₂ results in the formation of **5^{BArF}**. Moreover, exposure of the neutral cobalt(I) dinitrogen complex [CoN₂(L¹)] **10** to H₂ atmosphere results in the formation of [Co(H₂)(L¹)] **16**, identified by ¹H NMR spectroscopy. In contrast to **14** and **15**, no H₂ dissociation occurs upon removal of the H₂ atmosphere, which suggests that H₂-binding in **16** is stronger than that in **14** and **15**. Under H₂ atmosphere (5 bar), **16** slowly converts to **6** at room temperature (41% conversion in 21 h), while the conversion of **16** to **6** is slower *in vacuo*.

Exposure of **12** to H₂ atmosphere immediately gives a cobalt dihydrogen complex [Co(H₂)(L³)] **17**, which converts to **9** under H₂ (1 bar) atmosphere in several hours at room temperature. DFT calculations suggest a Co(I) dihydrogen complex, instead of a Co(III) dihydride, whereas experimental identification was unsuccessful. Computational analysis of **17** further reveals a Co–H bond strength ($BDFE_{\text{CoH}}$) of 37 kcal/mol. The reaction rate of conversion of **17** to **9** follows second order dependence in [**17**] and inverse dependence on H₂ pressure. This kinetic study is

consistent with a rapid equilibrium of **12** and H₂ with **17**, which is followed by comproportionation of **17** and **12** into **9** via formal HAT.

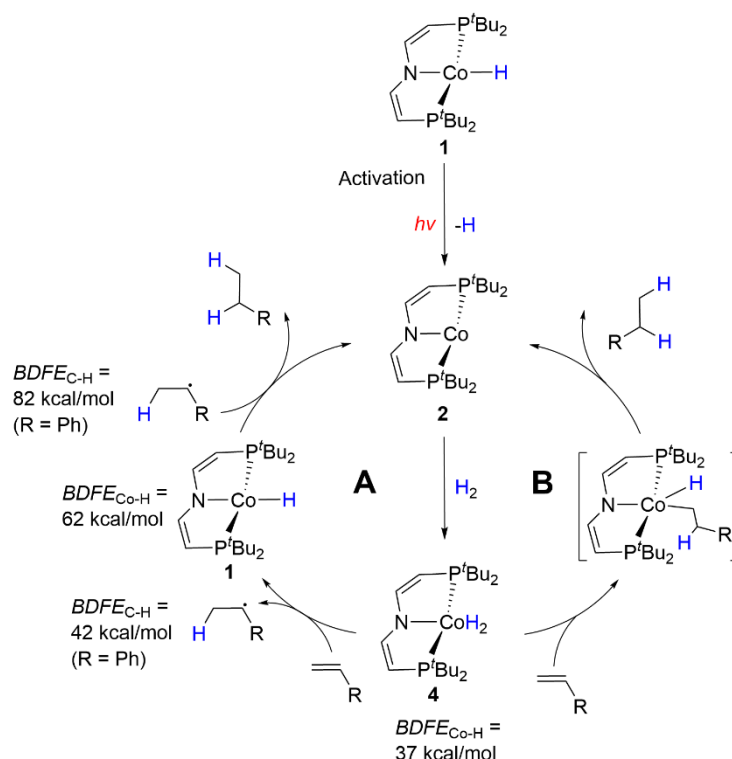
Complexes **5**^{BAr^F}, **6**, **7**^{BAr^F}, **9**, **11**, **12**, **13**^{BAr^F} were further probed in styrene hydrogenation under H₂ atmosphere. However, all complexes are less active than Hanson's precatalyst. In contrast to Hanson's system^[64] using cyclohexyl substituents, the steric bulk of *tert*-butyl substituents in our system might limit the reaction rate in hydrogenation. Among all these complexes, **12** shows the best activity in olefin hydrogenation. **12** reacts with H₂ (1 bar) to the dihydrogen complex **17** at room temperature, whereas the reaction of **5**^{BAr^F} with H₂ exhibits a low equilibrium constant ($K = 0.089 \text{ mM}^{-1}$), resulting likely in a slower catalytic rate in hydrogenation by **5**^{BAr^F} due to low concentration of the active dihydrogen resting state. However, **12** slowly converts to **9** under H₂ atmosphere, which competes with the thermal hydrogenation. To overcome the deactivation pathway, the photochemical method was applied in olefin hydrogenation by **9**.

Photo-induced olefin hydrogenation by **9** proceeds in C₆D₆ under mild conditions (with 10 mol% catalyst loading and 1 bar H₂ at r.t.) with stationary photolysis using a 390 nm LED as light source. No hydrogenation was observed in the absence of light. Aromatic and monosubstituted olefins can be hydrogenated to completion within 15 h under standard catalytic conditions, which are more favored than unactivated olefins. Hydrogenation of disubstituted olefins proceeds with slower reaction rate. No hydrogenation of a trisubstituted C=C bond was achieved. Furthermore, significant isomerization of chain α -olefins was observed.

Stoichiometric and catalytic control experiments reveal that **12** is the active catalyst species, which is formed by photochemical Co–H bond homolysis of **9**. Olefin hydrogenation by **12** proceeds under thermal conditions at a slower reaction rate than by **9** under photochemical conditions, owing to the deactivation process of **12** to the thermally inactive catalyst **9**. Kinetic studies support that active catalyst deactivation has a higher reaction order in [Co] than olefin hydrogenation. Therefore, irradiation is required in hydrogenation to regenerate the active species.

The reaction mechanism was examined with two radical clock test substrates. Hydrogenation of α -cyclopropylstyrene with **9** (photochemically) or **12** (thermally) gave only ring-opened products, whereas hydrogenation of vinyl cyclopropane with **9** (photochemically) or **12** (thermally) gave a mixture of ring-opened and ring-retention products. These results are indicative of co-existence of two reaction pathways, namely a radical mechanism via HAT and a non-radical mechanism via migratory insertion of olefins. For steric hindered olefins, such as α -cyclopropylstyrene, the insertion pathway is unfavored due to the bulkiness of ligand substituents around the metal center, which is further supported by hydrogenation using *para*-H₂.

A mechanistic picture of photo-induced olefin hydrogenation by **9** via HAT (Scheme 42, **A**) and the insertion (Scheme 42, **B**) pathway can be proposed based on all quantitative and qualitative results. **9** as pre-catalyst can be activated upon photolysis, which results in the formation of **12** via Co–H bond homolysis. H₂ binds reversibly to **12** to form the dihydrogen complex **17**, which transfer hydrogen atom to olefins (Scheme 42, **A**). The Bond strength of **17** ($BDFE_{CoH_2} = 37$ kcal/mol) is slightly lower than the bond strength of the C–H bond of α -methylbenzyl radicals, which favors a reversible initial HAT from **17** to styrene. Low Co–H bond strength also favors HAT to aliphatic, unactivated olefins. HAT from **17** to styrene gives **9** and the α -methylbenzyl radical. **9** cannot directly transfer one hydrogen atom to styrene, since the Co–H bond strength of **9** ($BDFE_{CoH} = 62$ kcal/mol) is greater than that of α -methylbenzyl radical. In contrast, HAT from **9** to α -methylbenzyl radical is sufficient to produce a stronger C–H bond (ethylbenzene: $BDFE_{C-H} = 82$ kcal/mol). Hydrogenation of sterically non-hindered olefins alternatively undergoes the non-radical insertion pathway (Scheme 42, **B**). A migratory insertion of an alkene into the Co–H bond of **17** to form a cobalt(III) alkyl hydride intermediate, which is followed by reductive elimination to release the hydrogenated product and regenerate the active catalyst **12**.



Scheme 42: Proposed mechanism for photo-induced olefin hydrogenation by **9**.

4 Experimental Section

4.1 General working techniques

All experiments were performed under an argon atmosphere (*Linde*) using standard Schlenk and glove box (MBraun) techniques. The atmosphere in glove-box was circulated through columns filled with activated carbon, copper catalyst and molecular sieves (4 Å) to remove traces of oxygen, moisture and solvents. All glassware was cleaned in KOH/*iso*-propanol baths, HCl baths, washed with demineralized water and dried in an oven at 110 °C. Experiments at low temperature (<-80 °C) were performed in Dewar vessels cooled with liquid nitrogen or dry ice with *iso*-propanol or acetone as refrigerant. Filtration was performed using pre-heated Whatmann Glasfiberfilter (GF/B, 25 mm) attached with PTFE tube or within a pipette. Experiments with irradiation were performed using a Kessil PR160-390 40 W monochromatic ($\lambda = 390$ nm) LED light source.

4.2 Chemicals and purification methods

All solvents were purchased in HPLC quality (Sigma Aldrich) and dried using a Solvent Purification System (MBraun). All deuterated solvents were purchased from *Eurio-Top* GMBH and dried over NaK for ca. One week, over-condensed and degassed prior to use. Solvents were purchased in HPLC quality (Sigma Aldrich) and dried using an MBraun Solvent Purification System. THF was additionally dried over Na/K. Deuterated solvents were obtained from Deutero GmbH and dried over Na/K (benzene- d_6 , THF- d_8 , Tol- d_8). 1-Cyclopropylvinyl)benzene was synthesized according to a reported procedure.^[1] All other chemicals were used as received: Styrene (TCI), 4-Fluorostyrene (TCI), 4-Chlorostyrene (TCI), 4-Methylstyrene (Sigma Aldrich), 4-Methoxystyrene (Sigma Aldrich), 4-*tert*-Butylstyrene (TCI), 1,4-Cyclohexadiene (Sigma Aldrich), cyclooctene (Sigma Aldrich), *trans*-2-hexene (Thermo Fischer), 1-octene (Sigma Aldrich), (*R*)-(+)-limonene (Sigma Aldrich), (+)- β -citronellene (Sigma Aldrich), 1,1-diphenylethylene (Sigma Aldrich), α -methylstyrene (Sigma Aldrich), LiALH₄ (Sigma Aldrich), LiHBEt₃ (1M in THF) (Sigma-aldrich). *Para*-hydrogen gas was obtained from Glögger group by enrichment of the *para*-spin isomer at 99% by using a custom ordered Sumitomo generator operating at 20 K.

4.3 Analytical methods

4.3.1 NMR Spectroscopy

NMR spectra were recorded on Bruker Avance III 300, Avance III 400 or Avance Neo 400 spectrometers and the spectra were calibrated to the residual solvent signals (benzene- d_6 : $\delta_H=7.16$ ppm, THF- d_8 : $\delta_H=1.74$ and 3.58 ppm, toluene- d_8 : $\delta_H=2.08$ ppm). Abbreviation of signal multiplicities are shown as: s (singlet), d (doublet), t (triplet) and m (multiplet).

4.3.2 Mass Spectrometry

Mass spectra were measured by the Zentrale Massenabteilung, Fakultät für Chemie, Georg-August-Universität, using a soft ionization technique: liquid-injected field desorption ionization (LIFDI-MS) on a JEOL AccuTOF JMS-T100GCV.

4.3.3 Elemental analysis (EA)

EA were obtained from the analytical laboratories at the Georg-August Universität Göttingen on an Elementar Vario EL 3.

4.3.4 UV/Vis Spectroscopy

UV/Vis spectra were recorded on a Varian Cary 300 Scan spectrophotometer and an Agilent Cary 60 equipped with an Unisoko Cryostat (CoolSpek) using *J*-Young quartz cuvettes.

4.3.5 Infrared Spectroscopy (IR)

IR spectra were recorded in Nujol on a Thermo Science Nicolet iZ10 and using a Bruker ALPHA FTIR spectrometer with Platinum ATR module.

4.3.6 EPR Spectroscopy

EPR measurements were performed in air-tight *J*-Young quartz tubes in an atmosphere of purified argon. Frozen solution EPR spectra were recorded on a Bruker EMX-plus CW X-band spectrometer equipped with a Bruker ER 4112HV-CF100 helium cryostat. The spectra were obtained on freshly prepared solutions of 1^{-10} mM compound and simulated using EasySpin^[158] via the cwEPR GUI^[159].

4.3.7 Quantum yield determination

4.3.7.1 Photochemical H/D exchange of **9** with C_6D_6

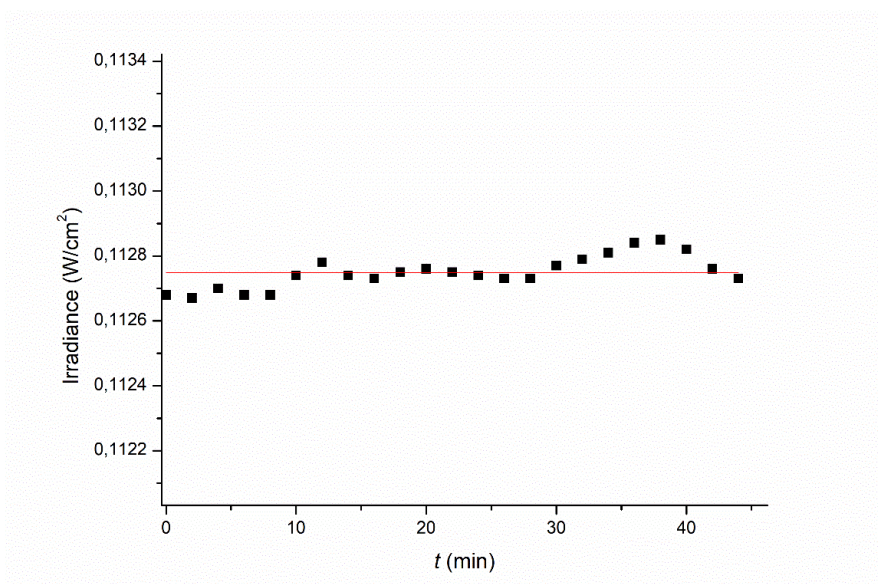


Figure 54: Determination of the irradiance of the 390 nm LED lamp (40 W, $E = 0.11275 \pm 0.00001$ W/cm²).

The photon flux of the 390 nm LED was determined using a Thorlabs S120VC, 200-1100 nm photodiode, which was placed in 3.5 cm distance to the lamp and photolyzed with 100 % power output. The photon flux of the lamp was determined by the following equation:

$$I = \frac{E}{h \cdot \nu \cdot N_A} = (2.2052 \pm 0.0002) \cdot 10^{-6} \text{ mol} \cdot \text{cm}^{-2} \cdot \text{min}^{-1}$$

where I is the photon flux, E is irradiance (W/cm²), h is Planck's constant, ν is the frequency of the lamp, and N_A is Avogadro's number. For the quantum yield determination, a solution of **9** in C_6D_6 (1 mL, $1.35 \cdot 10^{-5}$ mol·L⁻¹) was played in a *J*-Young cuvette with magnetic stir bar. After degassing the cuvette with three freeze-pump-thaw cycles, the sample was photolyzed with the same output power and distance from the LED lamp for 18 h. The solution was transferred into a *J*-Young NMR

tube and the concentration of **9-D** was determined by NMR spectroscopy (18% conversion), giving the quantum yield for photochemical H/D exchange of **9** with C₆D₆ from the following equation:

$$\Phi_{390} = \frac{\Delta n}{n_{\text{photons}} \cdot (1 - 10^{-A_{390}})} = 0.0957 \pm 0.0003 \%$$

where Δn is the amount of **9-D** that was formed and A_{390} is the absorbance of the solution at 390 nm.

4.3.7.2 Styrene hydrogenation by **9**

The photon flux was determined prior to the experiment using a Thorlabs S120VC, 200-1100 nm photodiode, which was placed in 2 cm distance to the lamp and photolyzed with 100 % power output. The photon flux of the lamp was determined by the following equation:

$$I = \frac{E}{h \cdot \nu \cdot N_A} = (3.0593 \pm 0.0002) \cdot 10^{-6} \text{ mol} \cdot \text{cm}^{-2} \cdot \text{min}^{-1}$$

where I is the photon flux, E is irradiance (W/cm²), h is Planck's constant, ν is the frequency of the lamp and N_A is Avogadro's number. For quantum yield determination, a solution of complex **9** (2.0 mg, 4.8·10⁻³ mmol, 5 mol%), styrene (11 μ L, 9.6·10⁻² mmol) and hexamethylbenzene (0.9 mg, 5.6·10⁻³ mmol) in C₆D₆ was prepared in a *J*-Young cuvette with the magnet stirring bar. After degassing the cuvette with three freeze-pump-thaw cycles, 1 bar of H₂ was added after warming to room temperature. The sample was photolyzed with the same output power and distance from the LED lamp for 192 min. The catalyst was then removed by a silica plug and the formation of ethylbenzene was determined by the NMR spectroscopy (3.5 % conversion). The quantum yield was calculated from the following equation:

$$\Phi = \frac{\Delta n}{n_{\text{photons}} \cdot (1 - 10^{-A_{390}})} = 2.2915 \pm 0.0003\%$$

where Δn is the amount of ethylbenzene formed, A_{390} is the absorbance of the solution at 390 nm at the beginning of photolysis.

4.3.8 Magnetic measurements

Magnetic moments were determined by Evans' method as modified by Sur and corrected for diamagnetic contributions.^[160] Temperature-dependent magnetic susceptibility measurement was carried out with a Quantum-Design MPMS3 SQUID magnetometer equipped with a 7 Tesla magnet in the range from 210 to 2.0 K at a magnetic field of 0.5 T. The powdered sample was contained in a polycarbonate capsule, covered with a few drops of low viscosity perfluoropolyether based inert oil Fomblin Y45 to fix the crystals, and fixed in a non-magnetic sample holder. The maximum measuring temperature of 210 K was chosen because of the pour point of the oil, in

order to keep the oil in the frozen state and to avoid therefore the orientation of the crystals parallel to the magnetic field. Each raw data file for the measured magnetic moment was corrected for the diamagnetic contributions of the polycarbonate capsule and of the inert oil according to $M^{\text{dia}} = \chi_g \cdot m \cdot H$, with experimentally obtained gram susceptibilities of the polycarbonate capsule ($\chi_g = -5.60 \cdot 10^{-7}$ emu/(g·Oe)) and of the oil ($\chi_g = -3.82 \cdot 10^{-7}$ emu/(g·Oe)). The molar susceptibility data were corrected for the diamagnetic contribution using the Pascal constants and the increment method according to Haberditzl.^[161,162] Experimental data were modelled with the *JulX* program^[163] using a fitting procedure to the spin Hamiltonian $\hat{H} = g\mu_B \vec{B} \cdot \vec{S}$. Temperature-independent paramagnetism (*TIP*) was included according to $\chi_{\text{calc}} = \chi + \text{TIP}$.

4.3.9 Transient Spectroscopy

Femtosecond UV-pump/mid-infrared-probe (UV/mIR) and UV-pump/near-UV-to-visible probe (UV/nUV-vis) spectroscopy was carried out with a setup previously described elsewhere.^[164] In brief, 60 fs-duration pulses with a center wavelength of 800 nm were provided by a commercial Ti:sapphire oscillator/regenerative amplifier front-end system (Newport Spectra Physics, Solstice Ace) at a repetition rate of 1 kHz. In both experiments, pump pulses centered at 400 nm were generated by frequency doubling the front-end output in a type-I BBO crystal. MIR-probe pulses tunable between 6 and 8 μ were generated by difference frequency mixing of the signal and idler pulses of a properly tuned home-built optical parametric amplifier (OPA) in a type-I AgGaS₂ crystal. Vis-to-near-UV white light continuum probe pulses with a spectrum covering the range from 380 nm to 950 nm were generated by focusing a small fraction of the signal pulses of a commercial OPA (tuned to 1240 nm, TOPAS prime, Light Conversion) into a CaF₂-substrate. UV/nUV-vis spectra were recorded with a commercial transient absorption spectrometer (TAS, Newport/Spectra Physics). Solutions of **9** and **9-D** in *n*-hexane, benzene-h₆, as well as benzene-d₆ were prepared in a glovebox and measured in a sealed stationary sample cell to minimize decomposition upon contact with moisture and air. For the UV/mIR experiments, the sample cell was equipped with two CaF₂ windows that were held apart by a lead spacer at a distance of 100 μ m. Probing in the mid-IR with benzene solutions was not possible due strong solvent background absorptions in the spectral regions of interest. For the UV/nUV-vis experiment, a commercial cell (Hellma, QS) with an optical pathlength of 1 mm optical path was used. Each measurement was repeated several times with fresh solutions in thoroughly cleaned cuvettes. A slow degradation of the sample over a period of several hours was observed and the dinitrogen complex **11** was found to accumulate in the small sample volume of about 350 μ L.

4.3.10 Computational Details.

Density functional theory (DFT) calculations of Gibbs free energies were carried out with the ORCA program package.^[165] Due to charge transfer between the sterically close-lying parts of the *tert*-butyl groups to the central cobalt atom in **9**, the range-separated ω B97X-D3BJ functional^[166] was employed together with the zeroth-order regular approximation (ZORA) for scalar relativistic effects^[167] and the corresponding ZORA-def2-TZVP basis set.^[168] The resolution of identity and chain of spheres exchange (RIJCOSX) algorithm^[169] with automatically selected auxiliary basis sets^[170] was invoked to speed up the calculations. The Conductor-like Polarizable Continuum Model (CPCM)^[171] was used to model the solvent benzene. In order to avoid numerical instabilities, a Gaussian smearing^[172] was employed for the point charges. The state characters and the electronic absorption spectrum were additionally modelled in ORCA with SC-NEVPT2/CASSCF (strongly contracted *N*-electron valence state perturbation theory on top of complete active space self-consistent field) calculations on a reduced model of **9**, where the *tert*-butyl groups were replaced with methyl groups, with ORCA employing an active space of 11 electrons in 14 orbitals, a def2-TZVP basis set,^[168] the RI-JK (resolution of identity for Coulomb and exchange integrals) approximation,^[173] and perturbative spin-orbit couplings for 20 quartet and 30 doublet states. EPR spectra of the complex **9** were calculated both with DFT as a single-reference method and SC-NEVPT2 as a multi-configurational method. These DFT calculations were carried out with the ADF program^[174] using the ω B97X-D functional,^[166] a TZ2P basis set,^[173] ZORA including spin-orbit effects, and toluene as implicit solvent. The SC-NEVPT2 calculations were done as described above, using only 2 quartet and 3 doublet states to save computational time.

4.4 Synthesis and characterization

[CoCH₂SiMe₃(L¹)] (1)

[CoCl(L²)] (15 mg, 0.033 mmol) was dissolved in pentane (6 ml). 0.55 mL solution of (CH₃)₃SiCH₂Li (0.067 M in pentane) was slowly dropwise added to the solution of [CoCl(L¹)], during which the color changed from green to brownish yellow. The reaction mixture was filtered through Celite/glass microfiber and the solution was concentrated and recrystallized at -36 °C.

The solution was decanted and the dark yellow crystalline material (yield: 11 mg, 66%) was dried *in vacuo*.

Anal. Found (Calcd.) for C₂₄H₅₅CoNP₂Si: C, 56.38 (56.89); H, 10.61 (10.94); N, 2.77(2.76).

¹H NMR (C₆D₆, 300 MHz, ppm): 1.90 (tBu), -4.93 (SiMe₃), -18.4.

[CoCH₂SiMe₃(L²)] (2)

[CoCl(L³)] (15 mg, 0.033 mmol) was dissolved in pentane (6 ml). 0.55 mL solution of (CH₃)₃SiCH₂Li (0.067 M in pentane) was slowly dropwise added to the solution of [CoCl(L¹)], during which the color changed from green to brownish yellow. The reaction mixture was filtered through Celite/glass microfiber and the solution was concentrated and recrystallized at -36 °C. The solution was decanted and the dark yellow crystalline material (yield: 11 mg, 66%) was dried *in vacuo*.

Anal. Found (Calcd.) for C₂₄H₅₃CoNP₂Si: C, 57.44 (57.12); H, 10.98 (10.59); N, 2.34 (2.78).

¹H NMR (C₆D₆, 300 MHz, ppm): 90.80, 7.63 (tBu), 7.25 (tBu), -12.28 (SiMe₃), -49.08, -98.97.

[CoCH₂SiMe₃(L¹H)]BAR^F₄ (3^{BARF})

1 (10 mg, 0.02 mmol) was dissolved in Et₂O (4 mL) in a glass vial. A solution of [H(Et₂O)₂]BAR^F₄ (20 mg, 0.02 mmol, in 2 mL diethyl ether) was added into the solution of **1** at r.t.. Volatiles was removed and the residual was washed with pentane (2 x 2 mL) and dried *in vacuo*. The solid residual was dissolved in Et₂O (6 mL) and filtered through glass microfiber and concentrated. Pentane was carefully layered and the resulting solution was stored at -35 °C overnight for recrystallization, which gave a pale yellow crystalline product in a yield of 75% (21 mg).

Anal. Found (Calcd.) for C₅₆H₆₇BCoF₂₄NP₂Si: C, 48.45 (49.10); H, 4.97 (4.93); N, 1.04 (1.02).

¹H NMR (THF-*d*₈, 300 MHz, ppm): 34.14, 7.75 (BAR^F₄), 7.51 (BAR^F₄), 13.36 (tBu), -18.93 (SiMe₃), -33.09, -47.43.

[CoCH₂SiMe₃(L¹H)]BF₄ (3^{BF4})

1 (10 mg, 0.02 mmol) was dissolved in Et₂O (4 mL) in a glass vial. A solution of [H(Et₂O)₂]BAr^F₄ (20 mg, 0.02 mmol, in 2 mL diethyl ether) was added into the solution of **1** at r.t.. Volatiles was removed and the residual was washed with pentane (2 x 2 mL) and dried *in vacuo*. The solid residual was dissolved in Et₂O (6 mL) and filtered through glass microfiber and concentrated. Pentane was carefully layered and the resulting solution was stored at -35 °C overnight for recrystallization, which gave a pale yellow crystalline product in a yield of 75% (21 mg).

Anal. Found (Calcd.) for C₂₄H₅₆BCoF₄NP₂Si: C, 47.49 (48.49); H, 9.39 (9.50); N, 2.33 (2.36).

¹H NMR (THF-*d*₈, 300 MHz, ppm): 33.62, 15.01 (*t*Bu), 12.21 (*t*Bu), -19.29 (SiMe₃), -31.19, -52.34.

ATR-IR: $\tilde{\nu}_{\text{NH}} = 3211 \text{ cm}^{-1}$.

[CoCH₂SiMe₃(L²)]BAr^F₄ (4**)**

2 (10 mg, 0.02 mmol) was dissolved in Et₂O (4 mL) in a glass vial. A solution of [H(Et₂O)₂]BAr^F₄ (20 mg, 0.02 mmol, in 2 mL diethyl ether) was added into the solution of **2** at r.t.. Volatiles was removed and the residual was washed with pentane (2 x 2 mL) and dried *in vacuo*. The solid residual was dissolved in Et₂O (6 mL) and filtered through glass microfiber and concentrated. Pentane was carefully layered and the resulting solution was stored at -35 °C overnight for recrystallization, which gave a pale yellow crystalline product in a yield of 81% (23 mg).

Anal. Found (Calcd.) for C₅₆H₆₅BCoF₄NP₂Si: C, 48.87 (49.17); H, 4.94 (4.79); N, 1.09 (1.02).

¹H NMR (THF-*d*₈, 300 MHz, ppm): 18.18, 10.72 (*t*Bu), 7.75 (BAr^F₄), 7.51 (BAr^F₄), 7.23 (*t*Bu), -12.74, -15.70 (SiMe₃), -27.68.

[Co(L¹H)]BAr^F₄ (5**)**

10 (20 mg, 0.045 mmol) was dissolved in Et₂O (4 mL) in a small glass vial. A solution of [H(Et₂O)₂]BAr^F₄ (46 mg, 0.044 mmol, in 4 mL diethyl ether) was added into the solution of **6** at – room temperature. Volatiles was removed and the residual was washed with pentane (2 x 3 mL) and dried *in vacuo*. The solid residual was dissolved in Et₂O to a concentrated solution. Pentane was carefully layered and the resulting solution was stored at -35 °C overnight for recrystallization. The yield of the dride green crystalline product **5** was 81% (47 mg).

Anal. Found (Calcd.) for C₂₀H₄₆BCoF₄NP₂: C, 48.50 (48.65); H, 4.51 (4.48); N, 1.41 (1.09).

$^1\text{H NMR}$ (THF- d_8 , 300 MHz, ppm): 64.47, 24.62 (tBu), 22.73 (tBu), 7.75 (BAr $^{\text{F}}_4$), 7.51 (BAr $^{\text{F}}_4$), -3.65, -62.48 (CH $_2$).

$^{11}\text{B}\{^1\text{H}\}$ NMR (THF- d_8 , 96 MHz, ppm): -6.64.

$^{19}\text{F}\{^1\text{H}\}$ NMR (THF- d_8 , 282 MHz, ppm) -62.87.

[CoH(L 1)] (6)

A frozen solution of [CoCl(L 1)] (200 mg, 0.44 mmol) in benzene (20 ml) was layered with LiHBEt $_3$ (0.1 M THF/benzene, 0.48 mmol, 1.1 eq.) solution. The reaction mixture was slowly warmed to RT under stirring for 1 h, resulting in yellowish suspension. The solvent was removed in *vacuo*. The reaction residual was extracted with pentane (10 mL). The resulting solution was filtered by celite/glass microfiber, which was followed by solvent evaporation, resulting in brownish yellow crystalline solid. Crystallization in pentane at -35 °C resulted in brownish yellow crystals (85% yield).

Anal. Found (Calcd.) for C $_{20}$ H $_{45}$ CoNP $_2$: C, 56.86 (57.13); H, 10.61 (10.79); N, 3.25 (3.33).

$^1\text{H NMR}$ (THF- d_8 , 300 MHz, ppm): 2.53 (br, s, tBu, 18H), -12.59 (br, s, CH $_2$, 8H), the hydride signal was not found.

ATR-IR: $\tilde{\nu}_{\text{CoH}}$ = 1727 cm $^{-1}$.

Evans' method: μ_{eff} = 1.75 μB .

[CoH(L ^1H)]BAr $^{\text{F}}_4$ (7 $^{\text{BArF}}$)

6 (28 mg, 0.066 mmol) was dissolved in Et $_2$ O (6 mL) in a small glass vial. A solution of [H(Et $_2$ O) $_2$]BAr $^{\text{F}}_4$ (68 mg, 0.066 mmol, in 4 mL diethyl ether) was added into the solution of **6** at -80 °C. The reaction mixture was slowly warmed to room temperature and stirred for 1 h. Volatiles was removed and the residual was washed with pentane (2 x 3 mL) and dried *in vacuo*. The solid residual was dissolved in Et $_2$ O (6 mL) and filtered through Celite/glass microfiber and concentrated to 3 mL. Pentane was carefully layered and the resulting solution was stored at -35 °C overnight for recrystallization, which gave a pale yellow crystalline product in a yield of 79% (68 mg).

Anal. Found (Calcd.) for C $_{52}$ H $_{58}$ BCoF $_{24}$ NP $_2$: C, 48.39 (48.62); H, 4.46 (4.55); N, 1.06 (1.09).

¹H NMR (THF-*d*₈, 300 MHz, ppm): 30.11 (CH₂), 7.75 (BAr^F₄), 7.51 (BAr^F₄), 7.20 (tBu), 3.06 (tBu), -0.50 (CH₂), -18.12 (CH₂).

¹¹B{¹H} NMR (THF-*d*₈, 96 MHz, ppm): -6.4.

¹⁹F{¹H} NMR (THF-*d*₈, 282 MHz, ppm) -63.4.

ATR-IR (in solid state): $\tilde{\nu}_{\text{CoH}} = 1869 \text{ cm}^{-1}$, $\tilde{\nu}_{\text{N-H}} = 3230 \text{ cm}^{-1}$

[CoH(L¹H)]BF₄ (7^{BF4}**)**

6 (62 mg, 0.147 mmol) was dissolved in Et₂O (10 mL) in a small glass vial. A solution of [H(Et₂O)]BF₄ (20 μ L, 0.147 mmol, in 5 mL diethyl ether) was dropwise added into the solution of **6** at room temperature. Precipitate was observed immediately upon addition of the acid solution. Volatiles in the resulting suspension was removed and the residual was washed with pentane (2 x 3 mL) and dried *in vacuo*, which gave **7^{BF4}** as a green powder in a yield of 57% (43 mg). Crystals suitable for X-Ray diffraction were obtained in THF by gas phase diffusion of pentane at RT.

Anal. Found (Calcd.) for C₂₀H₄₆BCoF₄NP₂: C, 47.24 (46.90); H, 8.77 (9.12); N, 2.70 (2.76).

¹H NMR (THF-*d*₈, 300 MHz, ppm): 30.94, 7.35 (tBu), 3.52 (tBu), -0.73, -19.96.

¹¹B{¹H} NMR (THF-*d*₈, 96 MHz, ppm): -12.7.

¹⁹F{¹H} NMR (THF-*d*₈, 282 MHz, ppm) -164.7.

FT-IR (in nujol): $\tilde{\nu}_{\text{CoH}} = 1816 \text{ cm}^{-1}$, $\tilde{\nu}_{\text{N-H}} = 3214 \text{ cm}^{-1}$

[CoH(L²)] (8**)**

A frozen solution of [CoCl(L²)] (60 mg, 0.13 mmol) in benzene (6 ml) was layered with LiHBEt₃ (0.1 M THF/benzene, 0.14 mmol, 1.1 eq.) solution. The reaction mixture was slowly warmed to RT under stirring for 1 h resulted in yellowish suspension. The solvent was removed in *vacuo*. The reaction residual was extracted with pentane (10 mL). The resulting solution was filtered by celite/glass microfiber, which was followed by solvent evaporation, resulting in brownish yellow crystalline solid. Crystallization in pentane at -85 °C resulted in brownish yellow crystals (75% yield).

Anal. Found (Calcd.) for C₂₀H₄₃CoNP₂: C, 57.39 (57.41); H, 10.12 (10.36); N, 3.30 (3.35).

¹H NMR (C₆D₆, 300 MHz, ppm): 8.63 (br, s, *t*Bu, 18H), 8.25 (br, s, *t*Bu, 18H), 76.79, 13.32, 46.18, 84.22, the hydride signal was not found.

ATR-IR: $\tilde{\nu}_{\text{CoH}} = 1738 \text{ cm}^{-1}$ ($\tilde{\nu}_{\text{CoD}} = 1238 \text{ cm}^{-1}$).

[CoH(L³)] (9)

[CoCl(L³)] (50.0 mg, 0.111 mmol) and LiAlH₄ (2.1 mg, 0.055 mmol) were dissolved in THF (10 mL). The mixture was stirred for 30 min. The solvent of the orange solution was evacuated *in vacuo*. The residue was extracted with pentanes and the resulting solution is filtered over Celite[®], and dried *in vacuo*. The solid was dissolved in minimal amount of pentanes and recrystallized at -35 °C. The orange crystalline solid (yield 35 mg, 76%) was obtained and dried *in vacuo*.

Anal. Found (Calcd.) for C₂₀H₄₁CoNP₂: C, 57.28 (57.68); H, 9.89 (9.92); N, 3.36 (3.36).

¹H NMR (C₆D₆, 300 MHz, ppm): 9.85 (*t*Bu), -26.28 (CH₂), -48.28 (CH₂), the hydride signal was not found.

ATR-IR: $\tilde{\nu}_{\text{CoH}} = 1756 \text{ cm}^{-1}$.

Evans' method: $\mu_{\text{eff}} = 1.97 \pm 0.27 \mu\text{B}$.

[CoD(L³)] (9-D)

[CoCl(L³)] (40.0 mg, 0.088 mmol) and LiAlD₄ (1.9 mg, 0.044 mmol) were dissolved in THF (10 mL). The mixture was stirred for 30 min. The solvent of the orange solution was evacuated *in vacuo*. The residue was extracted with pentanes and the resulting solution is filtered over Celite[®], and dried *in vacuo*. The solid was dissolved in minimal amount of pentanes and recrystallized at -35 °C. The orange crystalline solid (yield 25 mg, 69%) was obtained and dried *in vacuo*.

Anal. Found (Calcd.) for C₂₀H₄₁CoNP₂: C, 57.28 (57.68); H, 9.89 (9.92); N, 3.36 (3.36).

¹H NMR (C₆D₆, 300 MHz, ppm): 9.63 (*t*Bu), -26.53 (CH₂), -46.97 (CH₂).

ATR-IR: $\tilde{\nu}_{\text{CoH}} = 1269 \text{ cm}^{-1}$.

[CoN₂(L¹)] (10)

[CoCl(L¹)] (50 mg, 0.11 mmol) and KC₈ (15 mg, 0.11 mmol) were dissolved in THF (10 ml). The reaction mixture was stirred overnight under N₂ (1 bar) atmosphere. The volatile was removed in vacuo and the resulting residual was extracted and filtered with pentane. The solution was concentrated and recrystallized at -36 °C. The solution was decanted and the dark purple crystalline material (yield: 44 mg, 90%) was dried *in vacuo*.

Anal. Found (Calcd.) for C₂₀H₄₄CoN₃P₂: C, 54.03 (53.68); H, 9.29 (9.39); N, 8.18(9.39).

³¹P{¹H} NMR (C₆D₆, 121 MHz, ppm): 104.88 ppm.

¹H NMR (C₆D₆, 300 MHz, ppm): 1.42 (36 H, CH₃, A₁₈BCXX'C'B'A'₁₈, |³J_{AX} + ⁵J_{AX}| = 12.10 Hz), 1.73 (4H, PCH₂, ³J_{BC} = 8.66 Hz), 2.95 (4H, NCH₂, N = |³J_{CX} + ³J_{CX'}| = 16.26 Hz, ³J_{BC} = 6.50 Hz).

ATR-IR: $\tilde{\nu}_{\text{NN}} = 1980 \text{ cm}^{-1}$.

[CoN₂(L³)] (11)

A vial was charged with [CoCl(PNP)] (50.0 mg, 0.111 mmol), KC₈ (18 mg, 0.133 mmol) and THF (10 mL). The reaction mixture was stirred under N₂ atmosphere at room temperature overnight. The solvent of the solution was removed *in vacuo*. The residue was extracted with pentanes and the resulting solution was filtered, and dried *in vacuo*. The residue was dissolved in pentanes and recrystallized at -36 °C overnight. The solution was decanted and the dark purple crystalline material (yield: 44 mg, 90%) was dried *in vacuo*.

Anal. Found (Calcd.) for C₂₀H₄₁CoNP₂: C, 54.32 (54.17); H, 9.39 (9.09); N, 9.12(9.48).

³¹P{¹H} NMR (C₆D₆, 121 MHz, ppm): 81.6 ppm.

¹H NMR (C₆D₆, 300 MHz, ppm): 81.6. ¹H NMR (C₆D₆, 300 MHz, ppm): 1.47 (36 H, CH₃, A₁₈BCXX'A'₁₈B'C', ³J_{AX} = 12.97 Hz), 4.01 (2H, PCH, ³J_{BC} = 5.23 Hz), 6.65 (2H, NCH, N = |³J_{CX} + ³J_{CX'}| = 37.67Hz, ³J_{BC} = 5.23 Hz).

ATR-IR: $\tilde{\nu}_{\text{NN}} = 2012 \text{ cm}^{-1}$.

[Co(L³)] (12)

[CoCl(P=N=P)] (50.0 mg, 0.111 mmol) and KC₈ (18 mg, 0.133 mmol) were dissolved in Na/K dried THF (10 mL). The reaction mixture was stirred overnight in static vacuum at room temperature. The solvent was evacuated *in vacuo*.

$^1\text{H NMR}$ (C_6D_6 , 300 MHz, ppm): 27.35 (tBu), 86.84 (CH), -90.62 (CH).

[CoH(L²H)]BF₄ (13^{BF₄})

8 (10 mg, 0.024 mmol) was dissolved in Et₂O (3 mL) in a small glass vial. A solution of [H(Et₂O)]BF₄ (3.3 μL , 0.024 mmol, in 2 mL diethyl ether) was dropwise added into the solution of **8** at room temperature. Precipitate was observed immediately upon addition of the acid solution. Volatiles in the resulting suspension was removed and the residual was washed with pentane (3 x 2 mL) and dried *in vacuo*, which gave **13^{BF₄}** as a green powder in a yield of 85% (11.2 mg). Crystals suitable for X-Ray diffraction were obtained in THF at -35 °C.

Anal. Found (Calcd.) for C₂₀H₄₄BCoF₄NP₂: C, 47.24 (47.45); H, 8.72 (8.76); N, 2.50 (2.77).

$^1\text{H NMR}$ (THF-*d*₈, 300 MHz, ppm): 11.45 (br), 5.71 (br, tBu, 18H), 3.66 (br, tBu, 18H), -10.04 (br), -15.70 (br).

ATR-IR (in solid state): $\tilde{\nu}_{\text{CoH}} = 1804 \text{ cm}^{-1}$, $\tilde{\nu}_{\text{N=C}} = 1623 \text{ cm}^{-1}$

[CoH(L²H)]BAr^F₄ (13^{BAr^F})

8 (12 mg, 0.029 mmol) was dissolved in Et₂O (3 mL) in a small glass vial. A solution of [H(Et₂O)₂]BAr^F₄ (24 mg, 0.024 mmol, in 3 mL diethyl ether) was dropwise added into the solution of **6** at room temperature. Precipitate was observed immediately upon addition of the acid solution. Volatiles in the resulting suspension was removed and the residual was washed with pentane (3 x 2 mL) and dried *in vacuo*, which gave **13^{BAr^F}** as a pale green powder in a yield of 78% (24 mg). Crystals suitable for X-Ray diffraction were obtained in Et₂O layered with pentane at -35 °C.

Anal. Found (Calcd.) for C₂₀H₄₄BCoF₄NP₂: C, 47.24 (47.45); H, 8.72 (8.76); N, 2.50 (2.77).

$^1\text{H NMR}$ (THF-*d*₈, 300 MHz, ppm): 10.57, 7.75 (BAr^F₄), 7.51 (BAr^F₄), 5.37 (tBu), 3.40 (tBu), -3.60, -19.70.

[CoCH₂CH₂Ph(L³)] (19)

PhCH₂CH₂MgCl (1 M, 0.15 mL, in THF) was dropwise added to the solution of [CoCl(PNP)] (15.0 mg, 0.033 mmol) in THF (4 mL). The reaction mixture was stirred at room temperature for 1 h and the solvent subsequently removed *in vacuo*. The residue was extracted with pentanes.

After filtration, the solution was dried *in vacuo*. The residue was dissolved in pentanes and recrystallized at -36 °C overnight. The solution was decanted and the dark red crystalline product dried *in vacuo* (yield: 7.8 mg, 45%). Anal. Found (Calcd) for C₂₈H₄₉CoNP₂: C, 64.25 (64.60); H, 9.46 (9.49); N, 2.64(2.69). ¹H NMR (C₆D₆, 300 MHz, ppm): 13.98 (*t*Bu), 3.85, 0.24, -6.56, -23.01, -58.69, -71.92.

Anal. Found (Calcd.) for C₂₈H₄₉CoNP₂: C, 64.25 (64.60); H, 9.46 (9.49); N, 2.64(2.69).

¹H NMR (C₆D₆, 300 MHz, ppm): 13.98 (*t*Bu), 3.85, 0.24, -6.56, -23.01, -58.69, -71.92.

4.5 Photo-induced cobalt-catalyzed olefin hydrogenation

4.5.1 Procedure for catalytic hydrogenation in different conditions

General procedure for photo-induced olefin hydrogenation. In a typical experiment, complex **9** (2 mg, 4.8 μmol, 1 eq.) and hexamethylbenzene (2 mg, 12.3 μmol, 2.5 eq.) as internal standard were dissolved in C₆D₆ (0.45 mL) in a J-Young NMR tube. After addition of the substrate (48 μmol, 10 eq.), the NMR tube was degassed by one freeze-pump-thaw cycle and 1 bar of hydrogen gas was added after warming to room temperature. The resulting solution was then photolyzed at 390 nm (LED), while the temperature was kept at room temperature using a water bath. The conversion and yield were determined by ¹H NMR spectroscopy

Photo-induced hydrogenation of styrene in the presence of Hg. Complex **9** (4 mg, 9.6 μmol, 1 eq.) and hexamethylbenzene (4 mg, 24.6 μmol, 2.5 eq.) as an internal standard were dissolved in C₆D₆ (1.0 mL) in a J-Young UV/Vis cuvette. The substrate (11 μL, 96 μmol, 10 eq.), Hg (200 mg, 1 mmol) and a stirbar were added. The cuvette was evacuated by one freeze-pump-thaw cycle and refilled with 1 bar H₂ after warming to room temperature. The resulting solution was then stirred and photolyzed at 390 nm (LED) for 15 h and the temperature kept at room temperature using a water bath. The resulting solution was then transferred into a J-Young NMR tube and conversion and yield were determined by ¹H NMR spectroscopy.

Photo-induced hydrogenation of styrene by **9 (5 mol%) under different H₂ pressure.** Complex **9** (3.5 mg, 8.4 μmol, 1 eq.), styrene (19 μL, 168 μmol, 20 eq.) and hexamethylbenzene (1.2 mg, 7.4 μmol, 0.88 eq.) as internal standard were dissolved in C₆D₆ (0.6 mL). The solution was separated into three high pressure NMR tubes. The NMR tubes were degassed by one

freeze-pump-thaw cycle and 1 bar, 4 bar and 8 bar of hydrogen gas were added into three tubes after warming to room temperature, respectively. The resulting solution was then photolyzed at 390 nm (LED) for 15 h, while the temperature was kept at room temperature using a water bath. The conversion and yield were determined by ^1H NMR spectroscopy.

Photo-induced hydrogenation of styrene by **9 (1 mol%) under different H_2 pressure.** Complex **9** (2 mg, 4.8 μmol , 1 eq.), styrene (55 μL , 480 μmol , 100 eq.) and hexamethylbenzene (1 mg, 6.2 μmol , 1.3 eq.) as internal standard were dissolved in C_6D_6 (0.4 mL). The solution was separated into two high pressure NMR tubes. The NMR tubes were degassed by one freeze-pump-thaw cycle and 4 bar and 8 bar of hydrogen gas were added into two tubes after warming to room temperature, respectively. The resulting solution was then photolyzed at 390 nm (LED) for 15 h, while the temperature was kept at room temperature using a water bath. The conversion and yield were determined by ^1H NMR spectroscopy.

4.5.2 Spectroscopic data of substrate screening

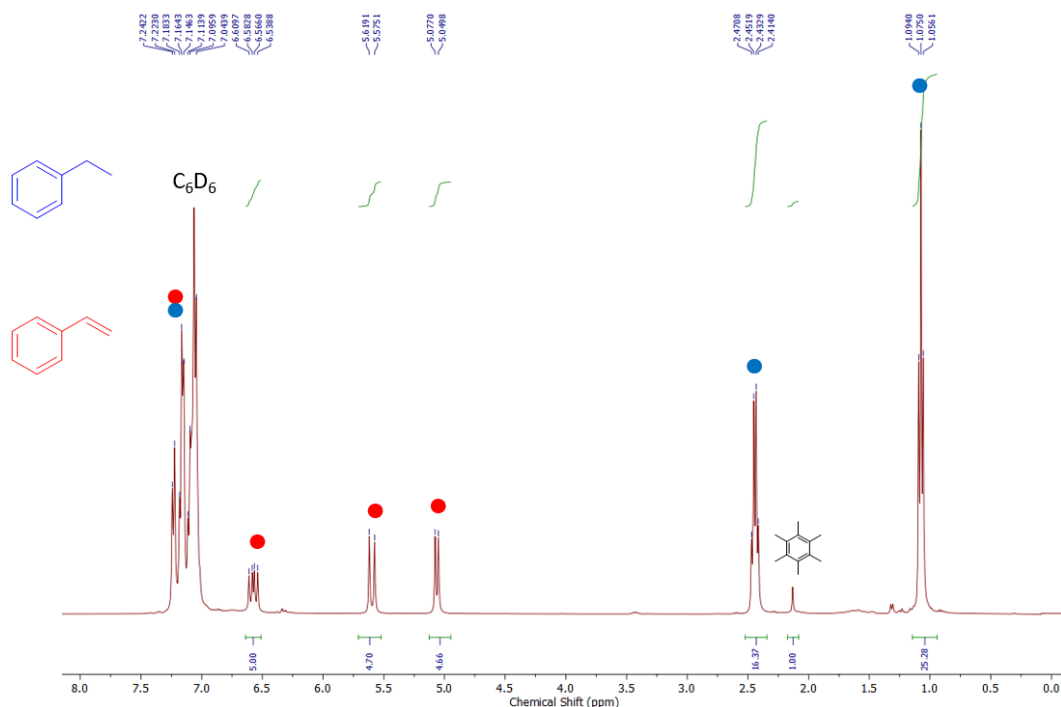


Figure 55: ^1H NMR (benzene- d_6 , rt) spectrum after the hydrogenation of styrene.

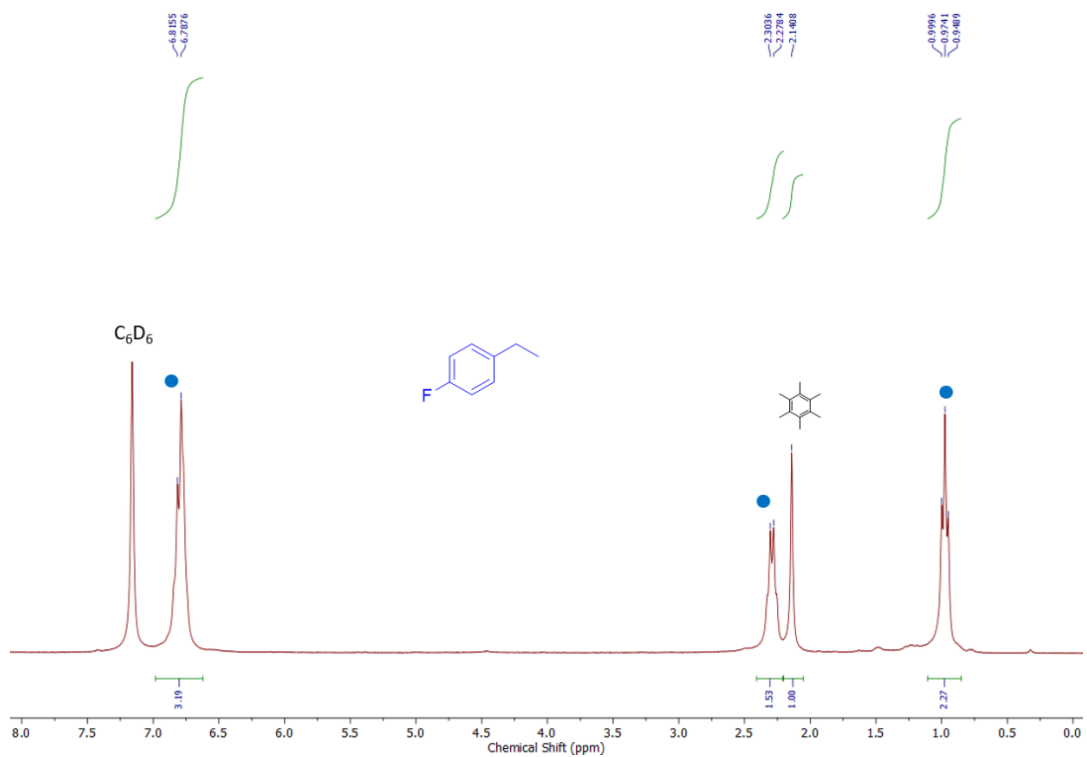


Figure 56: ^1H NMR (benzene- d_6 , rt) spectrum after the hydrogenation of 4-fluorostyrene.

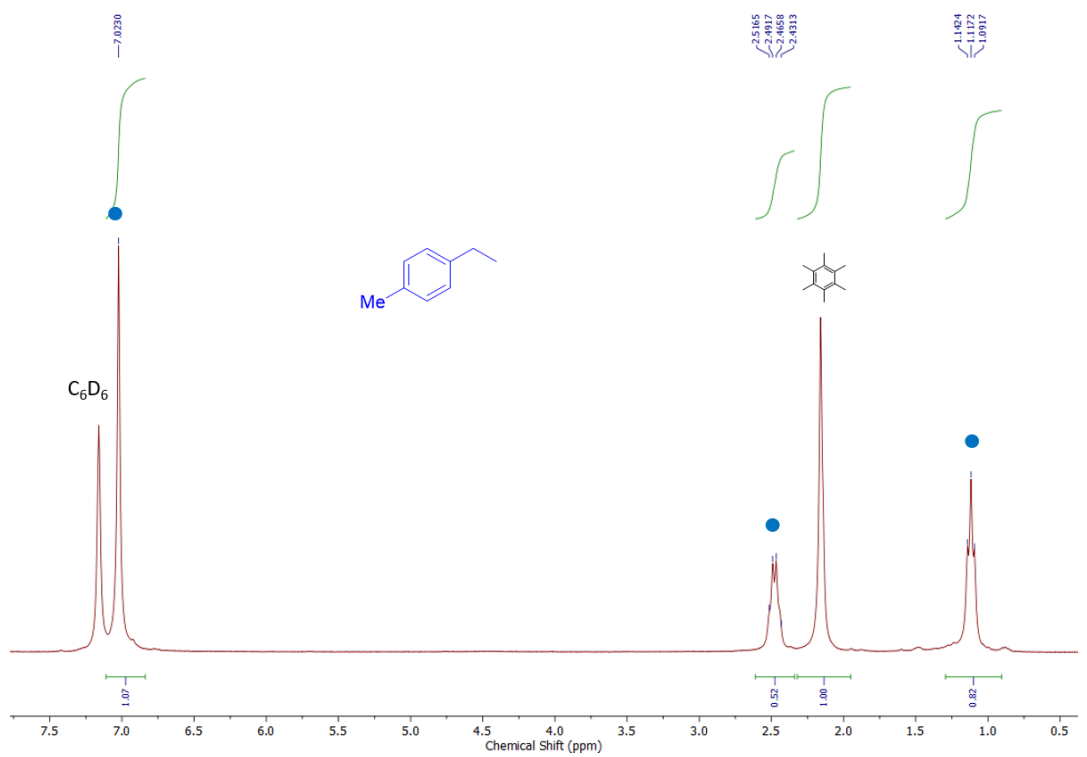


Figure 57: ^1H NMR (benzene- d_6 , rt) spectrum after the hydrogenation of 4-methylstyrene.

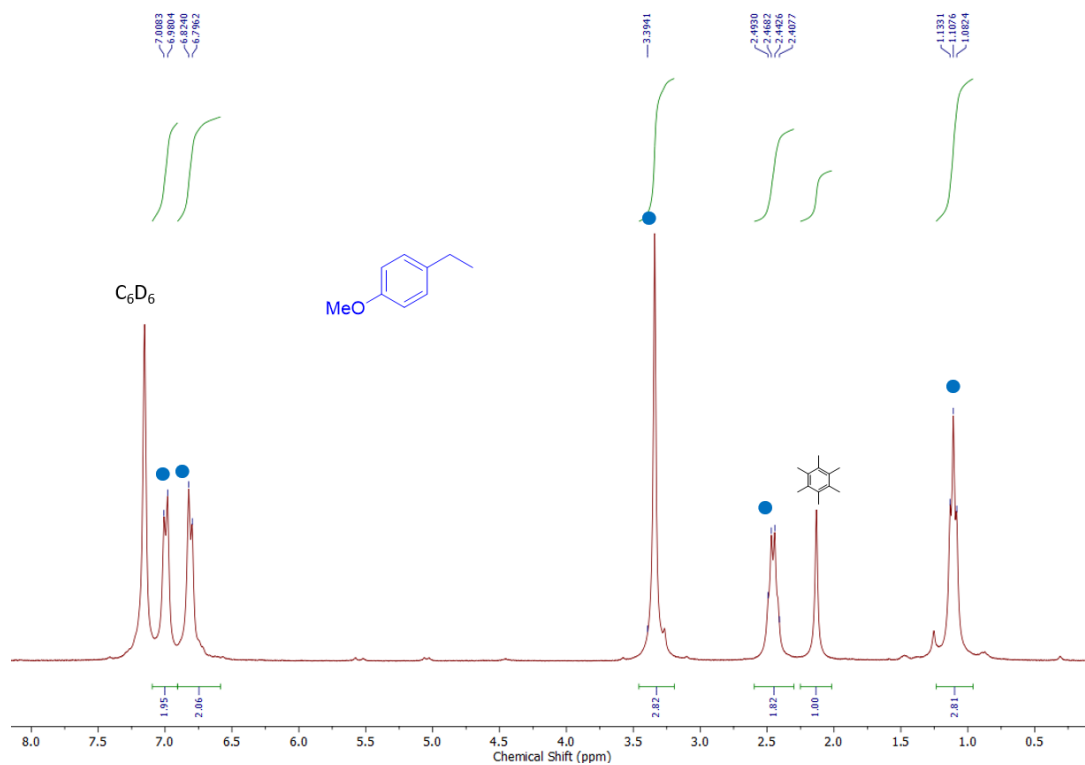


Figure 58: ^1H NMR (benzene- d_6 , rt) spectrum after the hydrogenation of 4-methoxystyrene.

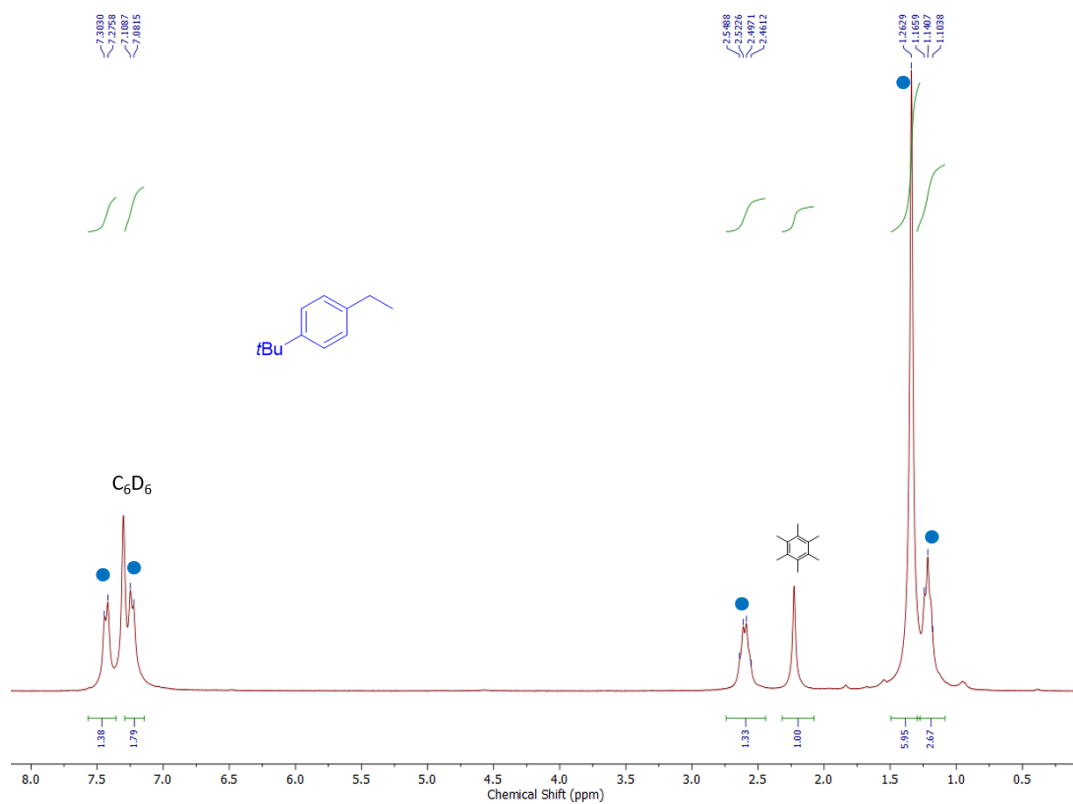


Figure 59: ^1H NMR (benzene- d_6 , rt) spectrum after the hydrogenation of 4-*tert*-butylstyrene.

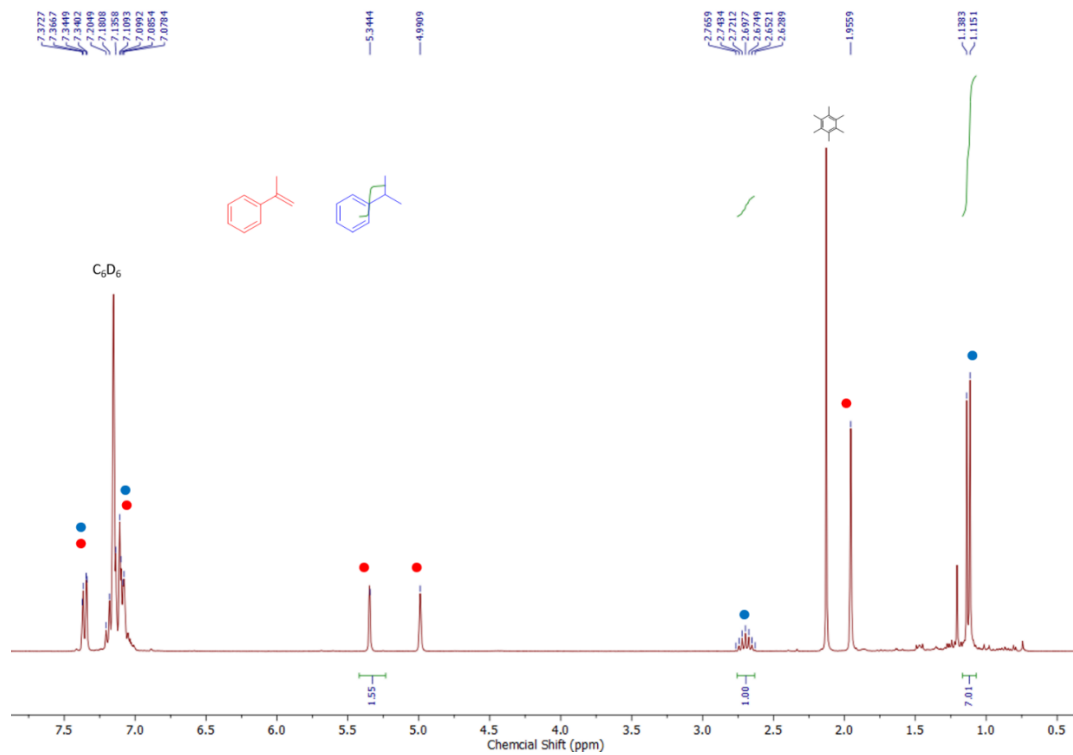


Figure 60: 1H NMR (benzene- d_6 , rt) spectrum after the hydrogenation of α -methylstyrene.

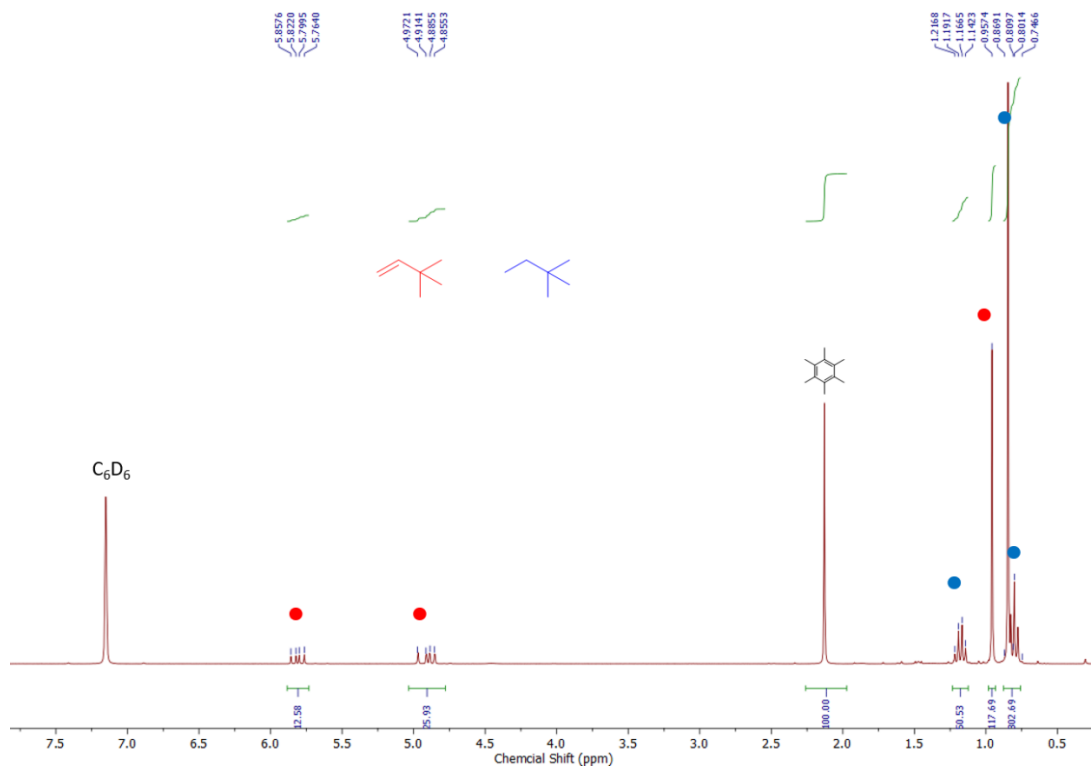


Figure 61: 1H NMR (benzene- d_6 , rt) spectrum after the hydrogenation of 3,3-dimethylbutene.

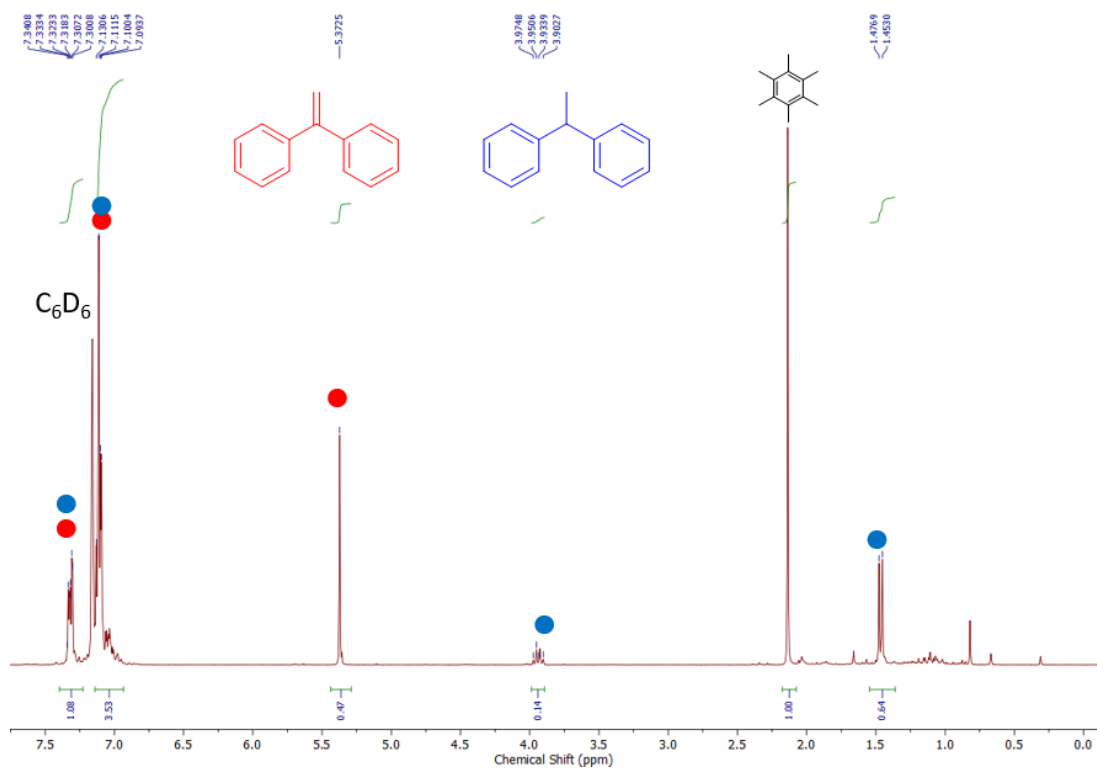


Figure 62: ^1H NMR (benzene- d_6 , rt) spectrum after the hydrogenation of 1,1-diphenylethylene.

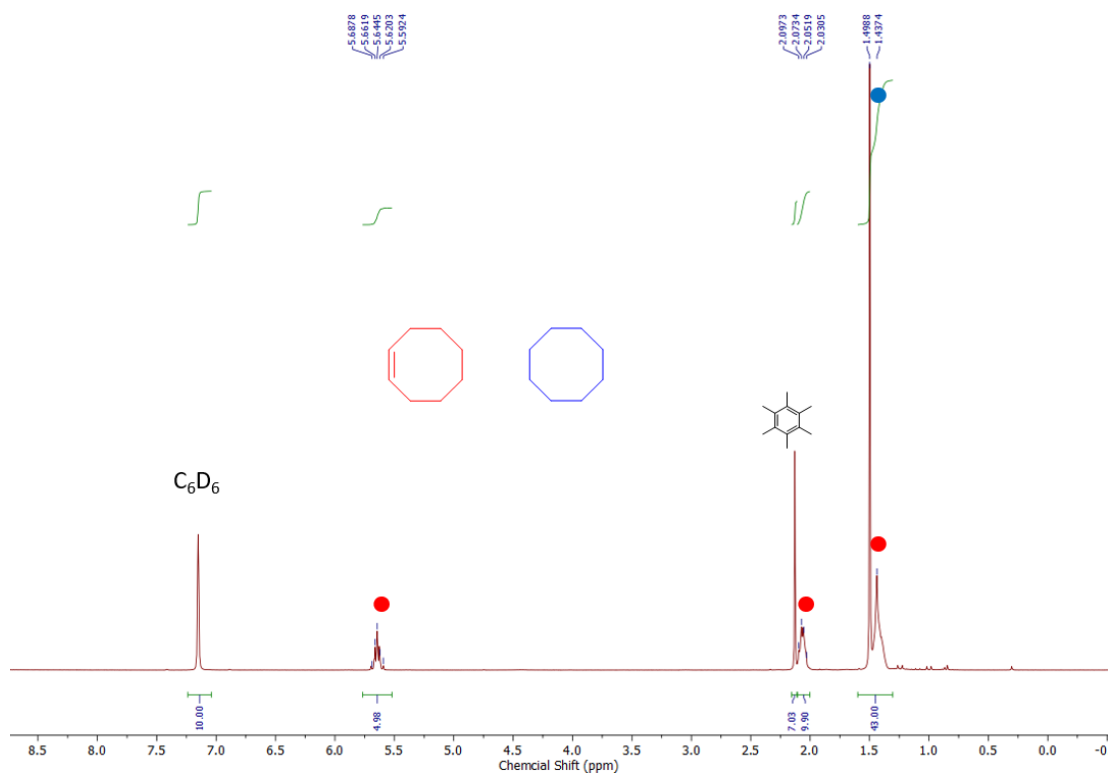


Figure 63: ^1H NMR (benzene- d_6 , rt) spectrum after the hydrogenation of cyclooctene.

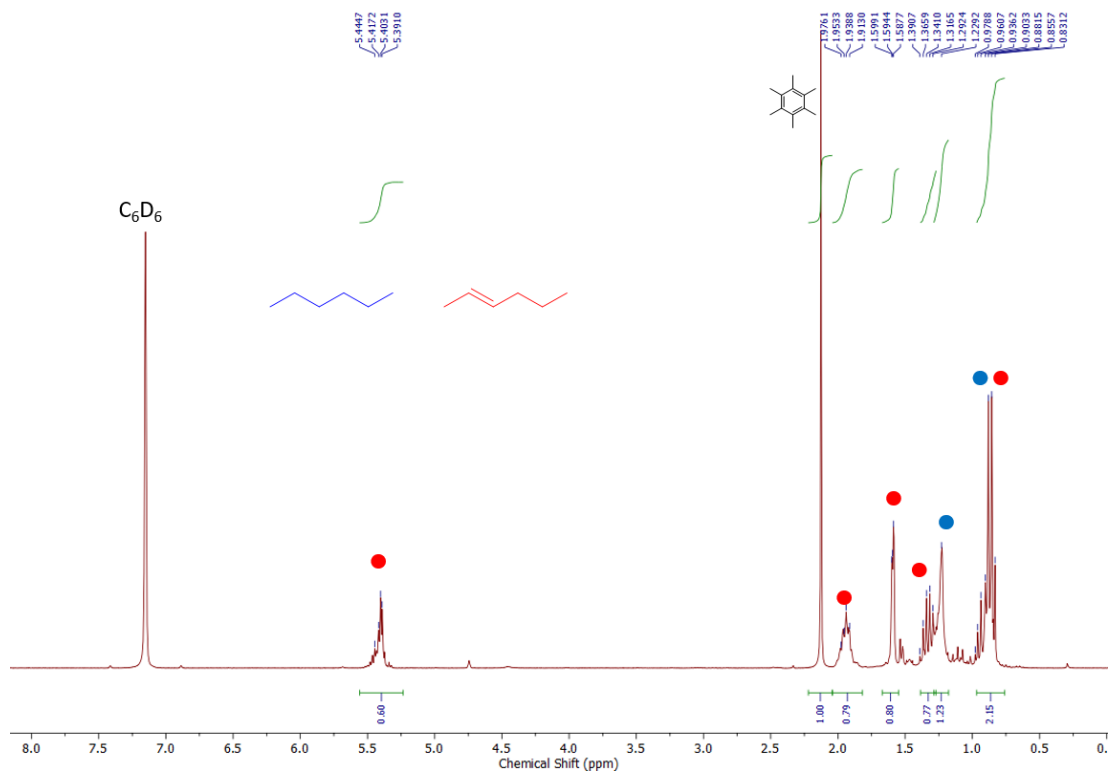


Figure 64: ^1H NMR (benzene- d_6 , rt) spectrum after the hydrogenation of 2-hexene.

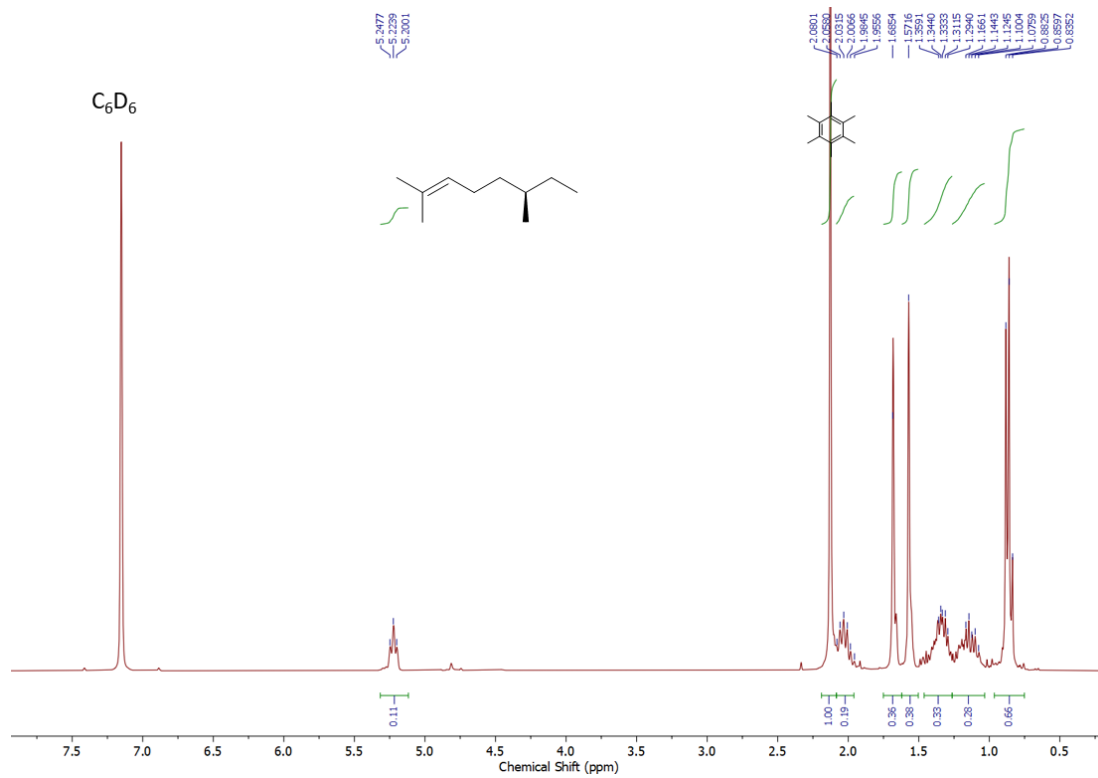


Figure 65: ^1H NMR (benzene- d_6 , rt) spectrum after the hydrogenation of (+)- β -citronellene.

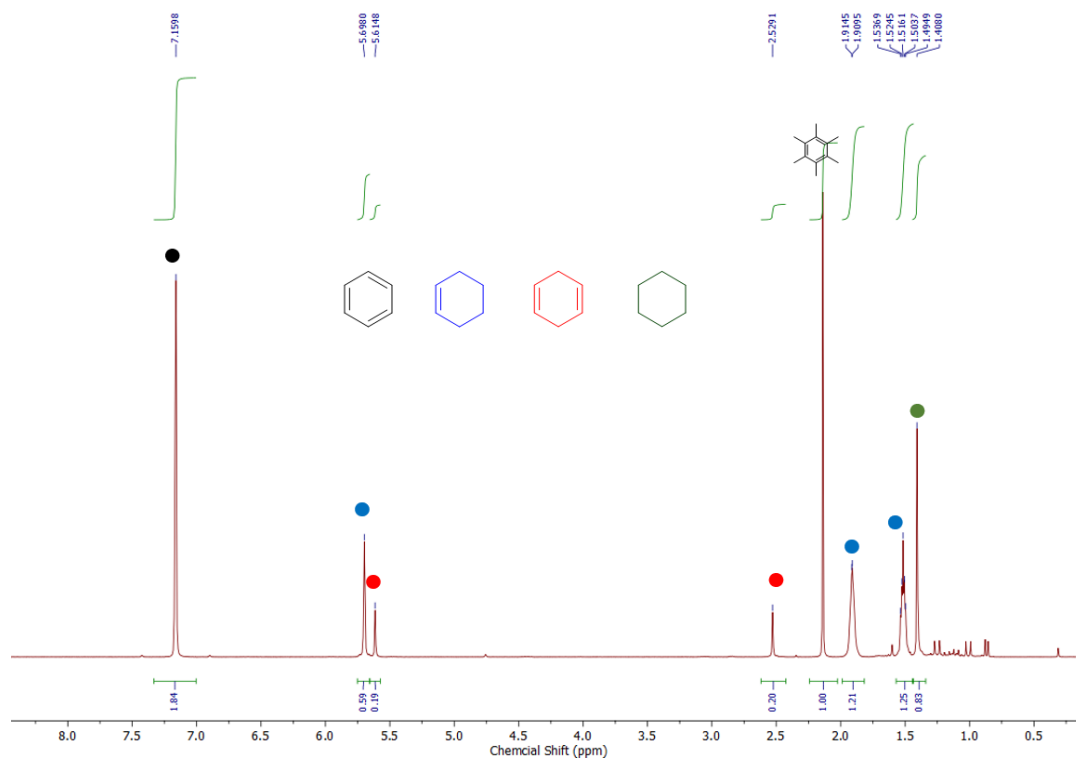


Figure 66: ^1H NMR (benzene- d_6 , rt) spectrum after the hydrogenation of cyclohexadiene.

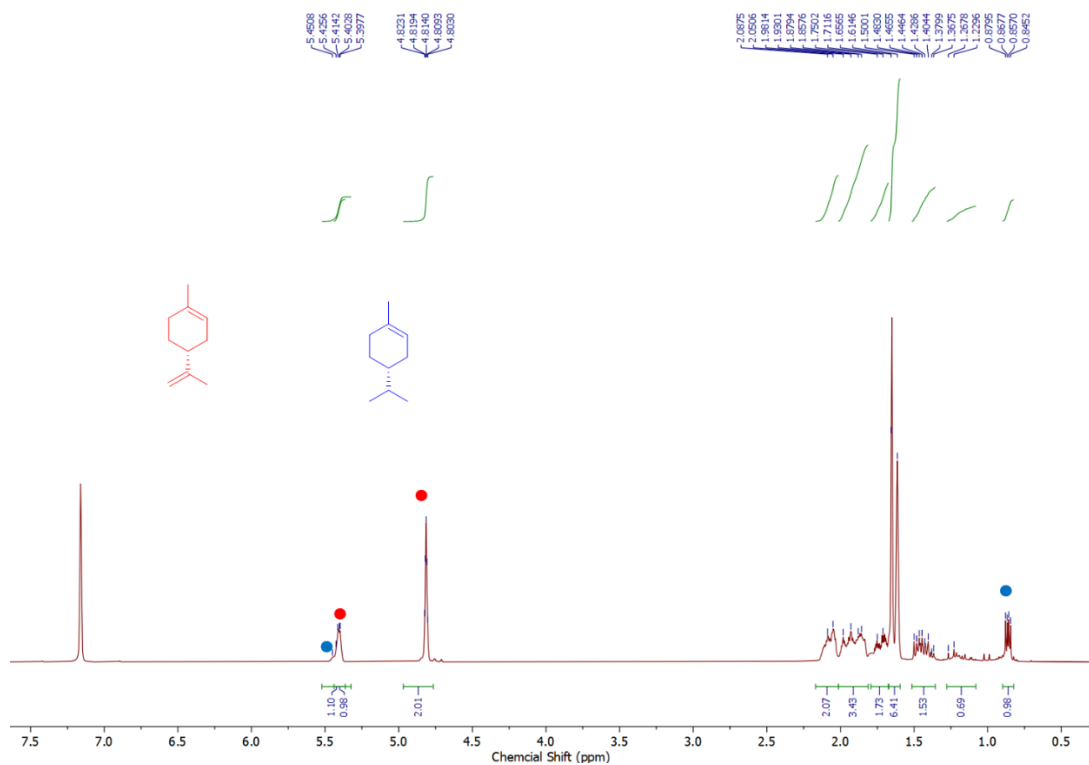


Figure 67: ^1H NMR (benzene- d_6 , rt) spectrum after the hydrogenation of (R)-(+)-limonene.

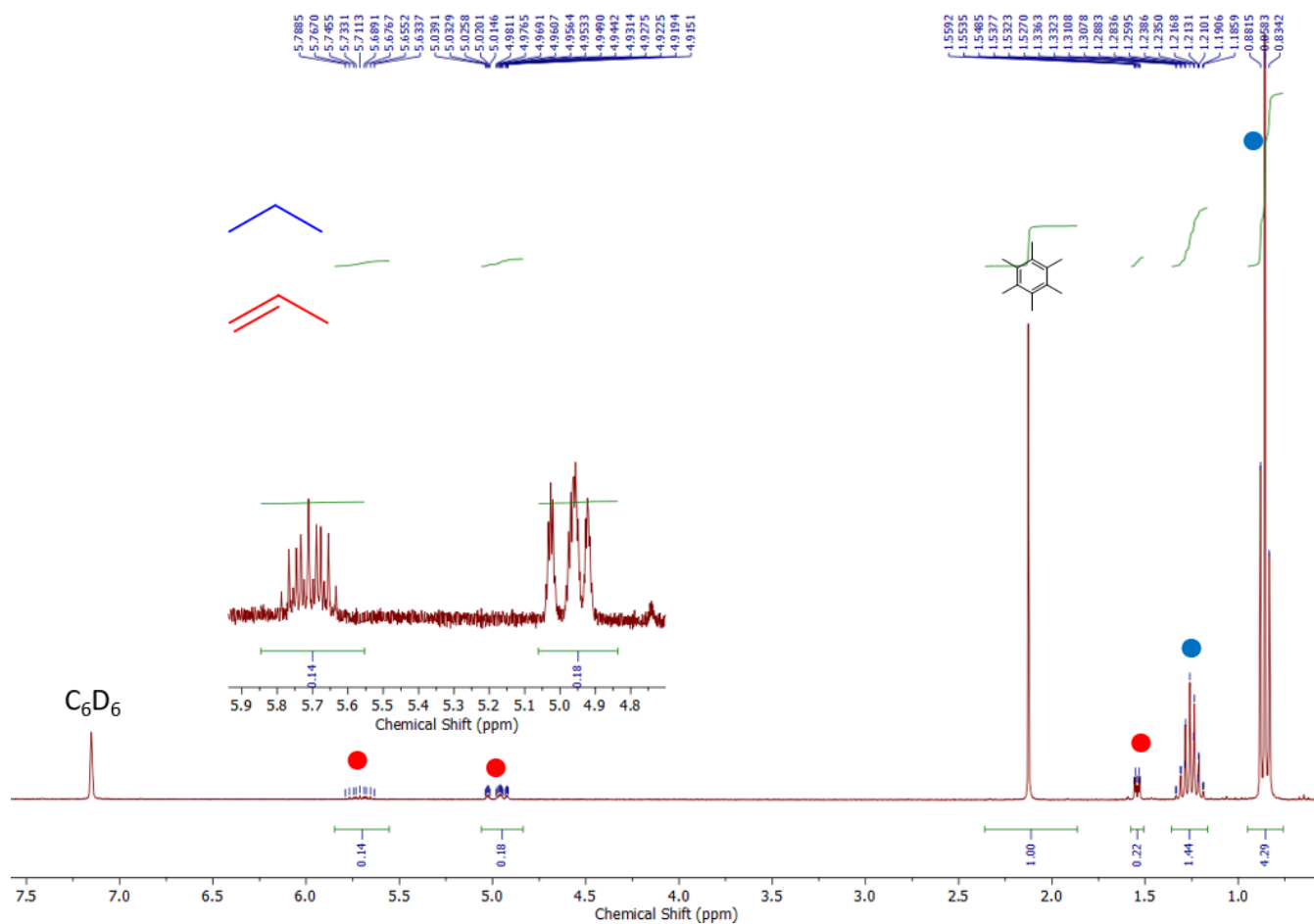


Figure 68. ^1H NMR (benzene- d_6 , rt) spectrum after the hydrogenation of propylene.

4.5.3 Parahydrogen induced polarization

Reaction of **12 with $p\text{-H}_2$.** A standard NMR tube was charged with a solution of **11** in pentane. The tube was connected with a Schlenk line via rubber septum and the solvent was removed in *vacuo*. The solid residual was sublimized by heat gun under dynamic vacuum with color change from purple (**11**) to orange (**12**). The NMR tube was then charged with C_6D_6 in Glovebox. The resulting solution was measured by ^1H NMR spectroscopy. $p\text{-H}_2$ was bubbled for 10 s at 7 bar directly into the NMR tube via an automated console controlled delivery system.^[175] ^1H polarization was probed in a single-scan acquisition.

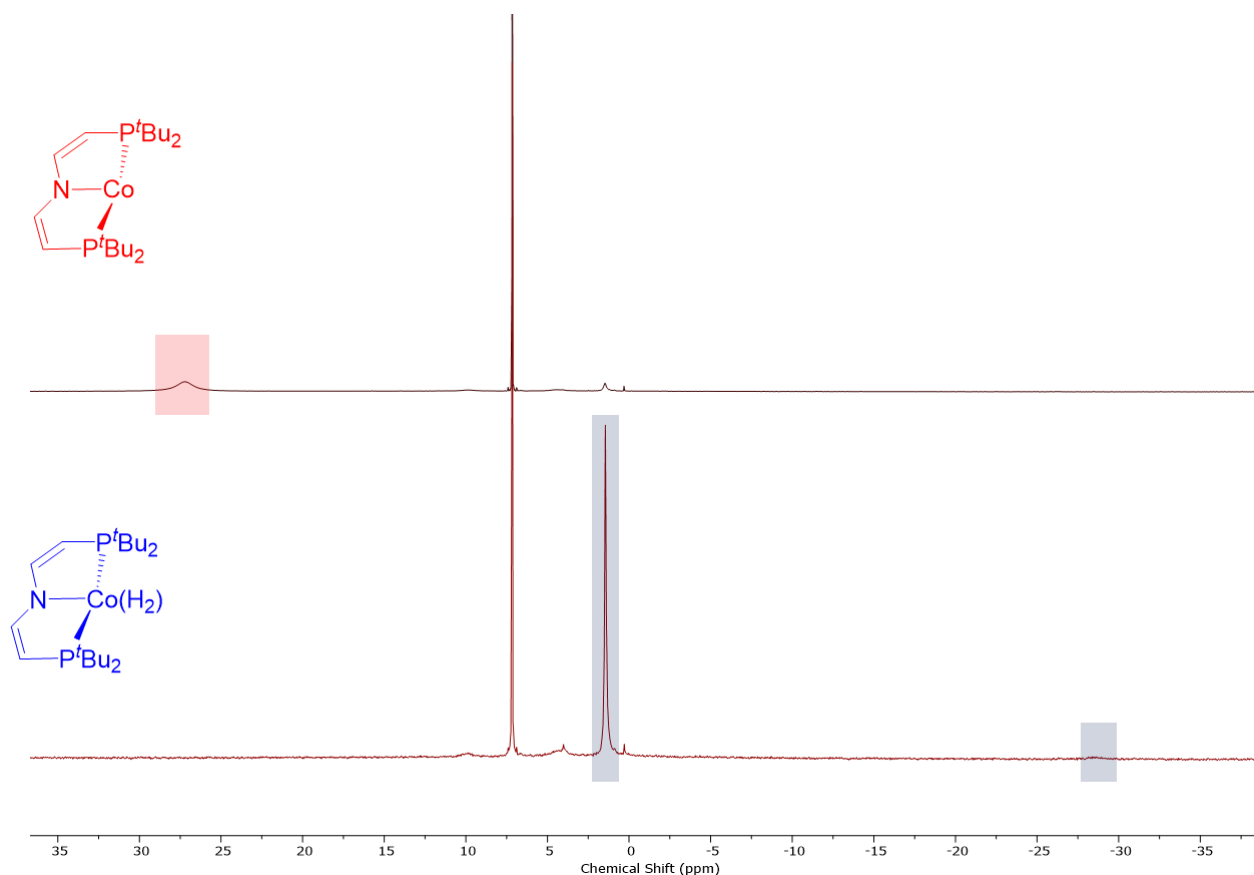


Figure 69: (Top) ¹H NMR spectrum of **12** in C₆D₆. (Bottom) ¹H NMR spectrum of formation of **17** upon bubbling *p*-H₂ (7 bar) into the solution of **12** in C₆D₆.

Hydrogenation of styrene by **12 using *p*-H₂.** A standard *J*-Young NMR tube was charged with a solution of **11** in pentane. The tube was connected with a Schlenk-line and the solvent was removed in *vacuo*. The solid residual was sublimized by heat gun under dynamic vacuum with color change from purple (**11**) to orange (**12**). The NMR tube was then charged with a solution of styrene in C₆D₆ in Glovebox. The resulting solution was degassed in *vacuo* via freeze-pump-thaw cycle and measured by ¹H NMR spectroscopy. Upon addition of *p*-H₂ (1 bar) into the tube, the reaction was immediately measured by ¹H NMR spectroscopy in a single-scan acquisition.

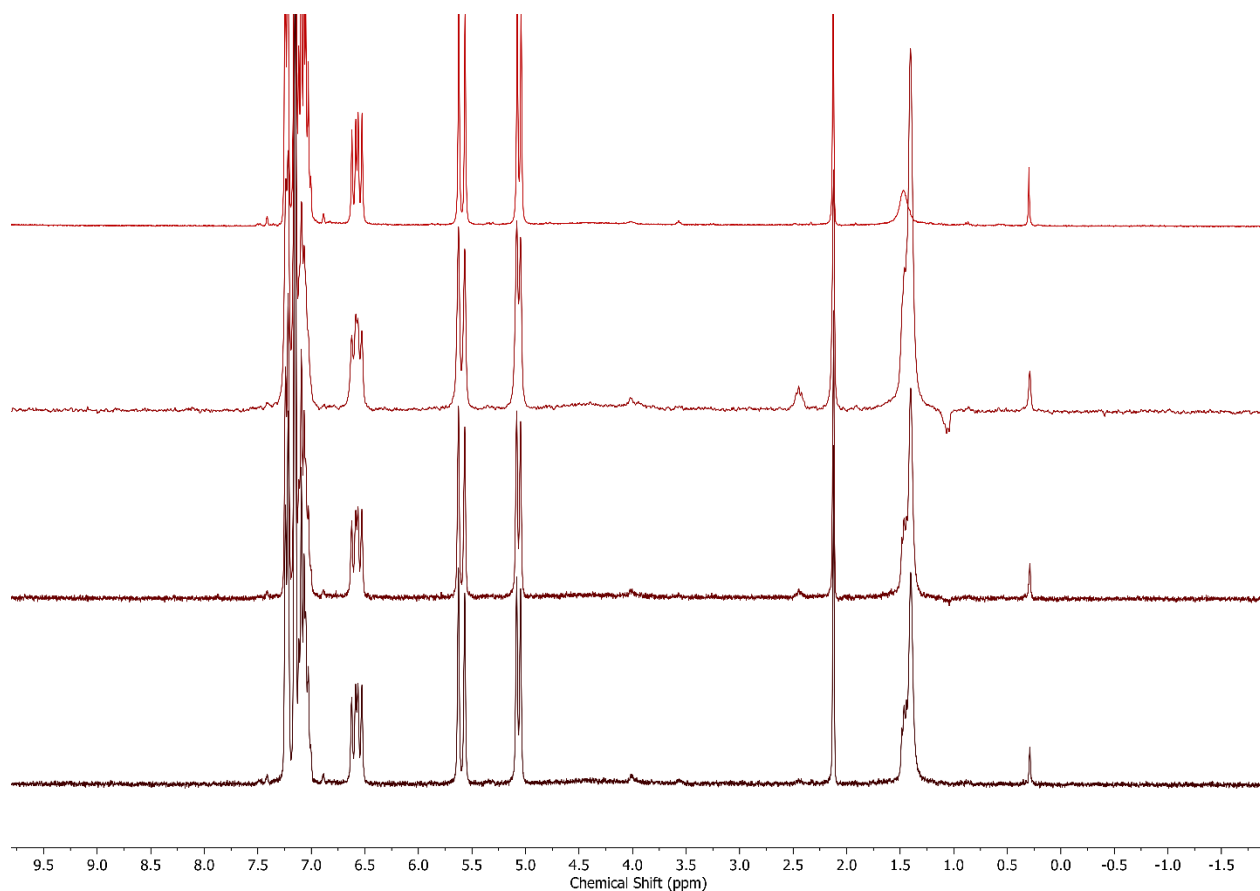
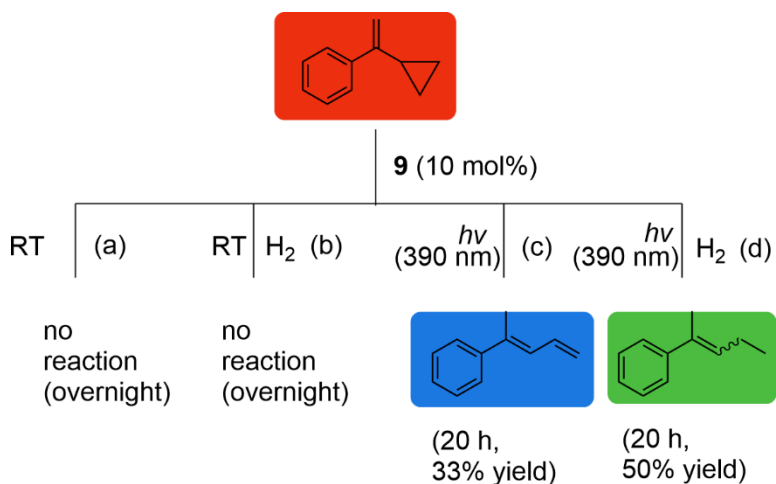


Figure 70: ^1H NMR spectra of styrene hydrogenation by **12** in C_6D_6 (from top to bottom: before $p\text{-H}_2$ addition, 1 s after addition of $p\text{-H}_2$, 5 s after addition of $p\text{-H}_2$, 8 s after addition of $p\text{-H}_2$).

Hydrogenation of α -cyclopropylstyrene by **12 using $p\text{-H}_2$.** A standard NMR tube was charged with a solution of **11** in pentane. The tube was connected with a Schlenk line via rubber septum and the solvent was removed in *vacuo*. The solid residual was sublimized by heat gun under dynamic vacuum with color change from purple (**11**) to orange (**12**). The NMR tube was then charged with a solution of α -cyclopropylstyrene in C_6D_6 in Glovebox. The resulting solution was measured by ^1H NMR spectroscopy. $p\text{-H}_2$ was bubbled for 10 s at 7 bar directly into the NMR tube via an automated console controlled delivery system. ^1H polarization was probed in a single-scan acquisition.

4.5.4 Radical clock experiments

For the radical clock experiments, complex **9** (2 mg, 4.8 μmol , 1 eq.) and hexamethylbenzene (2 mg, 12.3 μmol , 2.5 eq.) as an internal standard were dissolved in C_6D_6 (0.45 mL) in a *J*-Young NMR tube and (1-cyclopropylvinyl)benzene (7.2 μL , 48 μmol , 10 eq.) was added. The NMR tube was degassed by a freeze-pump-thaw cycle and either stirred at room temperature for 20 h (a), or refilled with H_2 (1 bar) and stirred at room temperature for 20 h (b), or photolyzed at 390 nm (LED) for 20 h at room temperature (c), or refilled with H_2 (1 bar) and photolyzed at 390 nm (LED) for 20 h at room temperature (d). The conversion and selectivity of was determined by ^1H NMR spectroscopy.



Scheme 43: Hydrogenation of (1-cyclopropylvinyl)benzene by **9** under different conditions

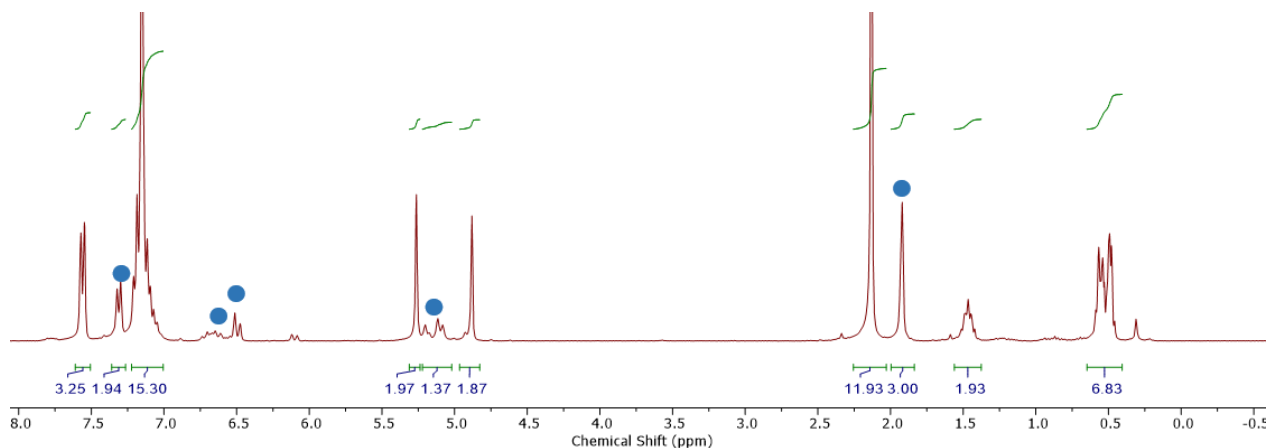


Figure 71: ^1H NMR spectrum after photolysis of (1-cyclopropylvinyl)benzene and **9** (10 mol%) *in vacuo* in C_6D_6 (Experiment c in Scheme 34).

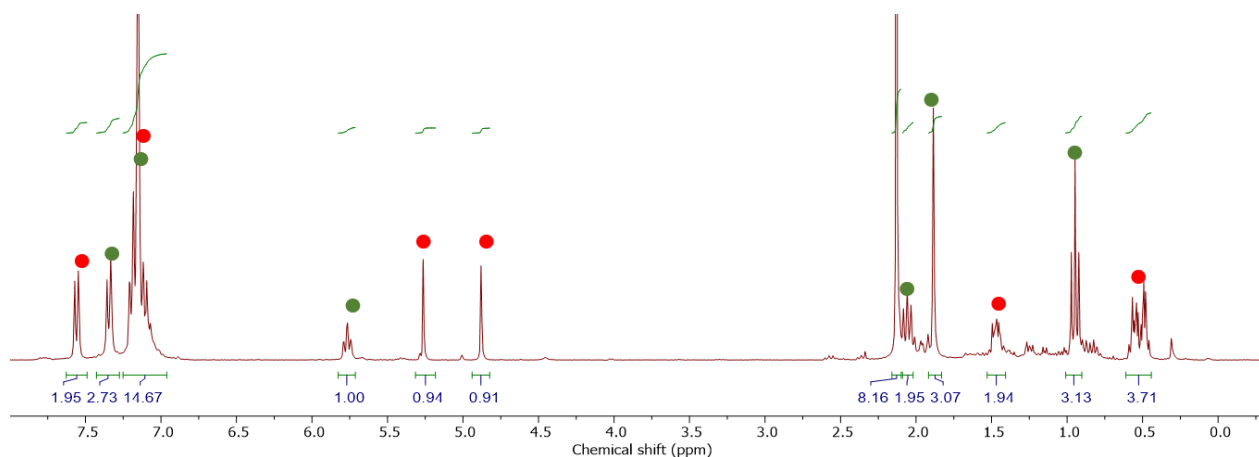
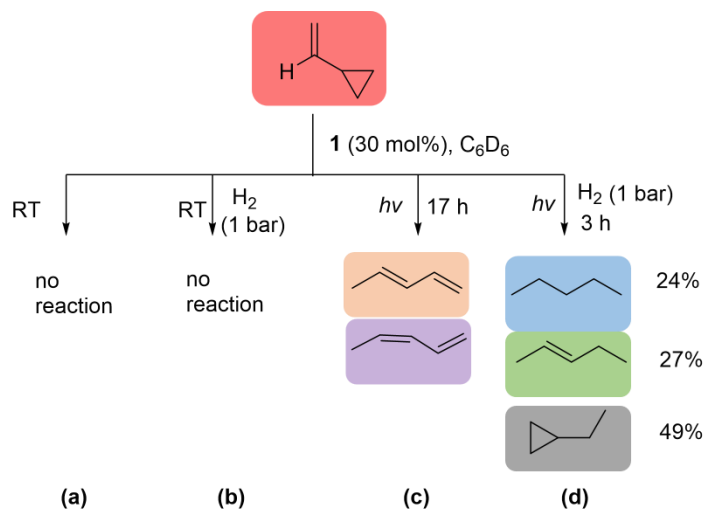


Figure 72: ^1H NMR spectrum after photolysis of (1-cyclopropylvinyl)benzene and **9** (10 mol%) under H_2 (1 bar) in C_6D_6 (Experiment d in Scheme 34)

For the radical clock experiments, complex **9** (1 mg, 2.4 μmol , 1 eq.) were dissolved in C_6D_6 (0.45 mL) in a *J*-Young NMR tube and 30 μL solution of vinyl cyclopropane (0.16 mM, 4.8 μmol , 3.3 eq.) was added. The NMR tube was degassed by a freeze-pump-thaw cycle and either stirred overnight at room temperature (a) or refilled with H_2 (1 bar) and stirred overnight at room temperature (b), or photolyzed at 390 nm (LED) for 17 h at room temperature (c) or refilled with H_2 (1 bar) and photolyzed at 390 nm (LED) for 3 h at room temperature (d). The yield and selectivity were determined by ^1H NMR spectroscopy.



Scheme 44: Hydrogenation of vinyl cyclopropane by **9** under different conditions.

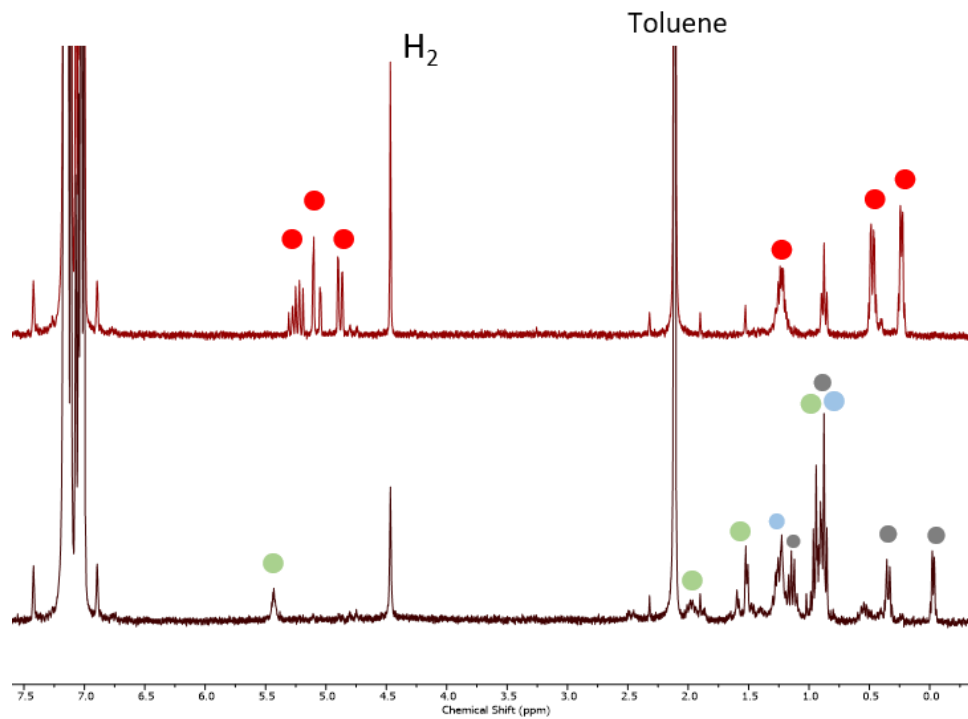


Figure 73: ^1H NMR spectra of vinyl cyclopropane and **9** (30 mol%) under H₂ (1 bar) in C₆D₆ (top) before photolysis and (bottom) after 17 h photolysis.

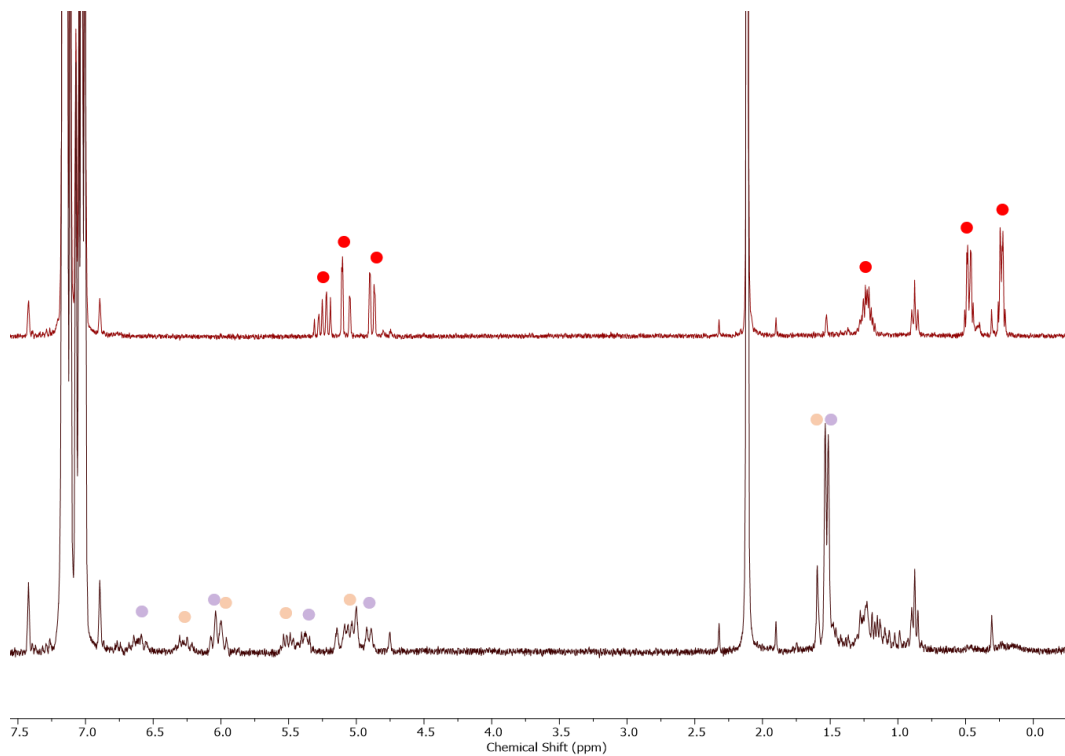
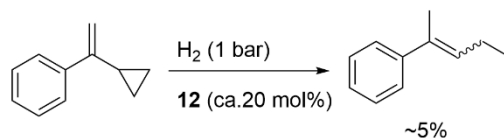


Figure 74: ^1H NMR spectra of vinyl cyclopropane and **9** (30 mol%) in vacuo in C₆D₆ (top) before photolysis and (bottom) after 17 h photolysis.

by ^1H NMR spectroscopy, degassed by one freeze-pump-thaw cycle and set under H_2 (1 bar) after warming to room temperature. The yield and selectivity of was determined by ^1H NMR spectroscopy after 20 h stirring.



Scheme 46: Hydrogenation of 1-cyclopropylvinylbenzene by **12** under standard conditions.

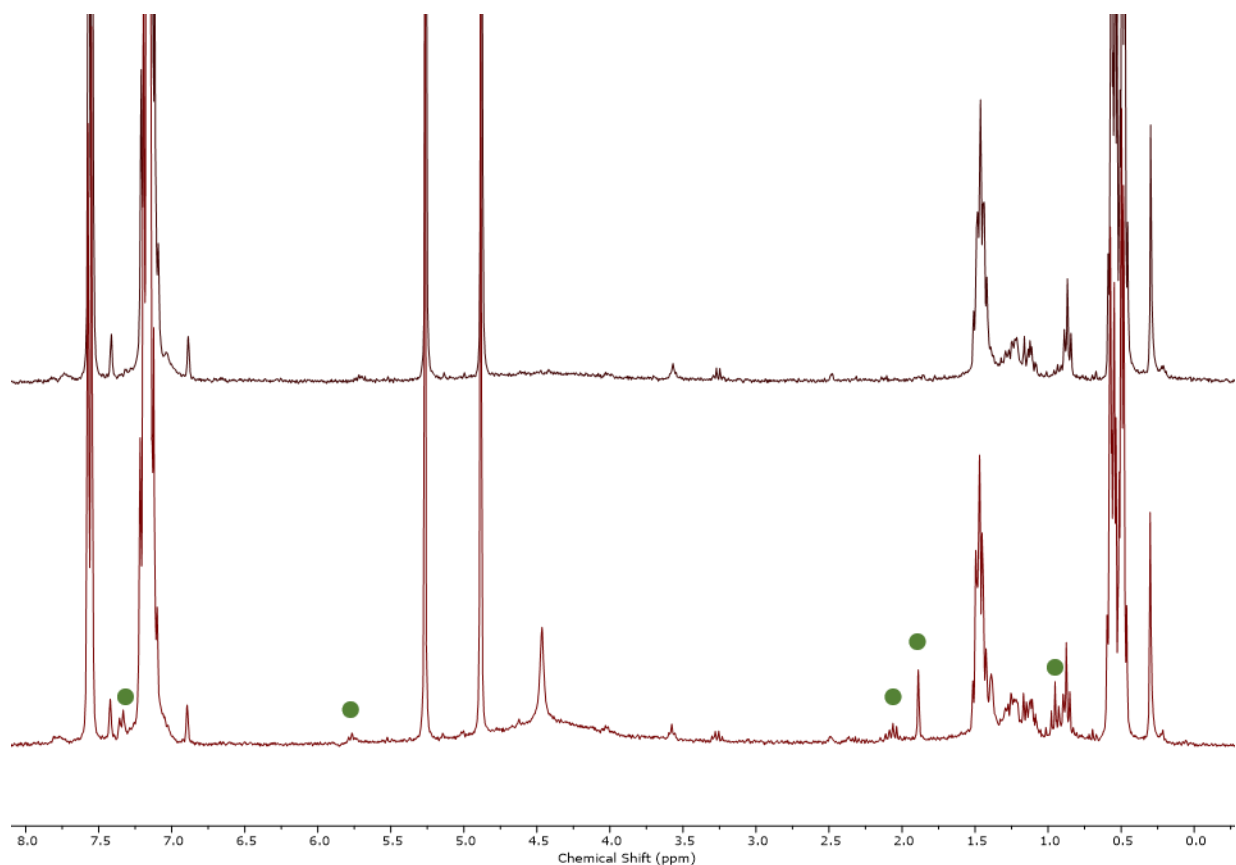


Figure 76: ^1H NMR spectra of (1-cyclopropylvinyl)benzene and **12** in C_6D_6 (top) before addition of H_2 and (bottom) after 20 h stirring under 1 bar H_2 . (green circles • denote the ring-opening product)

4.5.5 Hammett Plot

Hammett analyses were performed by competition experiments of styrene and *p*-X-styrene. σ parameters were taken from Hansch and Leo.^[28] To a solution of **9** (2 mg, 4.8 μmol , 1 eq.) in C_6D_6 (0.45 mL), styrene (10 eq.) and the respective *para*-substituted styrene (10 eq.) were added. The

reaction mixture was degassed, followed by addition of H₂ gas (1 bar). The resulting mixture was photolyzed (390 nm LED) for 3 h at room temperature. The ratio of formed ethylbenzene and *para*-substituted ethylbenzene was determined from a ¹H NMR spectrum.

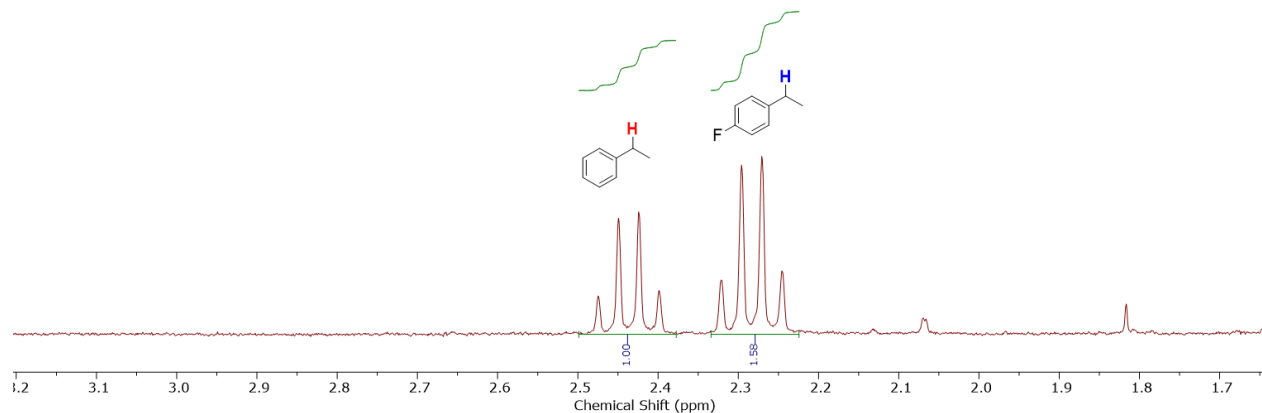


Figure 77: ¹H NMR spectrum of hydrogenation of styrene/*p*-fluorostyrene (1:1) by **9** in C₆D₆ under H₂ atmosphere (1 bar).

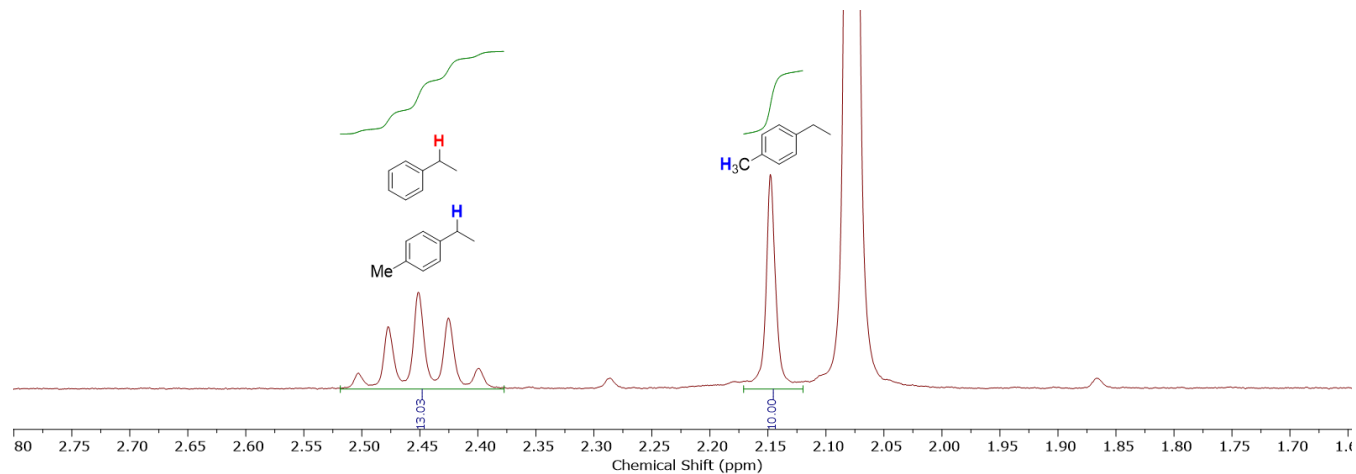


Figure 78: ¹H NMR spectrum of hydrogenation of styrene/*p*-methylstyrene (1:1) by **9** in C₆D₆ under H₂ atmosphere (1 bar).

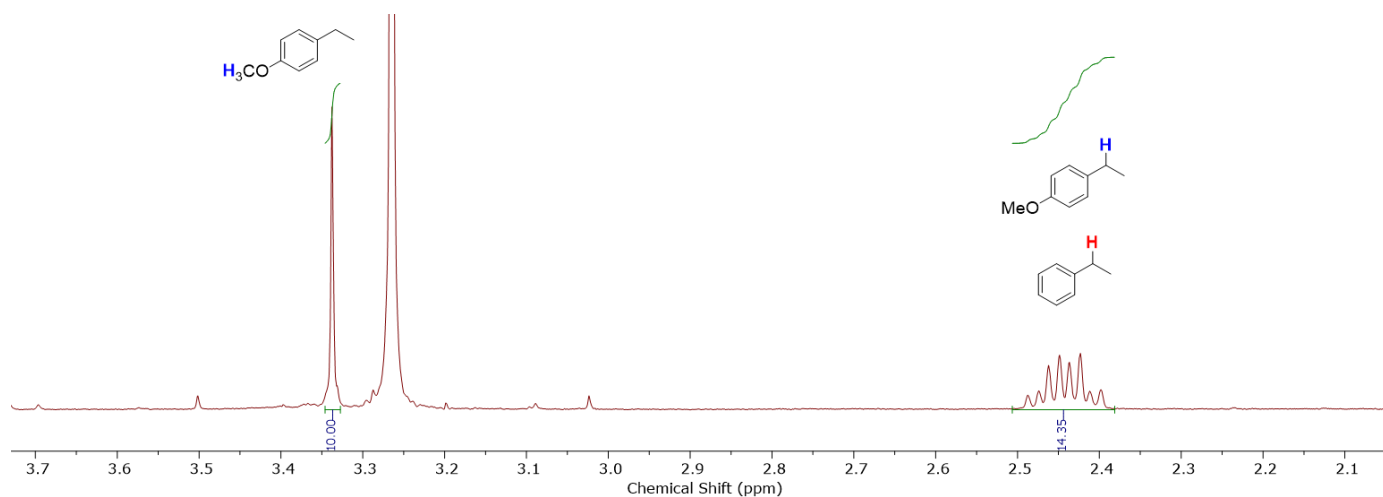


Figure 79: ¹H NMR spectrum of hydrogenation of styrene/p-methoxystyrene (1:1) by **9** in C₆D₆ under H₂ atmosphere (1 bar).

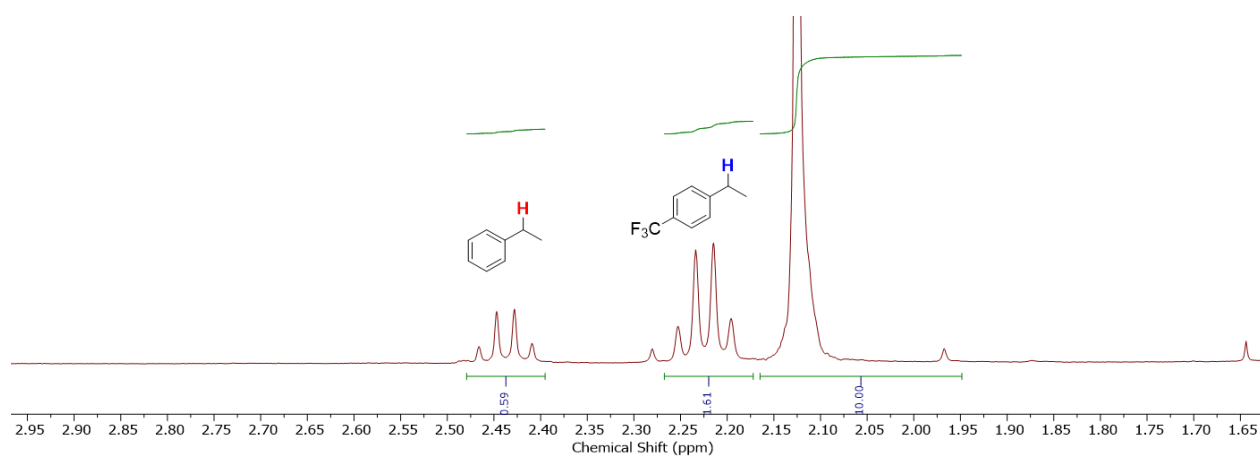


Figure 80: ¹H NMR spectrum of hydrogenation of styrene/p-trifluoromethylstyrene (1:1) by **9** in C₆D₆ under H₂ atmosphere (1 bar).

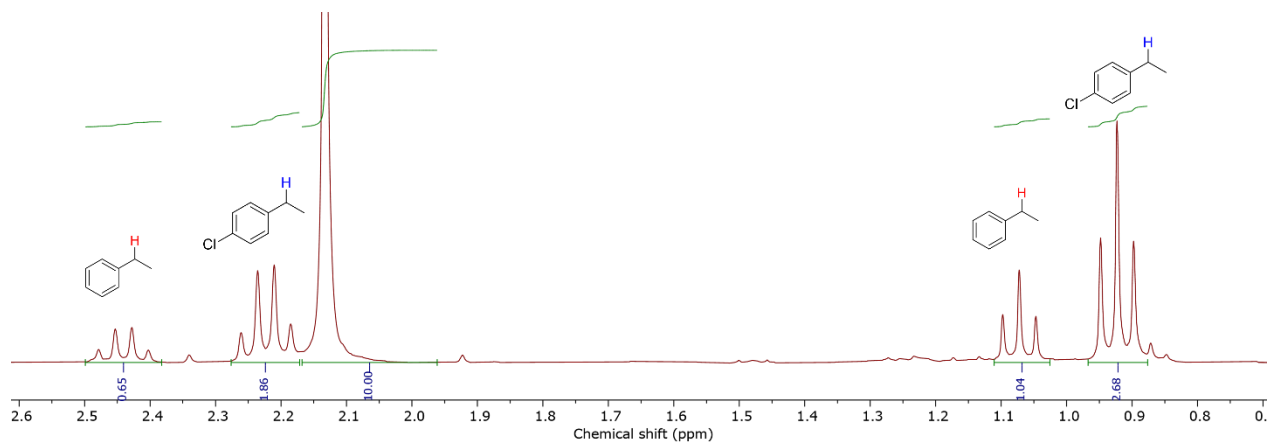


Figure 81: ^1H NMR spectrum of hydrogenation of styrene/p-chloromethylstyrene (1:1) by **9** in C_6D_6 under H_2 atmosphere (1 bar).

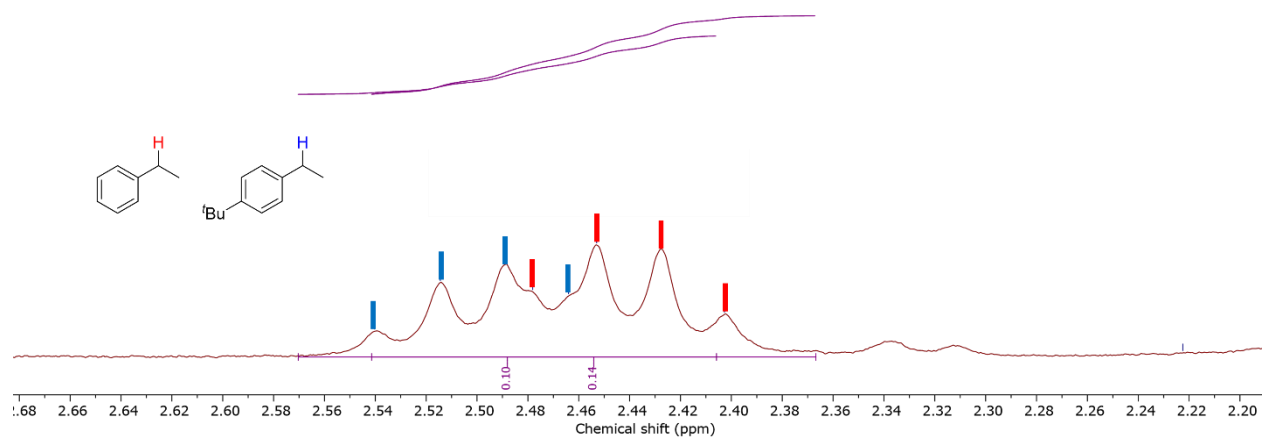


Figure 82: ^1H NMR spectrum of hydrogenation of styrene/p-tert-butylstyrene (1:1) by **9** in C_6D_6 under H_2 atmosphere (1 bar).

4.5.6 Control reactions

4.5.6.1 Radical clock experiments

For the radical clock experiments, complex **9** (2 mg, 4.8 μmol , 10 mol%) and hexamethylbenzene (2 mg, 12.3 μmol , 2.5 eq.) as an internal standard were dissolved in C_6D_6 (0.45 mL) in a J-Young NMR tube and (1-cyclopropylvinyl)benzene (7.2 μL , 48 μmol , 10 eq.) was added. The NMR tube was degassed by a freeze-pump-thaw cycle and either stirred at room temperature for 20 h (a) or refilled with H_2 (1 bar) and stirred at room temperature for 20 h (b), or photolyzed at 390 nm (LED) for 20 h at room temperature (c) or refilled with H_2 (1 bar) and photolyzed at 390 nm (LED) for 20 h at room temperature (d). The conversion and selectivity of was determined by ^1H NMR spectroscopy.

4.5.6.2 Hydrogenation of styrene with D_2

Complex **9** (2 mg, 4.8 μmol , 10 mol%) was dissolved in C_6D_6 (0.45 mL) in a J-Young NMR tube and the substrate (48 μmol , 10 eq.) was added. The NMR tube was degassed by one freeze-pump-thaw cycle and refilled with D_2 (1 bar) after warming to room temperature. The resulting solution was photolyzed at 390 nm (LED) for 15 h at room temperature and examined by ^1H and ^2H NMR spectroscopy.

4.5.6.3 Photolysis of **19** under H_2

Complex **19** (2 mg, 3.85 μmol) was dissolved in C_6D_6 in a J-Young NMR tube. The NMR tube was degassed by one freeze-pump-thaw cycle and refilled with H_2 (1 bar) after warming to room temperature. The resulting solution was photolyzed at 390 nm (LED) for 20 min at room temperature and examined by ^1H NMR spectroscopy.

4.5.6.4 Photolysis of **19** in vacuo.

Complex **19** (2 mg, 3.85 μmol) was dissolved in C_6D_6 in a J-Young NMR tube. The NMR tube was degassed by one freeze-pump-thaw cycle, photolyzed at 390 nm (LED) for 20 min at room temperature and examined by ^1H NMR spectroscopy.

4.5.6.5 Photolysis of **19** under D_2

Complex **19** (2 mg, 3.85 μmol) was dissolved in C_6D_6 in a J-Young NMR tube. The NMR tube was degassed by one freeze-pump-thaw cycle and refilled with D_2 (1 bar) after warming to room temperature. The solution was photolyzed at 390 nm (LED) for 90 min at room temperature and examined by ^2H NMR spectroscopy.

4.5.6.6 Styrene hydrogenation with **9** and photolytic activation

A J-Young NMR tube was charged with complex **9** (2 mg, 4.8 μmol , 1 eq.), styrene (5.5 μL , 48 μmol , 10 eq.) and hexamethylbenzene (1.2 mg, 7.4 μmol , 1.6 eq.). The mixture was dissolved in benzene- d_6 (0.5 mL). The NMR tube was degassed by freeze-pump-thaw and refilled with H_2 (1 bar) after warming to room temperature. The mixture was activated by photolysis (390 nm LED) for 1 h and then monitored by ^1H NMR spectroscopy without further photolysis.

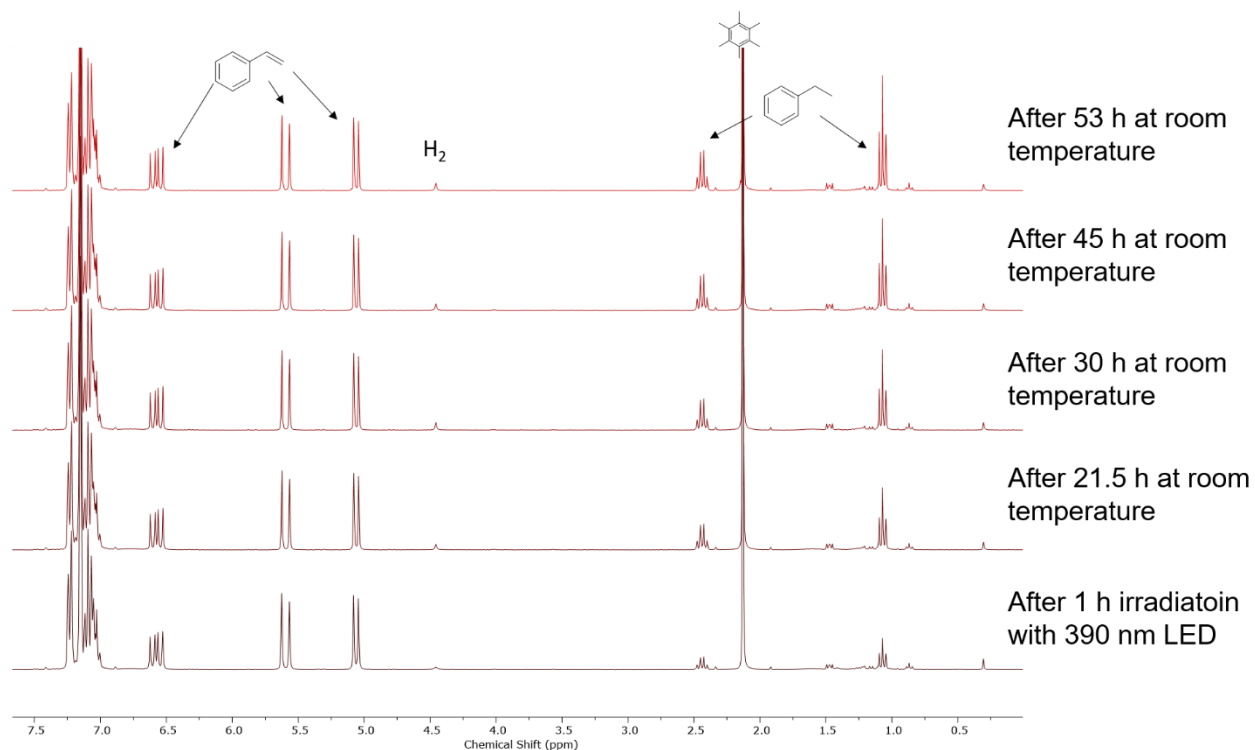


Figure 83: ^1H NMR spectra of styrene hydrogenation with **9** after activation by photolysis for 1 h.

4.5.6.7 Styrene hydrogenation catalyzed by **12**

12 was obtained by fresh sublimation **11** (1 mg, 2.3 μmol , 1 eq.) in a dynamic vacuum in a J-Young NMR tube and a solution of styrene (5.5 μL , 48 μmol , 20 eq.) and hexamethylbenzene (0.6 mg, 3.7 μmol , 1.6 eq.). Benzene- d_6 (0.5 mL) was trap-to-trap transferred into the NMR tube. The reaction mixture was first examined by ^1H NMR spectroscopy, degassed by one freeze-pump-thaw cycle and set under H_2 (1 bar) after warming to room temperature. The reaction progress was monitored by ^1H NMR spectroscopy over 20 h.

4.5.6.8 Styrene hydrogenation catalyzed by **9 with 1 mol% and 5 mol% catalyst loading**

Complex **9** (0.4 mg, 0.96 μmol , 1 mol% or 2.0 mg, 4.8 μmol , 5 mol%), styrene (11 μL , 96 μmol) and hexamethylbenzene (1.2 mg, 7.4 μmol , 0.88 eq.) as internal standard are dissolved in C_6D_6 (0.45 mL). The NMR tube is degassed by one freeze-pump-thaw cycle and 1 bar of hydrogen gas is added into the reaction mixture after warming to room temperature. The resulting solution is then photolyzed at 390 nm (LED) for 3 h, while the temperature is kept at room temperature using a water bath. The conversion and yield are determined by ^1H NMR spectroscopy.

4.6 Crystallographic Data

4.6.1 [CoCH₂SiMe₃(L¹)] (1)

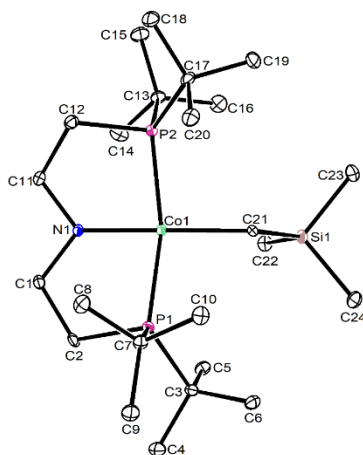


Figure 84: Thermal ellipsoid plot of **1** with the anisotropic displacement parameters drawn at the 50% probability level. The asymmetric unit contains one complex molecule and one disordered BARF anion. One disordered CF₃ group was refined in three different positions with population of 0.316(8), 0.608(7) and 0.077(5) using PART/SUMP commands and some restraints (SADI, RIGU). Two other disordered CF₃ groups were refined in two different positions with population of 0.574(9) and 0.722(5) on their main domains using PART commands and some restraints (SADI, RIGU). The Co-H hydrogen atom was found from the residual density map and isotropically refined. The N-H hydrogen atom was calculated using AFIX 13 command.

Table 5: Crystal data and structure refinement for **1**.

Identification code	t1_a
Empirical formula	C ₂₄ H ₅₅ CoNP ₂ Si
Formula weight	506.65
Temperature/K	100.00
Crystal system	triclinic
Space group	P-1
a/Å	11.1748(3)
b/Å	11.6889(4)

c/Å	12.6937(4)
α /°	65.266(2)
β /°	72.390(2)
γ /°	88.260(2)
Volume/Å ³	1426.49(8)
Z	2
ρ_{calc} /cm ³	1.180
μ /mm ⁻¹	0.767
F(000)	554.0
Crystal size/mm ³	0.187 × 0.156 × 0.088
Radiation	MoK α (λ = 0.71073)
2 θ range for data collection/°	3.728 to 50.05
Index ranges	-13 ≤ h ≤ 13, -13 ≤ k ≤ 13, -15 ≤ l ≤ 15
Reflections collected	32642
Independent reflections	5042 [Rint = 0.1165, Rsigma = 0.0697]
Data/restraints/parameters	5042/0/285
Goodness-of-fit on F ²	1.075
Final R indexes [$I \geq 2\sigma(I)$]	R1 = 0.0418, wR2 = 0.0928
Final R indexes [all data]	R1 = 0.0627, wR2 = 0.1034
Largest diff. peak/hole / e Å ⁻³	0.39/-0.46

4.6.2 [CoCH₂SiMe₃(L²)] (2)

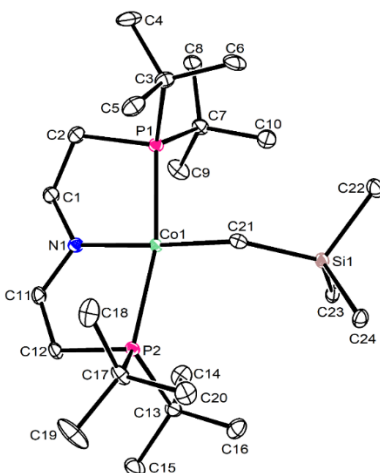


Figure 85: Thermal ellipsoid plot of **2** with the anisotropic displacement parameters drawn at the 50% probability level. The asymmetric unit contains one complex molecule and one disordered BARF anion. One disordered CF₃ group was refined in three different positions with population of 0.316(8), 0.608(7) and 0.077(5) using PART/SUMP commands and some restraints (SADI, RIGU). Two other disordered CF₃ groups were refined in two different positions with population of 0.574(9) and 0.722(5) on their main domains using PART commands and some restraints (SADI, RIGU). The Co-H hydrogen atom was found from the residual density map and isotropically refined. The N-H hydrogen atom was calculated using AFIX 13 command.

Table 6: Crystal data and structure refinement for **2**.

Identification code	T1_a
Empirical formula	C ₄ H _{8.83} Co _{0.17} N _{0.17} P _{0.33} Si _{0.17}
Formula weight	84.11
Temperature/K	100.00
Crystal system	triclinic
Space group	P-1
<i>a</i> /Å	8.3658(4)
<i>b</i> /Å	11.3185(6)
<i>c</i> /Å	15.7714(9)
<i>α</i> /°	94.717(4)
<i>β</i> /°	103.378(3)
<i>γ</i> /°	97.013(3)

Volume/Å ³	1432.50(13)
Z	12
$\rho_{\text{calc}}/\text{cm}^3$	1.170
μ/mm^{-1}	0.764
F(000)	550.0
Crystal size/mm ³	0.083 × 0.068 × 0.059
Radiation	MoK α ($\lambda = 0.71073$)
2 θ range for data collection/°	4.27 to 50.052
Index ranges	-9 ≤ h ≤ 9, -13 ≤ k ≤ 13, -18 ≤ l ≤ 18
Reflections collected	28417
Independent reflections	5052 [Rint = 0.1437, Rsigma = 0.0886]
Data/restraints/parameters	5052/0/285
Goodness-of-fit on F ²	1.012
Final R indexes [$I \geq 2\sigma(I)$]	R1 = 0.0520, wR2 = 0.0941
Final R indexes [all data]	R1 = 0.0816, wR2 = 0.1057
Largest diff. peak/hole / e Å ⁻³	0.34/-0.38

4.6.3 [CoCH₂SiMe₃(L¹H)] (3^{BARF})

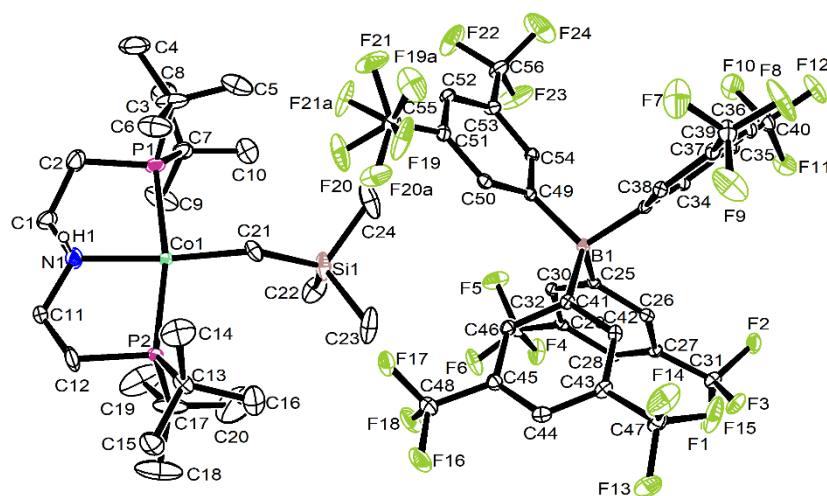


Figure 86: Thermal ellipsoid plot of 3^{BARF} with the anisotropic displacement parameters drawn at the 50% probability level. The asymmetric unit contains one complex molecule and one disordered BARF anion. One disordered CF₃ group was refined in three different positions with population of 0.316(8), 0.608(7) and 0.077(5) using PART/SUMP commands and some restraints (SADI, RIGU). Two other disordered CF₃ groups were refined in two different positions with population of 0.574(9) and 0.722(5) on their main domains using PART commands and some restraints (SADI, RIGU). The Co-H hydrogen atom was found from the residual density map and isotropically refined. The N-H hydrogen atom was calculated using AFIX 13 command.

Table 7: Crystal data and structure refinement for 3^{BARF} .

Identification code	t1
Empirical formula	C ₅₆ H ₆₈ BCoF ₂₄ NP ₂ Si
Formula weight	1370.88
Temperature/K	100.0
Crystal system	monoclinic
Space group	C2/c
a/Å	39.138(3)
b/Å	13.1275(9)
c/Å	26.413(2)
α/°	90
β/°	114.092(2)
γ/°	90
Volume/Å ³	12388.3(16)
Z	8
ρ _{calc} /cm ³	1.470
μ/mm ⁻¹	0.458
F(000)	5624.0
Crystal size/mm ³	0.134 × 0.108 × 0.084
Radiation	MoKα (λ = 0.71073)
2θ range for data collection/°	3.918 to 50.054
Index ranges	-46 ≤ h ≤ 46, -15 ≤ k ≤ 15, -31 ≤ l ≤ 31
Reflections collected	168495

Independent reflections	10945 [$R_{\text{int}} = 0.0845$, $R_{\text{sigma}} = 0.0291$]
Data/restraints/parameters	10945/6/826
Goodness-of-fit on F^2	1.037
Final R indexes [$I \geq 2\sigma(I)$]	$R_1 = 0.0782$, $wR_2 = 0.1830$
Final R indexes [all data]	$R_1 = 0.0893$, $wR_2 = 0.1909$
Largest diff. peak/hole / $e \text{ \AA}^{-3}$	1.38/-0.71

4.6.4 [CoH(L¹)] (6)

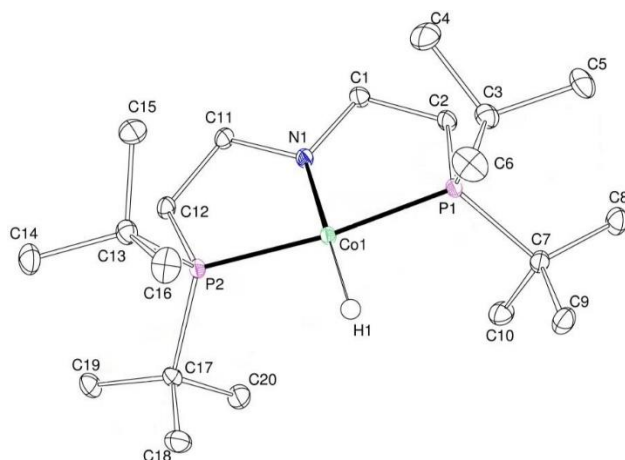


Figure 87: Thermal ellipsoid plot of **6** with the anisotropic displacement parameters drawn at the 50% probability level. The asymmetric unit contains one complex molecule. The Co-H hydrogen atom was found from the residual density map and isotropically refined.

Table 8: Crystal data and structure refinement for **6**.

Identification code	mo_SF_SR_040416_0m_a	
Empirical formula	C ₂₀ H ₄₅ Co N P ₂	
Formula weight	420.44	
Temperature	100(2) K	
Wavelength	0.71073 Å	
Crystal system	Monoclinic	
Space group	P2 ₁ /n	
Unit cell dimensions	a = 11.3810(6) Å	α = 90°
	b = 16.0594(9) Å	β = 114.016(2)°
	c = 13.9301(8) Å	γ = 90°
Volume	2325.6(2) Å ³	
Z	4	
Density (calculated)	1.201 Mg/m ³	
Absorption coefficient	0.879 mm ⁻¹	
F(000)	916	
Crystal size	0.145 x 0.100 x 0.086 mm ³	

Crystal shape and color	Block, clear dark orange-yellow	
Theta range for data collection	2.334 to 30.571°	
Index ranges	-16<=h<=16, -22<=k<=22, -19<=l<=19	
Reflections collected	118879	
Independent reflections	7105 [R(int) = 0.0567]	
Completeness to theta = 25.242°	100.0 %	
Max. and min. transmission	0.7461 and 0.7254	
Refinement method	Full-matrix least-squares on F ²	
Data / restraints / parameters	7105 / 0 / 233	
Goodness-of-fit on F ²	1.068	
Final R indices [I>2sigma(I)]	R1 = 0.0287,	wR2 = 0.0616
R indices (all data)	R1 = 0.0469,	wR2 = 0.0686
Largest diff. peak and hole	0.356 and -0.531 eÅ ⁻³	

4.6.5 [CoH(L³)] (9)

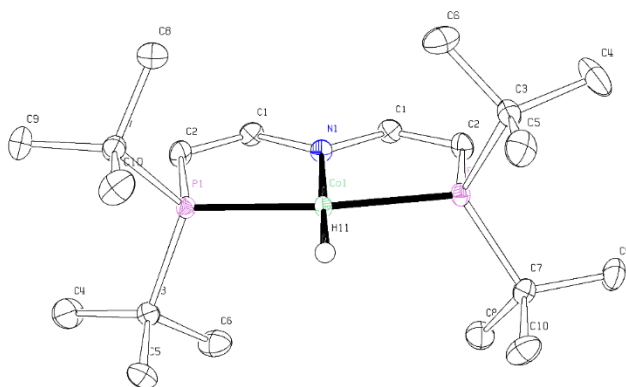


Figure 88: Thermal ellipsoid plot of **9** with the anisotropic displacement parameters drawn at the 50% probability level. The asymmetric unit contains one half of the complex molecule. The Co-H hydrogen atom was found from the residual density map and isotropically refined.

Table 9: Crystal data and structure refinement for **9**.

CCDC code	2078520
Empirical formula	C ₂₀ H ₄₁ CoNP ₂
Formula weight	416.41
Temperature	102(2) K

Wavelength	0.71073 Å	
Crystal system	Monoclinic	
Space group	C2/c	
Unit cell dimensions	a = 21.5332(12) Å	$\alpha = 90^\circ$
	b = 7.6684(4) Å	$\beta = 102.645(2)^\circ$
	c = 14.0778(8) Å	$\gamma = 90^\circ$
Volume	2268.2(2) Å ³	
Z	4	
Density (calculated)	1.219 Mg/m ³	
Absorption coefficient	0.900 mm ⁻¹	
F(000)	900	
Crystal size	0.238 x 0.124 x 0.058 mm ³	
Crystal shape and color	block	clear intense orange
Theta range for data collection	2.828 to 32.654°.	
Index ranges	-32<=h<=29, -11<=k<=11, -21<=l<=21	
Reflections collected	30702	
Independent reflections	4159 [R(int) = 0.0378]	
Completeness to theta = 25.242°	99.9 %	
Max. and min. transmission	0.7464 and 0.6983	
Refinement method	Full-matrix least-squares on F ²	
Data / restraints / parameters	4159 / 0 / 118	
Goodness-of-fit on F ²	1.050	
Final R indices [I>2sigma(I)]	R1 = 0.0280, wR2 = 0.0598	
R indices (all data)	R1 = 0.0410, wR2 = 0.0636	
Extinction coefficient	n/a	
Largest diff. peak and hole	0.373 and -0.451 eÅ ⁻³	

4.6.6 [CoN₂(L¹)] (10)

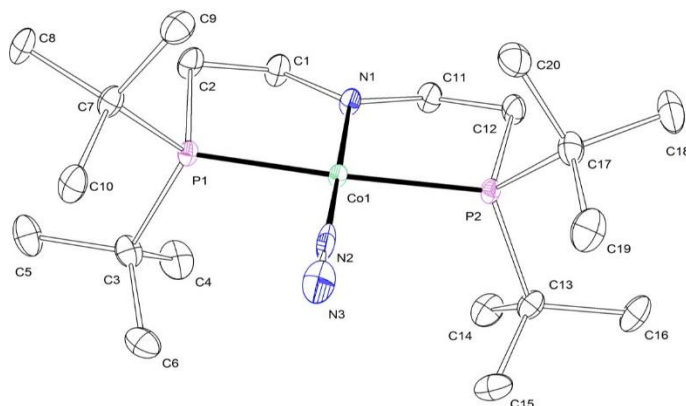


Figure 89: Thermal ellipsoid plot of **10** with the anisotropic displacement parameters drawn at the 50% probability level. The asymmetric unit contains one complex molecule.

Table 10: Crystal data and structure refinement for **10**.

Identification code	mo_CW_SR_170517_0m_a	
Empirical formula	C ₂₀ H ₄₄ CoN ₃ P ₂	
Formula weight	447.45	
Temperature	100(2) K	
Wavelength	0.71073 Å	
Crystal system	Monoclinic	
Space group	P2 ₁ /c	
Unit cell dimensions	a = 12.1339(7) Å	α = 90°
	b = 14.3485(8) Å	β = 104.627(2)°
	c = 14.3408(8) Å	γ = 90°
Volume	2415.9(2) Å ³	
Z	4	
Density (calculated)	1.230 Mg/m ³	
Absorption coefficient	0.852 mm ⁻¹	
F(000)	968	
Crystal size	0.482 x 0.193 x 0.133 mm ³	
Crystal shape and color	Block, clear dark red	
Theta range for data collection	2.241 to 28.367°	
Index ranges	-16 ≤ h ≤ 16, -19 ≤ k ≤ 19, -19 ≤ l ≤ 19	

Reflections collected	93705	
Independent reflections	6030 [R(int) = 0.1275]	
Completeness to theta = 25.242°	100.0 %	
Refinement method	Full-matrix least-squares on F ²	
Data / restraints / parameters	6030 / 0 / 247	
Goodness-of-fit on F ²	1.054	
Final R indices [I>2sigma(I)]	R1 = 0.0385,	wR2 = 0.0737
R indices (all data)	R1 = 0.0575,	wR2 = 0.0803
Largest diff. peak and hole	0.611 and -0.482 eÅ ⁻³	

4.6.7 [CoN₂(L³)] (11)

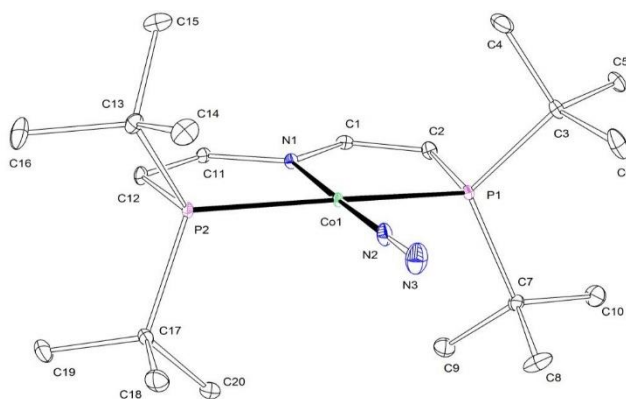


Figure 90: Thermal ellipsoid plot of **11** with the anisotropic displacement parameters drawn at the 50% probability level. The asymmetric unit contains one complex molecule.

Table 11: Crystal data and structure refinement for **11**.

CCDC code	2078519	
Empirical formula	C ₂₀ H ₄₀ CoN ₃ P ₂	
Formula weight	443.42	
Temperature	100(2) K	
Wavelength	0.71073 Å	
Crystal system	Monoclinic	
Space group	P21/c	
Unit cell dimensions	a = 7.8577(4) Å	α = 90°

	$b = 26.8870(13) \text{ \AA}$	$\beta = 107.711(2)^\circ$
	$c = 11.6697(6) \text{ \AA}$	$\gamma = 90^\circ$
Volume	2348.6(2) \AA^3	
Z	4	
Density (calculated)	1.254 Mg/m ³	
Absorption coefficient	0.876 mm ⁻¹	
F(000)	952	
Crystal size	0.449 x 0.341 x 0.267 mm ³	
Crystal shape and color	Block,	dark brown
Theta range for data collection	2.377 to 30.615°	
Index ranges	-11 ≤ h ≤ 11, -38 ≤ k ≤ 38, -16 ≤ l ≤ 16	
Reflections collected	97525	
Independent reflections	7204 [R(int) = 0.0913]	
Completeness to theta = 25.242°	100.0 %	
Refinement method	Full-matrix least-squares on F ²	
Data / restraints / parameters	7204 / 0 / 247	
Goodness-of-fit on F ²	1.084	
Final R indices [I > 2σ(I)]	R1 = 0.0466,	wR2 = 0.0854
R indices (all data)	R1 = 0.0689,	wR2 = 0.0915
Largest diff. peak and hole	0.579 and -0.477 e \AA^{-3}	

4.6.8 [CoH(L¹H)]BARF₄ (7^{BARF})

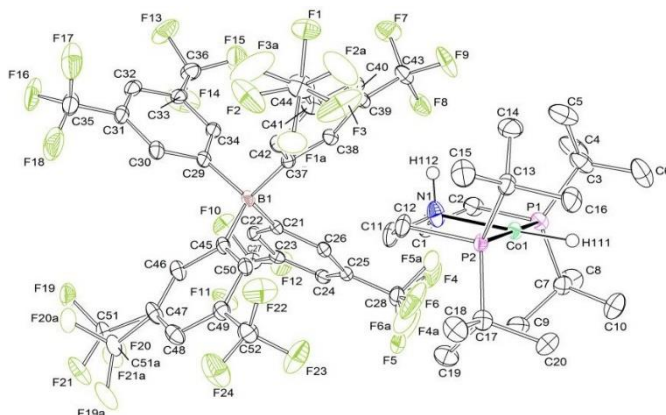


Figure 91: Thermal ellipsoid plot of **7^{BARF}** with the anisotropic displacement parameters drawn at the 50% probability level. The asymmetric unit contains one complex molecule and one disordered BARF anion. The disordered CF₃ groups were refined in two different positions with population of 0.840(2), 0.597(5) and 0.738(3) on their main domains using PART commands and some restraints and constraints (SADI, RIGU, EADP). The Co-H hydrogen atom was found from the residual density map and isotropically refined. The N-H hydrogen atom was calculated using AFIX 13 command.

Table 12: Crystal data and structure refinement for **7^{BARF}**.

Identification code	mo_CW_SR_030517_0m_a	
Empirical formula	C ₅₂ H ₅₈ BCoF ₂₄ NP ₂	
Formula weight	1284.67	
Temperature	100(2) K	
Wavelength	0.71073 Å	
Crystal system	Triclinic	
Space group	P-1	
Unit cell dimensions	a = 12.1384(4) Å	α = 85.717(2)°
	b = 15.1113(5) Å	β = 85.646(2)°
	c = 15.6111(5) Å	γ = 85.093(2)°
Volume	2838.06(16) Å ³	
Z	2	
Density (calculated)	1.503 Mg/m ³	
Absorption coefficient	0.474 mm ⁻¹	
F(000)	1310	

Crystal size	0.431 x 0.406 x 0.313 mm ³
Crystal shape and color	Block, clear intense yellow
Theta range for data collection	2.209 to 30.627°
Index ranges	-17<=h<=17, -21<=k<=21, -22<=l<=22
Reflections collected	219042
Independent reflections	17480 [R(int) = 0.0828]
Completeness to theta = 25.242°	99.9 %
Refinement method	Full-matrix least-squares on F ²
Data / restraints / parameters	17480 / 606 / 773
Goodness-of-fit on F ²	1.037
Final R indices [I>2sigma(I)]	R1 = 0.0529, wR2 = 0.1090
R indices (all data)	R1 = 0.0882, wR2 = 0.1268
Largest diff. peak and hole	1.264 and -0.780 eÅ ⁻³

4.6.9 [CoH(L¹H)]BF₄ (7^{BF4})

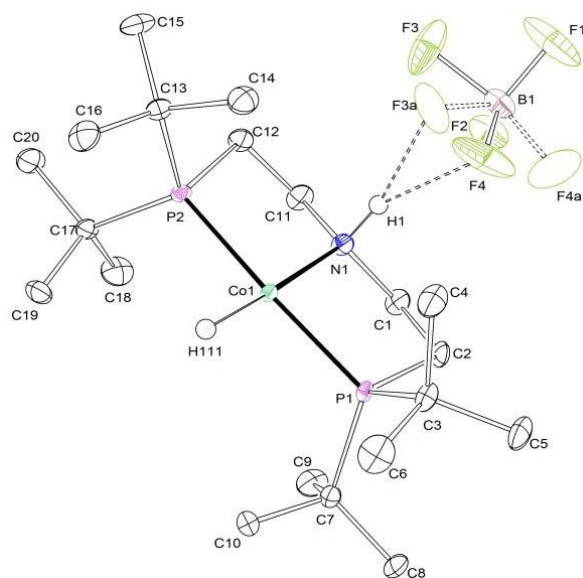


Figure 92: Thermal ellipsoid plot of **7^{BF4}** with the anisotropic displacement parameters drawn at the 50% probability level. The structure was refined as an inversion twin using the twin law -100 0-10 00-1 (BASF: 0.496(15)). The asymmetric unit contains one complex molecule and one disordered BF₄ anion. The disordered BF₄ anion was refined with population of 0.545(9) on the main domain. The Co–H hydrogen atom was found from the residual density map and constrained to 1.5 U_{eq} of the connected cobalt atom.

Table 13: Crystal data and structure refinement for **7^{BF4}**.

Identification code	mo_CW_SR_271016_0m_a	
Empirical formula	C ₂₀ H ₄₆ BCoF ₄ NP ₂	
Formula weight	508.26	
Temperature	101(2) K	
Wavelength	0.71073 Å	
Crystal system	Orthorhombic	
Space group	P212121	
Unit cell dimensions	a = 8.4311(3) Å	α = 90°
	b = 12.4415(4) Å	β = 90°
	c = 24.6820(8) Å	γ = 90°
Volume	2589.03(15) Å ³	
Z	4	
Density (calculated)	1.304 Mg/m ³	
Absorption coefficient	0.822 mm ⁻¹	
F(000)	1084	
Crystal size	0.181 x 0.088 x 0.063 mm ³	
Crystal shape and color	Block, clear intense yellow	
Theta range for data collection	1.833 to 30.574°	
Index ranges	-12 ≤ h ≤ 12, -17 ≤ k ≤ 17, -35 ≤ l ≤ 35	
Reflections collected	94801	

4.6.10 [Co(L¹H)]BArF₄ (5^{BArF})

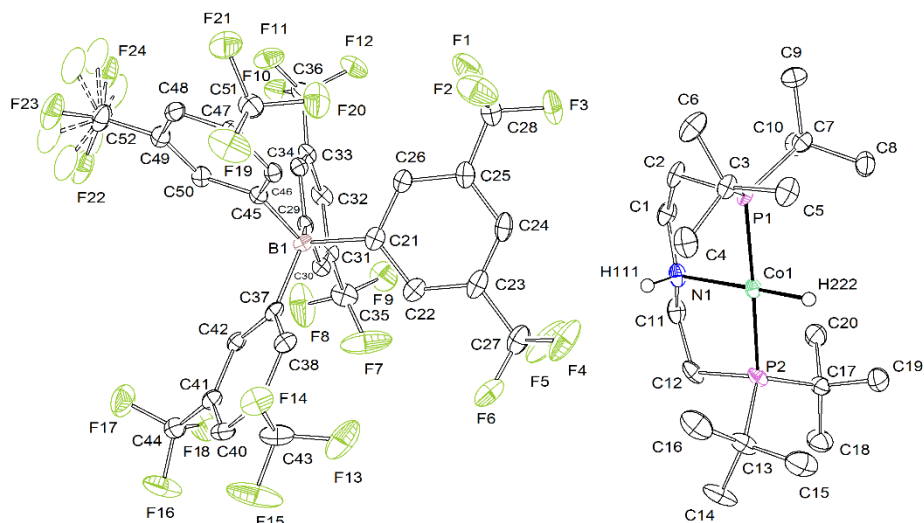


Figure 93: Thermal ellipsoid plot of **5^{BArF}** with the anisotropic displacement parameters drawn at the 50% probability level. The asymmetric unit contains one complex molecule and one disordered counter ion. The N-H and Co-H hydrogen atoms were found from the residual density map and isotropically refined. One disordered CF₃ group of the counter ion was refined in three different positions with population of 0.45(5), 0.33(4) and 0.21(0) using PART/SUMP commands and constraints (EADP).

Table 14: Crystal data and structure refinement for **5^{BArF}**.

Identification code	MO_SS_09102020 (SSA310)
Empirical formula	C ₅₂ H ₅₈ BCoF ₂₄ NP ₂
Formula weight	1284.67
Temperature	100(2) K
Wavelength	0.71073 Å
Crystal system	Triclinic
Space group	P-1
Unit cell dimensions	a = 12.1563(8) Å α = 85.656(3)° b = 15.1562(10) Å β = 86.034(3)° c = 15.5768(10) Å γ = 85.133(4)°
Volume	2845.7(3) Å ³
Z	2
Density (calculated)	1.499 Mg/m ³
Absorption coefficient	0.473 mm ⁻¹

F(000)	1310
Crystal size	0.268 x 0.268 x 0.092 mm ³
Crystal shape and color	Plate, clear intense green
Theta range for data collection	2.201 to 25.448°.
Index ranges	-14<=h<=14, -18<=k<=18, -18<=l<=18
Reflections collected	160955
Independent reflections	10411 [R(int) = 0.0634]
Completeness to theta = 25.242°	99.0 %
Refinement method	Full-matrix least-squares on F ²
Data / restraints / parameters	10411 / 1 / 759
Goodness-of-fit on F ²	1.028
Final R indices [I>2sigma(I)]	R1 = 0.0531, wR2 = 0.1192
R indices (all data)	R1 = 0.0679, wR2 = 0.1318
Largest diff. peak and hole	1.815 and -0.985 e ^Å -3

4.6.11 [CoH(L²H)]BARF₄ (**13**^{BARF})

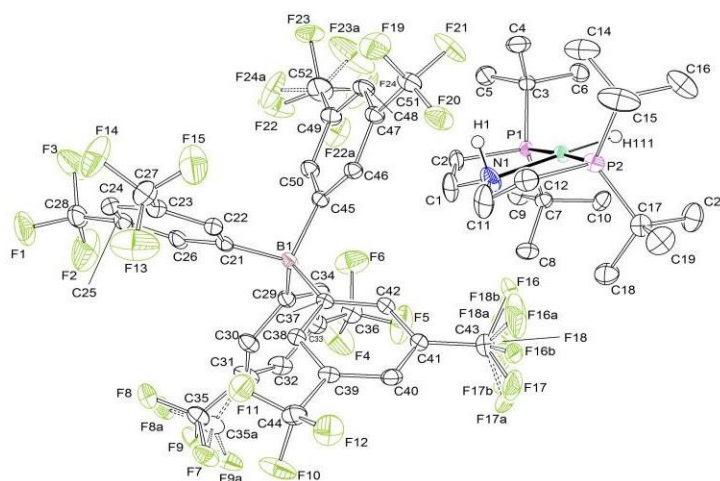


Figure 94: Thermal ellipsoid plot of **13**^{BARF} with the anisotropic displacement parameters drawn at the 50% probability level. The asymmetric unit contains one complex molecule and one disordered BARF anion. One disordered CF₃ group was refined in three different positions with population of 0.316(8), 0.608(7) and 0.077(5) using PART/SUMP commands and some restraints (SADI, RIGU). Two other disordered CF₃ groups were refined in two different positions with population of 0.574(9) and 0.722(5) on their main domains using PART commands and some restraints (SADI, RIGU). The Co-H hydrogen atom was found from the

residual density map and isotropically refined. The N-H hydrogen atom was calculated using AFIX 13 command.

Table 15: Crystal data and structure refinement for **13^{BARF}**.

Identification code	mo_CW_SR_250816_0m_a
Empirical formula	C ₅₂ H ₅₈ BCoF ₂₄ NP ₂
Formula weight	1284.67
Temperature	104(2) K
Wavelength	0.71073 Å
Crystal system	Triclinic
Space group	P-1
Unit cell dimensions	a = 12.1390(11) Å α = 85.651(3)° b = 15.1582(14) Å β = 85.267(3)° c = 15.6537(15) Å γ = 85.057(3)°
Volume	2853.0(5) Å ³
Z	2
Density (calculated)	1.495 Mg/m ³
Absorption coefficient	0.472 mm ⁻¹
F(000)	1310
Crystal size	0.508 x 0.418 x 0.308 mm ³
Crystal shape and color	Block, clear intense yellow
Theta range for data collection	2.214 to 28.379°
Index ranges	-16 ≤ h ≤ 16, -20 ≤ k ≤ 20, -20 ≤ l ≤ 20
Reflections collected	157697
Independent reflections	14229 [R(int) = 0.0488]
Completeness to theta = 25.242°	99.9 %
Max. and min. transmission	0.7457 and 0.6997
Refinement method	Full-matrix least-squares on F ²
Data / restraints / parameters	14229 / 590 / 859
Goodness-of-fit on F ²	1.061
Final R indices [I > 2σ(I)]	R1 = 0.0467, wR2 = 0.1032
R indices (all data)	R1 = 0.0640, wR2 = 0.1194

Largest diff. peak and hole

0.743 and -0.706 eÅ⁻³

4.6.12 [CoF(L³)] (18)

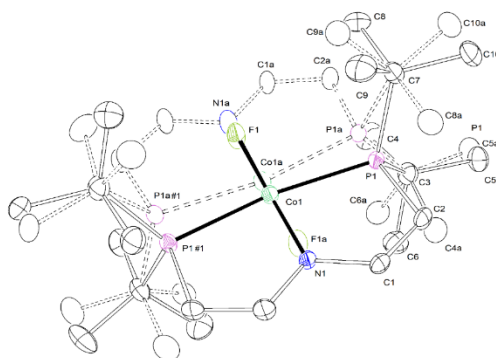


Figure 95: Thermal ellipsoid plot of **18** with the anisotropic displacement parameters drawn at the 50% probability level. The asymmetric unit contains a half disordered complex molecule. The disordered complex molecule was refined with population of 0.918(1) on the main domain using some restraints and constraints (SADI, RIGU, SIMU, EADP).

Table 16: Crystal data and structure refinement for **18**.

Identification code	mo_CW_SS_130619_0m_a (SSA72)	
Empirical formula	C ₂₀ H ₄₀ CoFNP ₂	
Formula weight	434.40	
Temperature	100(2) K	
Wavelength	0.71073 Å	
Crystal system	Monoclinic	
Space group	C2/c	
Unit cell dimensions	a = 21.6550(16) Å	α = 90°
	b = 7.5875(6) Å	β = 102.413(3)°
	c = 14.1343(10) Å	γ = 90°
Volume	2268.1(3) Å ³	
Z	4	
Density (calculated)	1.272 Mg/m ³	

Absorption coefficient	0.909 mm ⁻¹	
F(000)	932	
Crystal size	0.333 x 0.330 x 0.102 mm ³	
Crystal shape and color	Plate,	clear intense red
Theta range for data collection	2.852 to 30.603°	
Index ranges	-30<=h<=30, -9<=k<=10, -20<=l<=20	
Reflections collected	49565	
Independent reflections	3475 [R(int) = 0.0896]	
Completeness to theta = 25.242°	99.9 %	
Refinement method	Full-matrix least-squares on F ²	
Data / restraints / parameters	3475 / 558 / 214	
Goodness-of-fit on F ²	1.057	
Final R indices [I>2sigma(I)]	R1 = 0.0434,	wR2 = 0.1012
R indices (all data)	R1 = 0.0725,	wR2 = 0.1192
Largest diff. peak and hole	0.853 and -0.601 eÅ ⁻³	

5 Reference

- [1] C. J. Elsevier, J. G. de Vries, *The Handbook of Homogeneous Hydrogenation*, VCH-Wiley, Weinheim, **2007**.
- [2] H. U. Blaser, C. Malan, B. Pugin, F. Spindler, H. Steiner, M. Studer, *Adv. Synth. Catal.* **2003**, *345*, 103–151.
- [3] W. Ai, R. Zhong, X. Liu, Q. Liu, *Chem. Rev.* **2019**, *119*, 2876–2953.
- [4] L. Alig, M. Fritz, S. Schneider, *Chem. Rev.* **2019**, *119*, 2681–2751.
- [5] S. Koumi Ngoh, D. Njomo, *Renew. Sustain. Energy Rev.* **2012**, *16*, 6782–6792.
- [6] T. Zell, R. Langer, *ChemCatChem* **2018**, *10*, 1930–1940.
- [7] J. F. Young, J. A. Osborn, F. H. Jardine, G. Wilkinson, *Chem. Commun.* **1965**, 131–132.
- [8] J. A. Osborn, F. H. Jardine, J. F. Young, G. Wilkinson, *J. Chem. Soc. A Inorganic, Phys. Theor.* **1966**, 1711–1732.
- [9] M. Kitamura, T. Ohkuma, S. Inoue, N. Sayo, H. Kumobayashi, S. Akutagawa, T. Ohta, H. Takaya, R. Noyori, *J. Am. Chem. Soc.* **1988**, *110*, 629–631.
- [10] R. R. Schrock, J. A. Osborn, *J. Am. Chem. Soc.* **1976**, *98*, 2134–2143.
- [11] R. H. Crabtree, H. Felkin, G. E. Morris, *J. Organomet. Chem.* **1977**, *141*, 205–215.
- [12] H. Shimizu, I. Nagasaki, K. Matsumura, N. Sayo, T. Saito, *Acc. Chem. Res.* **2007**, *40*, 1385–1393.
- [13] B. J. A. Osborn, F. H. Jardine, J. F. Young, G. Wilkinson, *Chemical Communications (London)* **1965**, *7*, 131–132.
- [14] S. B. Duckett, C. L. Newell, R. Eisenberg, *J. Am. Chem. Soc.* **1994**, *116*, 10548–10556.
- [15] C. A. Meakin, P. Jesson, J. P.; Tolman, *J. Am. Chem. Soc.* **1972**, *2*, 3240–3242.
- [16] J. E. Perea-Buceta, I. Fernández, S. Heikkinen, K. Axenov, A. W. T. King, T. Niemi, M. Nieger, M. Leskelä, T. Repo, *Angew. Chemie - Int. Ed.* **2015**, *54*, 14321–14325.
- [17] J. Halpern, *Inorganica Chim. Acta* **1981**, *50*, 11–19.
- [18] B. C. Hui, B. R. James, *Can. J. Chem.* **1974**, *52*, 348–357.
- [19] B. R. James, *Adv. Organomet. Chem.* **1979**, *17*, 319–405.
- [20] M. W. Davis, R. H. Crabtree, *J. Org. Chem.* **1986**, *51*, 2655–2661.
- [21] A. S. C. Chan, J. J. Pluth, J. Halpern, *J. Am. Chem. Soc.* **1980**, *102*, 5952–5954.
- [22] J. Halpern, *Asymmetric Synth.* **1985**, 41–69.
- [23] J. Halpern, *Science* **1982**, *217*, 401–407.
- [24] S. Bhaduri, D. Mukesh, *Homogeneous Catalysis: Mechanisms and Industrial Applications, Second Edition.*, **2014**.
- [25] B. Heaton, *Mechanisms in Homogeneous Catalysis-A Spectroscopic Approach*, John Wiley & Sons, Weinheim, **2005**.
- [26] S. B. Duckett, R. E. Mewis, *Acc. Chem. Res.* **2012**, *45*, 1247–1257.
- [27] S. R. Muhammad, R. B. Greer, S. B. Ramirez, B. M. Goodson, A. R. Fout, *ACS Catal.* **2021**, *11*, 2011–2020.
- [28] C. Hansch, A. Leo, R. W. Taft, *Chem. Rev.* **1991**, *91*, 165–195.

- [29] X. K. Jiang, *Acc. Chem. Res.* **1997**, *30*, 283–289.
- [30] J. M. Dust, D. R. Arnold, *J. Am. Chem. Soc.* **1983**, 1221–1227.
- [31] M. Gómez-Gallego, M. A. Sierra, *Chem. Rev.* **2011**, *111*, 4857–4963.
- [32] R. M. Bullock, J. G. Chen, L. Gagliardi, P. J. Chirik, O. K. Farha, C. H. Hendon, C. W. Jones, J. A. Keith, J. Klosin, S. D. Minter, R. H. Morris, A. T. Radosevich, T. B. Rauchfuss, N. A. Strotman, A. Vojvodic, T. R. Ward, J. Y. Yang, Y. Surendranath, *Science* **2020**, 369.
- [33] M. Swart, Marcel; Costas, *Spin States in Biochemistry and Inorganic Chemistry: Influence on Structure and Reactivity*, John Wiley & Sons, **2015**.
- [34] Y. Wang, M. Wang, Y. Li, Q. Liu, *Chem* **2021**, *7*, 1180–1223.
- [35] M. R. Elsby, R. T. Baker, *Chem. Soc. Rev.* **2020**, *49*, 8933–8987.
- [36] W. Liu, B. Sahoo, K. Junge, M. Beller, *Acc. Chem. Res.* **2018**, *51*, acs.accounts.8b00262.
- [37] A. Mukherjee, D. Milstein, *ACS Catal.* **2018**, *8*, 11435–11469.
- [38] S. W. M. Crossley, C. Obradors, R. M. Martinez, R. A. Shenvi, *Chem. Rev.* **2016**, *116*, 8912–9000.
- [39] V. Arora, H. Narjinari, P. G. Nandi, A. Kumar, *Dalt. Trans.* **2021**, *50*, 3394–3428.
- [40] W. H. Harman, J. C. Peters, *J. Am. Chem. Soc.* **2012**, *134*, 5080–5082.
- [41] T. P. Lin, J. C. Peters, *J. Am. Chem. Soc.* **2014**, *136*, 13672–13683.
- [42] M. Shevlin, M. R. Friedfeld, H. Sheng, N. A. Pierson, J. M. Hoyt, L. C. Campeau, P. J. Chirik, *J. Am. Chem. Soc.* **2016**, *138*, 3562–3569.
- [43] K. V. Vasudevan, B. L. Scott, S. K. Hanson, *Eur. J. Inorg. Chem.* **2012**, 4898–4906.
- [44] B. J. Boro, E. N. Duesler, K. I. Goldberg, R. A. Kemp, *Inorg. Chem.* **2009**, *48*, 5081–5087.
- [45] I. M. Angulo, E. Bouwman, R. Van Gorkum, S. M. Lok, M. Lutz, A. L. Spek, *J. Mol. Catal. A Chem.* **2003**, *202*, 97–106.
- [46] C. Gonzalez-Arellano, E. Gutierrez-Puebla, M. Iglesias, F. Sanchez, *Eur. J. Inorg. Chem.* **2004**, 1955–1962.
- [47] M. P. Lücke, S. Yao, M. Driess, *Chem. Sci.* **2021**, *12*, 2909–2915.
- [48] P. L. Holland, *Acc. Chem. Res.* **2015**, *48*, 1696–1702.
- [49] P. J. Chirik, K. Wieghardt, *Science* **2010**, *327*, 794–795.
- [50] J. C. Ott, D. Bürgy, H. Guan, L. H. Gade, *Acc. Chem. Res.* **2021**, *55*, 857–868.
- [51] R. Xu, S. Chakraborty, S. M. Bellows, H. Yuan, T. R. Cundari, W. D. Jones, *ACS Catal.* **2016**, *6*, 2127–2135.
- [52] S. C. Bart, E. Lobkovsky, P. J. Chirik, *J. Am. Chem. Soc.* **2004**, *126*, 13794–13807.
- [53] R. P. Yu, J. M. Darmon, J. M. Hoyt, G. W. Margulieux, Z. R. Turner, P. J. Chirik, *ACS Catal.* **2012**, *2*, 1760–1764.
- [54] M. A. Schroeder, M. S. Wrighton, *J. Am. Chem. Soc.* **1976**, *98*, 551–558.
- [55] E. J. Daida, J. C. Peters, *Inorg. Chem.* **2004**, *43*, 7474–7485.
- [56] C. Bianchini, A. Meli, M. Peruzzini, P. Frediani, C. Bohanna, M. A. Esteruelas, L. A. Oro, *Organometallics* **1992**, *11*, 138–145.

- [57] N. Guo, M. Y. Hu, Y. Feng, S. F. Zhu, *Org. Chem. Front.* **2015**, *2*, 692–696.
- [58] R. M. Bullock, *Catalysis without Precious Metals*, John Wiley & Sons, **2011**.
- [59] R. J. Trovitch, E. Lobkovsky, E. Bill, P. J. Chirik, *Organometallics* **2008**, *27*, 1470–1478.
- [60] F. Kallmeier, R. Kempe, *Angew. Chemie - Int. Ed.* **2018**, *57*, 46–60.
- [61] S. Weber, K. Kirchner, *Acc. Chem. Res.* **2022**, *55*, 2740–2751.
- [62] S. M. W. Rahaman, D. K. Pandey, O. Rivada-Wheellaghan, A. Dubey, R. R. Fayzullin, J. R. Khusnutdinova, *ChemCatChem* **2020**, *12*, 5912–5918.
- [63] S. Weber, B. Stöger, L. F. Veiros, K. Kirchner, *ACS Catal.* **2019**, *9*, 9715–9720.
- [64] G. Zhang, B. L. Scott, S. K. Hanson, *Angew. Chemie - Int. Ed.* **2012**, *51*, 12102–12106.
- [65] R. Xu, S. Chakraborty, H. Yuan, W. D. Jones, *ACS Catal.* **2015**, *5*, 6350–6354.
- [66] Z. Yin, H. Zeng, J. Wu, S. Zheng, G. Zhang, *ACS Catal.* **2016**, *6*, 6546–6550.
- [67] J. Yuwen, S. Chakraborty, W. W. Brennessel, W. D. Jones, *ACS Catal.* **2017**, *7*, 3735–3740.
- [68] G. Zhang, J. Wu, H. Zeng, S. Zhang, Z. Yin, S. Zheng, *Org. Lett.* **2017**, *19*, 1080–1083.
- [69] G. Zhang, Z. Yin, J. Tan, *RSC Adv.* **2016**, *6*, 22419–22423.
- [70] G. Zhang, K. V. Vasudevan, B. L. Scott, S. K. Hanson, *J. Am. Chem. Soc.* **2013**, *135*, 8668–8681.
- [71] D. Gärtner, A. Welther, B. R. Rad, R. Wolf, A. J. Von Wangelin, *Angew. Chemie - Int. Ed.* **2014**, *53*, 3722–3726.
- [72] S. Gülak, O. Stepanek, J. Malberg, B. R. Rad, M. Kotora, R. Wolf, A. Jacobi Von Wangelin, *Chem. Sci.* **2013**, *4*, 776–784.
- [73] P. Büschelberger, D. Gärtner, E. Reyes-Rodriguez, F. Kreyenschmidt, K. Koszinowski, A. Jacobi von Wangelin, R. Wolf, *Chem. - A Eur. J.* **2017**, *23*, 3139–3151.
- [74] K. Tokmic, C. R. Markus, L. Zhu, A. R. Fout, *J. Am. Chem. Soc.* **2016**, *138*, 11907–11913.
- [75] K. Tokmic, A. R. Fout, *J. Am. Chem. Soc.* **2016**, *138*, 13700–13705.
- [76] S. R. Muhammad, J. W. Nugent, K. Tokmic, L. Zhu, J. Mahmoud, A. R. Fout, *Organometallics* **2019**, *38*, 3132–3138.
- [77] R. Mondal, A. K. Guin, G. Chakraborty, N. D. Paul, *Org. Biomol. Chem.* **2022**, *20*, 296–328.
- [78] J. R. Khusnutdinova, D. Milstein, *Angew. Chemie - Int. Ed.* **2015**, *54*, 12236–12273.
- [79] Q. Knijnenburg, A. D. Horton, H. Van Der Heijden, T. M. Kooistra, D. G. H. Hetterscheid, J. M. M. Smits, B. De Bruin, P. H. M. Budzelaar, A. W. Gal, *J. Mol. Catal. A Chem.* **2005**, *232*, 151–159.
- [80] Q. Knijnenburg, D. Hetterscheid, T. Martijn Kooistra, P. H. M. Budzelaar, *Eur. J. Inorg. Chem.* **2004**, 1204–1211.
- [81] Q. Knijnenburg, S. Gambarotta, P. H. M. Budzelaar, *J. Chem. Soc. Dalton Trans.* **2006**, 5442–5448.
- [82] S. Monfette, Z. R. Turner, S. P. Semproni, P. J. Chirik, *J. Am. Chem. Soc.* **2012**, *134*, 4561–4564.
- [83] M. R. Friedfeld, M. Shevlin, G. W. Margulieux, L. C. Campeau, P. J. Chirik, *J. Am. Chem. Soc.* **2016**, *138*, 3314–3324.
- [84] P. Viereck, S. Krautwald, T. P. Pabst, P. J. Chirik, *J. Am. Chem. Soc.* **2020**, *142*, 3923–3930.
- [85] S. P. Semproni, C. Milsmann, P. J. Chirik, *J. Am. Chem. Soc.* **2014**, *136*, 9211–9224.

- [86] T. J. Hebden, A. J. St. John, D. G. Gusev, W. Kaminsky, K. I. Goldberg, D. M. Heinekey, *Angew. Chemie - Int. Ed.* **2011**, *50*, 1873–1876.
- [87] M. R. Friedfeld, G. W. Margulieux, B. A. Schaefer, P. J. Chirik, *J. Am. Chem. Soc.* **2014**, *136*, 13178–13181.
- [88] T. Lin, J. C. Peters, *J. Am. Chem. Soc.* **2013**, *135*, 15310–15313.
- [89] F. Collins, *Isr. J. Chem.* **1990**, *31*, 55–66.
- [90] I. Wender, R. Levine, M. Orchin, *J. Am. Chem. Soc.* **1950**, *72*, 4375–4378.
- [91] P. D. Taylor, M. Orchin, *J. Org. Chem.* **1972**, *37*, 3913–3915.
- [92] S. Friedman, S. Metlin, A. Svedi, I. Wender, *J. Org. Chem.* **1959**, *24*, 1287–1289.
- [93] I. Wender, H. Greenfield, M. Orchin, *J. Am. Chem. Soc.* **1951**, *73*, 2656–2658.
- [94] J. Feder, H. M.; Halpern, *J. Am. Chem. Soc.* **1975**, *97*, 7186–7188.
- [95] T. E. Nalesnik, M. Orchin, *Organometallics* **1982**, *1*, 222–223.
- [96] S. L. Shevick, C. V. Wilson, S. Kotesova, D. Kim, P. L. Holland, R. A. Shenvi, *Chem. Sci.* **2020**, *11*, 12401–12422.
- [97] J. Hore, R. W. Broadhurst, *Prog. Nucl. Magn. Reson. Spectrosc.* **1993**, *25*, 345–402.
- [98] J. Sweany, R. L.; Halpern, *J. Am. Chem. Soc.* **1977**, *99*, 8335–8337.
- [99] S. W. Anferov, A. S. Filatov, J. S. Anderson, *ACS Catal.* **2022**, *12*, 9933–9943.
- [100] S. A. Green, S. W. M. Crossley, J. L. M. Matos, S. Vásquez-Céspedes, S. L. Shevick, R. A. Shenvi, *Acc. Chem. Res.* **2018**, *51*, 2628–2640.
- [101] K. Iwasaki, K. K. Wan, A. Oppedisano, S. W. M. Crossley, R. A. Shenvi, *J. Am. Chem. Soc.* **2014**, *136*, 1300–1303.
- [102] C. Obradors, R. M. Martinez, R. A. Shenvi, *J. Am. Chem. Soc.* **2016**, *138*, 4962–4971.
- [103] X. Ma, S. B. Herzon, *Chem. Sci.* **2015**, *6*, 6250–6255.
- [104] J. L. Kuo, J. Hartung, A. Han, J. R. Norton, *J. Am. Chem. Soc.* **2015**, *137*, 1036–1039.
- [105] L. Tang, E. T. Papish, G. P. Abramo, J. R. Norton, M. H. Baik, R. A. Friesner, A. Rappé, *J. Am. Chem. Soc.* **2006**, *128*, 11314.
- [106] J. Choi, L. Tang, J. R. Norton, *J. Am. Chem. Soc.* **2007**, *129*, 234–240.
- [107] J. Choi, M. E. Pulling, D. M. Smith, J. R. Norton, *J. Am. Chem. Soc.* **2008**, *130*, 4250–4252.
- [108] J. F. Garst, T. M. Bockman, R. Batlaw, *J. Am. Chem. Soc.* **1986**, *5*, 1689–1691.
- [109] C. Lorenc, H. B. Vibbert, C. Yao, J. R. Norton, M. Rauch, *ACS Catal.* **2019**, *9*, 10294–10298.
- [110] D. M. Smith, M. E. Pulling, J. R. Norton, *J. Am. Chem. Soc.* **2007**, *129*, 770–771.
- [111] G. Kiss, K. Zhang, S. L. Mukerjee, C. D. Hoff, *J. Am. Chem. Soc.* **1990**, *112*, 5657–5658.
- [112] I. L. Fedushkin, A. A. Skatova, V. A. Chudakova, G. K. Fukin, *Angew. Chemie - Int. Ed.* **2003**, *42*, 3294–3298.
- [113] S. Sandl, T. M. Maier, N. P. Van Leest, S. Kröncke, U. Chakraborty, S. Demeshko, K. Koszinowski, B. De Bruin, F. Meyer, M. Bodensteiner, C. Herrmann, R. Wolf, A. Von Jacobi Wangelin, *ACS Catal.* **2019**, *9*, 7596–7606.

- [114] O. S. Wenger, *J. Am. Chem. Soc.* **2018**, *140*, 13522–13533.
- [115] L. N. Mendelsohn, C. S. MacNeil, L. Tian, Y. Park, G. D. Scholes, P. J. Chirik, *ACS Catal.* **2021**, *11*, 1351–1360.
- [116] R. N. Perutz, B. Procacci, *Chem. Rev.* **2016**, *116*, 8506–8544.
- [117] A. J. Teator, H. Shao, G. Lu, P. Liu, C. W. Bielawski, *Organometallics* **2017**, *36*, 490–497.
- [118] E. Bergamaschi, F. Beltran, C. J. Teskey, *Chem. - A Eur. J.* **2020**, *26*, 5180–5184.
- [119] C. K. Prier, D. A. Rankic, D. W. C. MacMillan, *Chem. Rev.* **2013**, *113*, 5322–5363.
- [120] M. R. Schreier, B. Pfund, X. Guo, O. S. Wenger, *Chem. Sci.* **2020**, *11*, 8582–8594.
- [121] C. S. MacNeil, L. N. Mendelsohn, H. Zhong, T. P. Pabst, P. J. Chirik, *Angew. Chemie - Int. Ed.* **2020**, *59*, 8912–8916.
- [122] A. J. McNeece, K. A. Jesse, A. S. Filatov, J. E. Schneider, J. S. Anderson, *Chem. Commun.* **2021**, *57*, 3869–3872.
- [123] Y. Jing, X. Chen, X. Yang, *Organometallics* **2015**, *34*, 5716–5722.
- [124] L. M. Guard, T. J. Hebden, D. E. Linn, D. M. Heinekey, *Organometallics* **2017**, *36*, 3104–3109.
- [125] L. S. Merz, C. K. Blasius, H. Wadepohl, L. H. Gade, *Inorg. Chem.* **2019**, *58*, 6102–6113.
- [126] H. Alawisi, H. D. Arman, Z. J. Tonzetich, *Organometallics* **2021**, *40*, 1062–1070.
- [127] P. O. Lagaditis, B. Schluschaß, S. Demeshko, C. Würtele, S. Schneider, *Inorg. Chem.* **2016**, *55*, 4529–4536.
- [128] T. R. Dugan, E. Bill, K. C. Macleod, W. W. Brennessel, P. L. Holland, *Inorg. Chem.* **2014**, *53*, 2370–2380.
- [129] J. C. Ott, H. Wadepohl, M. Enders, L. H. Gade, *J. Am. Chem. Soc.* **2018**, *140*, 17413–17417.
- [130] R. R. Horn, G. W. Everett, *J. Am. Chem. Soc.* **1970**, *93*, 7173–7178.
- [131] B. Evans, K. M. Smith, G. N. L. Mar, D. B. Viscio, *J. Am. Chem. Soc.* **1977**, *99*, 7070–7072.
- [132] K. E. Schwarzans, *Angew. Chemie Int. Ed. English* **1970**, *9*, 946–953.
- [133] J. Silvestre, K. H. Theopold, E. K. Byrne, D. S. Richeson, *Organometallics* **1989**, *8*, 2001–2009.
- [134] R. A. Heintz, T. G. Neiss, K. H. Theopold, **1994**, 10–12.
- [135] R. Beck, M. Shoshani, S. A. Johnson, *Angew. Chemie - Int. Ed.* **2012**, *51*, 11753–11756.
- [136] C. J. Medforth, F. Shiao, G. N. La Mar, K. M. Smith, **1991**, 590–592.
- [137] N. L. Wieder, M. Gallagher, P. J. Carroll, D. H. Berry, *J. Am. Chem. Soc.* **2010**, *132*, 4107–4109.
- [138] I. Bertini, C. Luchinat, *Coord. Chem. Rev.* **1996**, *150*, 29–75.
- [139] B. Martin, J. Autschbach, *J. Chem. Phys.* **2015**, *142*, 054108.
- [140] S. Kuriyama, K. Arashiba, H. Tanaka, Y. Matsuo, K. Nakajima, K. Yoshizawa, Y. Nishibayashi, *Angew. Chemie - Int. Ed.* **2016**, *55*, 14291–14295.
- [141] S. Kuriyama, S. Wei, H. Tanaka, A. Konomi, K. Yoshizawa, Y. Nishibayashi, *Inorg. Chem.* **2022**, *61*, 5190–5195.
- [142] S. S. Rozenel, R. Padilla, J. Arnold, *Inorg. Chem.* **2013**, *52*, 11544–11550.
- [143] C. C. Hojilla Atienza, C. Milsman, S. P. Semproni, Z. R. Turner, P. J. Chirik, *Inorg. Chem.* **2013**,

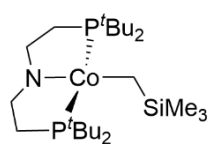
52, 5403–5417.

- [144] M. Ingleson, H. Fan, M. Pink, J. Tomaszewski, K. G. Caulton, *J. Am. Chem. Soc.* **2006**, *128*, 1804–1805.
- [145] J. Choi, Y. Lee, *Angew. Chemie* **2019**, *131*, 7012–7016.
- [146] D. L. M. Suess, C. Tsay, J. C. Peters, *J. Am. Chem. Soc.* **2012**, *134*, 14158–14164.
- [147] S. Sang, T. Unruh, S. Demeshko, L. I. Domenianni, N. P. van Leest, P. Marquetand, F. Schneck, C. Würtele, F. J. de Zwart, B. de Bruin, L. González, P. Vöhringer, S. Schneider, *Chem. - A Eur. J.* **2021**, *27*, 16978–16989.
- [148] C. L. Young, *IUPAC Solubility Data Series: Hydrogen and Deuterium*, Pergamon Press, New York, **1981**.
- [149] A. Sattler, *ACS Catal.* **2018**, *8*, 2296–2312.
- [150] F. Alonso, I. P. Beletskaya, M. Yus, *Chem. Rev.* **2002**, *102*, 4009–4092.
- [151] S. M. Barrett, B. M. Stratakes, M. B. Chambers, D. A. Kurtz, C. L. Pitman, L. Dempsey, A. J. M. Miller, *Chem. Sci.* **2020**, *11*, 6442–6449.
- [152] S. J. Blanksby, G. B. Ellison, *Acc. Chem. Res.* **2003**, *36*, 255–263.
- [153] J. Masnovi, E. G. Samsel, R. M. Bullock, *J. Chem. Soc. Chem. Commun.* **1989**, 1044–1045.
- [154] J. J. Warren, T. A. Tronic, J. M. Mayer, *Chem. Rev.* **2010**, *110*, 6961–7001.
- [155] E. Brunner, *J. Chem. Eng. Data* **1985**, *30*, 269–273.
- [156] D. J. Goebbert, P. G. Wenthold, *Int. J. Mass Spectrom.* **2006**, *257*, 1–11.
- [157] J. L. Dempsey, B. S. Brunschwig, J. R. Winkler, H. B. Gray, *Acc. Chem. Res.* **2009**, *42*, 1995–2004.
- [158] S. Stoll, A. Schweiger, *J. Magn. Reson.* **2006**, *178*, 42–55.
- [159] T. Casey, *MATLAB Cent. File Exch.* **2021**.
- [160] S. K. Sur, *J. Magn. Reson.* **1989**, *82*, 169–173.
- [161] G. A. Bain, J. F. Berry, *J. Chem. Educ.* **2008**, *85*, 532–536.
- [162] W. Haberditzl, *Angew. Chemie Int. Ed. English* **1966**, *5*, 288–298.
- [163] E. Bill, *JulX, Program for Simulation of Molecular Magnetic Data*, **2008**.
- [164] S. Straub, L. I. Domenianni, J. Lindner, P. Vöhringer, *J. Phys. Chem. B* **2019**, *123*, 7893–7904.
- [165] F. Neese, F. Wennmohs, U. Becker, C. Riplinger, *J. Chem. Phys.* **2020**, *152*, 224108.
- [166] Y. S. Lin, G. De Li, S. P. Mao, J. Da Chai, *J. Chem. Theory Comput.* **2013**, *9*, 263–272.
- [167] E. Van Lenthe, J. G. Snijders, E. J. Baerends, *J. Chem. Phys.* **1996**, *105*, 6505–6516.
- [168] F. Weigend, R. Ahlrichs, *Phys. Chem. Chem. Phys.* **2005**, *7*, 3297–3305.
- [169] F. Neese, F. Wennmohs, A. Hansen, U. Becker, *Chem. Phys.* **2009**, *356*, 98–109.
- [170] G. L. Stoychev, A. A. Auer, F. Neese, *J. Chem. Theory Comput.* **2017**, *13*, 554–562.
- [171] V. Barone, M. Cossi, *J. Phys. Chem. A* **1998**, *102*, 1995–2001.
- [172] D. M. York, *J. Phys. Chem. A* **1999**, *103*, 11040–11044.

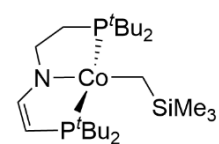
- [173] E. Van Lenthe, E. J. Baerends, *J. Comput. Chem.* **2003**, *24*, 1142–1156.
- [174] G. te Velde, F. M. Bickelhaupt, E. J. Baerends, C. Fonseca Guerra, S. J. A. van Gisbergen, J. G. Snijders, T. Ziegler, *J. Comput. Chem.* **2001**, *22*, 931–967.
- [175] S. Korchak, S. Yang, S. Mamone, S. Glöggl, *ChemistryOpen* **2018**, *7*, 344–348.

6 Appendix

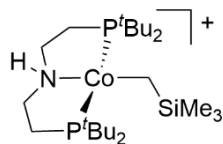
6.1 List of compounds



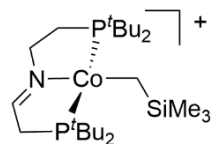
1



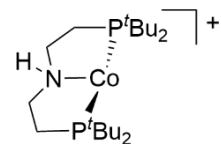
2



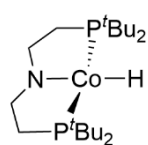
3⁺



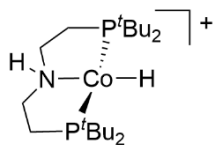
4⁺



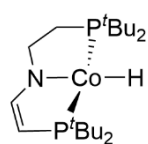
5⁺



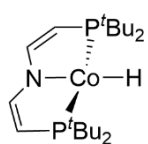
6



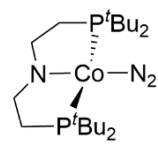
7⁺



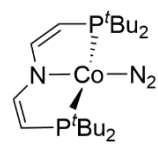
8



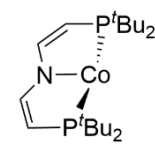
9



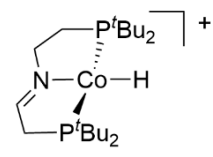
10



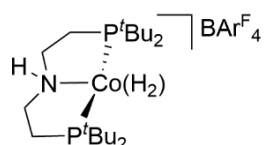
11



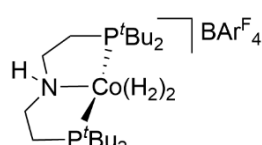
12



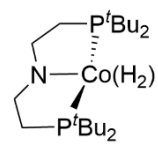
13⁺



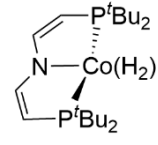
14



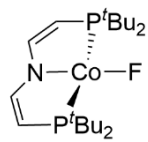
15



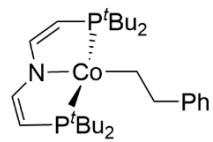
16



17



18



19

6.2 List of abbreviations

Abkürzungen	vollständige Namen
δ	chemical shift
λ	wavelength
μ_{eff}	effective magnetic moment
μ_{B}	bohr magneton
Ar	ambiguous: Aryl group or Argon
B	magnetic flux density
$[\text{BAr}^{\text{F}_4}]^-$	tetrakis(3,5-bis(trifluoromethyl)phenyl)borate
BDE	bond dissociation energy
BDFE	bond dissociation free energy
BINAP	racemic-2,2'-Bis(diphenylphosphino)-1,1'-binaphthyl
c	concentration
COD	1,5-cyclooctadiene
Cy	cyclohexyl
d	day
DCM	dichloromethane
DFT	density functional theory
EPR	electron Paramagnetic Resonance
equiv.	equivalent
h	hour
H ₂	dihydrogen molecule
HAT	Hydrogen atom transfer
HFI	Hyperfine Interaction
IR	Infrared
KIE	Kinetic isotope effect
L ¹	$\text{N}(\text{CH}_2\text{CH}_2^t\text{Bu}_2\text{P})_2$
L ¹ H	$\text{HN}(\text{CH}_2\text{CH}_2^t\text{Bu}_2\text{P})_2$
L ²	$\text{N}(\text{CH}_2\text{CH}_2^t\text{Bu}_2\text{P})(\text{CHCH}^t\text{Bu}_2\text{P})$
L ² H	$\text{N}(\text{CHCH}_2^t\text{Bu}_2\text{P})(\text{CH}_2\text{CH}_2^t\text{Bu}_2\text{P})$
L ³	$\text{N}(\text{CHCH}^t\text{Bu}_2\text{P})_2$

LIFDI	liquid Field Desorption Ionisation
Me	methyl group
min	minute
MLCT	metal to Ligand Charge Transfer
MS	mass spectrometry
NMR	nuclear Magnetic Resonance
PDI	pyridine(diimine) ligand
Ph	phenyl group
ppm	parts per million
r.t.	room Temperature
SQUID	superconducting Quantum Interference Device
<i>t</i> Bu	<i>tert</i> -butyl group
THF	tetrahydrofuran
TIP	temperature Independent Paramagnetism
UV/vis	ultraviolet / visible
vs.	versus

6.3 Curriculum Vitae

Name: Sier Sang
Nationality: Chinese
Place of birth: Nei Mongol, China
Date of birth: 15.02.1993

Education

07/2018 – present Graduate Student
Georg-August Universität Göttingen
Institute of Inorganic Chemistry
Research Group of Prof. Dr. Sven Schneider

10/2015 – 05/2018 Master of Science in Chemistry
Georg-August Universität Göttingen
Master thesis: Mechanistic investigation of cobalt-catalysed olefin hydrogenation

10/2011 – 07/2015 Bachelor of Engineering in Chemical Engineering and Technology
Dalian University of Technology, China
Bachelor thesis: Synthesis and Application of Fluorescent Dyes Targeted Protooncogene Pim-1 Kinase

Publication and Presentation

2018 Oral presentation: Koordinationstreffen in Heidelberg
Investigation of Active Cobalt(II) Pincer Complexes for Olefin Hydrogenation

2021 Oral presentation: Göttinger Chemie Forum
Photo-Initiated Cobalt Catalyzed Radical Olefin Hydrogenation

2021 Publication: S. Sang, T. Unruh, Vöhringer, S. Schneider et. al., Photo-Initiated Cobalt Catalyzed Radical Olefin Hydrogenation, [Chem. Eur. J. 2021, 27, 16978-16989.](#)